

# Adsorption of alkyl amides: monolayer structures and mixing behaviour

Tej Bhide

Jesus College

University of Cambridge

October 2010



This dissertation is submitted for the degree of Doctor of Philosophy

# **Preface**

This dissertation is submitted for the degree of Doctor of Philosophy at the University of Cambridge, U.K. and describes research carried out under the supervision of Dr. S. M. Clarke between October 2007 and September 2010. This dissertation is the result of my own work and includes nothing which is the outcome of work done in collaboration except where specifically indicated in the text. No part of this dissertation has been or is currently being submitted for any other qualification. This dissertation does not exceed 60,000 words in length.

T. Bhide

October 2010

## **Acknowledgements**

I would like to thank my supervisor, Stuart Clarke, for his constant encouragement and enthusiasm. I cannot put into words the amount of support and guidance he has given me, and I would like to specially thank him for providing feedback on my thesis in record time. I would also like to thank Tom Arnold for being a great source of ideas, for his valuable contributions to my work and for providing very useful advice throughout my course. I am indebted to the Nehru Trust for Cambridge University for providing me with a scholarship.

Many thanks are due to Tamsin Philips for her help in all the experiments, and also for her wisdom in answering all my questions. Special thanks to everyone at the BPI, especially everyone in Stuart's group, for all their help. My close friends have always been there for me, and have made my time at Cambridge deeply memorable.

Words cannot express my deepest gratitude to my family for their love, support and encouragement.

## Adsorption of alkyl amides: monolayer structures and mixing behaviour

Tej Bhide

### Abstract

In this work monolayers of alkyl amides adsorbed on a graphite surface have been successfully identified and investigated using a combination of synchrotron X-ray and neutron diffraction and Differential Scanning Calorimetry (DSC). Exceptionally stable solid layers have been observed at temperatures well above the bulk melting point, at both high multilayer coverages and, very unusually, at sub-monolayer coverages. The molecular structure of the two-dimensional crystals of these alkyl amides has been obtained from diffraction and interpreted in terms of the subtle intermolecular interactions, particularly the contribution of hydrogen bonding in monolayer assembly. Thermodynamic information provides insight on the mixing behaviour in adsorbed amide layers.

A systematic study on the variation in monolayer crystal structures with alkyl chain length (between five and sixteen carbon atoms) of saturated alkyl amides using diffraction identifies that all the amide molecules investigated lie flat on the graphite surface. An odd-even variation is observed in the monolayer crystal structures and this is supported by the melting enthalpies of the amides determined by DSC. The structure of the even members is found to support the qualitative monolayer arrangement proposed by an STM report of one member of the series, but with more quantitative insight here. Significantly, a new monolayer symmetry group for odd members of the homologous series has been identified. Characteristics of the hydrogen bond geometry between the molecules in the solid monolayers are reported exploiting the high level of detail available from the diffraction techniques.

Secondly, the formation of solid monolayers of unsaturated alkyl amides has been reported and their crystal structures determined. This is believed to be the first report of these monolayer structures. The position and nature of the double bond have an important effect in the stability of the monolayer. Unusually, certain unsaturated amides that have a double bond conjugated with the amide group are found to form considerably more stable layers than their saturated

homologues. The abnormally high melting points and enhanced stability of amide monolayers have been attributed to the existence of a network of hydrogen bonds in the layer.

Phase diagrams obtained by DSC for binary mixtures of alkyl amides on graphite have been quantitatively analysed using a combination of thermodynamic models (ideal, eutectic and the regular solution models). The determined mixing behaviour is supported by conclusions based on the monolayer crystal structures of the individual components calculated using diffraction. Saturated amide mixtures that have the same plane group symmetry are found to mix non-ideally in the solid layer and phase separate if the symmetry is different, whereas the mixing behaviour of saturated/unsaturated amides considered here was found to depend on the nature of the double bond (*cis/trans*).

Results from an initial investigation into the adsorption of alkyl amides at the polymer/air interface are also presented. This complements the study above and provides an alternative situation where amide monolayers have a central role. A reduction in the coefficient of friction is seen with increasing bulk concentration of the amide and with increasing time indicating migration of the amide to the surface. A powerful combination of surface reflection techniques including neutron and X-ray reflection and ellipsometry have been used to gain uniquely quantitative insight into this system. Initial estimates of the concentration of amides at the polystyrene surface are presented for the first time.

# Table of Contents

|                        |    |
|------------------------|----|
| Preface.....           | i  |
| Abstract.....          | ii |
| Acknowledgements.....  | iv |
| Table of contents..... | v  |

## Chapter 1

|  |            |
|--|------------|
| <b>Introduction.....</b>                         | <b>1-1</b> |
| 1.1 Background.....                              | 1-1        |
| 1.2 Adsorbed monolayers on graphite.....         | 1-2        |
| 1.2.1 Noble gases.....                           | 1-3        |
| 1.2.2 Diatomics.....                             | 1-6        |
| 1.2.3 Dipolar adsorbates.....                    | 1-7        |
| 1.2.4 Alkanes.....                               | 1-8        |
| 1.2.5 Alkyl species and recent developments..... | 1-10       |
| 1.3 Alkyl amides.....                            | 1-12       |
| 1.3.1 Properties and uses.....                   | 1-12       |
| 1.3.2 Amides on surfaces.....                    | 1-14       |
| 1.3.3 Bulk behaviour of amides.....              | 1-17       |
| 1.3.4 Nomenclature.....                          | 1-18       |
| 1.4 Intermolecular interactions.....             | 1-19       |

|  |      |
|--|------|
| 1.4.1 Hydrogen bonding .....             | 1-19 |
| 1.4.2 Van der Waals forces .....         | 1-20 |
| 1.4.3 Dipole interactions .....          | 1-21 |
| 1.5 Summary and scope of this work ..... | 1-21 |
| 1.6 References .....                     | 1-23 |

## Chapter 2

|  |            |
|--|------------|
| <b>Diffraction - Theory and Experiment .....</b>         | <b>2-1</b> |
| 2.1 Properties of X-rays and neutrons .....              | 2-1        |
| 2.2 Interaction of X-rays and neutrons with matter ..... | 2-2        |
| 2.3 Diffraction in 3D .....                              | 2-4        |
| 2.4 Diffraction from adsorbed layers .....               | 2-6        |
| 2.4.1 Diffraction peak positions .....                   | 2-6        |
| 2.4.2 Diffraction peak intensities .....                 | 2-7        |
| 2.4.3 Peak shape – preferred orientation .....           | 2-9        |
| 2.4.4 Diffraction peak widths .....                      | 2-10       |
| 2.5 Correction factors .....                             | 2-11       |
| 2.5.1 Absorption corrections .....                       | 2-11       |
| 2.5.2 The Lorentz and polarization corrections .....     | 2-11       |
| 2.5.3 The Temperature factor .....                       | 2-12       |
| 2.5.4 Multiplicity factor .....                          | 2-12       |
| 2.6 Symmetry Considerations .....                        | 2-13       |
| 2.7 X-ray and neutron facilities .....                   | 2-14       |

|   |      |
|---|------|
| 2.7.1 Synchrotrons X-ray sources .....                                    | 2-14 |
| 2.7.2 Neutron sources .....   | 2-16 |
| 2.7.3 Optics .....  | 2-17 |
| 2.7.4 Detectors .....   | 2-18 |
| 2.8 Instrumentation .....   | 2-19 |
| 2.8.1 Materials science X04SA beam line .....                             | 2-19 |
| 2.8.2 Beamline I11 .....  | 2-20 |
| 2.8.3 Diffractometer D20 .....  | 2-21 |
| 2.9 Sample preparation .....  | 2-22 |
| 2.10 Data treatment .....   | 2-23 |
| 2.10.1 Scattering from the graphite substrate .....                       | 2-23 |
| 2.10.2 Scattering from the amide monolayer adsorbed on graphite .....     | 2-25 |
| 2.10.3 Optimisation of experimental conditions .....                      | 2-26 |
| 2.10.4 Wavelength Calibration and offset correction .....                 | 2-27 |
| 2.11 Data fitting and structural solution .....                           | 2-29 |
| 2.11.1 Generating the coordinates of all atoms in an amide molecule ..... | 2-29 |
| 2.11.2 The model .....  | 2-31 |
| 2.11.3 Preferred orientation and peak shape parameters .....              | 2-31 |
| 2.12 References .....   | 2-33 |

## **Chapter 3**

|   |            |
|---|------------|
| <b>Mixing and Calorimetry .....</b>                         | <b>3-1</b> |
| 3.1 Mixing Theory .....                                     | 3-1        |
| 3.1.1 Ideal Mixing .....                                    | 3-1        |
| 3.1.2 Eutectic behaviour .....                              | 3-4        |
| 3.1.3 Non-ideal mixtures – The regular solution model ..... | 3-6        |

|  |      |
|--|------|
| 3.1.4 Preferential adsorption .....                    | 3-8  |
| 3.1.5 Other mixing models.....                         | 3-8  |
| 3.2 Differential Scanning Calorimetry.....             | 3-10 |
| 3.2.1 The technique.....                               | 3-10 |
| 3.2.2 Melting of pure materials.....                   | 3-12 |
| 3.2.3 Thermograms for eutectic and ideal mixtures..... | 3-14 |
| 3.3 Experimental details.....                          | 3-17 |
| 3.4 Summary .....                                      | 3-18 |
| 3.5 References.....                                    | 3-19 |

## Chapter 4

|  |            |
|--|------------|
| <b>Saturated amides - diffraction.....</b>                                   | <b>4-1</b> |
| 4.1 Preliminary analysis.....  | 4-1        |
| 4.1.1 In-plane tilt of the molecules with respect to the $a$ -direction..... | 4-7        |
| 4.1.2 Commensurate monolayers.....   | 4-8        |
| 4.2 Monolayer structure fitting .....  | 4-9        |
| 4.3 Hydrogen bond geometry .....   | 4-11       |
| 4.4 Even chain length amides .....   | 4-12       |
| 4.4.1 Hexanamide (C6:0 amide) .....  | 4-12       |
| 4.4.2 Octanamide (C8:0 amide).....   | 4-14       |
| 4.4.3 Decanamide (C10:0 amide) .....   | 4-15       |
| 4.4.4 Dodecanamide (C12:0 amide) .....                                       | 4-16       |
| 4.4.5 Tetradecanamide (C14:0 amide) and hexadecanamide (C16:0 amide) .....   | 4-17       |
| 4.4.6 Discussion.....  | 4-18       |
| 4.5 Odd chain length amides.....   | 4-20       |

|   |      |
|---|------|
| 4.5.1 Pentanamide (C5:0 amide).....       | 4-21 |
| 4.5.2 Heptanamide (C7:0 amide).....       | 4-22 |
| 4.5.3 Nonanamide (C9:0 amide).....        | 4-26 |
| 4.5.4 Undecanamide (C11:0 amide) .....    | 4-27 |
| 4.5.5 Discussion.....                     | 4-27 |
| 4.6 Melting of the solid monolayers ..... | 4-29 |
| 4.7 High coverage behaviour .....         | 4-32 |
| 4.8 Summary .....                         | 4-33 |
| 4.9 References.....                       | 4-34 |

## Chapter 5

|   |            |
|---|------------|
| <b>Unsaturated amides - diffraction</b> .....         | <b>5-1</b> |
| 5.1 Experimental details and structural solution..... | 5-2        |
| 5.2 Amides with six carbons.....                      | 5-3        |
| 5.3 C9:1 t-2 amide.....                               | 5-5        |
| 5.4 C11:1 c-10 amide.....                             | 5-7        |
| 5.5 C12:1 c-5 amide.....                              | 5-9        |
| 5.6 Discussion and summary .....                      | 5-11       |
| 5.7 References.....                                   | 5-12       |

## Chapter 6

|   |            |
|---|------------|
| <b>Calorimetry</b> .....                          | <b>6-1</b> |
| 6.1 DSC of pure amides adsorbed on graphite ..... | 6-2        |
| 6.1.1 DSC data.....                               | 6-3        |

|  |      |
|--|------|
| 6.1.2 Trends in monolayer melting points .....                                       | 6-5  |
| 6.1.3 Monolayer melting enthalpies.....  | 6-6  |
| 6.1.4 Unsaturated amides.....  | 6-7  |
| 6.2 Binary mixtures of adsorbed amides.....  | 6-8  |
| 6.2.1 Saturated/saturated amide mixtures .....                                       | 6-9  |
| 6.2.2 Saturated/unsaturated amide mixtures .....                                     | 6-15 |
| 6.3 Coverage dependence study of undecanamide (C11:0 amide) on graphite by DSC ..... | 6-23 |
| 6.3.1 C11:0 coverage dependence - introduction.....                                  | 6-23 |
| 6.3.2 C11:0 coverage dependence - experimental details.....                          | 6-26 |
| 6.3.3 C11:0 coverage dependence - results and discussion .....                       | 6-26 |
| 6.4 A note on purities.....  | 6-28 |
| 6.5 Summary.....   | 6-29 |
| 6.6 References.....  | 6-30 |

## Chapter 7

|   |            |
|---|------------|
| <b>Adsorption at the Polymer/Air interface.....</b> | <b>7-1</b> |
| 7.1 Background.....                                 | 7-2        |
| 7.1.1 Neutron reflection .....                      | 7-2        |
| 7.1.2 X-ray reflectivity.....                       | 7-6        |
| 7.1.3 Ellipsometry.....                             | 7-7        |
| 7.1.4 Coefficient of friction measurements.....     | 7-8        |
| 7.2 Experimental details.....                       | 7-9        |
| 7.2.1 Materials .....                               | 7-9        |
| 7.2.2 Sample preparation and characterisation ..... | 7-10       |
| 7.3 Results and Discussion .....                    | 7-11       |
| 7.3.1 Coefficient of friction .....                 | 7-11       |

|                               |      |
|-------------------------------|------|
| 7.3.2 X-ray reflectivity..... | 7-14 |
| 7.3.3 Neutron reflection..... | 7-17 |
| 7.4 Summary.....              | 7-25 |
| 7.5 References.....           | 7-26 |

## Chapter 8

|  |            |
|--|------------|
| <b>Future directions.....</b>                    | <b>8-1</b> |
| 8.1 Hydrogen bonded monolayers: alkyl ureas..... | 8-1        |
| 8.1.1 Introduction.....                          | 8-1        |
| 8.1.2 Experimental details.....                  | 8-1        |
| 8.1.3 Results and further work.....              | 8-2        |
| 8.2 Amides at the polymer/air interface.....     | 8-3        |
| 8.3 Mixing in amide monolayers on graphite.....  | 8-4        |
| 8.3.1 X-ray diffraction.....                     | 8-4        |
| 8.3.2 High coverage mixtures by DSC.....         | 8-6        |
| 8.4 Molecular dynamics simulations.....          | 8-6        |
| 8.5 Longer term directions.....                  | 8-7        |
| 8.6 References.....                              | 8-8        |

## Chapter 9

|                                |            |
|--------------------------------|------------|
| <b>Concluding remarks.....</b> | <b>9-1</b> |
|--------------------------------|------------|

## Appendices

|                                   |     |
|-----------------------------------|-----|
| A Fitted atomic coordinates ..... | A-1 |
| B Sample purities .....           | B-1 |

# Chapter 1

## Introduction

---

### 1.1 Background

Adsorbed molecular layers are the characteristic feature of many important academic and industrial problems: some applications include detergency, colloidal stability, catalysis and friction. Alkyl amides (and their salts) have several commercial surface applications including friction modifiers at polymer surfaces [1] and as corrosion inhibitors [2]. In the bulk, the amide hydrogen bond plays an important role in the formation of higher structures in proteins, in DNA and it is also predominant in synthetic species such as nylon [3].

In general, molecules can be held on surfaces either by intermolecular interactions alone (physisorption) or by the formation of covalent bonds (chemisorption). Physisorbed molecules typically have low enthalpies of adsorption (approximately  $<20$  kJ/mol, depending on the molecule adsorbed) and the adsorption process is often reversible (e.g. molecular species on graphite). Chemisorption is characterised by higher enthalpies ( $20 < \Delta H < 800$  kJ/mol) [4] (e.g. oxygen on gold).

Lamellar solids such as graphite are advantageous as adsorbents owing to their chemical inertness and near-ideal uniform surface [5]. Other popular substrates for studying molecular monolayers include Magnesium Oxide (MgO), Boron Nitride (BN), and metals such as gold, silver, platinum etc. Physisorbed monolayers, of alkyl amides on graphite, have been the focus of this work as intermolecular interactions within the adsorbed monolayer such as melting,

hydrogen bonding and phase transitions can be probed, without being dominated by strong substrate-adsorbate forces. An understanding of these non-covalent interactions in adsorbed layers can underpin their applications for a variety of commercial and academic problems.

This chapter begins with a review of physisorbed layers on graphite, and a detailed description of studies concerning the adsorption of alkyl amides specifically on different surfaces is provided. The bulk behaviour of alkyl amides is discussed, and a comparison between relevant non-covalent interactions present in 2D molecular layers is made. Finally, the scope of this work is outlined.

## 1.2 Adsorbed monolayers on graphite

Adsorbed monolayers provide several challenges to study: techniques that are sensitive to the tiny quantities of material present in the monolayer without being affected by the much larger quantities of bulk materials are required to study these systems. A wide variety of experimental and theoretical approaches have been used to characterise the surface behaviour of adsorbates on graphite and other substrates. These include calorimetry, scanning probe microscopy, X-ray and neutron scattering techniques, electron diffraction, molecular dynamics simulations, adsorption isotherms, NMR etc. A summary of some of these studies can be found in reviews [6-8].

As explained above, exfoliated graphite (prepared by rapid heating of intercalated graphite at high temperatures) has become popular in adsorption studies since it meets conflicting requirements: a large surface area (typically 10-50 m<sup>2</sup>/g) and small extent of surface heterogeneity [7]. The energetic uniformity of the basal planes of graphite makes it ideal for the study of 2D phase transitions, since shallow potential wells do not hinder the mobility of the adsorbed molecules [8]. Graphite substrates also have an advantage from theoretical standpoints that relatively reliable empirical inter-atomic potentials are available for representing the molecule/substrate interactions [9].

This section provides an overview of the structure and phase behaviour of two-dimensional layers physisorbed on the surface of graphite. The adsorption of gaseous substances such as noble gases and other simple compounds is reviewed first, where the surface ordering is

dependent only on the van der Waals interactions between the molecules and molecule/substrate interactions. Progressing in increasing complexity of intermolecular interactions, polar molecules are discussed next, followed by longer chain alkyl adsorbates which have additional non-covalent interactions such as hydrogen bonds.

### 1.2.1 Noble gases

Early work focused on understanding the adsorption behaviour of atomic species such as the noble gases xenon [10, 11], krypton [12, 13], argon [14], neon [15] and helium [16-18]. Structures of the adsorbed phases were calculated using Low Energy Electron Diffraction (LEED) and X-ray and neutron diffraction techniques. Studies of molecular adsorbates such as nitrogen [19-22], oxygen [23], hydrogen [24-26] and carbon monoxide [22] can also be found in literature. A variety of 2D transitions such as '2D gas-liquid-solid' transitions, and 'commensurate-incommensurate' transitions have been reported for many systems [8]. Detailed reviews and reference lists can be found in [5-8, 27, 28]

It is interesting to discuss the phase behaviour of xenon and krypton below.

#### 1.2.1.1 Xenon

Thomy et al. [5] studied the adsorption of Xenon on graphite using volumetric methods. The phase diagram obtained illustrates successive transitions of the 'Solid-Liquid-Gaseous' states of the Xe/Graphite system with increasing coverage (below one monolayer) as shown in Figure 1-1.

Between 100.1 and 117 K, the xenon layer undergoes two first order phase transitions where it passes through three distinct 2D states: "gaseous" (G), "liquid" (L) and "solid" (S). The phase diagram exhibits 2D gas, liquid and solid coexistence at the triple point. The triple point and critical point have been reported as (100.1 K,  $2.4 \times 10^{-4}$  Torr) and (117 K,  $1.0 \times 10^{-2}$  Torr) respectively [5].

The monolayer of xenon on graphite condenses in the major part of the phase diagram in a hexagonal incommensurate structure [27]. Xenon undergoes a 2D incommensurate-commensurate phase transition [10, 27] on increasing the coverage close to a monolayer. The noble gases are all found to form such simple closed-packed structures. The arrangement of xenon atoms on the substrate in registry with the underlying graphite in the (110) direction is shown in Figure 1-2.

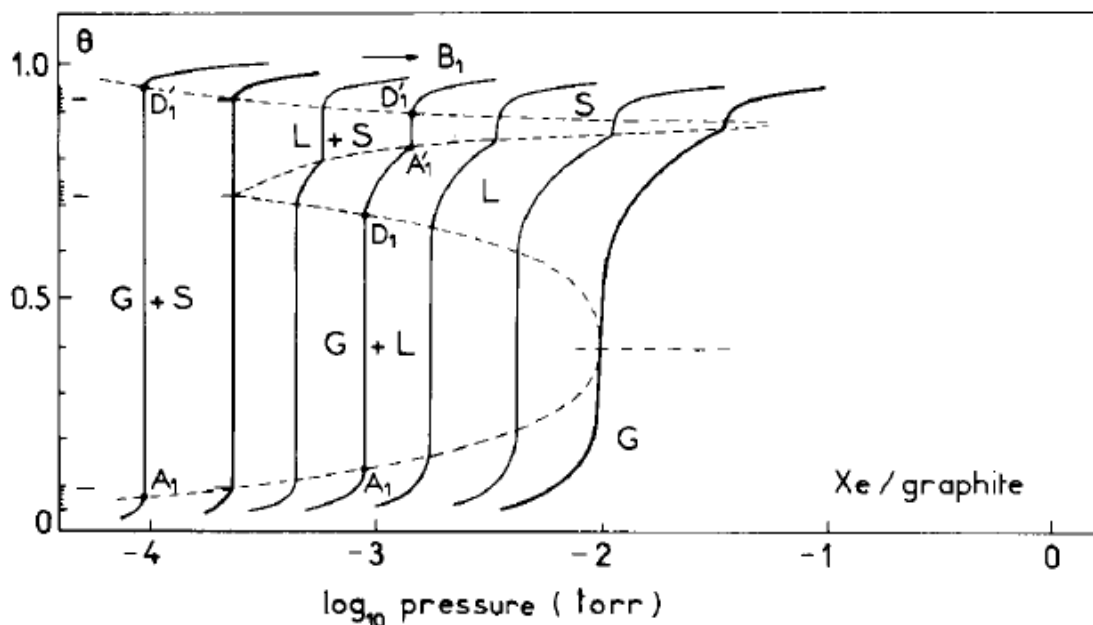


**Figure 1-1** Phase diagram showing the evolution of Xenon adsorption isotherms between 97 and 117 K on a homogeneous graphite surface ( $\theta$  is the coverage of xenon). Isotherm temperatures are: 97.4, 100.1, 102.4, 105.4, 108.3, 112.6, and 117.0 K. From [5].

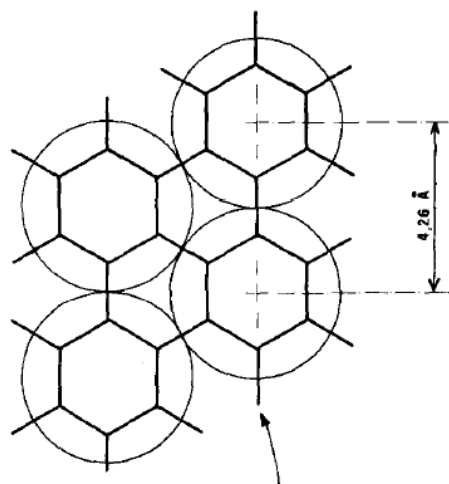


**Figure 1-2** Orientation of atoms in the commensurate  $(\sqrt{3} \times \sqrt{3}) R30^\circ$  phase of xenon. From [11].

## 1.2.1.2 Krypton

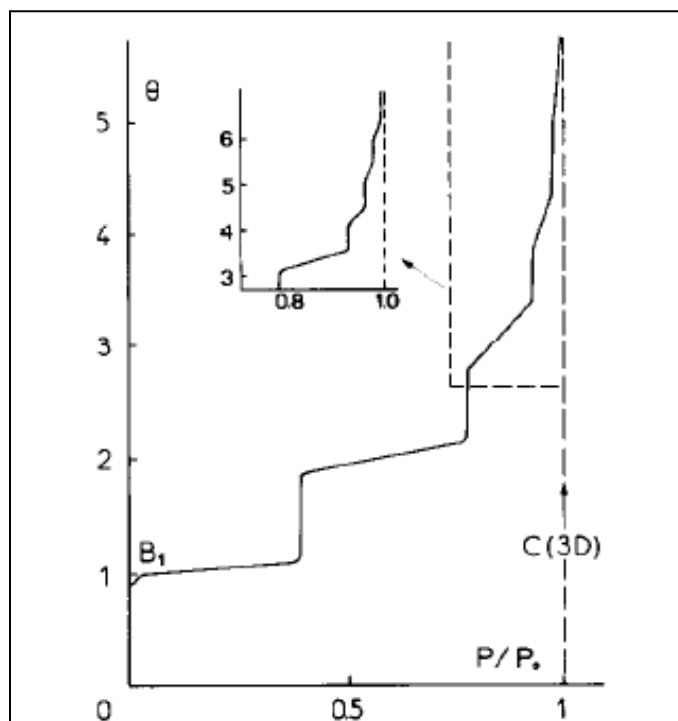


**Figure 1-3** Adsorption isotherm of krypton on graphite at 77.3 K showing the formation of successive layers above a monolayer (from [8]).  $P/P_0$  is the ratio of the vapour pressure of the gaseous krypton to the saturation vapour pressure at 77.3 K and  $\theta$  is the coverage. Each 'step' represents an additional layer being formed.

The 2D phase diagram of krypton adsorbed on graphite has also been measured by Thomy et al. [5]. Unlike xenon, there is no liquid-gas coexistence domain in the phase diagram [27], and the critical point has been reported to be (86 K,  $5.7 \times 10^{-3}$  Torr). Krypton exists as a commensurate solid in a large part of the phase diagram and a commensurate-incommensurate transition is observed on increasing temperature. Figure 1-3 shows an example adsorption isotherm of krypton which has distinct 'steps' that represent an additional layer being formed.

Similar behaviour has been reported for the other noble gases. Step-wise isotherms indicate that the molecular films grow continuously from the 2D to the 3D state. Argon has 2D gas, liquid and incommensurate hexagonal solid phases and neon was also found to exhibit three phases, including a commensurate solid phase [27].

## 1.2.2 Diatomics

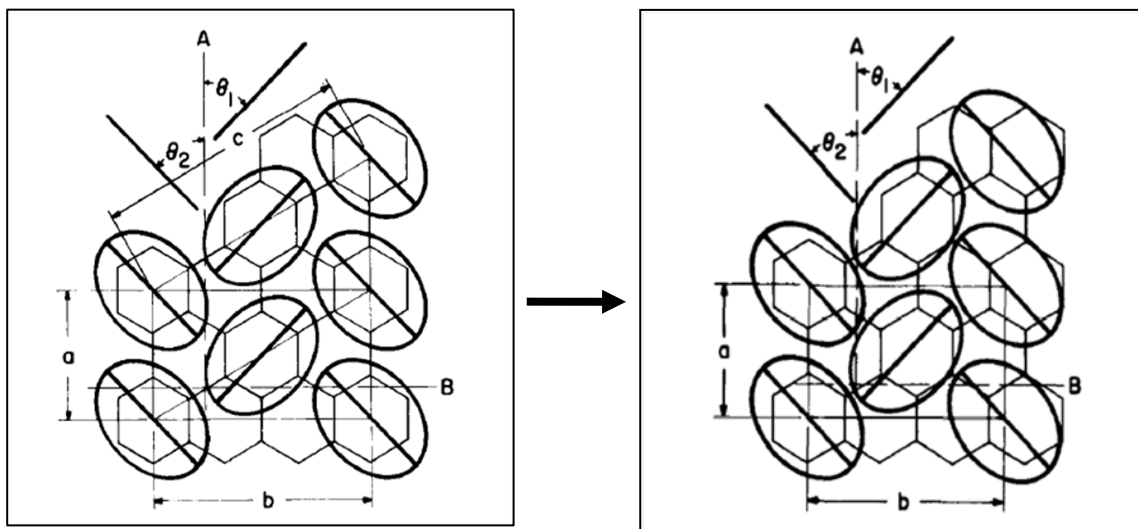


**Figure 1-4** ( $\sqrt{3} \times \sqrt{3}$ )  $R30^\circ$  commensurate structure of  $N_2$  on graphite and the triangular incommensurate phase calculated using LEED. The molecules are drawn as ellipses. The phase transition was observed to occur between 31 and 35 K (images from [29]). The unit cell parameters  $a$  and  $b$  in this figure are opposite to the convention used in this work: the longer length of the unit cell is denoted as  $a$  here.

Carbon monoxide (CO) and molecular nitrogen ( $N_2$ ) are both quadrupolar molecules and have a negligible (or no) dipole moment. CO has a quadrupole moment about 50 % greater than  $N_2$ , and has a small dipole (0.11 D) which does not have any effect on ordering until below 10 K [30].

Both CO and  $N_2$  molecules were found to be in registry with the underlying hexagons as shown in Figure 1-4: the centres of mass assume the ( $\sqrt{3} \times \sqrt{3}$ )  $R30^\circ$  commensurate structure with the nearest-neighbour separation of 0.426 nm which is longer than that found in the bulk solids (0.399 nm) [22, 29]. The surface-molecule interactions constrain the molecular axes of both CO and  $N_2$  to lie parallel to the graphite surface and quadrupolar interactions combined with packing requirements ensure that the molecules are arranged in a herringbone lattice [30]. Both molecules undergo an orientation phase transition below 30 K.  $N_2$  was found to undergo a commensurate-incommensurate transition to form an incommensurate phase between 31 and 35 K (Figure 1-4) [29].

### 1.2.3 Dipolar adsorbates

Simple dipolar adsorbates were interesting to study to observe the effects of an electric dipole present in the molecules on ordering in the adsorbed layer. A study of the structure and dynamics of ammonia ( $\text{NH}_3$ ) adsorbed on graphite was made by R. K. Thomas *et. al.* [31, 32]. Values of heats and entropies of adsorption of ammonia were calculated from the adsorption isotherms. The structure of  $\text{NH}_3$  monolayers determined by low energy helium diffraction experiments indicated that there was a large degree of orientational disorder among the adsorbed domains, although the degree of order within the domain was relatively high [33]. The monolayer structure was found to consist of alternating ‘dipole-up dipole-down’ configurations. Results of molecular dynamics simulations of  $\text{NH}_3$  by Cheng and Steele [34, 35] matched well with these diffraction results.

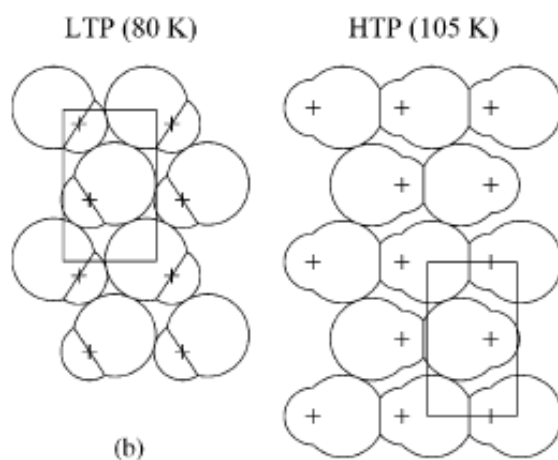


**Figure 1-5** Structure of the low (LTP) and high (HTP) temperature phases of  $\text{CD}_3\text{F}$  on graphite [36]. From [7].

Clarke *et al.* reported the structures of halomethane monolayers on graphite using X-ray and neutron scattering [36-40]. The structures of  $\text{CH}_3\text{Br}$ ,  $\text{CH}_3\text{F}$ ,  $\text{CH}_3\text{Cl}$  and  $\text{CH}_3\text{I}$  consisted of the polar molecules lying flat on the graphite surface with alternating dipole orientations, and the adsorbed layer was found to be identical to bulk crystal planes. Chloromethane and fluoromethane monolayers showed additional high temperature phases prior to melting (the chloromethane phases are shown in Figure 1-5). A review of polar methanes on graphite can be

found in [41], which summarises the different structures and phases formed by the dipolar molecules.

### 1.2.4 Alkanes

Alkanes are a fundamental group of organic compounds whose general properties underpin the understanding of more complex compounds. Initial work using simple isotherm and calorimetric techniques indicated that graphite strongly adsorbs hydrocarbons from liquid media [42-44]. Groszek [42] provided an explanation for the high affinity of the graphite surface for the hydrocarbons. The zigzag structure of the hydrocarbon fits well into the graphite hexagons (Figure 1-6), and Groszek calculated the areas occupied per molecule on the graphite surface. However recent neutron diffraction and simulations show that intermediate length alkanes ( $C_{24}$  and  $C_{32}$ ) deposited from the vapour phase undergo commensurate-incommensurate phase transitions in the monolayer, with neither phase being entirely consistent with Groszek's model [9].

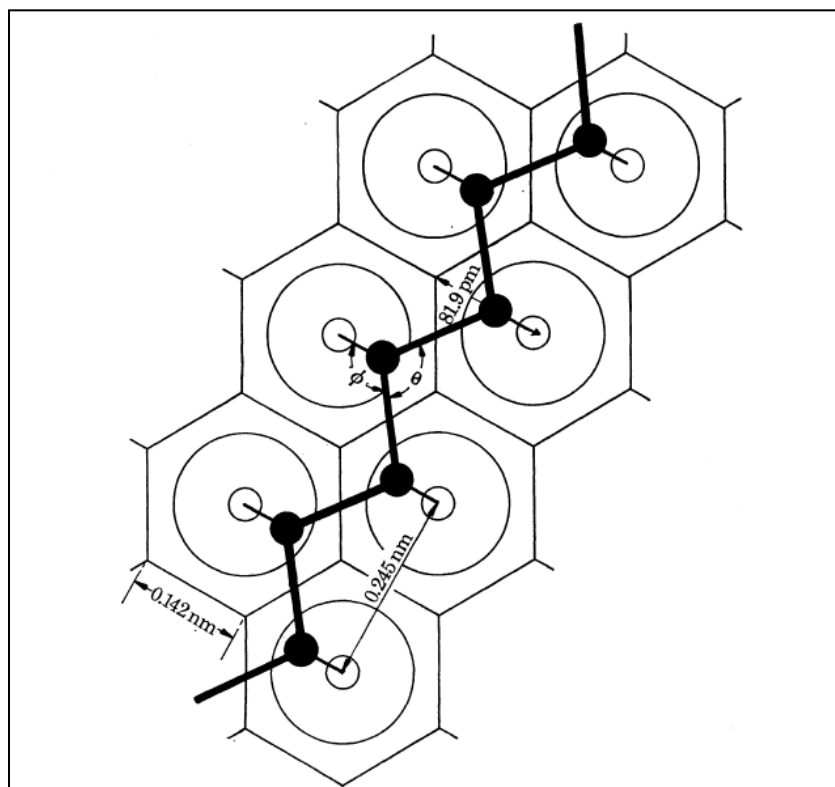


**Figure 1-6** An alkane molecule adsorbed at the graphite basal plane. (From [42]). C-C bond length = 1.54 Å, bond angle  $\theta = 105^{\circ}44'$ , planar angle  $\phi = 127^{\circ}8'$ .

The structure of adsorbed monolayers of pure alkanes has been studied by combined X-Ray and neutron diffraction [45-47]. Alkanes exhibit a pronounced odd-even alternation in structure with alkyl chain length, particularly for the shorter members (up to 10 carbons long) of the series. As shown in Figure 1-7, odd members have molecules that are essentially parallel to each other, belonging to the 2D space group  $cm$  [48]. Shorter even alkanes have a herringbone or zigzag array of molecules ( $pgg$  plane group), with longer members reverting back to the centred phase [49].

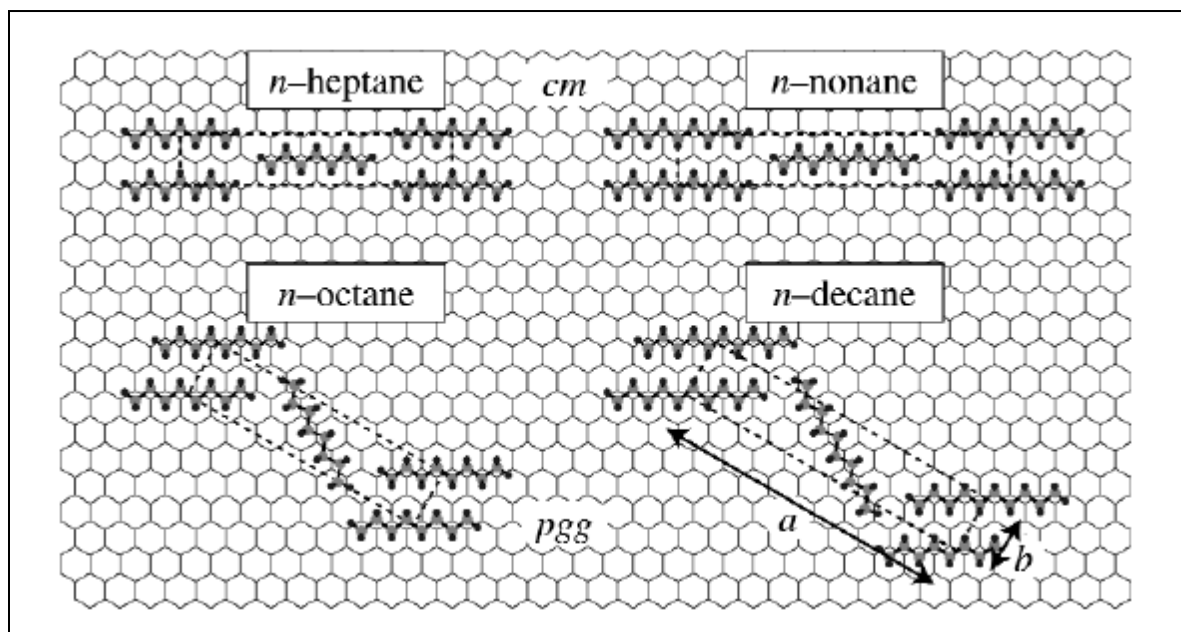


**Figure 1-7** Monolayer crystal structures of the even alkanes  $n$ -octane and  $n$ -decane adsorbed on graphite [49] and the odd alkanes  $n$ -heptane and  $n$ -nonane [48]. From [7].

In many alkyl species, packing arrangements for odd and even homologues are different: a difference that is attributed to the packing of methyl groups at the end of the molecule. Odd-even alternation in symmetry is one of the key elements in understanding the mixing behaviour of these compounds on the surface. Monolayers of  $n$ -heptane and  $n$ -nonane, which belong to the same space group, were found to mix whereas  $n$ -nonane and  $n$ -decane, belonging to different space groups have only limited miscibility, at  $\sim 0.85$  monolayers coverage [50].  $N$ -octane and  $n$ -nonane were found to demix in the monolayer at high coverages (10-40 monolayers), with the longer component being preferentially adsorbed [51]. Such preferential adsorption between homologous alkyl species has been attributed to entropic arguments (preferential adsorption is discussed further in chapter 3, and also in [52]). Interestingly, at coverages below a monolayer ( $\sim 0.5/0.8$

monolayers), neutron diffraction data indicates that *n*-octane and *n*-nonane do mix over a certain range of composition, a phenomenon attributed to the expansion in the unit cell at low coverages allowing for the accommodation of molecules of a different kind [47, 53].

*n*-Alkanes have up to five plastic-crystalline ‘rotator phases’ which occur between the low temperature crystalline phases and the melting temperature [54]. These rotator phases are layered structures with the long axis of the molecule lying nearly along the layer normal. They exhibit crystalline order, but there is no long-range order in the rotational degree of freedom of the molecules about their long axis.

### 1.2.5 Alkyl species and recent developments

Solid monolayers co-existing with liquid bulk material of a variety of adsorbates have been studied using several experimental and theoretical techniques such as X-ray and neutron scattering, calorimetry, NMR, scanning probe microscopy and molecular dynamics simulations. Studies of monolayers of alcohols [55, 56], carboxylic acids [57-59], amines [60], ethers [61], aldehydes [62], amides [63-66] and fluoroalkanes [67, 68] adsorbed on the surface of graphite have been reported in literature. In all cases solid monolayers of the adsorbates were identified, and a detailed structural analysis revealed the symmetries and phase transitions within these layers.

Adsorbed fluoroalkanes show rich phase behaviour on graphite - shorter odd chain length fluoroalkanes have a *pgg* space group, while shorter even ones have a primitive unit cell, and all long fluoroalkanes (chain length  $\geq 12$ ) have a centred unit cell at low temperatures [68]. A significant number of fluoroalkanes have additional higher temperature phases, as these arrangements could possibly facilitate the rotations of the molecules in the rotator phases.

Carboxylic acids also exhibit an odd-even effect, where the odd chain-length members of the series possess structures with *pgg* symmetry and even members have *p2* symmetry, as shown in Figure 1-8 [69]. Again, phase separation in the monolayer for binary mixtures of carboxylic acids was reported for shorter members possessing different symmetries by DSC [59] and recently by X-ray diffraction [70].

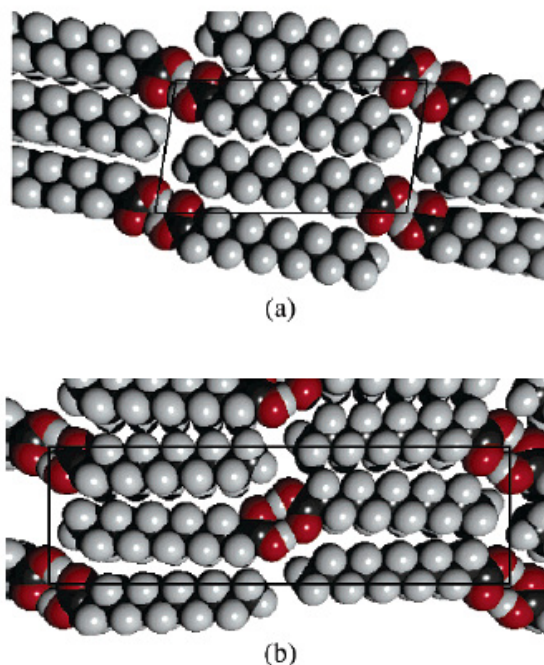


**Figure 1-8** Illustrations of the monolayer structures for (a) the  $p2$  phase of dodecanoic acid ( $C_{12}$ ) and (b)  $pgg$  phase of undecanoic acid ( $C_{11}$ ). The unit cell is shown by the solid box. From [69].

The unusual behaviour of binary alcohols has been summarised in a recent study [56]. For mixtures differing in chain length by one carbon atom, if the shorter member is odd then mixing is essentially ideal, and if the shorter member is even, then a molecular complex is formed. Adsorbed alcohols possess either a ‘herringbone’, ‘parallel’ or ‘mixed’ arrangement of molecules as studied by STM and X-ray diffraction, with phase changes reported with a change in temperature/coverage (e.g. dodecanol changes phase from herringbone to parallel between 308 and 313 K). Primary alcohols also show an odd-even effect in their monolayer melting points [7].

A study of dodecanol on graphite by DSC showed that this molecule forms several layers above a monolayer, with solid layers existing at temperatures where the bulk material was liquid [71]. This has important implications in understanding growth of alcohol crystals: bulk crystals can be expected to grow in a layer-by-layer fashion. As explained previously (§1.2.1), many adsorbates on graphite such as noble gases also show the formation of several layers above a monolayer.

The monolayer formation of aldehydes on graphite by X-ray and neutron scattering, calorimetry and Scanning Tunnelling Microscopy (STM) has been reported recently [62]. Several possible

structures for the dodecanal monolayer are presented that fit with the scattering data. Those that favour effective dipole-dipole interactions between the aldehyde functional groups are thought to be most likely, as seen for other simple dipolar molecules previously (§1.2.3).

Recently, NMR has proved to be a useful tool in the study of adsorbed layers. Studies of dodecane [72] and fluoroalkane [73] monolayers on graphite showed the existence of a solid 2D layer at temperatures where the bulk adsorbate was liquid. For a mixed system of *n*-decane and *n*-heptanol [74], NMR provided independent information on each component in the system, and data showed that decane is preferentially adsorbed onto the surface over most of the composition range.

## 1.3 Alkyl amides

In this section the properties and applications of alkyl amides are explained, and a review of the adsorption of amides on different surfaces such as graphite, polymer surfaces and water is provided. The bulk behaviour of amide crystals, including structures and phase behaviour, is described, and the nomenclature adopted for the alkyl amides used in this work is explained.

### 1.3.1 Properties and uses

Primary alkyl amides are molecules that have an amide head group () and an alkyl chain (for example, dodecanamide, shown in Figure 1-9). Oxygen and nitrogen being electronegative impart these molecules with interesting properties such as enabling amide groups to form hydrogen bonds (discussed in detail later in this chapter). The N-C=O bond possesses a relatively high rotational barrier (~20 kcal/mol) and this has been explained by the resonance stabilisation of the planar amide functional group [3] as shown in Figure 1-10. This also makes these compounds relatively unreactive [75].

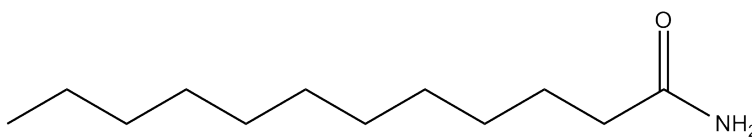


**Figure 1-9** A typical primary alkyl amide molecule: dodecanamide (C<sub>12</sub>)

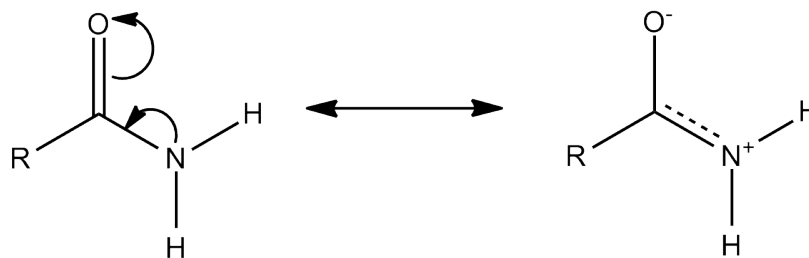


**Figure 1-10** Resonance forms of the amide functional group

Commercially, amides are important additives to reduce friction in polymer films, particularly in polyethylene and polypropylene. Pure polymers can often be very ‘sticky’ (e.g. as seen in plastic bags). To prevent this tack, alkyl amides, particularly unsaturated amides such as erucamide, are added to the bulk polymer prior to extrusion of the polymer sheet. It is hypothesised that the amide molecules migrate to the surface, thereby causing reduction in friction and tack [76]. Amide salts can also be used as corrosion inhibitors when they adsorb on metal substrates such as aluminium [2].

In the bulk, amides play a very important role in biological systems. Proteins are formed from amino acids; the amino acids are linked together by peptide (amide) bonds, resulting in a polypeptide. The hydrogen bonding within amide groups is a central feature in the formation of higher order protein structures ( $\beta$ -sheets and  $\alpha$ -helices) and the double-helical DNA molecule. This non-covalent interaction is important in protein folding and assembly.  $\beta$ -Lactams, a class of cyclic amides, have played a critical role in antibiotics such as Penicillin [3]. Biological receptors and signalling sensors bind to specific biological compounds, and the recognition process for this specificity involves the formation of hydrogen bonds. Nylon, a commercially important synthetic polymer, is also formed using amide bonds.

By forming hydrogen bonded structures, amides have played a valuable role in the assembly of a variety of supramolecular structures. These non-covalently bound self-assembled structures have diverse applications such as catalysis, liquid crystals, crystal engineering and the formation of encapsulating molecules for drug delivery [3].

### 1.3.2 Amides on surfaces

#### 1.3.2.1 The solid/liquid interface

Commercially used amides are often derived from plant sources and usually consist of a mixture of alkyl chain lengths, and it is thus important to consider the mixing behaviour of these molecules in adsorbed layers. Mixing in the solid phase depends upon both the symmetry and the quantitative similarity of the unit cells of the two pure monolayers [77].

A preliminary study on the binary mixing behaviour in the monolayers of alkyl amides on graphite using Differential Scanning Calorimetry (DSC) has been reported by Arnold and Clarke [66]. This initial study has indicated that the amides mix more readily in the monolayer as compared to the bulk, a phenomenon which is observed for several other alkyl species. Amides were also found to be strongly preferentially adsorbed over alkanes of the same chain length.

The ratio of the monolayer melting point to the bulk melting point ( $T_{2D}/T_{3D}$ ) can be considered to be a measure of the stability of the monolayer. For different materials this ratio is, approximately: fluoroalkanes, 1.03; alcohols, 1.10; carboxylic acids, 1.10 and alkanes, 1.13. Preliminary studies of the amides indicated that the ratio is higher than any of these materials studied previously (1.15-1.16), with some unsaturated amides having a ratio as high as 1.20 [66]. This stability can be attributed to the existence of hydrogen bonds in the amide monolayers; stronger than that for carboxylic acids [78] and the ability to form more than one hydrogen bond per molecule.

Scanning Tunnelling Microscopy (STM) has proven to be a useful technique for investigating adsorbed monolayers. STM images of a variety of adsorbates on graphite and other substrates have been reported recently [79-82]. However, the adsorbed layer is thought to be affected during the measurement, and hence STM is often used in combination with diffraction. It has also been found that different solid monolayer structures are formed depending on solvent used and method of deposition on the substrate (e.g.  $C_{24}$  and  $C_{32}$  alkanes have different monolayer structures depending on whether the film is deposited from the vapour phase or from solution with *n*-heptane [9]).

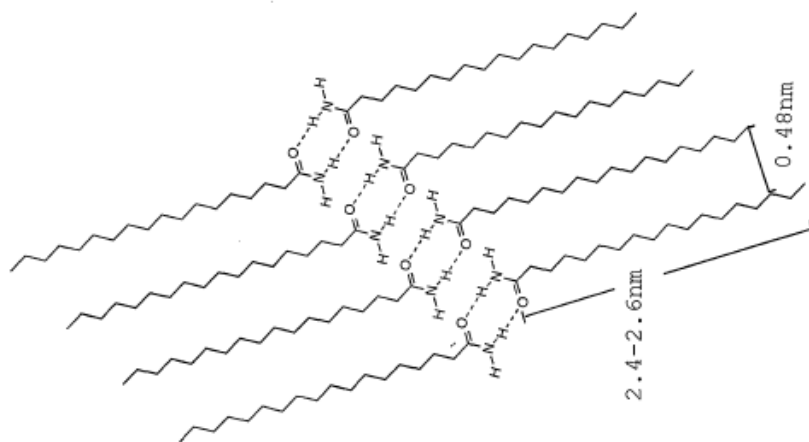


**Figure 1-11** Molecular arrangement of stearoyl amide (C<sub>18</sub>) adsorbed on the surface of graphite as interpreted from its STM image. From [65].

STM has been used to characterise the 2D layers of amides on the surface of graphite from phenyloctane [65]. An ordered array of molecules was observed to lie flat on the surface, with the carbon backbone parallel to the graphite surface. The STM image of C<sub>18</sub> amide has been interpreted to indicate that the amide heads are hydrogen-bonded into a dimer, with adjacent head groups forming further hydrogen bonds to make the adsorbed layer, as shown in Figure 1-11.

Apart from primary alkyl amides, STM investigations of di-amides [83] and *N*-alkyl amides [84] at the graphite/solution interface show that the amide group enables the formation of hydrogen bonds repeating over a long range in the two-dimensional crystalline phase. De Feyter et al. have reported several STM images of self-assembled monolayers that are formed by hydrogen bonding [81, 85, 86]. In particular, initial STM images of molecules with a urea group show that a self-assembled two-dimensional hydrogen-bonded monolayer is again formed [87].

A very recent modification of conventional low-temperature STM which involves condensing molecular hydrogen on the STM tip has been reported [88]. Intermolecular bonds, such as hydrogen bonds, have been claimed to be ‘imaged’ directly by this technique [89]. Understanding the self-assembly of hydrogen bonded systems is a big field of study, with many potential academic and commercial applications.

### ***1.3.2.2 The polymer/air interface***

As discussed in §1.3.1, primary alkyl amides find applications as friction modifiers in polymer systems. The adsorption of amides at the polymer/air interface has been previously studied by various macroscopic approaches, including variation of friction coefficient on adsorption, IR studies and scanning probe and electron microscopy.

Hirt et al. have reported several studies on the adsorption of amides in polyethylene films [90, 91]. The work shows that the coefficient of friction decreases as surface concentration of the amide additive is increased [92]. The coefficient drops by ~50% for low surface concentrations, and remains approximately constant beyond a ‘critical’ concentration. Atomic Force Microscopy [1] and electron microscopy [93] images showed that the polyethylene surface need not be entirely covered by the amides to cause friction reduction. However, there is poor composition data and essentially no structural data available for these systems. This issue has been partially addressed in this work, as will be discussed in chapter 7.

Recently an investigation into the adsorption kinetics and equilibrium composition of alkyl amides on polyethylene and polypropylene surfaces was reported by Environmental Scanning Electron Microscopy (ESEM) [76]. ESEM is advantageous to conventional electron microscopy in that high vacuum is not required in the sample chamber, thereby preventing desorption of the physisorbed layers of interest. The initial ESEM results found that the amides slowly diffuse to the surface, and the surface amounts of amides increased with time over a period of ~14 days.

### ***1.3.2.3 Langmuir layers of amides***

Adsorption at the graphite/air and graphite/liquid interface has been the primary focus of this work. It is interesting to review Langmuir layers here, as ordered layers of molecules at the water/air interface are known to show a variety of interesting phenomena, such as the formation of crystalline layers, ‘gas-liquid-solid’ transitions and solid-solid phase transitions [94].

Monolayers of molecules containing amide groups have been investigated by pressure-area ( $\pi$ -A) isotherms, Brewster Angle Microscopy (BAM) [95] and Grazing Incidence X-ray Diffraction (GIXD) [96] at the air/water and air/solution interface. Gibbs and Langmuir layers of hydrogen bonded amide molecules have been studied by Vollhardt, Mohwald et al. [97, 98]. Long chain amphiphilic amide molecules were found to spontaneously assemble into two-dimensional

crystallites containing hydrogen bonds of the amides with the aqueous sub-phase, with other soluble amides and between adsorbed molecules [99].  $\pi$ -A isotherms, GIXD and BAM revealed that crystalline layers of the amides are formed, and a phase change in the layer was identified upon increasing the temperature [100, 101].

### 1.3.3 Bulk behaviour of amides

An initial investigation into the bulk crystal structures of saturated amides made by X-ray diffraction revealed that there was a pronounced odd-even effect in the longest unit cell spacings with chain length [102]. Indexing the diffraction patterns [103] revealed that all saturated alkyl amides between chain lengths  $C_3$  to  $C_{16}$  have the space group  $P2_1/a-C_{2h}^5$ , except  $C_9$  which has the space group  $C2/c-C_{2h}^6$  [104].

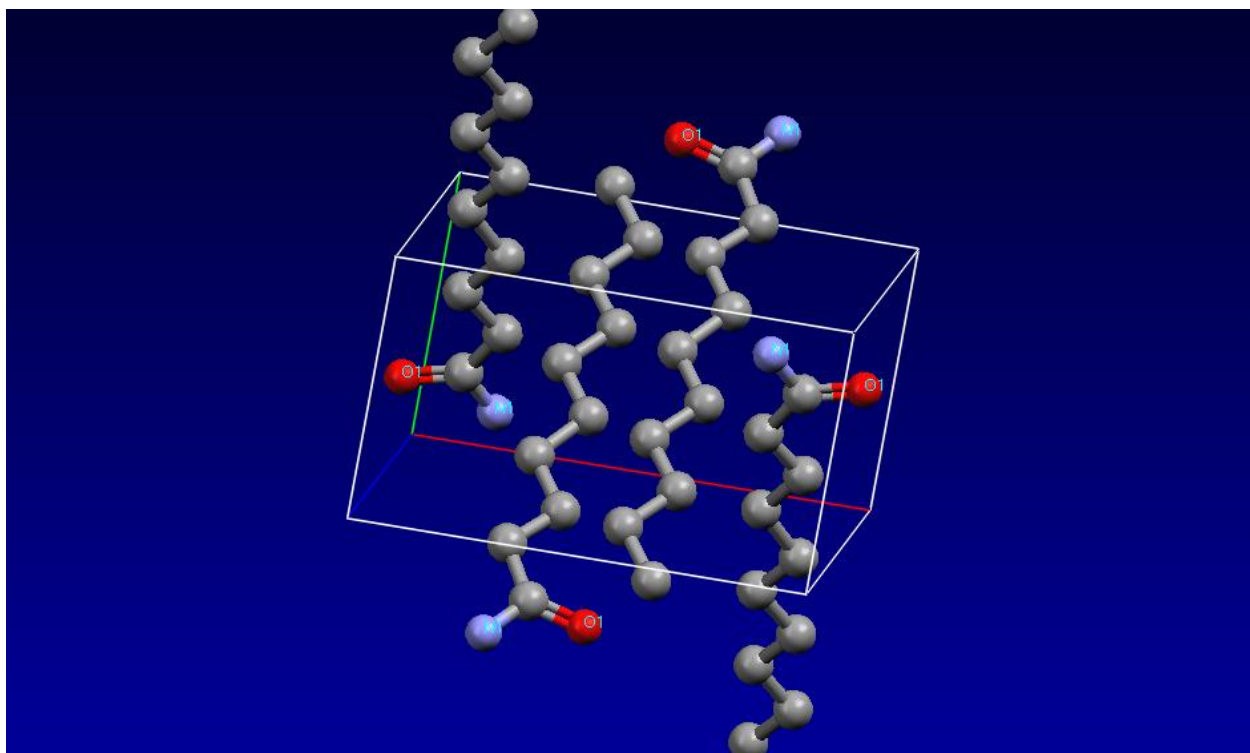


**Figure 1-12** The crystal structure of decanamide (CCDC ref: DECAAM). The unit cell is shown by the box; oxygen atoms are denoted as red, nitrogens as blue and methyl groups as grey spheres.

The crystal structure of decanamide ( $C_{10}$ ) [105] obtained from the Cambridge Crystallographic Data Centre (CCDC) is shown in Figure 1-12. The molecules are arranged such that they are hydrogen bonded into dimers, and the (001) plane contains dimers that are hydrogen bonded into extensive chains (the hydrogen bonding can be visualised with additional unit cells in Figure

1-12). However, crystal structures of the unsaturated amides used in this work were not found in literature.

Leiserowitz et al. [106, 107] analysed a variety of amide crystals and argued that idealised hydrogen bond arrangements should have the N-H...O hydrogen bond within the dimer to be linear, and between dimers at an angle of  $\sim 120^\circ$ , as found for most amide crystals. Extensive surveys of hydrogen bond lengths and angles in bulk amide crystals can be found in [108, 109]. Hydrogen bonding will be discussed further in §1.4.1 and in chapter 4.

Several alkyl amides show solid-solid phase transitions in the bulk prior to melting. Importantly, the melting points, enthalpies and entropies of fusion of bulk amides exhibit an odd-even effect with chain length. Abate et. al [110] tabulated the heat capacities, enthalpies of fusion and solid-solid phase transitions for primary amides, and the results agree with the values reported by Arnold and Clarke for the bulk ( $\pm 5$  K) [66] and with other literature.

### 1.3.4 Nomenclature

A convenient system for naming primary alkyl amides has been adapted in this work. According to this system each amide molecule is named as ‘C $n$ : $x$  c/ $t$ - $\alpha$ ’, where  $n$  is the total number of carbon atoms in the chain,  $x$  is the number of double bonds (either 0 or 1 in this work),  $c$  or  $t$  indicate whether the double bond is *cis* or *trans* in form, and  $\alpha$  gives the position of the double bond relative to the amide group.

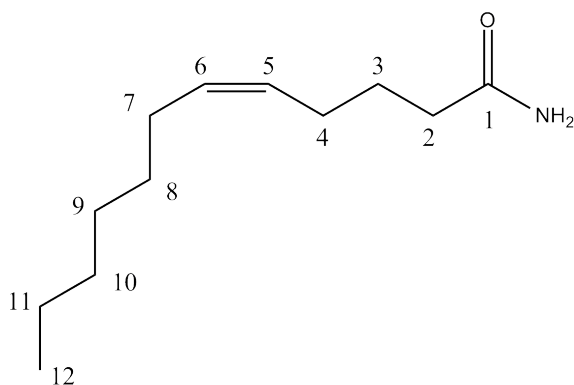


**Figure 1-13** *cis*-5-dodecenamide molecule

As an example, consider the unsaturated molecule *cis*-5-dodecenamide, which has 12 carbon atoms in total and has a *cis*-double bond at the 5<sup>th</sup> carbon atom from the amide carbon (Figure 1-13). According to the nomenclature explained here, this amide will be written as C12:1 *c*-5.

## 1.4 Intermolecular interactions

Key intermolecular interactions encountered in adsorbed layers are discussed here, such as hydrogen bonding, van der Waals forces and dipole interactions. The characteristics and relative strengths of these are compared, with emphasis on hydrogen bonding.

### 1.4.1 Hydrogen bonding

Hydrogen bonding has attracted considerable study in the last few decades and a variety of experimental and theoretical approaches have been used. These include thermodynamic methods, (calculating association energies and equilibrium constants), vibrational spectroscopy, <sup>1</sup>H NMR, diffraction techniques and computational chemistry [111, 112]. A hydrogen bond may be defined as being a three-centre-four-electron shared-proton interaction between two electronegative atoms (a proton donor and a proton acceptor or lone pair carrier) [78].

The hydrogen bond is thought to be a complex interaction composed of several different effects such as electrostatics, polarization, dispersion and charge transfer. The electrostatic term is directional and relatively long range ( $r^{-2}$  or  $r^{-3}$  for dipole interactions), polarization decreases faster ( $r^{-4}$ ) and charge transfer even faster ( $\sim e^{-r}$ ) with distance ( $r$ ). The dispersion term can be approximated into a contribution described by the Lennard-Jones potential  $E \sim Ar^{-12} - Br^{-6}$ . Depending on the species involved and the geometry, these terms contribute in different weights. In general the interaction is attractive at long range, becoming repulsive at short range [113].

Hydrogen bonds are of several types and cover a vast range of energies, from the weak van der Waals/dipole energies ( $\sim 1$ -2 kJ/mol) to the strong covalent/electrostatic interactions ( $\sim 150$  kJ/mol). Depending upon the strength of the hydrogen bond interaction, they may be classified as strong, moderate or weak hydrogen bonds, as shown in Table 1-1 [113].

**Table 1-1** Classification of X-H...A hydrogen bonds, from [113]. The numerical data are guiding values only, and the borderlines between the categories are not stringent.

|                              | Strong  | Moderate  | Weak                     |
|------------------------------|---|---|--------------------------|
| <b>Interaction type</b>      | strongly covalent   | mostly electrostatic                                      | electrostatic/dispersive |
| <b>Bond energy (kJ/mol)</b>  | 60-175  | 15-60   | <15                      |
| <b>H...A bond length (Å)</b> | 1.2-1.5   | 1.5-2.2   | >2.2                     |
| <b>X...A bond length (Å)</b> | 2.2-2.5   | 2.5-3.2   | >3.2                     |
| <b>X-H...A angle (°)</b>     | 170-180   | >130  | >90                      |
| <b>Directionality</b>        | strong  | moderate  | weak                     |
| <b>Examples</b>              | Between acids and complementary bases:<br>H-O-H...O <sup>-</sup> -H<br>NH <sub>3</sub> <sup>+</sup> ...N etc. | Amide N-H...O<br>Carboxylic acid O-H...O<br>Water O-H...O | C-H...N<br>C-H...O       |

At the low energy end of the range, weak hydrogen bonds generally fade into a van der Waals attraction. The hydrogen bonds are characterised by decreasing bond lengths, increasing directionality and an increasing tendency towards linearity as the strength of the hydrogen bond increases (Table 1-1). Most commonly encountered hydrogen bonds have energies between 10-50 kJ/mol; amide hydrogen bonds fall into the ‘moderate’ category [113]. For moderately strong amide hydrogen bonds, their presence is confirmed by the working rule that the N-H...O distance is less than the sum of the van der Waals radii of the individual atoms (N, H and O) [78].

As discussed in §1.3, hydrogen bonding is an important feature in the self assembly of adsorbed layers of amides on graphite, water and other surfaces. In general, it has been found that the hydrogen bonding dominates the overall structure of the layer, and the molecules then pack in a manner which maximises the van der Waals attractions.

### 1.4.2 Van der Waals forces

Dispersion forces play a key role in a variety of important phenomena such as adhesion, surface tension, physical adsorption, aggregation in colloidal systems, properties of gases and liquids and

structures of condensed phases. In contrast to other forces that may or may not be present depending on the nature of the interacting species, van der Waals forces are always present. The origin of van der Waals forces is quantum mechanical, the basis of which is the interactions between instantaneous dipoles within atoms. Their main features may be summarised as follows [114]:

1. They are long range forces (effective between  $\sim 0.2$  to 10 nm).
2. These forces may be repulsive or attractive, and in general do not follow a simple power law
3. They play a relatively weak role in orienting and aligning molecules
4. The interactions are affected by the presence of other bodies, and the forces are strictly non-additive

### 1.4.3 Dipole interactions

Many molecules such as carbonyl compounds carry no net charge, but possess an electric dipole. The bond moment of the C=O bond in various molecules is 2.3-2.7 D. Dipole interactions are directional; the energy of a dipole-dipole interaction varies as  $r^{-3}$ , and for a dipole-charge interaction as  $r^{-2}$  where  $r$  is the distance from the dipole [114]. For example, the energies of dipole-dipole interactions within aldehyde monolayers are  $\sim 5$ -8 kJ/mol [62].

## 1.5 Summary and scope of this work

A review of adsorbed monolayers on graphite has been provided in this chapter, which shows that there is a rich variety of phenomena that occur in adsorbed layers. 2D layers of a variety of adsorbates on graphite show many different structural phases and phase transitions. Several approaches, such scattering techniques, thermodynamic measurements, scanning probe microscopy, NMR and simulations are available to probe this behaviour.

Amides have the ability to form extensive hydrogen bonded networks which allow these molecules to have a diverse range of applications. Initial investigations into understanding the behaviour of alkyl amides have been reported which show that adsorbed amides show

particularly different behaviour. The focus of this work is to understand the structures of these interesting molecules and how they correlate with functionality.

In this work the adsorption of primary alkyl amides onto graphite from the bulk liquid and vapour phase is investigated. An introductory overview of X-ray and neutron diffraction techniques, with descriptions of the experimental setup is provided first, followed by an explanation of calorimetry and mixing models relevant to this work. Chapter 4 presents X-ray diffraction results from sub-monolayer coverage saturated amides. Solid ordered monolayers of these molecules are identified over a range of temperatures above the bulk melting point. The crystalline structures of unsaturated amides are discussed in Chapter 5. Chapter 6 presents results of the adsorption of pure amides and binary mixtures at the graphite/liquid interface by calorimetry. Finally, results from an initial investigation into the adsorption of amides at the polymer/air interface are presented.

## 1.6 References

1. Ramirez, M.X., D.E. Hirt, and L.L. Wright, *AFM Characterization of Surface Segregated Erucamide and Behenamide in Linear Low Density Polyethylene Film*. Nano Letters, 2002. **2**(1): p. 9-12.
2. Sayed, S., A.E. Rehum, H.H. Hassan, and M.A. Amin, *Corrosion inhibition of Aluminium by 1, 1(laryl amido)propyl ammonium chloride in HCl solution*. Mater. Chem.Phys., 2001. **70**: p. 64-72.
3. *The amide linkage: selected structural aspects in chemistry, biochemistry, and materials science*, ed. A. Greenberg, C.M. Breneman, and J.F. Liebman. 2000, New York: Wiley-Interscience.
4. Cussler, E.L., *Diffusion: Mass Transfer in Fluid Systems*. 2nd ed. 1997, New York: Cambridge University Press.
5. Thomy, A., X. Duval, and J. Regnier, *Two-dimensional phase transitions as displayed by adsorption isotherms on graphite and other lamellar solids*. Surf. Sci. Rep., 1981. **1**(1): p. 1-38.
6. Bruch, L.W., R.D. Diehl, and J.A. Venables, *Progress in the measurement and modeling of physisorbed layers*. Reviews of Modern Physics, 2007. **79**(4): p. 1381-74.
7. Inaba, A., *Structure and phase behaviour of two-dimensional solids formed at interfaces*. Pure Appl. Chem, 2006. **78**(5): p. 1025-1037.
8. Thomy, A. and X. Duval, *Stepwise isotherms and phase transitions in physisorbed films*. Surface Science, 1994. **299-300**: p. 415-425.
9. Diama, A., B. Matthies, K.W. Herwig, F.Y. Hansen, L. Criswell, H. Mo, M. Bai, and H. Taub, *Structure and phase transitions of monolayers of intermediate-length n-alkanes on graphite studied by neutron diffraction and molecular dynamics simulation*. The Journal of Chemical Physics, 2009. **131**(8): p. 084707-10.
10. Mowforth, C.W., T. Rayment, and R.K. Thomas, *Long-period Commensurate structures near the Incommensurate-Commensurate Phase transition in Xenon Layers adsorbed on Graphite observed by X-Ray Diffraction*. J. Chem. Soc., Faraday Trans. 2, 1986. **82**: p. 1621-1634.
11. Suzanne, J., J.P. Coulomb, and M. Bienfait, *Auger electron spectroscopy and leed studies of adsorption isotherms: Xenon on (0001) graphite*. Surface Science, 1973. **40**(2): p. 414.
12. Chinn, M.D. and S.C.J. Fain, *Structural phase transition in Epitaxial Solid Krypton Monolayers on Graphite*. Phys. Rev. Lett., 1977. **39**(3): p. 146-149.
13. Stephens, P.W., P.A. Heiney, R.J. Birgeneau, P.M. Horn, D.E. Moncton, and G.S. Brown, *High resolution x-ray scattering study of the commensurate-incommensurate transition of monolayer Kr on graphite*. Phys. Rev. B, 1984. **29**(6): p. 3512-3532.
14. Larese, J.Z., *Multilayer Argon Films on Graphite: Structural and Melting properties*. Accounts of Chemical Research, 1993. **26**(7): p. 353-360.
15. Hanono, F., C. Gatts, and E. Lerner, *Multilayer isotherms of neon adsorbed on exfoliated graphite*. J. Low Temp. Phys., 1985. **60**(1): p. 73-84.
16. Goellner, G.J., J.G. Daunt, and E. Lerner, *Helium adsorption on exfoliated graphite*. J. Low Temp. Phys., 1975. **21**(3): p. 347-358.

17. Carneiro, K., L. Passell, W. Thomlinson, and H. Taub, *Neutron-diffraction study of the solid layers at the liquid-solid boundary in He4 films adsorbed on graphite*. Phys. Rev. B, 1981. **24**(3): p. 1170.
18. Bienfait, M., J.G. Dash, and J. Stoltenberg, *Growth of 4He films on graphite, krypton-plated graphite, magnesium oxide, and Mylar substrates*. Physical Review B, 1980. **21**(7): p. 2765.
19. Kjems, J.K., L. Passell, H. Taub, J.G. Dash, and A.D. Novaco, *Neutron scattering study of nitrogen adsorbed on basal-plane-oriented graphite*. Phys. Rev. B., 1976. **13**(4): p. 1446-1462.
20. Asada, H., M. Udaka, and S. Doi, *Phase transition of nitrogen adsorbed on benzene-preplated graphite at 77K*. Surface Science, 1993. **296**: p. 21-24.
21. Chung, T.T. and J.G. Dash, *N2 Monolayers on graphite: Specific heat and vapor pressure measurements -- thermodynamics of size effects and steric factors*. Surface Science, 1977. **66**(2): p. 559-580.
22. Morishige, K., C. Mowforth, and R.K. Thomas, *Orientalional order in CO and N2 monolayers on graphite studied by X-ray diffraction*. Surface Science, 1985. **151**: p. 189-300.
23. McTague, J.P. and M. Nielsen, *Magnetic and Structural Phases of Monolayer O2 on Graphite*. Physical Review Letters, 1976. **37**(10): p. 596.
24. Freimuth, H., H. Wiechert, and H.J. Lauter, *The commensurate-incommensurate transition of hydrogen monolayers physisorbed on graphite*. Surface Science, 1987. **189-190**: p. 548-556.
25. Freimuth, H., H. Wiechert, H.P. Schildberg, and H.J. Lauter, *Neutron-diffraction study of the commensurate-incommensurate phase transition of deuterium monolayers physisorbed on graphite*. Physical Review B, 1990. **42**(1): p. 587.
26. Wiechert, H., H. Freimuth, and H.J. Lauter, *Heat-capacity and neutron-diffraction studies of HD monolayers physisorbed on graphite*. Surface Science, 1992. **269-270**: p. 452-459.
27. Bienfait, M., *Adsorbed layers on surfaces*, in *The Landolt-Bornstein database*. 2001, Springer-Verlag. p. 117-130.
28. Suzanne, J., J.M. Gay, and W.N. Unertl, *Chapter 10 The structure of physically adsorbed phases*, in *Handbook of Surface Science*. 1996, North-Holland. p. 503-575.
29. Diehl, R.D. and S.C. Fain Jr, *Structure and orientational ordering of nitrogen molecules physisorbed on graphite*. Surface Science, 1983. **125**(1): p. 116-152.
30. Clarke, S.M. and R.K. Thomas, *The structure and dynamics of molecules adsorbed on graphite*, in *Dynamics of molecular crystals*, J. Lascombe, Editor. 1987, Elsevier: Amsterdam.
31. Bomchil, G., N. Harris, M. Leslie, J. Tabony, J.W. White, P.H. Gamlen, R.K. Thomas, and T.D. Trewern, *Structure and dynamics of ammonia adsorbed on graphitized carbon black. Part 1.—Adsorption isotherms and thermodynamic properties*. J. Chem. Soc. Faraday Trans. 1, 1979. **75**: p. 1535 - 1541.
32. Gamlen, P.H., R.K. Thomas, T.D. Trewern, G. Bomchil, N. Harris, M. Leslie, J. Tabony, and J.W. White, *Structure and dynamics of ammonia adsorbed on graphitized carbon black. Part 2.—Neutron diffraction*. J. Chem. Soc., Faraday Trans 1, 1979. **75**: p. 1542 - 1552.

33. Rowntree, P., G. Scoles, and J. Xu, *The structure of ammonia overlayers physisorbed onto the surface of single crystal graphite, determined by means of atomic beam diffraction*. The Journal of Chemical Physics, 1990. **92**(6): p. 3853-3857.
34. Cheng, A. and W.A. Steele, *Computer simulation of ammonia on graphite. I. Low temperature structure of monolayer and bilayer films*. The Journal of Chemical Physics, 1990. **92**(6): p. 3858-3866.
35. Cheng, A. and W.A. Steele, *Computer simulation of ammonia on graphite. II. Monolayer melting*. The Journal of Chemical Physics, 1990. **92**(6): p. 3867-3873.
36. Morishige, K., Y. Tajima, S. Kittaka, S.M. Clarke, and R.K. Thomas, *The structure of chloromethane monolayers adsorbed on graphite*. Molecular Physics, 1991. **72**(2): p. 395-411.
37. Clarke, S.M. and R.K. Thomas, *The structure of a bromomethane monolayer adsorbed on graphite*. Molecular Physics, 1991. **72**(2): p. 413 - 423.
38. Clarke, S.M., *The Structure and Properties of Adsorbed Layers by X-Ray and Neutron Scattering*, in *Physical Chemistry Laboratory*. 1989, University of Oxford: Oxford.
39. Bucknall, R.E., S.M. Clarke, R.A. Shapton, and R.K. Thomas, *The structure of a methyl iodide monolayer adsorbed on graphite*. Mol. Phys., 1989. **67**(2): p. 439 - 446.
40. Inaba, A., H. Chihara, S.M. Clarke, and R.K. Thomas, *The structure and heat capacity of fluoromethane monolayers adsorbed on graphite*. Molecular Physics, 1991. **72**(1): p. 109-120.
41. Knorr, K., *Monolayers of polar methane derivatives physisorbed on graphite*. Physics Reports, 1992. **214**(2): p. 113-157.
42. Groszek, A.J. *Selective adsorption at Graphite/Hydrocarbon interfaces*. in *Proceedings of the Royal Society of Chemistry*. 1970. London: The Royal Society.
43. Kern, H., W. Rybinski, and G.H. Findenegg, *Prefreezing of Liquid n-alkanes near Graphite surfaces*. J. Colloid Interface Sci., 1977. **59**(2): p. 301-307.
44. Domingo-García, M., F.J. López-Garzón, R. López-Garzón, and C. Moreno-Castilla, *Gas chromatographic determination of adsorption isotherms, spreading pressures, london force interactions and equations of state for n-alkanes on graphite and carbon blacks*. J. Chromatography A, 1985. **324**: p. 19-28.
45. Espeau, P., P.A. Reynolds, T. Dowling, D. Cookson, and J.W. White, *X-Ray diffraction from layers of n-alkanes adsorbed on graphite*. J. Chem. Soc., Faraday Trans., 1997. **93**(17): p. 3201 - 3208.
46. Herwig, K.W., Matthies, B., Taub, H., *Solvent effects on the Monolayer Structure of Long n-Alkane molecules Adsorbed on Graphite*. Physical Review Letters, 1995. **75**(17): p. 3154-3157.
47. Arnold, T., *The adsorption of alkanes from their liquids and binary mixtures*. 2001, D. Phil Thesis, University of Oxford: Oxford.
48. Arnold, T., Dong, C. C., Thomas, R. K., Castro, M. A., Perdigon, A., Clarke, S. M., Inaba, A., *The crystalline structures of the odd alkanes pentane, heptane, nonane, undecane, tridecane and pentadecane monolayers adsorbed on graphite at submonolayer coverages and from the liquid*. Phys. Chem. Chem. Phys., 2002. **4**: p. 3430-3435.
49. Arnold, T., R.K. Thomas, M.A. Castro, S.M. Clarke, L. Messe, and A. Inaba, *The crystalline structures of the even alkanes hexane, octane, decane, dodecane and tetradecane monolayers adsorbed on graphite at submonolayer coverages and from the liquid*. Phys. Chem. Chem. Phys., 2001. **4**: p. 345-351.

50. Inaba, A., S.M. Clarke, T. Arnold, and R.K. Thomas, *Mixing behaviour in 2D layers of linear alkanes adsorbed on graphite*. Chem. Phys. Lett., 2002. **352**: p. 57-62.
51. Castro, M.A., S.M. Clarke, A. Inaba, T. Arnold, and R.K. Thomas, *The investigation of mixed monolayers adsorbed from solution: octane and nonane mixtures on graphite*. Phys. Chem. Chem. Phys., 1999. **1**: p. 5017-5023.
52. Everett, D.H., *Adsorption at the Solid/Liquid Interface: Non-aqueous Systems*, in *A specialist periodical report - Colloid Science*, D.H. Everett, Editor. 1973, Adlard & Son Ltd., Bartholomew Press: Dorking. p. 49.
53. Castro, M., S.M. Clarke, A. Inaba, R.K. Thomas, and T. Arnold, *Adsorption behaviour of the binary mixtures of octane and nonane at sub-monolayer coverage on graphite*. Physical Chemistry Chemical Physics, 2001. **3**(17): p. 3774-3777.
54. Sirota, E.B., H.E.J. King, H.H. Shao, and D.M. Singer, *Rotator phases in Mixtures of n-Alkanes*. J. Phys. Chem., 1995. **99**: p. 798-804.
55. Findenegg, G.H., *Ordered layers of aliphatic alcohols and carboxylic acids at the pure liquid/graphite interface*. J. Chem. Soc., Faraday Trans. 1, 1973. **69**: p. 1069 - 1078.
56. Wang, G., S. Lei, S. De Feyter, R. Feldman, J.E. Parker, and S.M. Clarke, *Behavior of Binary Alcohol Mixtures Adsorbed on Graphite Using Calorimetry and Scanning Tunneling Microscopy*. Langmuir, 2008. **24**(6): p. 2501-2508.
57. Liphard, M., P. Glanz, G. Pilarski, and G.H. Findenegg, *Adsorption of carboxylic acids and other chain molecules from n-heptane onto graphite*. Progr. Colloid and Polymer Sci., 1980. **67**: p. 131-140.
58. Castro, M.A., S.M. Clarke, A. Inaba, C.C. Dong, and R.K. Thomas, *Crystalline Monolayer of Dodecanoic Acid Adsorbed on Graphite from n-Heptane Solution*. J. Phys. Chem. B, 1998. **102**(5): p. 777-781.
59. Bickerstaffe, A.K. and S.M. Clarke, *The interpretation of mixing behaviour in carboxylic acid monolayers adsorbed on graphite using a regular solution description*. Colloids Surf. A: Physicochem. and Engg. Aspects, 2007. **298**(1-2): p. 80-82.
60. Cheah, N.P., L. Messe, and S.M. Clarke, *The Formation of Solid Monolayers of Linear Amines Adsorbed on Graphite from the Liquid*. J. Phys. Chem. B, 2004. **108**: p. 4466-4469.
61. Duim, W.C. and S.M. Clarke, *Adsorption and mixing behaviour of ethers and alkanes at the solid/liquid interface*. J. Phys. Chem. B, 2006. **110**: p. 23853-23859.
62. Phillips, T.K., T. Bhide, S.M. Clarke, S.Y. Lee, K.S. Mali, and S.D. Feyter, *Adsorption of Aldehydes on a Graphite Substrate: Combined Thermodynamic Study of C6-C13 Homologues with a Structural and Dynamical Study of Dodecanal*. The Journal of Physical Chemistry C, 2010. **114**(13): p. 6027-6034.
63. Bhide, T., T. Arnold, and S.M. Clarke, *The structure of dodecanamide monolayers adsorbed on graphite*. Progress in Colloid and Polymer Science, 2010. **137**: p. 5-8.
64. Bhide, T., S.M. Clarke, T.K. Phillips, T. Arnold, and J.E. Parker, *Crystalline Structures of Alkylamide Monolayers Adsorbed on the Surface of Graphite*. Langmuir, 2010. **26**(11): p. 8201-8206.
65. Takeuchi, H., S. Kawauchi, and A. Ikai, *Differentiation in Chemically Functional Groups in Stearoyl Amide and Anilide with Scanning Tunneling Microscopy*. Jpn. J. Appl. Phys., 1996. **35**: p. 3754-3758.
66. Arnold, T., Clarke, S. M., *Thermodynamic Investigation of the Adsorption of Amides on Graphite from Their Liquids and Binary Mixtures*. Langmuir, 2008. **24**(7): p. 3325-3335.

67. Parker, J.E. and S.M. Clarke, *Mixing in Adsorbed Monolayers: Perfluorinated Alkanes*. Langmuir, 2008. **24**: p. 4833-4844.
68. Parker, J.E., S.M. Clarke, A.C. Perdigon, and A. Inaba, *The Crystalline Structures of Fluoroalkane Monolayers Adsorbed on Graphite at Submonolayer Coverages*. The Journal of Physical Chemistry C, 2009. **113**(51): p. 21396-21405.
69. Bickerstaffe, A.K., N.P. Cheah, S.M. Clarke, J.E. Parker, A. Perdigon, L. Messe, and A. Inaba, *The Crystalline Structures of Carboxylic Acid Monolayers Adsorbed on Graphite*. J. Phys. Chem. B, 2006. **110**: p. 5570-5575.
70. Alba, M.D., A.K. Bickerstaffe, M.A. Castro, S.M. Clarke, S. Medina, C. Millán, M.M. Orta, E. Pavón, and A.C. Perdigón, *Phase separation of carboxylic acids on graphite surface at submonolayer regime*. The European Physical Journal - Special Topics, 2009. **167**(1): p. 151-156.
71. Messé, L., A. Perdigon, S.M. Clarke, M.A. Castro, and A. Inaba, *Layer-by-layer surface freezing of linear alcohols at the graphite/liquid interface*. Journal of Colloid and Interface Science, 2003. **266**(1): p. 19-27.
72. Alba, M.D., M.A. Castro, S.M. Clarke, and A.C. Perdigón, *NMR study of n-dodecane adsorbed on graphite*. Solid State NMR, 2003. **23**(3): p. 174-181.
73. Parker, J.E., S.M. Clarke, and A.C. Perdigón, *Preferential adsorption of solid monolayers of hydrocarbons over fluorocarbons at the solid/liquid interface*. Surface Science, 2007. **601**(18): p. 4149-4153.
74. Alba, M.D., M.A. Castro, S. Clarke, S. Medina, L. Messe, C. Millán, M.M. Orta, and A.C. Perdigon, *Preferential adsorption from binary mixtures on graphite: The n-decane-n-heptan-1-ol system*. J. Phys. Chem. C, 2009. **113**(8): p. 3176-3180.
75. Morrison, R.T. and R.M. Boyd, *Organic Chemistry*. 6th ed: Prentice-Hall international.
76. Dragnevski, K.I., A.M. Donald, S.M. Clarke, and A. Maltby, *Novel applications of ESEM and EDX for the study of molecularly thin amide monolayers on polymer films*. Colloids and Surfaces A: Physicochem. Engg. Aspects, 2009. **337**(1-3): p. 47-51.
77. Clarke, S.M., L. Messe, J. Adams, A. Inaba, T. Arnold, and R.K. Thomas, *A quantitative parameter for predicting mixing behaviour in adsorbed layers: the 2D isomorphism coefficient*. Chem.Phys. Lett., 2003. **373**: p. 480-485.
78. Gilli, G. and P. Gilli, *The Nature of the Hydrogen Bond*. International Union of Crystallography Book Series. 2009, New York: Oxford University Press.
79. Frommer, J., *Scanning Tunneling Microscopy and Atomic Force Microscopy in Organic Chemistry*. Angew. Chem. Int. Ed. Engl., 1992. **31**(10): p. 1298-1328.
80. Giancarlo, L.C. and G.W. Flynn, *Scanning Tunneling and Atomic Force Microscopy probes of self-assembled, physisorbed monolayers: Peeking at the Peaks*. Annu. Rev. Phys. Chem., 1998. **49**: p. 297-336.
81. Kudernac, T., S. Lei, J.A.A.W. Elemans, and S. De Feyter, *Two-dimensional supramolecular self-assembly: nanoporous networks on surfaces*. Chemical Society Reviews, 2009. **38**(2): p. 402-421.
82. Claypool, C.L., F. Faglioni, W.A. Goddard III, H.B. Gray, N. Lewis, and R.A. Marcus, *Source of image contrast in STM images of functionalized alkanes on graphite: A systematic functional group approach*. J. Phys. Chem. B., 1997. **101**: p. 5978-5995.
83. Lim, R., J. Li, and S.F.Y. Li, *The Formation of Two-Dimensional Supramolecular Chiral Lamellae by Diamide Molecules at the Solution/Graphite Interface: A Scanning Tunneling Microscopy Study*. Langmuir, 2000. **16**: p. 7023.

84. Zou, B., K. Dreger, C. Muck-Lichtenfeld, S. Grimme, H.J. Schafer, H. Fuchs, and L. Chi, *Simple and Complex Lattices of N-Alkyl Fatty Acid Amides on a Highly Oriented Pyrolytic Graphite Surface*. Langmuir, 2005. **21**: p. 1364-1370.
85. Thalacker, C., A. Miura, S.D. Feyter, F.C.D. Schryver, and F. Wurthner, *Hydrogen bond directed self-assembly of core-substituted naphthalene bisimides with melamines in solution and at the graphite interface*. Organic & Biomolecular Chemistry, 2005. **3**(3): p. 414-422.
86. De Feyter, S., A. Miura, S. Yao, Z. Chen, F. Wurthner, P. Jonkheijm, A.P.H.J. Schenning, E.W. Meijer, and F.C. De Schryver, *Two-Dimensional Self-Assembly into Multicomponent Hydrogen-Bonded Nanostructures*. Nano Letters, 2005. **5**(1): p. 77-81.
87. De Feyter, S. and F.C. De Schryver, *Self-Assembly at the Liquid/Solid Interface: STM Reveals*. The Journal of Physical Chemistry B, 2005. **109**(10): p. 4290-4302.
88. Temirov, R., S. Soubatch, O. Neucheva, A.C. Lassise, and F.S. Tautz, *A novel method achieving ultra-high geometrical resolution in scanning tunnelling microscopy*. New Journal of Physics, 2008. **10**(5): p. 053012.
89. Weiss, C., C. Wagner, R. Temirov, and F.S. Tautz, *Direct Imaging of Intermolecular Bonds in Scanning Tunneling Microscopy*. Journal of the American Chemical Society, 2010.
90. Joshi, N.B. and D.E. Hirt, *Evaluating Bulk-to-Surface Partitioning of Erucamide in LLDPE Films Using FT-IR Microspectroscopy*. Applied Spectroscopy, 1999. **53**: p. 11-16.
91. Sankhe, S.Y. and D.E. Hirt, *Characterization of Erucamide Profiles in Multilayer Linear Low-Density Polyethylene and Propylene-Ethylene Copolymer Films Using Synchrotron-Based FT-IR Microspectroscopy*. Applied Spectroscopy, 2002. **56**: p. 205-211.
92. Ramirez, M.X., K.B. Walters, and D.E. Hirt, *Relationship between Erucamide Surface Concentration and Co-efficient of Friction of LLDPE film*. J. Vinyl Additive Tech., 2005. **11**: p. 9-12.
93. Allan, D., B.J. Briscoe, and D. Tabor, *Lubrication of polythene by oleamide and stearamide-II*. Wear, 1973. **25**: p. 393-397.
94. Kaganer, V.M., H. Möhwald, and P. Dutta, *Structure and phase transitions in Langmuir monolayers*. Reviews of Modern Physics, 1999. **71**(3): p. 779.
95. Kaercher, T., D. Hönig, and D. Möbius, *Brewster angle microscopy*. International Ophthalmology, 1993. **17**(6): p. 341-348.
96. Als-Nielsen, J., D. Jacquemain, K. Kjaer, F. Leveiller, M. Lahav, and L. Leiserowitz, *Principles and applications of grazing incidence X-ray and neutron scattering from ordered molecular monolayers at the air-water interface*. Physics Reports, 1994. **246**: p. 251-313.
97. Melzer, V., D. Vollhardt, G. Brezesinski, and H. Möhwald, *Competition of interactions in monolayers of amphiphilic acid amides at the air-water interface*. Thin Solid Films, 1998. **327-329**: p. 857-860.
98. Vollhardt, D. and R. Wagner, *Effect of the Exchange of Substituent Position in an Amide Amphiphile on the Monolayer Characteristics*. J. Phys. Chem. B, 2006. **110**(30): p. 14881-14889.
99. Weinbach, S.P., D. Jacquemaint, F. Leveiller, K. Kjaer, J. Als-Nielsen, and L. Leiserowitz, *Effect of Cosolvent on the Lateral Order of Spontaneously Formed*

- Amphiphilic Amide Two-Dimensional Crystallites at the Air-Solution Interface*. Journal of the American Chemical Society, 1993. **115**: p. 11110-11118.
100. Melzer, V., D. Vollhardt, G. Weidemann, G. Brezesinski, R. Wagner, and H. Mohwald, *Structure formation and phase transitions in Gibbs and Langmuir monolayers of amphiphilic acid amides*. Physical Review E, 1998. **57**(1): p. 901.
  101. Vollhardt, D., V. Melzer, and V. Fainerman, *Phase transition in adsorption layers at the air-water interface: structure features of the condensed phase*. Thin Solid Films, 1998. **327-329**: p. 842-845.
  102. Wurz, D.H. and N.E. Sharpless, *Amides of Saturated Aliphatic Acids*. Analytical Chemistry, 1949. **21**(12): p. 1446-1448.
  103. Turner, J.D. and E.C. Lingafelter, *The X-ray crystallography of the n-aliphatic amides*. Acta Crystallographica, 1955. **8**(9): p. 549-550.
  104. Hahn, T., *Space group symmetry*. 4th ed. International tables for crystallography. Vol. A. 1995, London: Kluwer Academic.
  105. Brathovde, J.R. and E.C. Lingafelter, *The crystal structure of decanamide*. Acta Cryst., 1958. **11**: p. 729.
  106. Leiserowitz, L. and G.M.J. Schmidt, *Molecular packing modes. Part III. Primary amides*. J. Chem. Soc. A, 1969: p. 2372 - 2382.
  107. Leiserowitz, L. and A.T. Hagler, *The Generation of Possible Crystal Structures of Primary Amides*. Proceedings of the Royal Society of London. Series A, Mathematical and Physical Sciences (1934-1990), 1983. **388**(1794): p. 133-175.
  108. Taylor, R., O. Kennard, and W. Versichel, *The geometry of the N-H...O=C Hydrogen Bond. 3. Hydrogen-Bond distances and Angles*. Acta Cryst., 1984. **B40**: p. 280-288.
  109. Gavezzotti, A. and G. Filippini, *Geometry of the Intermolecular X-H...Y (X, Y = N, O) Hydrogen Bond and the Calibration of Empirical Hydrogen-Bond Potentials*. J. Phys. Chem., 1994. **98**(18): p. 4831-4837.
  110. Abate, L., E. Badea, I. Blanco, and G. Della Gatta, *Heat Capacities and Enthalpies of Solid-Solid Transitions and Fusion of a Series of Eleven Primary Alkylamides by Differential Scanning Calorimetry*. J. Chem. Engg. Data, 2008. **53**(4): p. 959-965.
  111. Pimentel, G.C. and A.L. McClellan, *The Hydrogen Bond*. 1960, San Francisco and London: W. H. Freeman and Co.
  112. Vinogradov, S.N. and R.H. Linnell, *Hydrogen Bonding*. 1971: Van Nostrand Reinhold Company.
  113. Steiner, T., *The hydrogen bond in the solid state*. Angew. Chem. Int. Ed., 2002. **41**: p. 48-76.
  114. Israelachvili, J., *Intermolecular & surface forces*. 2nd ed. 1992, London: Academic Press.

# Chapter 2

## Diffraction – Theory and Experiment

---

In this chapter the theory of X-ray and neutron scattering is explained, along with the theory of diffraction from adsorbed layers. A detailed description of the experimental procedures relevant to this work is given. The process of diffraction data reduction and fitting to obtain the final structural solution is also discussed. A more detailed treatment to the theory of X-ray and neutron scattering can be found in standard texts on diffraction [1-4].

### 2.1 Properties of X-Rays and neutrons

X-Rays have a wavelength ( $\lambda$ ) of  $10^{-2}$  to  $10^2$  Å and propagate with a speed of  $c=2.998 \times 10^8$  m/s. Those used in the study of the structure of materials have wavelengths confined to the range of 0.5-2.5 Å. This is of the order of inter-atomic distances encountered in condensed matter which makes X-rays play a very important role in probing its structure.

A neutron is an uncharged elementary particle having a mass  $m=1.675 \times 10^{-24}$  g and a spin =  $\frac{1}{2}$ . The kinetic energy  $E$  and momentum  $p$  of a neutron are given by:

$$E = \frac{1}{2}mv^2$$

... Eqn. 2-1

and

$$p = mv = \frac{h}{\lambda}$$

... Eqn. 2-2

where  $v$  is the neutron velocity and  $h$  is the Planck's constant ( $h=6.626 \times 10^{-34}$  J·s). Thermal neutrons have similar wavelengths to X-rays, also making them valuable in the study of matter. X-rays and neutrons exhibit dual character of behaving both as a wave and as a particle. This wave-particle duality is expressed by the *de Broglie* relation (Eqn. 2-2). A photon does not possess mass or any elementary charge.

## 2.2 Interaction of X-rays and neutrons with matter

X-Rays, being electromagnetic radiation, interact with electrons in matter. The sinusoidal electric field of X-Rays sets electrons oscillating, which results in re-emission of electromagnetic radiation of the same frequency propagating in all directions. This is referred to as scattering of an X-ray by an electron. Absorption of X-rays is an important factor when they interact with matter and can result in ionization.

The scattering behaviour of neutrons is similar to that of X-rays, but since a neutron is a nuclear particle and does not possess any charge, it is only affected by very short range nuclear forces. In addition it can also be affected by the magnetic properties of an atom. In most cases however the magnetic interaction is negligibly small compared to the nuclear interaction. Neutrons are also unaffected by the electron cloud in an atom. When a neutron passes near a nucleus it can be either absorbed or scattered. Absorption of a neutron results in the nucleus of the atom achieving an excited state, which then returns back to the ground state. This can occur by the emission of a  $\gamma$ -ray photon (Eg.  $^3\text{He}$  nucleus), or by nuclear fission (Eg.  $^{235}\text{U}$  reactor core). In addition to being absorbed, low energy thermal neutrons can be scattered by a nucleus, which results in a change in the direction of motion and energy of the neutron.

The scattering amplitude (referred to as the scattering length  $b$  for neutrons or the atomic scattering factor  $f$  for X-rays) is a measure of how strongly an atom will scatter an incoming beam of X-rays or neutrons.

$$f = \frac{\text{amplitude of wave scattered by an atom}}{\text{amplitude of wave scattered by one electron}}$$

... Eqn. 2-3

Thus,  $f=Z$  (the atomic number) for any atom scattering in the forward direction for X-rays. While X-ray scattering amplitudes increase linearly with atomic number (due to the increase in the electron density), the dependence of neutron scattering amplitude on atomic number appears to be random.

The atomic scattering factor arises from the fact that the electron cloud around an atom is similar in size to the wavelength of the radiation, hence there is interference from X-rays scattered by one side of the electron cloud and the other. As the scattering angle  $\theta$  increases, the scattered X-rays become more and more out of phase and  $f$  decreases.  $f$  also depends upon the wavelength, and for each element the variation of  $f$  with  $(\sin\theta/\lambda)$  can be calculated and plotted [1]. In contrast, since neutron wavelengths are much bigger than the size of the nucleus from which they are scattered, the neutron scattering length for an element remains essentially constant with  $(\sin\theta/\lambda)$ .

Importantly, the neutron scattering lengths of hydrogen and deuterium are significantly different, which makes neutron diffraction particularly useful for studying hydrogen containing alkyl molecules, where the weak scattering of the hydrogen atoms by X-ray alone cannot help locate the position of the hydrogen atoms precisely.

The differential scattering cross section is the probability that a photon or a neutron impinging on a sample is scattered into a unit solid angle in the given direction:

$$\frac{d\sigma}{d\Omega} = \frac{\text{Number of particles scattered into a unit solid angle in a given direction per second}}{\text{incident beam flux}}$$

... Eqn. 2-4

The partial differential scattering cross section is defined as the fraction of the incident neutrons/photons scattered into a solid angle  $d\Omega$  having energy between  $E$  and  $E+dE$  and is given by  $\frac{\partial^2\sigma}{\partial\Omega\partial E}$ . It is essentially this quantity that is measured in a scattering experiment. The quantity  $\sigma$  is the total scattering cross section, which is simply the total amount of the incident flux that is scattered by the sample.

If there is no correlation between the scattering amplitudes of the atoms in an assembly, then the partial differential scattering cross section can be split into two parts that correspond to coherent and incoherent scattering. Coherent scattering, which is explained here, provides information about the structure of the material being studied. Incoherent scattering of neutrons cannot provide any structural information but provides useful information about the motion of the molecules. Incoherent scattering of X-rays is usually very small and produces a background over which the diffraction peaks are superimposed.

### 2.3 Diffraction in 3D

When a beam of white radiation impinges on a crystal with its surface cut parallel to a crystallographic plane (h,k,l), reflection can only take place for the component of the beam having a single wavelength  $\lambda$  (or  $n$  multiples of) that satisfies the Bragg relation:

$$n\lambda = 2d \sin\theta$$

... Eqn. 2-5

where  $d$  is the spacing of the (h,k,l) planes [1].

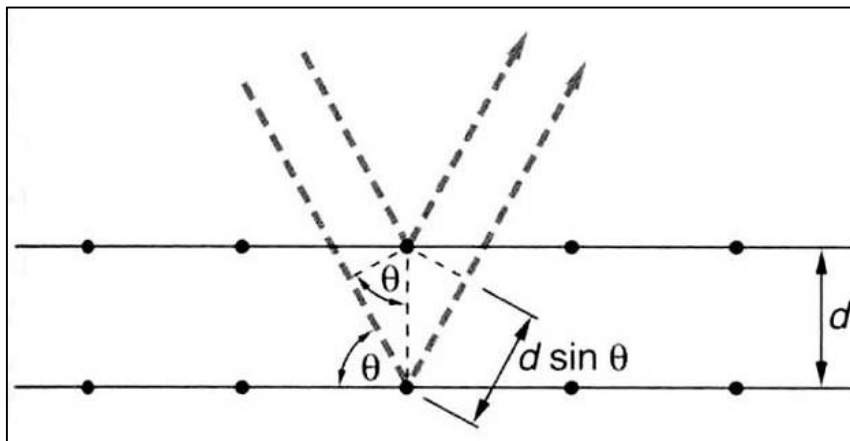
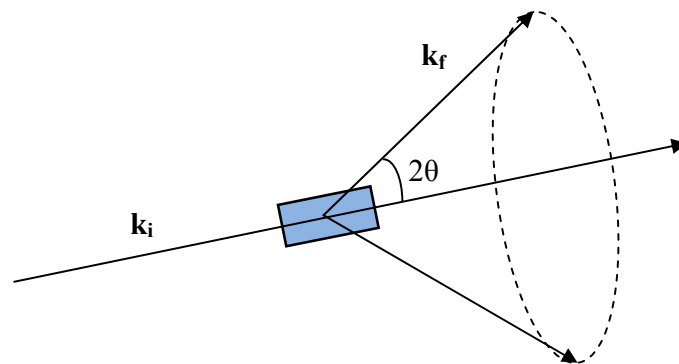


Figure 2-1 Bragg's law

In a diffraction pattern from a single crystal, high intensity diffraction spots are observed at different angles which satisfy the Bragg law. In contrast, a powder sample consists of a large number of small crystalline regions randomly oriented in space. If the orientations of the crystals

are perfectly random, then some of these will satisfy Bragg's law at a given angle  $2\theta$ . Therefore, the diffracted beams all lie along the surface of a cone such that the axis of the cone is along the incident-beam direction and the cone angle is  $2\theta$  (Figure 2-2).

For the same wavelength, there may be other crystalline regions having different spacings that make the incident beam diffract at some other angle, and another cone will be produced at a different angle  $2\theta$  to the incident beam. In this way co-axial cones are produced for all the possible lattice planes for a monochromatic beam of X-rays. The intensities integrated around the circular cross-section of the diffraction cones for each angle can be measured and plotted to obtain a diffraction pattern.



**Figure 2-2** A diffraction cone from a powdered sample

In essence, the following information can be obtained from an X-Ray diffraction pattern:

- From the set of different angles at which the Bragg peaks are observed, the lattice parameters  $a$ ,  $b$ ,  $c$  and the angles between them that define the unit cell geometry can be calculated.
- By collecting integrated intensities of diffraction peaks and subjecting them to subsequent analysis, it is possible to determine the symmetry of the structure and positions of the atoms packed in the unit cell.
- The widths of the reflections depend on the crystallite size and other factors.

## 2.4 Diffraction from adsorbed layers

Diffraction from two-dimensional systems was first considered by Max von Laue in 1932 [5]. Further treatments were made later by others, including Warren in particular and also by Wilson [6-8].

### 2.4.1 Diffraction peak positions

A two-dimensional unit cell is represented in Figure 2-3, in which two lattice planes are separated by a distance  $d_{hk}$ . The unit cell has lengths  $a$ ,  $b$  and a unit cell angle  $\nu$ .

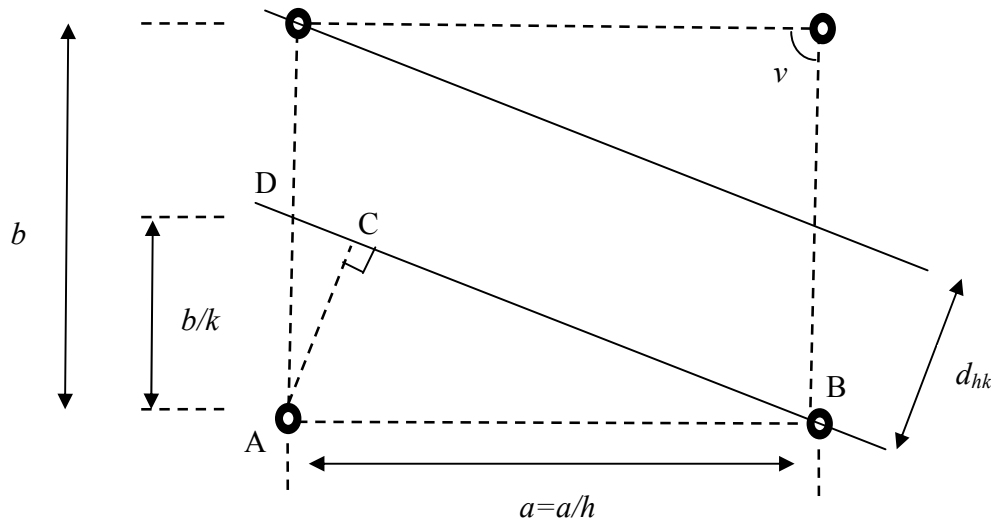


**Figure 2-3** Two-dimensional lattice planes (solid lines), characterised by the Miller indices  $(h,k)=(1,2)$ .  
The unit cell is shown by the dotted lines.

For a given reflection  $(h,k)$ , the inter-planar spacing is related to the unit cell dimensions by:

$$\frac{1}{d_{hk}^2} = \left( \frac{h^2}{a^2} + \frac{k^2}{b^2} - \frac{2hk}{ab} \cos \nu \right) \frac{1}{\sin^2 \nu}$$

... Eqn. 2-6

It is worth noting that for the rectangular unit cell, the same value of  $d$  will be obtained for  $(-h,k)$  as for  $(h,k)$  and the same is true for any combination of negative values for  $(h,k)$ .

In a diffraction experiment, it is convenient to define a momentum transfer (scattering vector)  $q$  ( $=\mathbf{k}_f - \mathbf{k}_i$ , Figure 2-2) such that:

$$|q| = \frac{4\pi \sin \theta}{\lambda}$$

... Eqn. 2-7

From Bragg's law (Eqn. 2-5) and Eqn. 2-7, we get:

$$q = \frac{2\pi}{d}$$

... Eqn. 2-8

Thus, it can be seen that the peak positions for a sample as a function of  $q$  depend only on  $d$  (which can be calculated from Eqn. 2-6) and are independent of the particular experiment ( $\lambda$  and  $\theta$ ). This enables simultaneous comparison of X-ray and neutron data measured at different instruments.

### 2.4.2 Diffraction peak intensities

The diffracting powder is treated as an assembly of planar arrays that are randomly oriented in space. The intensity of a diffraction peak is proportional to the square of the structure factor  $F_{hk}$ , where  $F_{hk}$  is given by [6]:

$$F_{hk} = \sum_n f_n \exp \left\{ 2\pi i \left[ \left( \frac{hx}{a} \right) + \left( \frac{ky}{b} \right) + \frac{2lz}{\lambda} \sqrt{\sin^2 \theta - \sin^2 \theta_{hk}} \right] \right\}$$

... Eqn. 2-9

Here  $f_n$  is the angle dependant X-ray atomic scattering factor of atom  $n$  in the unit cell (Eqn. 2-3) which has the fractional co-ordinates  $(x/a, y/b)$  and a Z-coordinate  $z$ , with  $l$  being the distance between the 2D planes. For neutrons,  $f_n$  is replaced by  $b_n$ , the neutron scattering length of atom  $n$ , so that X-rays and neutrons can produce diffraction peaks of very different intensities.

The expression for the intensity of the  $(h, k)^{\text{th}}$  Bragg reflection [6, 9] is:

$$I_{hk} \propto \frac{m_{hk} |F_{hk}|^2 e^{-2W}}{(\sin \theta)^{3/2}} \left( \frac{L}{\lambda \pi^{1/2}} \right)^{1/2} \mathfrak{S}(a)$$

... Eqn. 2-10

where  $m_{hk}$  represents the multiplicity of the  $(h,k)$ <sup>th</sup> reflection,  $e^{-2W}$  is the Debye-Waller factor, and  $L$  is a parameter that depends on the size of the 2D crystallites (§2.5).

The function  $\mathfrak{S}(a)$  is defined by:

$$\mathfrak{S}(a) \equiv \int_0^\infty e^{-(x^2 - a)^2} dx$$

... Eqn. 2-11

where

$$a = \left( \frac{2\pi^{1/2} L}{\lambda} \right) (\sin \theta - \sin \theta_{hk})$$

... Eqn. 2-12

Here  $\theta_{hk}$  is the Bragg angle. The consequence is that there is constructive interference when  $\theta \geq \theta_{hk}$ , so that after the initial rise at  $\theta_{hk}$ , the intensity will decrease only slowly at higher angles. This results in a characteristic saw-tooth shape to the Bragg peak rather than the symmetrical peaks seen in three-dimensional diffraction patterns (an example 2D diffraction pattern is shown in Figure 2-4).

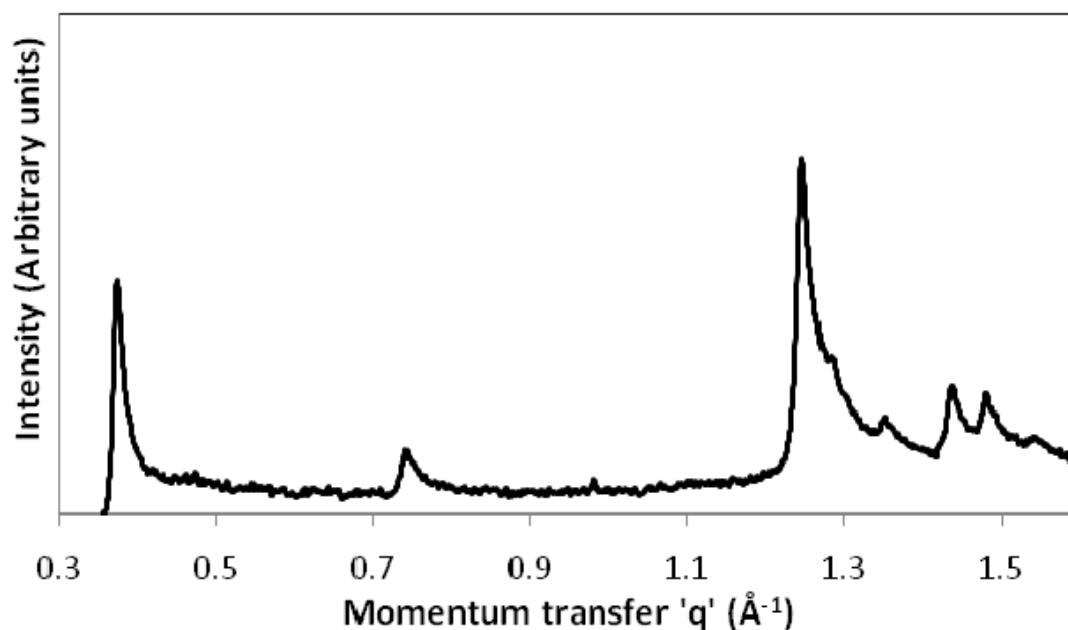


**Figure 2-4** Experimental X-ray diffraction pattern for pentanamide (C5:0) on graphite showing the characteristic asymmetric diffraction peaks obtained from adsorbed layers

### 2.4.3 Peak shape – preferred orientation

The *Papyex* substrate used for diffraction studies in this work is not a completely random powder sample. It has some amount of preferred orientation i.e. the crystallites tend to orient themselves more in a direction such that their *c*-axes are normal to the surface of the graphite. Kjems [9] accounted for the sharper fall-off in intensity observed for molecules adsorbed on a graphite substrate by introducing a probability distribution function  $H(\gamma)$  for the graphite crystallite orientation  $\gamma$  with respect to the foil plane:

$$H(\gamma) = H_0 + H_1 \exp\left[-\frac{1}{2}\left(\frac{\gamma}{\delta}\right)^2\right]$$

... Eqn. 2-13

Here  $H_0$  accounted for the purely random part of the distribution and  $H_1$  for the preferentially oriented part (a Gaussian distribution of width  $\delta$  about the mean orientation  $\gamma$ ). The function  $H(\gamma)$  is normalised by requiring that:

$$\int_0^{\pi} H(\gamma) d\gamma = 1$$

... Eqn. 2-14

This gives two independent variables  $H_0/H_1$  and  $\delta$  that can be fitted to the experimental line-shape (§2.11.3). As a result of preferred orientation, the tail of the 2D diffraction peaks falls quicker in intensity with increasing scattering angle as compared to the Warren model.

#### 2.4.4 Diffraction peak widths

If the size of the crystallites is very large relative to the radiation wavelength, then the diffraction peaks are relatively sharp. However if the size of the crystallites is comparable to the wavelength, then the diffraction peaks become broader. The relation between peak width ( $B$ ), i.e., the full width of the peak at half its maximum intensity (FWHM), and the size of the 2D crystallites ( $L$ ) is given by [6]:

$$L = \frac{1.84\lambda}{B \cos \theta_B}$$

... Eqn. 2-15

where  $\theta_B$  is the Bragg angle of the peak.

Other factors that affect the line width are due to the fact that that the crystalline regions in the substrate are not always perfect and the incident beam also possesses some divergence and may not be perfectly monochromatic. All these factors make the powder diffraction cones have a finite thickness, and cause broadening of the diffraction peaks.

The last factor is reflected in an experimental resolution function. Each instrument has a different detector resolution, which also accounts for peak broadening. This resolution function is represented by a Gaussian of finite width (or a pseudo-voigt function). The calculated peak intensity is then convoluted with this Gaussian function to obtain a peak-shape that can be

compared to the experimental data, after accounting for the preferred orientation as explained above.

## 2.5 Correction factors

### 2.5.1 Absorption corrections

When radiation is incident on a sample, the sample may absorb some and diffract some of it. For most organic materials the proportion of neutron radiation absorbed is significantly smaller than that which is scattered, and thus absorption may be neglected. For X-rays, the corrections for absorption are more complex. Empirical corrections may be applied [10]; however the sample thickness have been optimised here such that absorption effects are reduced by decreasing the thickness without substantially compromising on the scattered intensity, and thus absorption corrections have not been considered in this work.

### 2.5.2 The Lorentz and polarization corrections

When X-rays or neutrons are reflected they become partially polarised. Neutrons can only become magnetically polarised, and this effect is not considered in this work. Polarisation of X-rays on the other hand results in the reduction of intensity of the diffraction peak, depending upon the diffraction geometry.

The polarisation factor is not required to be taken into account if the plane of polarisation of the X-rays is perpendicular to the 2D layers as is the case for the powder diffraction instruments at the synchrotrons in this work. Also, for neutron diffraction the polarisation factor was not considered since the neutrons used here were not polarised. The Lorentz factor (LF) depends on the instrumental set-up and is applicable to both neutron and X-ray diffraction. For normal powder diffraction it has the form [3]:

$$LF = \frac{1}{\sin 2\theta}$$

... Eqn. 2-16

### 2.5.3 The Temperature factor

Thermal motion of atoms has an effect on X-ray and neutron intensities. The normal scattering factor curves (§2.2) are calculated on the basis of electron distribution in a stationary system; however atoms in crystals are always vibrating about their equilibrium positions. The magnitude of the vibration depends on the temperature, the mass of the atom, and the firmness to which it is held in place by bonds and other forces. The effect of such thermal motion is to spread the electron cloud over a larger volume and thus cause the scattering power of an atom to fall off more rapidly than the ideal, stationary model. The Debye-Waller correction factor ( $e^{-W}$ ) for temperature, for both X-rays and neutrons, is given by the following expression:

$$e^{-W} = e^{\frac{-q^2 \langle u^2 \rangle}{2}}$$

... Eqn. 2-17

Here  $\langle u^2 \rangle$  is the mean square amplitude of the atomic vibration. The proper scattering factor is then related to the one without correction  $f_o$  as:

$$f = f_o e^{-W}$$

... Eqn. 2-18

For the purposes of this work, the Debye-Waller factor has been set equal to one since the amplitude of vibrations in the adsorbed layer is small compared to the distances between the atoms at the temperatures here.

### 2.5.4 Multiplicity factor

Consider the case of a 2D rectangular lattice. The  $d$ -spacings of lattice planes (h, k) are the same as those for (h,-k), (-h, k) and (-h, -k) (Eqn. 2-6). In a powder diffraction experiment all the crystallites are randomly oriented in space. This implies that the powder diffraction cones for these four set of lattice planes will be at the same angle and thus the intensity for the observed (h, k) reflection will be four times greater than one might have expected. A similar argument exists for the 3D case, and values of the multiplicity factor  $p$  tabulated for the various crystal systems can be found in [1].

## 2.6 Symmetry Considerations

Knowledge of symmetry relationships in the unit cell is important since it simplifies the actual number of parameters to be determined from a diffraction pattern. There are seven three-dimensional crystal systems that are defined by their symmetry [1, 2, 4, 10]. Cubic crystal systems (e.g. NaCl) are most symmetric, while triclinic (seen, for example, in many bulk alkanes) are the least symmetric having no intrinsic symmetry elements.

The two-dimensional case is simpler with only four symmetry systems (square, rectangular, hexagonal and oblique). Each kind of symmetry system can be of several types depending upon the symmetry operation performed on them, the main symmetry operations being rotation, reflection and inversion. This gives rise to 17 possible plane groups.

**Table 2-1** Information on relevant two-dimensional plane groups

| Plane group       | Symmetry system | Symmetry elements present                                   | Systematic absences                          | Symmetry-induced transformations*   |
|-------------------|-----------------|---|--|---|
| <i>p2</i>         | Oblique         | Two-fold rotation points                                    | None   | $x, y \rightarrow \bar{x}, \bar{y}$   |
| <i>pgg (p2gg)</i> | Rectangular     | 1. Two-fold rotation points<br>2. Perpendicular glide lines | 1. (h,0) where h=odd<br>2. (0,k) where k=odd | $x, y \rightarrow \bar{x}, \bar{y}$<br>$\rightarrow \bar{x} + \frac{1}{2}, y + \frac{1}{2}$<br>$\rightarrow x + \frac{1}{2}, \bar{y} + \frac{1}{2}$ |

\*Symmetry induced transformations transform a point (x,y) in the unit cell to a new point with after the application of a symmetry operation.

In a monolayer diffraction experiment it is possible that some of the expected peaks for a crystal are absent from the pattern. Systematic absences of this kind help gain insight into the symmetry of the given sample. For example, if the molecules are arranged so that there is a two-fold screw axis parallel to the a-axis, then the distances between the (h,0) planes will be half as that

expected from the unit cell dimension. Hence, reflections will only be observed for even values of  $h$  in this system.

A complete list of two-dimensional space groups and further information on each can be found in [11]. Two plane groups relevant for the amide monolayers in this work are  $p2$  and  $pgg$ ; their details are given in Table 2-1.

In the next few sections an overview of centralised facilities for X-ray and neutron production and a description of instruments used in this work is provided.

## 2.7 X-ray and neutron facilities

X-rays are produced whenever a charged particle is rapidly accelerated or decelerated. This can be brought about by striking an electron at a metal target (X-ray tubes), or by bending an electron circulating at high speeds (synchrotron). X-rays are generated in the laboratory by a filament tube, originally invented by Coolidge in 1913. Electrons released from a hot tungsten filament are accelerated towards a metal target (usually Copper or Molybdenum) and X-rays are generated on impact of the electron at the target. The need for a more intense source of X-rays has led to the development of synchrotron radiation source in recent years. All X-ray diffraction experiments in this work were performed at synchrotron sources, and these are described briefly below.

### 2.7.1 Synchrotrons X-ray sources

A synchrotron is a large facility in which high-energy electrons, circulating in a large closed orbit under high vacuum at speeds approaching the speed of light, are led to emit intense beams of X-rays and other electromagnetic radiation. The closed orbit is achieved by bending the path of the electron with a series of bending magnets placed along the ring circumference. The flux of X-rays emitted is several orders of magnitude greater than that obtained by X-ray tubes, allowing for very short times of measurement and can be useful in studying the dynamic behaviour of samples or systems where there is very little material available (i.e. this work).

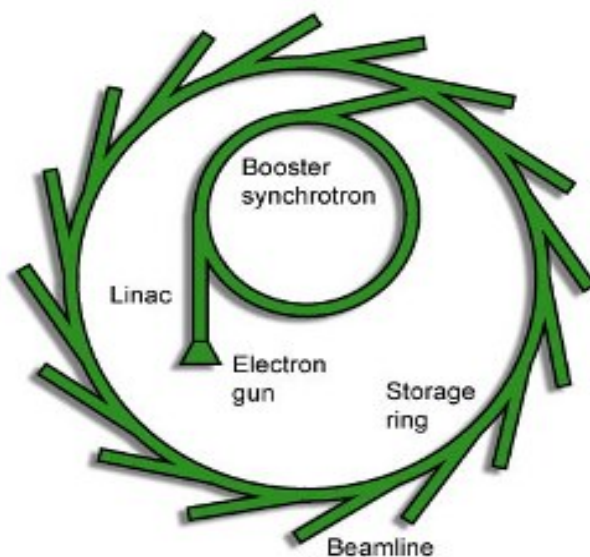


**Figure 2-5** Synchrotron layout [12]

The different systems that make up a synchrotron are described below:

1. *The injection system* – this generates electrons, accelerates them, and injects them into the vacuum chamber. This is achieved by an electron gun, the *Linac* (Linear accelerator) and the booster synchrotron, respectively.
2. *The storage ring* – this consists of alternating straight and curved sections in which the electrons circulate along a closed trajectory. Vacuum is maintained at  $10^{-10} \sim 10^{-11}$  Torr in the ring to prevent collisions of the electrons with air molecules which can greatly reduce their speed.
3. *The radiofrequency cavity system* - this acts on the circulating electrons and restores the energy they lose through the emission of electromagnetic radiation as they accelerate around the synchrotron.
4. *Magnets* - the bending magnets bend the trajectory of the electrons and force them to circulate in a closed orbit as they emit radiation, and the focussing magnets fine tune the electron trajectory to keep them in a well defined path.
5. *The beam lines*, through which the X-rays exit to the user's experimental chambers.
6. *The insertion devices* – Third generation synchrotron sources which are optimised for brightness include insertion devices such as wigglers and undulators in the straight sections

of the ring. These consist of an array of vertically oriented dipole magnets which produce synchrotron radiation with significantly higher brightness [13].

The spectral distribution of the emitted synchrotron radiation is very broad, from the infrared ( $\lambda \sim 10^{-2}$  cm) to the hard X-ray ( $\lambda \sim 10^{-2}$  nm) region. The whole spectrum shifts to shorter wavelengths if the energy of the orbiting electron is increased or the radius of curvature  $R$  is made smaller. The X-ray beam is highly collimated as it emerges, since at relativistic speeds the electrons forced along a curved path emit radiation which is sharply concentrated in the direction of their motion. The emitted radiation is also highly polarised in the plane of the electron motion (horizontal plane).

### 2.7.2 Neutron sources

Neutrons are generated by either fission reactors (for example, at the *Institut Laue Langevin, ILL* or the *Laboratoire Léon Brillouin, LLB*, France) or at a spallation source i.e. by the bombardment of heavy metal targets with an accelerated proton beam (for example, at *ISIS*, U.K or *SINQ*, Switzerland) [14].

#### 2.7.2.1 Nuclear reactors

In a nuclear reactor a sustained nuclear fission reaction takes place, for example in the fuel rods of  $^{235}\text{U}$ , and produces fast neutrons in the energy range of 1-2 MeV. In the reactor core the fuel rods are surrounded by a thermal moderator, usually  $\text{D}_2\text{O}$ , which slows down the neutrons thereby making them suitable for experimental purposes. Unlike synchrotron radiation, neutrons emerging from the reactor core are not collimated and emerge in all directions. To channel them to the user, neutron guides, that are essentially evacuated tubes with thick glass walls having an inner coating of Nickel, are used. The guides work on the principle of total internal reflection.

Neutrons, in thermal equilibrium with the moderator, have a Maxwellian velocity distribution. A moderator at 300 K has neutrons with a most probable wavelength of 1.45 Å, while that at 25 K (cold source) for instance has a peak wavelength of around 3.5 Å. Shorter wavelengths may be reached by taking the moderator to a high temperature  $\sim 2000$  K (hot source).

### 2.7.2.2 Spallation neutron sources

In proton spallation sources, protons are accelerated using a linear accelerator and/or a synchrotron, and a heavy metal target is bombarded by such a proton beam. Neutrons are ‘chipped off’ the metal target, with each proton producing  $\sim 30$  neutrons. Moderators placed around the target slow the neutrons to the useful wavelength range, and reflectors direct the neutrons in the desired direction. The whole acceleration process occurs every 20 ms, resulting in a pulsed neutron source of 50 Hz (ISIS, U.K.). The pulsed nature of this type of source has significant implications in the type of instruments found at these facilities, and further details can be found in [15].

### 2.7.3 Optics

To choose the desired wavelength from the range of wavelengths made available during production of the radiation, a crystal monochromator may be used. For X-rays, a narrowly limited range of wavelengths can be selected by reflecting the beam from a selected crystallographic plane in a single crystal (Bragg’s law).

The incoming beam flux is considerably reduced by this process. However, in practice, the incoming beam is slightly divergent and the crystal also has some mosaic spread. The combined effect of these is to allow the outgoing beam to have sufficient flux.

The velocity of a neutron depends upon its wavelength (Eqn. 2-2) and hence monochromation of neutrons can also be achieved by mechanical means such as co-axially rotating discs. Often crystal monochromators are used in reactor sources which choose the desired wavelength depending on the  $d$ -spacings in the crystal (Eqn. 2-5).

The X-ray and neutron beams are usually collimated using sets of vertical and horizontal slits which define the beam size. Mirrors help steer the X-ray beam, provide focusing of the beam and help in the rejection of harmonics. Filters may also be used for both X-ray and neutrons to remove higher order harmonics.

### 2.7.4 Detectors

Some principal methods of detecting X-ray and neutron radiation are given below.

### 2.7.4.1 X-ray detectors

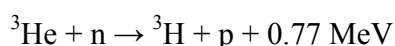
Historically fluorescent screens and photographic films have been the primary means of detecting X-rays. Scintillators are widely used in recent times where a typical scintillator crystal (Sodium Iodide + Thallium) emits visible light when it absorbs ionizing radiation. Absorption of an X-ray photon produces ionisation in the crystal, which induces fluorescence in the thallium sites. A photomultiplier tube converts the light energy into an electric pulse. The very short decay time (~30 ns) of the scintillator crystals allows a very fast counting rate of the radiation.

A multi-analysing crystal (MAC) detector consists of parallel analyser-detector systems which provide exceptional angular resolution in synchrotron facilities [16]. A series of Si (1,1,1) crystals analyze the scattered radiation again and scintillators then measure the beam intensity. The resultant loss in X-ray intensity is considerable which makes these detectors nearly unusable for this work.

A micro-strip position sensitive detector (PSD), which allows for simultaneous measurement of X-ray intensities over the entire angular range, has proved invaluable here. This Mythen detector, developed in-house at the Swiss Light Source (SLS), Switzerland, consists of thousands of parallel channels (microstrips), each consisting of Si *p-n* junctions with Al contacts [17]. Electron-hole pairs created by the absorbed photon are then measured by the associated circuitry.

### 2.7.4.2 Neutron detectors

Neutron detection is accomplished by inducing nuclear reactions that produce charged particles. Thus, in a  $^3\text{He}$  filled detector, the following reaction takes place:



These secondary charged particles induce ionisation in the  $^3\text{He}$  gas, and the resulting electric pulse is measured. For neutrons, scintillator counters work on a principle similar to that for X-rays.

These detectors need to be moved to each position to detect the scattered radiation. Area detectors (PSDs), however, can be held stationary and have the ability to resolve the position coordinates of the scattered radiation. For example, the electric pulses generated in a gas filled detector held perpendicular to the incoming radiation reach the end of the tube at different times

which can be related to the position at which the incoming radiation was detected. Micro-strip detectors for neutrons, such as those used on the instrument D20 at ILL [18], have proven to be particularly valuable as they reduce count times by measuring radiation at different angles simultaneously.

## 2.8 Instrumentation

Synchrotron X-ray diffraction experiments in this work were performed on the Materials Science beam-line X04SA at SLS with an incident beam wavelength of 1 Å (12.4 keV) and at the high resolution powder diffraction beam-line I11 at *Diamond Light Source*, U.K. at an incident beam wavelength of 1.06 Å [16, 19]. The instrument D20 at the *Institut Laue-Langevin* (ILL), France was used for the neutron diffraction experiments [20]. A description of these instruments is given below.

### 2.8.1 Materials science X04SA beam line

The Materials Science (MS) beam line at SLS produces a high flux of hard X-Rays using a wiggler source [19]. The energy range of the beam line is 5-40 keV and the focussed spot size is 500 μm x 500 μm. The optics consists of a vertically collimating mirror, a double-crystal monochromator with horizontal focussing and a second vertically focussing mirror.

The diffractometer consists of three coaxial heavy-duty rotation stages on a horizontal axis perpendicular to the X-ray beam (Figure 2-6). The stages provide the necessary angular movements to the sample. A position sensitive micro-strip detector described earlier was used to detect the scattered X-rays.

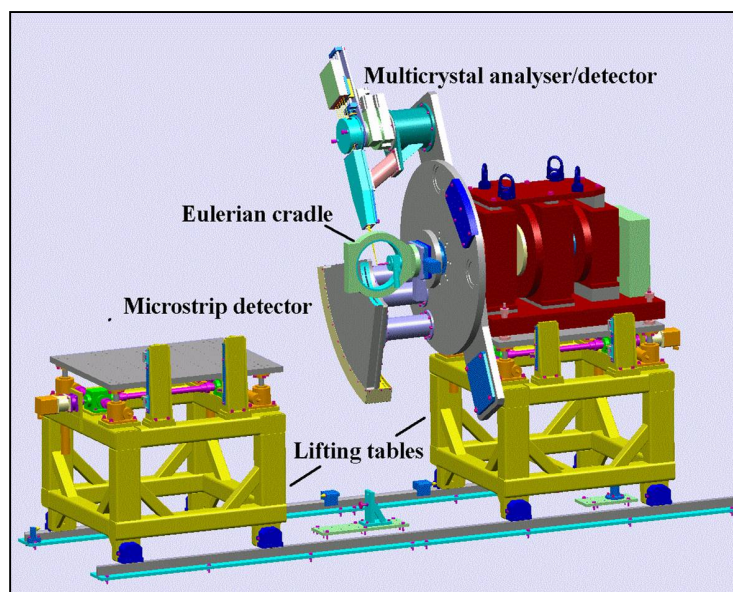


Figure 2-6 The powder diffractometer on the MS beamline [21]

### 2.8.2 Beamline I11

Figure 2-7 shows the layout of the beamline I11 at Diamond Light Source [16]. The beam-size at the sample is approximately 0.8 mm (vertical) x 5 mm (horizontal), and a high photon flux of  $\sim 10^{14}$  photons/s is obtained at the sample due to the use of an in-vacuum undulator within the synchrotron. The beam size can be trimmed using the primary slits and monochromated using Si (1,1,1) crystals in the optics hutch (Figure 2-7). An intensity monitor (comprising of a thin Kapton foil and scintillation counter) allows correction for changes in beam intensity.

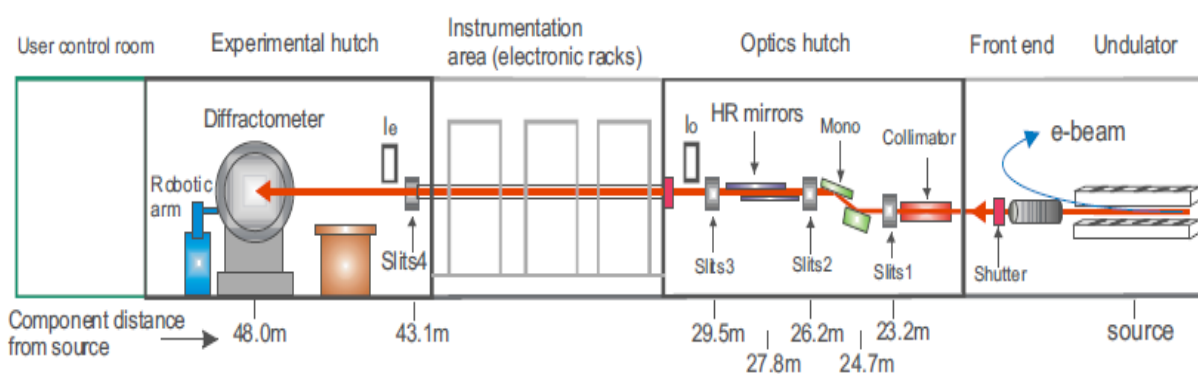
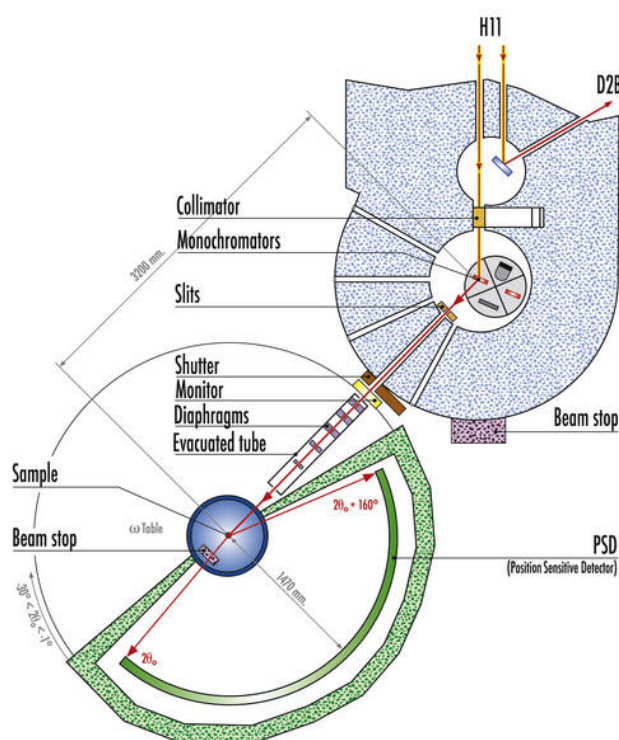


Figure 2-7 Schematic of the beamline I11 at Diamond Light Source (taken from [16])

I11 is equipped with a choice of two detectors – a multi-analysing crystal (MAC) detector for high resolution, and a position sensitive detector (PSD) similar to the one at SLS. The PSD was found more useful for this work as it reduced sample count times considerably as compared to the MAC detector and the resulting (minor) loss in resolution was not an important factor for the broad monolayer peaks.

### 2.8.3 Diffractometer D20



**Figure 2-8** Top-view schematic of the instrument D20 at ILL [22]

D20 is a high-intensity two-axis neutron powder diffractometer with variable resolution at ILL and is equipped with a large-area one-dimensional position-sensitive detector (PSD). D20 can be operated in high-flux or high-resolution modes, and choosing one mode (say high flux) usually results in a loss in the other (i.e. resolution). D20 has four possible monochromator options that are mounted upon a monochromator changer (Figure 2-8) [20]. For purposes of this study the Highly-Ordered Pyrolytic Graphite (HOPG) option was used, working in reflection from the

(0,0,2) plane. The resultant wavelength obtained is 2.42 Å. Graphite filters are in place between the collimator and monochromator to remove unwanted wavelengths. Two sets of slits are present after the monochromator to define the beam size and degree of collimation. A monitor is located between these two sets of slits to allow normalisation by the incident neutron intensity which can vary by up to 10% depending on reactor performance.

The D20 detector is a 1600 cell PSD filled with a mixture of  $^3\text{He}$  (3 bars) and  $\text{CF}_4$  (1 bar) and has a detection efficiency of 90% at the working wavelength [18]. Such a micro-strip detector allows for a stable and high counting rate.

## 2.9 Sample preparation

The alkyl amides used in this work were either purchased (from Sigma-Aldrich) or prepared from the corresponding carboxylic acid by the method described in [23]. Deuterated amides were prepared from the corresponding perdeuterated acid for the neutron scattering experiments to minimise the very strong incoherent scattering that would have arisen with protonated samples. In X-ray scattering both protonated and perdeuterated samples have very similar scattering and hence protonated materials can be used. Due to the very high cost, only a limited number of deuterated amides were available which restricted the number of neutron measurements that could be made.

Detailed diffraction and DSC measurements were made possible in this work by the synthesis of several odd members of the homologous series and shorter chain unsaturated amides which were not available in a previous initial study [24]. The purities of all the amides were analyzed by elemental analysis,  $^1\text{H}$  (and  $^{13}\text{C}$ ) NMR and Liquid Chromatography/Mass Spectrometry and most amides were found to be  $\geq 97\%$  pure (purity information can be found in Appendix B).

Recompressed exfoliated graphite (Papyex from Le Carbone Lorraine), was out-gassed under vacuum at 350°C before use. The cleaned graphite was dosed with the appropriate amounts of amide under vacuum and annealed at 180°C. While dosing the graphite it is convenient to know the approximate number of equivalent monolayers adsorbed. This was estimated from the area per molecule of the corresponding carboxylic acid [25] and the specific surface area of graphite (30.1 m<sup>2</sup>/g as measured by nitrogen adsorption isotherm).

For X-ray diffraction experiments, the dosed graphite was cut into disks (2 mm diameter) and placed in a 3.5 mm glass capillary. The capillary was then sealed and placed in the beam while spinning gently to enhance powder averaging (~60 rpm). A cryo-jet was used to achieve temperature control. In practice the fragile glass capillaries were found to fracture on cooling and this effectively limited the accessible temperature range to approximately 200 K.

For neutron diffraction experiments, the neutron wavelength of 2.42 Å was used on the instrument D20. A standard orange cryo-furnace was used for temperature control. The samples contained in aluminium cans were able to be cooled to 10 K. The procedures used to obtain X-ray and neutron diffraction patterns from adsorbed layers have also been described in detail in other works. [25, 26]

## 2.10 Data treatment

The raw data from the instrument is usually normalised and corrected for detector efficiencies. The data is then background subtracted and corrected as described below for X-rays, and similar treatments are applied to neutron data.

### 2.10.1 Scattering from the graphite substrate

Figure 2-9 shows the diffraction pattern of the graphite substrate at 300 K. The bare graphite has characteristic strong peaks at 1.87 Å<sup>-1</sup>, 2.95 Å<sup>-1</sup> and 3.09 Å<sup>-1</sup>. In addition, at low angles, there is significant small angle scattering from the individual graphite crystallites. This can be expected to follow a Porod Law [1]:

$$I(q) = \frac{S_T / V}{8\pi^3 q^4}$$

... Eqn. 2-19

Here  $I$  is the intensity of scattering in the small angle region,  $S_T$  is the total surface area in the volume  $V$  irradiated by the X-rays and  $q$  is the momentum transfer vector. Porod scattering of this form is expected for any object made of small particles. Thus the small angle scattering can be seen to be proportional to  $q^{-4}$ , with the proportionality constant being related to the surface:volume ratio. The Porod form is only valid over a limited range of  $q$  and for other  $q$

values the shape and size of the graphite crystallites become significant which changes the  $q$  dependence of the scattering.

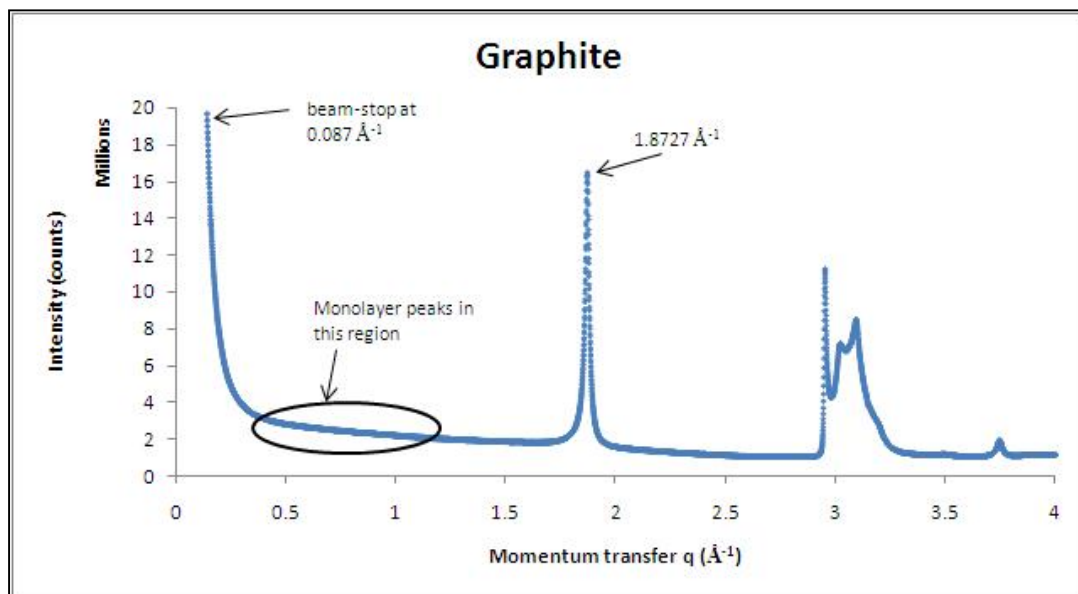


Figure 2-9 Diffraction pattern of the graphite substrate at 300 K

The diffraction pattern from an adsorbed monolayer is obtained by subtraction of the scattering from the graphite substrate alone from that of the substrate and the adsorbed material together (graphite + amide). It is necessary to scale the diffraction pattern from the bare graphite appropriately to ensure a satisfactory subtraction. This scaling arises from the small variation in transmission of the X-rays through the sample due to the presence of the adsorbed layer and the amount of graphite in the beam.

At higher coverage of the adsorbate on graphite, the diffraction peaks from the bulk often coincide with the weak monolayer peaks. In order to obtain the monolayer pattern at high coverage, a background pattern collected at a temperature where both the bulk and monolayer are liquid is subtracted from a diffraction pattern measured at a temperature when the bulk is liquid but the monolayer is still solid.

The Porod form given in Eqn. 2-19 provides a reasonable estimate to correct for the intense small angle scattering from the graphite crystallites. Hence, a small angle correction of  $q^{-4}$  (with appropriate scaling) is subtracted from the diffraction pattern obtained after background

subtraction. The scale factors for the graphite subtraction and the small angle correction are chosen by ‘trial-and-error’ till a reasonably flat base line is obtained for the pattern. The outcome of this process means that the intensities of peaks at very low  $q$  can be unreliable; this is accounted for in the fitting procedure.

### 2.10.2 Scattering from the amide monolayer adsorbed on graphite

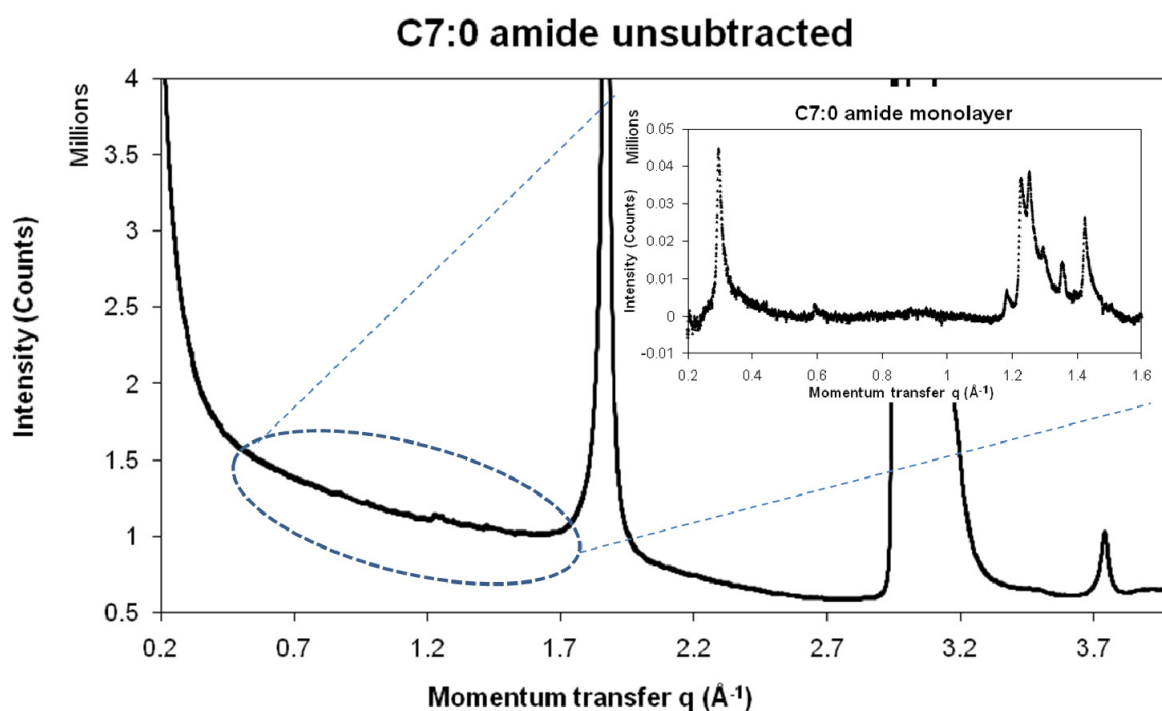


**Figure 2-10** Unsubtracted diffraction pattern for the amide C7:0. Weak features that are confirmed to be monolayer peaks can be seen in the unsubtracted pattern. (Inset) subtracted pattern for the same sample.

The amide monolayer peaks of interest are in the region indicated in Figure 2-10 ( $0.2\text{--}1.6 \text{ \AA}^{-1}$ ). From the diffracted X-ray intensities shown in Figure 2-10 it can be seen that the monolayer peak signal is less than 1% of the substrate, and hence long count times are required to obtain statistically significant data. This issue is addressed by taking several one-minute runs (the maximum count time per measurement on the SLS instrument) and combining the runs together. In this way, the peaks scale according to the number of runs added, but the noise scales only according to their square root. A single long run cannot be used as the detector is only limited to a certain number of photon counts in total if it is to operate in its linear region (the operating region of the detector where the output voltage from the detector is linear with the photon

counts/second). Given that the monolayer scattering is obtained by subtraction, an equivalently long run of the graphite substrate is also necessary to obtain a good subtraction.

The subtraction and correction procedure discussed here often leave monolayer patterns with a curved baseline that can be corrected for by fitting a polynomial through it. The polynomial is then subtracted from the diffraction pattern; this procedure is illustrated in Figure 2-11. To obtain the final pattern which is suitable for fitting, a local average of the data can be performed to improve statistics. This means that the intensity at each  $q$  can be taken as the average intensity at adjacent  $q$ -values. For most patterns, an average of 3-4 local points is usually sufficient in reducing the noise, without significantly compromising resolution with respect to the broad monolayer line-shape.

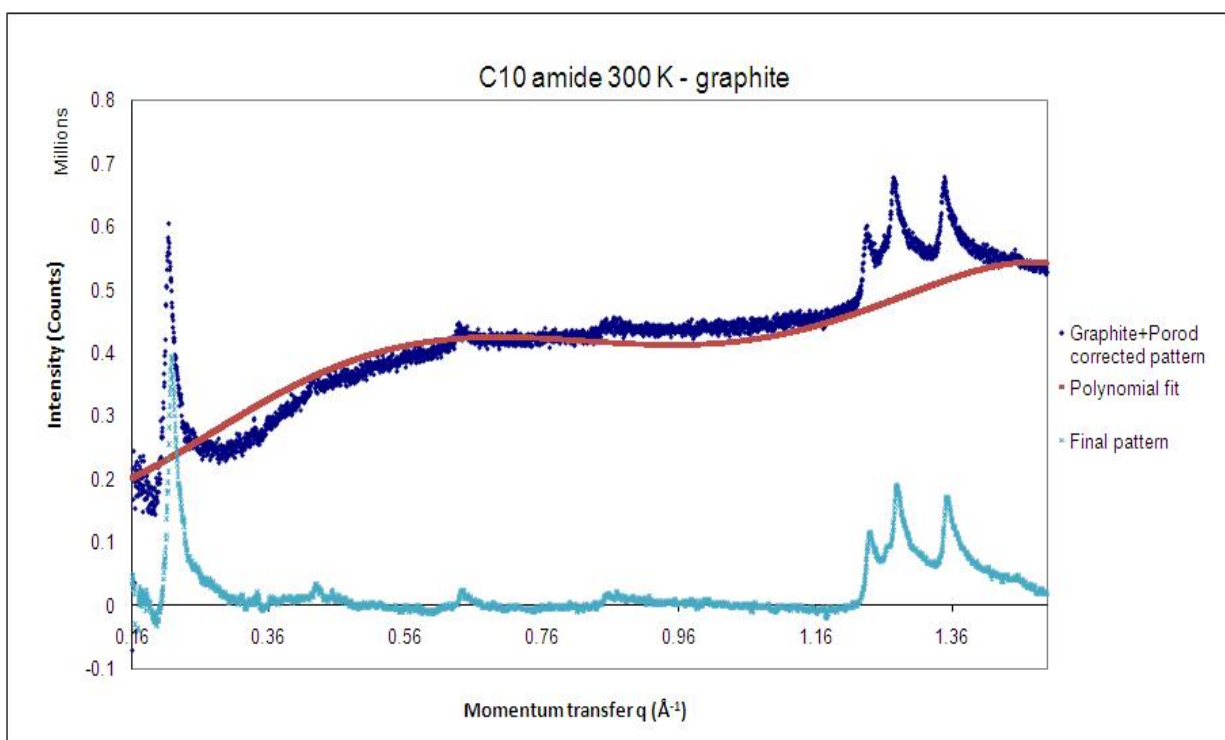


Figure 2-11 Monolayer pattern for the amide C10:0

### 2.10.3 Optimisation of experimental conditions

A ‘beam-stop’ is usually placed before the detector on the beam-line to prevent the straight-through beam from damaging the detector, given its very high flux. In addition, as outlined

above, the small angle scattering from sample can be quite high. The beam-stop thus ensures that the detector is operating in its linear region. The beam-stop however limits the lowest angle at which the diffraction pattern can be collected. In this work, where the long homologues of the alkyl amides need investigation, the longer the  $d$ -spacings (lower  $q$ ) accessible the better.

Lower  $q$  can be accessed by either increasing the wavelength, or changing the beam-stop position, or both. The beam-line at SLS is optimised for maximum X-ray flux at 1 Å wavelength. Increasing the wavelength causes a dramatic decrease in flux, and an appropriate compromise can be sought between the flux and the shortest accessible  $q$ . By adjusting the beam-stop position and optimising the incident beam size and wavelength, it was determined that the lowest angle at which the pattern can be collected was  $0.797^\circ$  in  $2\theta$  or  $0.087 \text{ \AA}^{-1}$  in  $q$ .

#### 2.10.4 Wavelength Calibration and offset correction

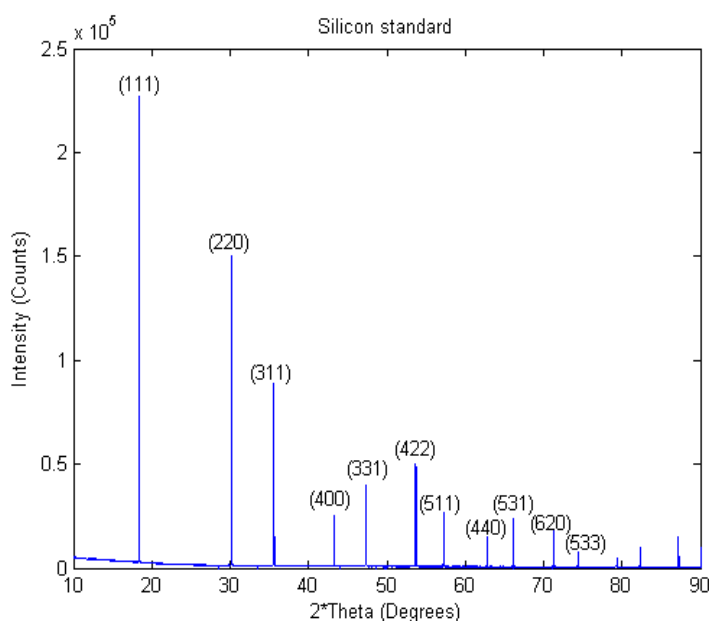


**Figure 2-12** A diffraction pattern for the Silicon standard (NIST 640c) collected at SLS for an X-Ray energy of 12KeV. The peaks are indexed in accordance with the certificate of analysis

The X-ray wavelength can be calibrated accurately using the diffraction pattern from a standard (Silicon - NIST 640c). The standard can also be used to correct any possible offset in the data due to the instrument set-up and alignment. Using Bragg's law at two different wavelengths for the same material, we obtain:

$$\frac{\lambda_1}{\lambda_2} = \frac{\sin \theta_1}{\sin \theta_2}$$

... Eqn. 2-20

where the subscript 1 corresponds to the reflections at the unknown wavelength and 2 corresponds to the reflections at the standard wavelength (1.5405929 Å). Thus, different values of  $\theta_1$  have been calculated using trial values of  $\lambda_1$  and the offset and compared to the standard peak positions till a satisfactory match was obtained (i.e. minimising the entries of the error column of Table 2-2). Using this procedure, the wavelength of the X-rays was determined as 1.001155 Å and the offset as +0.001° in  $2\theta$  at SLS. All patterns collected at this wavelength were then offset by this number.

**Table 2-2** Values used for the calibrating the X-Ray wavelength and determining the offset

| Standard <sup>a</sup> ( $\lambda=1.5405929$ Å) |               |                      | Calculated<br>$2\theta$ (°) | Observed<br>$2\theta$ (°) | Error in<br>$2\theta$ (°) |
|--|---------------|----------------------|-----------------------------|---------------------------|---------------------------|
| (h,k,l)  | $2\theta$ (°) | q (Å <sup>-1</sup> ) |                             |                           |                           |
| 111  | 28.4409       | 2.003755             | 18.373                      | 18.375                    | 0.002                     |
| 220  | 47.3003       | 3.272124             | 30.223                      | 30.225                    | 0.002                     |
| 311  | 56.1193       | 3.836901             | 35.600                      | 35.602                    | 0.002                     |
| 400  | 69.1261       | 4.62748              | 43.268                      | 43.268                    | 0.000                     |
| 331  | 76.3718       | 5.042681             | 47.376                      | 47.376                    | 0.000                     |
| 422  | 88.0247       | 5.667482             | 53.684                      | 53.684                    | 0.000                     |
| 511  | 94.9463       | 6.011271             | 57.230                      | 57.232                    | 0.002                     |
| 440  | 106.7009      | 6.544246             | 62.850                      | 62.849                    | -0.001                    |
| 531  | 114.0834      | 6.844134             | 66.087                      | 66.083                    | -0.004                    |
| 620  | 127.533       | 7.316687             | 71.313                      | 71.31                     | -0.003                    |
| 533  | 136.8789      | 7.586104             | 74.370                      | 74.368                    | -0.002                    |

<sup>a</sup> From certificate of analysis

For the estimated wavelength and offset, the graphite peak positions were observed at the expected positions (§2.10.1). A similar calibration was done to determine the wavelength and offset of the X-ray beam at Diamond accurately ( $\lambda=1.0624315$  Å, offset = 0.0° in  $2\theta$ ). Other mathematical refinement methods also exist for calibrating the wavelength and offset, such as the Rietveld method [27]. The wavelength and offset at Diamond as determined by the Rietveld

method were 1.0625(1) Å and  $-0.061(4)^\circ$  respectively, and these compare well with the combination of wavelength and offset determined using the method explained here.

## 2.11 Data fitting and structural solution

The program *pattern\_nx* written in the programming language *PV-Wave* was used to calculate a diffraction pattern based on a given molecular structure. The program was based on one of a similar name written for the D.Phil work of Mowforth [28], and re-written completely for Windows by Dr. S. M. Clarke.

### 2.11.1 Generating the coordinates of all atoms in an amide molecule

*Pattern\_nx* asks an input from the user to generate a possible monolayer structure by defining the unit cell dimensions, the position (x,y) of each molecule within the unit cell, and the rotation of each molecule within and about the graphite plane. The program can also generate the positions of other molecules in the unit cell based on the position of one molecule and the specified two-dimensional symmetry. The molecular arrangement is then plotted by the program and the user is prompted to ensure that the structure is physically reasonable.

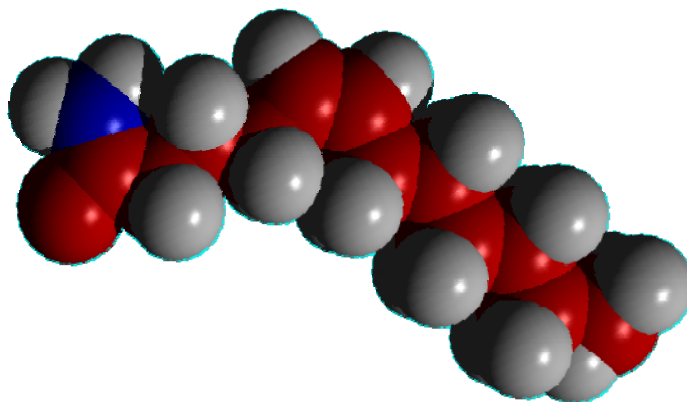


**Figure 2-13** C12:1 c-5 amide molecule generated by the program molgenamide. Carbon and oxygen atoms are shown in red, nitrogen in blue and hydrogens in grey.

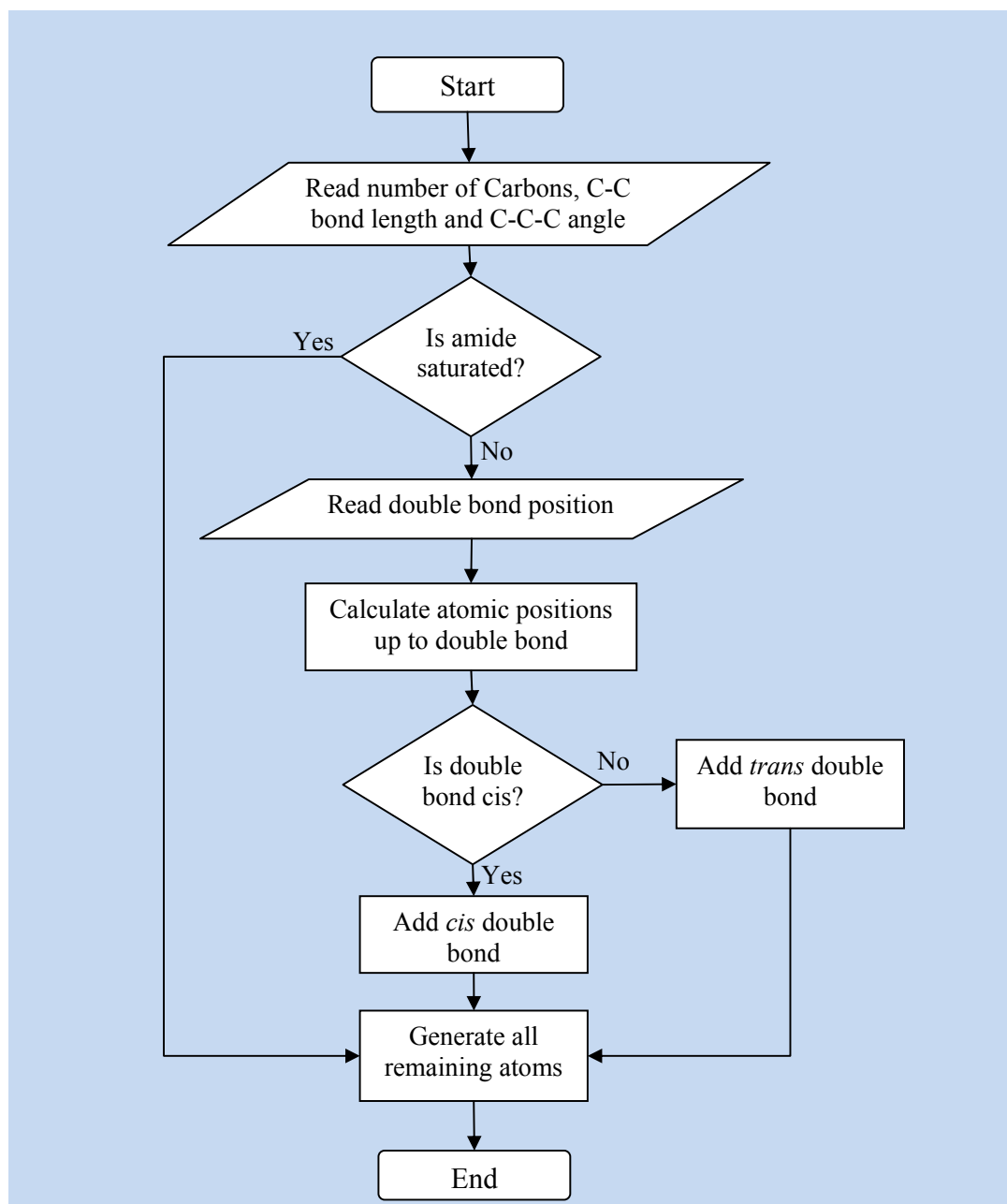


**Figure 2-14** Flowchart for the sub-program *molgenamide* written in this work which calculates the coordinates of all atoms of an amide molecule

A sub-program ‘*Molgenamide*’ was written here by me to generate the atomic coordinates of a single amide molecule. The sub-program asks the user for the number of carbons, the C-C bond length and C-C-C angle, and then generates the coordinates of all the atoms of the molecule to be used by the program *pattern\_nx*. The program was also expanded as part of this work to generate

coordinates of an unsaturated amide molecule. An example unsaturated molecule generated by this program is shown in Figure 2-13 and the algorithm is shown in Figure 2-14.

In this program the amide head group was placed at the origin. The coordinates of an atom along the carbon chain was calculated based on the coordinates of the previous atom and the bulk bond lengths and angles (taken from [29]). In this way the positions of all atoms were generated.

### 2.11.2 The model

Once the experimental monolayer diffraction pattern is obtained (as discussed in §2.10), it can be compared to a diffraction pattern calculated using a trial structure and the Warren/Kjem's model [6, 9]. It is not trivial to determine the molecular arrangements (i.e. the electron density function) within the unit cell from the observed intensities directly owing to the phase problem [30], and hence diffraction patterns from trial structures need to be compared with experimental observations till satisfactory match is obtained.

A subroutine of *pattern\_nx* (*int\_calc\_nx*) creates integer arrays (h,k) in which all possible Miller indices within adjustable limits are stored. The peak positions are determined using Eqn. 2-6. The peak-intensities are calculated from the structure-factor (Eqn. 2-9 and Eqn. 2-10), combined with appropriate correction factors (§2.5). The diffraction pattern is calculated for the angular range of  $0^\circ \leq 2\theta \leq 80^\circ$ .

### 2.11.3 Preferred orientation and peak shape parameters

A subroutine to account for the preferred orientation of the graphite crystallites (explained in §2.4.3) was written and incorporated into the main program by me. The adjustable parameters to fit the line-shape are the ratio of random to oriented part ( $H_0/H_1$ ) and the width of the oriented distribution  $\delta$ . The influence of changing the ratio  $H_0/H_1$  on the peak shape of hexanamide (C6:0) is shown in Figure 2-15. A value of 0.4 was found best for the graphite in this work and was used in the fitting program.

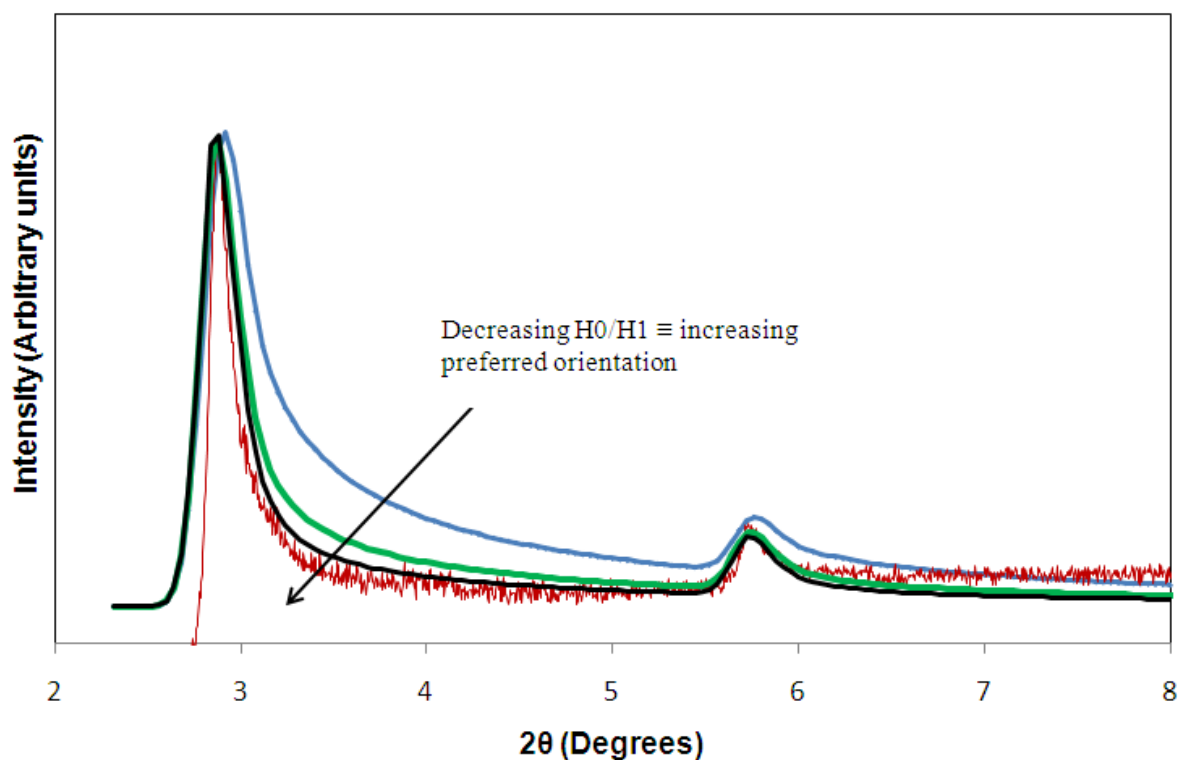


**Figure 2-15** Influence of changing the preferred orientation parameter  $H_0/H_1$  on the calculated peak shape of C6:0 amide. The red curve is the experimental pattern, blue is the calculated pattern without any preferred orientation correction, green  $\equiv H_0/H_1=0.78$  (Kjem's value [9]) and black  $H_0/H_1=0.4$ . In all cases  $\delta=12.7^\circ$  [9].

Other parameters that were calculated by fitting the peak width include the instrument resolution function (Gaussian) Full Width at Half Maximum (FWHM), and the size of the crystallites 'L' [6], explained in §2.4.4. A smaller FWHM for the detector resolution makes the peaks sharper while smaller L value makes the peaks broader.

Table 2-3 lists the fitting parameters that were used for this work. The remaining adjustable parameters are the unit cell values  $a$ ,  $b$ ,  $v$ , the number of molecules and the position of each molecule in the unit cell. The structural solution of individual amide monolayers will be discussed in Chapters 4 and 5.

Table 2-3 Peak shape parameters used for fitting in this work

| Parameter                                   | X-Rays (SLS and Diamond) | Neutrons (ILL) |
|---|--------------------------|----------------|
| Crystallite size 'L' (Å)                    | 250                      | 250            |
| Instrument resolution:<br>Gaussian FWHM (°) | 10                       | 250            |
| H <sub>0</sub> /H <sub>1</sub>              | 0.4                      | 0.4            |
| δ (°)                                       | 12.7                     | 12.7           |

## 2.12 References

1. Cullity, B.D., Stock, S. R., *Elements of X-Ray diffraction*. 3rd ed. 2001, New Jersey: Prentice Hall Inc.
2. Giacovazzo, C., H.L. Monaco, G. Artioli, D. Viterbo, G. Ferraris, G. Gilli, G. Zabotti, and M. Catti, *Fundamentals of Crystallography*. 2nd ed. IUCr texts in Crystallography, ed. C. Giacovazzo. 2002, New York: Oxford University Press.
3. Warren, B.E., *X-Ray Diffraction*. 1990: Courier Dover Publications.
4. Woolfson, M.M., *An introduction to X-Ray Crystallography*. 2nd ed. 1997, Cambridge: Cambridge University Press.
5. vonLaue, M., *Z. Kristallogr*, 1932. **82**.
6. Warren, B.E., *X-Ray Diffraction in random layer lattices*. *The Physical Review*, 1941. **9**(69): p. 693-698.
7. Wilson, A.J.C., *X-ray diffraction by random layers: ideal line profiles and determination of structure amplitudes from observed line profiles*. *Acta Cryst.*, 1949. **2**: p. 245-251.
8. Warren, B.E. and P. Bodenstein, *The shape of two-dimensional carbon black reflections*. *Acta Cryst.*, 1966. **20**: p. 602-605.
9. Kjems, J.K., L. Passell, H. Taub, J.G. Dash, and A.D. Novaco, *Neutron scattering study of nitrogen adsorbed on basal-plane-oriented graphite*. *Physical Review B*, 1976. **13**(4): p. 1446-1462.
10. Stout, G.H., Jensen, L. H., *X-Ray structure determination - A Practical guide*. 2nd ed. 1989, New York: John Wiley and Sons.
11. Hahn, T., *Space group symmetry*. 4th ed. International tables for crystallography. Vol. A. 1995, London: Kluwer Academic.
12. Source: [www.diamond.ac.uk](http://www.diamond.ac.uk).
13. Brown, G., K. Halback, J. Harris, and H. Winick, *Wiggler and Undulator Magnets - A Review*. *Nuclear Instruments and Methods*, 1983. **208**: p. 65-77.
14. Teixeira, S.C.M., et al., *New sources and instrumentation for neutrons in biology*. *Chemical Physics*, 2008. **345**(2-3): p. 133-151.

15. Bauer, G.S., *Physics and technology of spallation neutron sources*. Nuclear Instruments and Methods in Physics Research Section A: Accelerators, Spectrometers, Detectors and Associated Equipment, 2001. **463**(3): p. 505-543.
16. Thompson, S.P., J.E. Parker, J. Potter, T.P. Hill, A. Birt, T.M. Cobb, F. Yuan, and C.C. Tang, *Beamline III at Diamond: A new instrument for high resolution powder diffraction*. Review of Scientific Instruments, 2009. **80**(7): p. 075107-9.
17. Schmitt, B., C. Bronnimann, E.F. Eikenberry, F. Gozzo, C. Hormann, R. Horisberger, and B. Patterson, *Mythen detector system*. Nuclear Instruments and Methods in Physics Research A, 2003. **501**: p. 267-272.
18. Convert, P., M. Berneron, R. Gandelli, T. Hansen, A. Oed, A. Rambaud, J. Ratel, and J. Torregrossa, *A large high counting rate one-dimensional position sensitive detector: the D20 banana*. Physica B: Condensed Matter, 1997. **234-236**: p. 1082-1083.
19. Gozzo, F., B. Schmitt, T. Bortolamedi, C. Giannini, A. Guagliardi, M. Lange, D. Meister, D. Maden, P. Willmott, and B.D. Patterson, *First experiments at the Swiss Light Source Materials Science beamline powder diffractometer*. J. Alloys and Compounds, 2004. **362**(1-2): p. 206-217.
20. Hansen, T.C., P.F. Henry, H.E. Fischer, J. Torregrossa, and P. Convert, *The D20 instrument at the ILL: a versatile high-intensity two-axis neutron diffractometer*. Measurement Sci. and Tech., 2008. **19**(3): p. 034001.
21. Source: <http://sls.web.psi.ch>.
22. Source: [www.ill.eu](http://www.ill.eu).
23. Kent, R.E. and S.M. McElvain, *Organic Syntheses Collective*. Vol. 3. 1955. pp. 490.
24. Arnold, T., Clarke, S. M., *Thermodynamic Investigation of the Adsorption of Amides on Graphite from Their Liquids and Binary Mixtures*. Langmuir, 2008. **24**(7): p. 3325-3335.
25. Bickerstaffe, A.K., N.P. Cheah, S.M. Clarke, J.E. Parker, A. Perdigon, L. Messe, and A. Inaba, *The Crystalline Structures of Carboxylic Acid Monolayers Adsorbed on Graphite*. J. Phys. Chem. B, 2006. **110**: p. 5570-5575.
26. Clarke, S.M., *The Structure and Properties of Adsorbed Layers by X-Ray and Neutron Scattering*, in *Physical Chemistry Laboratory*. 1989, University of Oxford: Oxford.
27. *The Rietveld Method*. IUCr Monographs on Crystallography, ed. R.A. Young. Vol. 5. 1995: Oxford University Press.
28. Mowforth, C.W., *D. Phil Thesis*. 1983, University of Oxford: Oxford.
29. Lide, D.R., *CRC Handbook of Chemistry and Physics*. 85th ed. 2004.
30. Hauptman, H.A., *The phase problem of X-ray crystallography*. Reports on Progress in Physics, 1991. **54**(11): p. 1427.

# Chapter 3

## Mixing and Calorimetry

---

A brief overview of the theory behind solid-liquid phase diagrams for a binary mixture is provided in this chapter. The thermal behaviour of a binary mixture depends upon the extent of mixing in the layer. Equations are developed for the cases where there is ideal mixing and phase separation in the solid phase, with ideal mixing assumed in the liquid phase. Preferential adsorption of one component over the other in the 2D layer is discussed. The regular solution model for non-ideal mixing in the solid phase is explained. The principles behind the use of a differential scanning calorimeter in constructing phase diagrams for binary mixtures are also presented and experimental details provided.

### 3.1 Mixing Theory

#### 3.1.1 Ideal Mixing

In ideal mixing, it is assumed that the two components mix ideally both in the solid and liquid phases. In this case, the enthalpy of mixing is zero [1]. Figure 3-1 shows a phase diagram for an ideal mixture. The lower line is the solidus and gives the composition (i.e. mole fraction  $x$ ) of the solid solution in equilibrium with the liquid. The upper line is the liquidus and gives the composition of the liquid solution in equilibrium. The composition of the system at any

temperature may be found by drawing a horizontal ‘tie’ line through the two phase region and reading the solid and liquid compositions as shown in the figure.

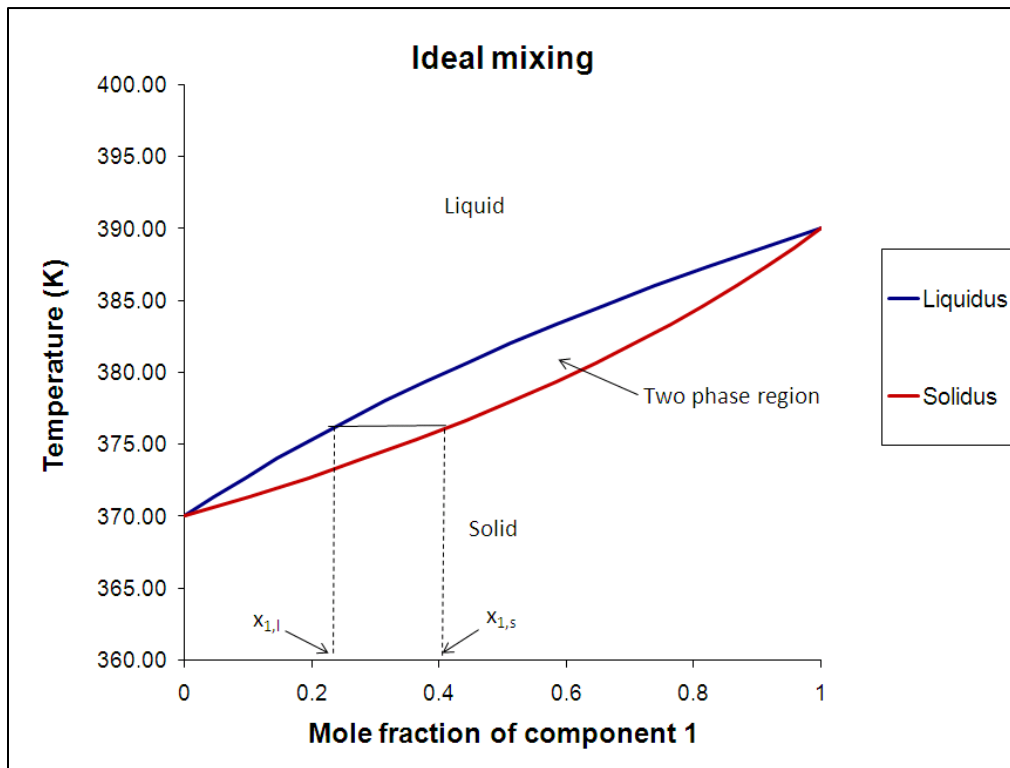


Figure 3-1 Phase diagram for ideal mixing

At the melting temperature of the mixture, we must have the two phases in equilibrium. Therefore, the chemical potentials ( $\mu$ ) for each component in the two phases must be equal:

$$\mu_{i,s} = \mu_{i,l}$$

... Eqn. 3-1

Where the subscript  $i$  refers to the components ( $i=1, 2$  for binary mixing), and  $s$  and  $l$  refer to solid and liquid phases respectively. For an ideal mixture of composition  $x$  this becomes [1]:

$$\mu_{i,s}^o + RT \ln x_{i,s} = \mu_{i,l}^o + RT \ln x_{i,l}$$

... Eqn. 3-2

$$\mu_{i,l}^o - \mu_{i,s}^o = RT \ln \left( \frac{x_{i,s}}{x_{i,l}} \right)$$

where  $R$  is the gas constant. The left hand side is the standard Gibb's free energy change for component  $i$  on melting ( $\Delta G_i^o$ ). Differentiating w.r.t temperature ( $T$ ):

$$\frac{1}{R} \frac{d}{dT} \left( \frac{\Delta G_i^o}{T} \right) = \frac{d}{dT} \ln \left( \frac{x_{i,s}}{x_{i,l}} \right)$$

Using the Gibbs-Helmholtz relation [1] and integrating, this becomes:

$$\frac{1}{R} \int_{T_i}^T \left( \frac{-\Delta H_i^o}{T^2} \right) dT = \int_0^{\ln \left( \frac{x_{i,s}}{x_{i,l}} \right)} \frac{d}{dT} \ln \left( \frac{x_{i,s}}{x_{i,l}} \right) dT$$

Here, the limits correspond to the melting of the pure material and the mixture along the composition axis of the phase diagram (Figure 3-1);  $\Delta H_i^o$  is the enthalpy of melting. Solving this gives:

$$\frac{x_{i,s}}{x_{i,l}} = \exp(\alpha_i)$$

... Eqn. 3-3

Where

$$\alpha_i = \frac{\Delta H_i^o}{RT} \left( 1 - \frac{T}{T_i} \right)$$

... Eqn. 3-4

This relationship holds for each component in the mixture. Using the fact that the sum of the mole fractions in each phase is equal to 1, the following relations can be derived for binary mixing:

$$x_{1,s} = \frac{\exp(\alpha_2) - 1}{\exp(\alpha_2) - \exp(\alpha_1)} \exp(\alpha_1)$$

... Eqn. 3-5

$$x_{1,l} = \frac{\exp(\alpha_2) - 1}{\exp(\alpha_2) - \exp(\alpha_1)}$$

... Eqn. 3-6

Eqns. 3-5 and 3-6 represent the solidus and liquidus curves in the phase diagram respectively, plotted in Figure 3-1 with  $\Delta H^0_1 = \Delta H^0_2 = 20$  kJ/mol,  $T_1 = 370$  K and  $T_2 = 390$  K. In essence, unlike a pure material, the mixture no longer melts at one temperature [2]. The temperature of the mixture keeps changing when melting ‘begins’ at the solidus and ‘ends’ at the liquidus temperature at each composition. As the amount of component *1* is increased, the melting temperature of the mixture changes monotonically from that of pure material 2 to pure material *1*.

### 3.1.2 Eutectic behaviour

Eutectic behaviour is a case when the components do not mix in the solid phase but mix ideally in the liquid phase. Such a system exhibits a depression in freezing point of the mixture, as shown in the phase diagram of Figure 3-2 for a binary mixture of components 1 and 2. The solidus and liquidus curves represent the phase boundaries as described in the previous section. In a eutectic mixture all compositions begin to melt at the same temperature, known as the eutectic temperature and the horizontal line through the phase diagram at the eutectic temperature is the solidus. The point E where the liquidus curves and solidus intersect is known as the eutectic point. At the eutectic point in this two component system, all three phases, i.e. liquid, solid A and solid B co-exist in equilibrium.

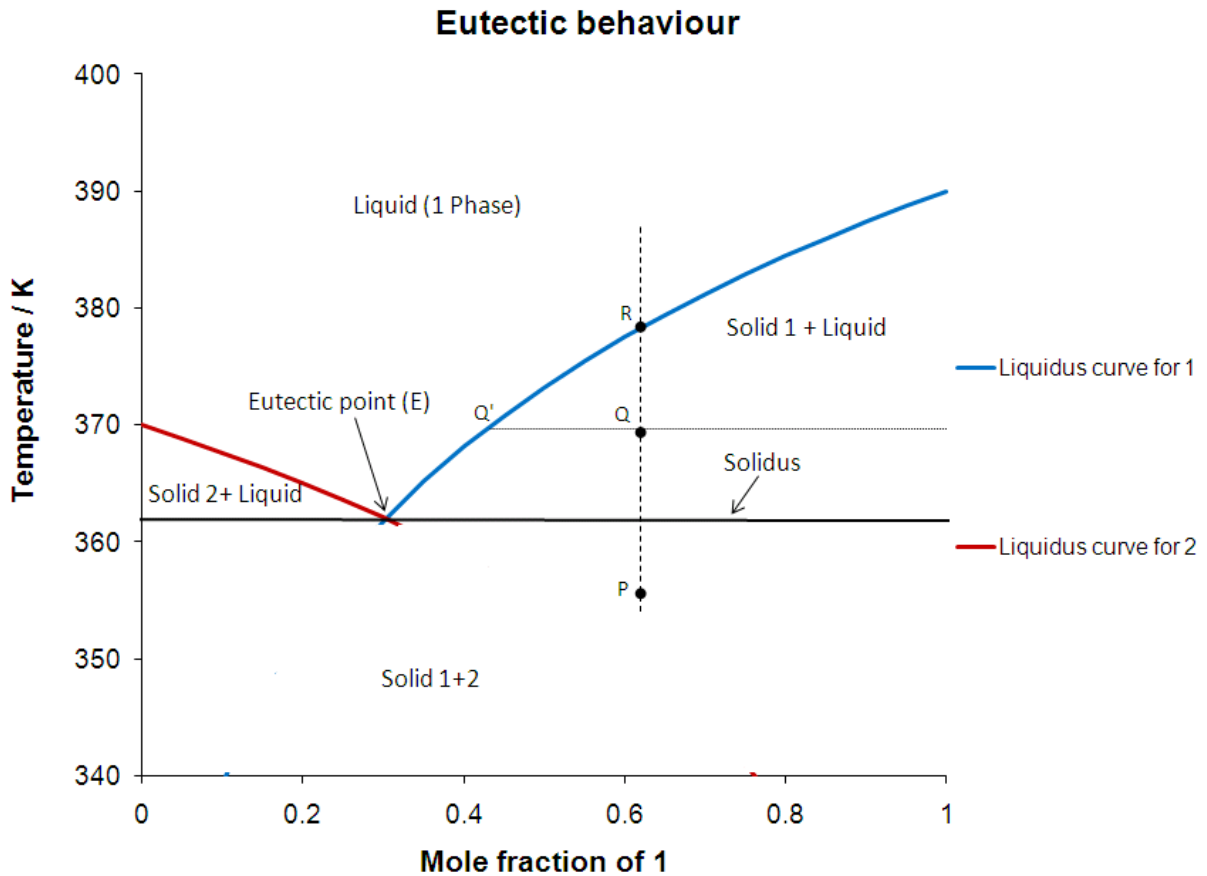


**Figure 3-2** Phase diagram for a eutectic system

Consider point P in the phase diagram above which has a composition  $x_1=0.62$ , where both components 1 and 2 exist in the solid phase and do not mix. As the temperature of this mixture is increased, both components begin to melt at the eutectic temperature until all of 2 has melted. The composition of the system then becomes the eutectic composition (point E) in the liquid phase, and pure 1 in the solid phase. As the temperature is increased further (point Q), more of 1 begins to melt. The composition at this temperature is given by the intersection of a horizontal 'tie' line with the liquidus (point Q') in the liquid phase, and pure 1 in the solid phase. The liquid phase keeps getting richer in component 1 as the temperature is increased till it reaches point R on the liquidus, where all solid has melted, and the mixture is now an ideal liquid.

To derive equations for the liquidus curves, we start again from Eqn. 3-1 for the two phases of each component in equilibrium. For the eutectic case, this equation becomes:

$$\mu_{i,s}^o = \mu_{i,l}^o + RT \ln x_{i,l}$$

... Eqn. 3-7

Solving similarly as the ideal mixing case, we get the following equation for the liquidus curve for each component  $i$ :

$$T = \frac{\Delta H_i^o T_i}{\Delta H_i^o - RT_i \ln x_{i,l}}$$

... Eqn. 3-8

This equation has been plotted in Figure 3-2 for a binary mixture with  $\Delta H_1^o = \Delta H_2^o = 20$  kJ/mol,  $T_1 = 370$  K and  $T_2 = 390$  K.

### 3.1.3 Non-ideal mixtures – The regular solution model

The deviation of non-ideal solutions from the ideal model is accounted for by the introduction of excess functions for the thermodynamic variables in consideration. For example, the difference between the ‘real’ and the ideal Gibb’s free energy for each component  $i$  is the excess Gibb’s free energy, given by:

$$G_i^E(T, P, x) = G_i(T, P, x) - G_i^{ideal}(T, P, x)$$

... Eqn. 3-9

A regular solution is a non-ideal solution in which the enthalpy of mixing i.e. the excess enthalpy is non-zero. According to the Regular Solution theory [3], the excess enthalpy of mixing depends on the composition of the components according to the relation:

$$H^E = \Omega x_A x_B$$

... Eqn. 3-10

Here,  $\Omega$  is the interaction parameter which is proportional to the difference in energy between A-B pairs and the mean of A-A and B-B pairs in the system.

$$\Omega\alpha(2E_{AB} - E_{AA} - E_{BB})$$

... Eqn. 3-11

Thus, a value of  $\Omega=0$  would recover the ideal mixing case and increasing values of  $\Omega$  indicate strong non-ideal mixing to phase separation when  $\Omega/(2RT) > 1$ . In the regular solution theory the entropy of mixing is assumed to be the same as the ideal case, i.e. the excess entropy of mixing is set to zero. The excess Gibbs free energy then becomes the same as the excess enthalpy (Eqn. 3-10).

The non-ideality of mixing in the solid state may be incorporated into the equations developed earlier (§3.1.1) by introducing an activity coefficient  $\gamma$ . Eqn. 3-2 then becomes:

$$\mu_{i,s}^o + RT \ln \gamma_{i,s} x_{i,s} = \mu_{i,l}^o + RT \ln x_{i,l}$$

... Eqn. 3-12

Here, the liquid phase is assumed to mix ideally. Proceeding as in §3.1.1, the following equations can be derived:

$$\exp(\alpha_1) \left( 1 - \frac{\gamma_{2,s} x_{2,s}}{\exp(\alpha_2)} \right) = \gamma_{2,s} (1 - x_{2,s})$$

... Eqn. 3-13

$$x_{2,l} = \frac{\gamma_{2,s} x_{2,s}}{\exp(\alpha_2)}$$

... Eqn. 3-14

For the regular solution model, the activity coefficient is related to the interaction parameter:

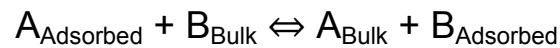
$$\gamma_{2,s} = \exp(\Omega x_{2,s}^2)$$

... Eqn. 3-15

Given values of melting points and enthalpies of melting of pure 1 and 2 and a value for  $\Omega$  Eqn. 3-13 and Eqn. 3-14 can be solved numerically at each temperature to give the phase diagram.

### 3.1.4 Preferential adsorption

In considering two-dimensional mixing behaviour of binary mixtures adsorbed on graphite, the composition of the mixture in the monolayer may not be the same as that in the bulk. In general, it is found that a longer homologue will be adsorbed in preference to a short one [4-6]. This can be explained using arguments for the translational entropy of the system: a system with more small molecules in the bulk and fewer bigger molecules on the surface is entropically favourable to the one having fewer bigger molecules in the bulk and more small ones on the surface (given that the total surface area must be conserved). Preferential adsorption can be accounted for in the equations developed above by defining the following equilibrium between two species  $A$  and  $B$  having a constant  $K$  [7]:



$$K = \frac{(x_A^{\text{Bulk}} / x_A^{\text{Adsorbed}})}{(x_B^{\text{Bulk}} / x_B^{\text{Adsorbed}})}$$

... Eqn. 3-16

A value of  $K$  greater than 1 implies that there is a preference for the adsorption of B over A on the surface.

### 3.1.5 Other mixing models

Apart from the ideal and regular solution models presented here to explain the phase behaviour of binary mixtures, a number of alternative models are also available in literature. Many of these are based upon the regular solution model and require the calculation of activity coefficients by different approaches. The general rules that apply to solid solution formation in binary alloys [8] are thought to be equally applicable to predict mixing in the monolayer i.e., increasing miscibility can occur if the two components have similar crystal structures and atomic sizes.

Specifically, the calculation of a 2D isomorphism co-efficient [9] helps predict miscibility in adsorbed layers based on the unit cells of the monolayer structures of the individual components. Analogous to the three-dimensional case, the 2D isomorphism coefficient ( $\epsilon$ ) is given by:

$$\varepsilon = 1 - \frac{\Delta}{\Gamma}$$

... Eqn. 3-17

Here  $\Delta$  is the area of the non-overlapping part of the two unit cells when both are positioned so as to achieve maximum overlap, and  $\Gamma$  is the area due to the overlapping part. A value of  $\varepsilon$  equal to 1 indicates complete miscibility in the monolayer. For binary alcohol mixtures on graphite, values of the isomorphism coefficient less than 0.76 indicate complete phase separation; between 0.76 and 0.89 indicate partial miscibility; and those greater than 0.89 show complete miscibility in the monolayer [9]. Similar values of the isomorphism coefficient can help predict mixing in binary alkane mixtures.

The solid-liquid equilibrium of *n*-alkanes in the bulk with chain lengths between 20-40 carbons has been calculated using the Chain Delta Lattice Parameter model [10]. The excess entropy of mixing is assumed to be zero again, and the excess enthalpy and excess Gibb's free energy of mixing are given by:

$$G^E = H^E = \Omega x_1 x_2 = \Theta \frac{(l_l - l_s)^2}{l_s^3} x_1 x_2$$

... Eqn. 3-18

Here  $l_l$  and  $l_s$  are the unit cell lengths of the long and short mixture components. Importantly, this model defines  $\Omega$  as a function of chain lengths of the alkanes but the parameter  $\Theta$  is constant for the entire homologous series. The value of  $\Theta$  was calculated to be 2317 kJ Å/mol [10].

Matheson and Smith [11] have developed a simple model to predict which pairs of *n*-alkanes can form a series of solid solutions. Their scheme focuses solely on geometrical factors such as lattice chain length and volumes and presupposes regular solution behaviour. There are also many models from the field of chemical thermodynamics to predict activity coefficients for non-ideal mixtures. For example the UNIFAC system [12] uses combinations of interactions between different functional groups that make up a molecule to calculate activity coefficients for vapour-liquid equilibria.

## 3.2 Differential Scanning Calorimetry

### 3.2.1 The technique

Differential Scanning Calorimetry is a technique for studying thermal transitions in systems [13]. Most Differential Scanning Calorimeters (DSCs) fall into one of two categories depending on their operating principle – power compensation or heat flux.

#### 3.2.1.1 Power compensation DSC

A power compensation DSC is equipped with a sample furnace and a reference furnace, both heated at a fixed temperature rate given by the user. In the event of a temperature difference arising between the sample and the reference (which is usually an empty sample pan), differential power is supplied to the heaters to eliminate this difference and to maintain the temperature to the program value. This differential power is the source of the DSC signal. Sensitivities of the order of  $1 \times 10^{-6}$  W can be achieved. The DSC thus helps measure calorimetric data of the sample such as temperatures of melting and other transitions, glass transition temperatures as well as the enthalpies associated with these transitions. Figure 3-3 (a) shows a schematic of a power-compensation DSC.

The instrument contains independent heaters and platinum resistance thermometers under each of the sample and reference furnaces. The DSC is designed so that the sample and reference furnaces are identical i.e.  $R_s = R_r = R$  and  $T_{sp} = T_{rp} = T_p$  (the symbols and subscripts are explained in Figure 3-3 below). The DSC signal is then given by [14]:

$$\frac{dq}{dt} = \frac{dq_s}{dt} - \frac{dq_r}{dt} = \frac{dT_p}{dt} (C_s - C_r)$$

... Eqn. 3-19

Here  $q$  is the heat flow and  $dT_p/dt$  is the heating rate maintained by the DSC.

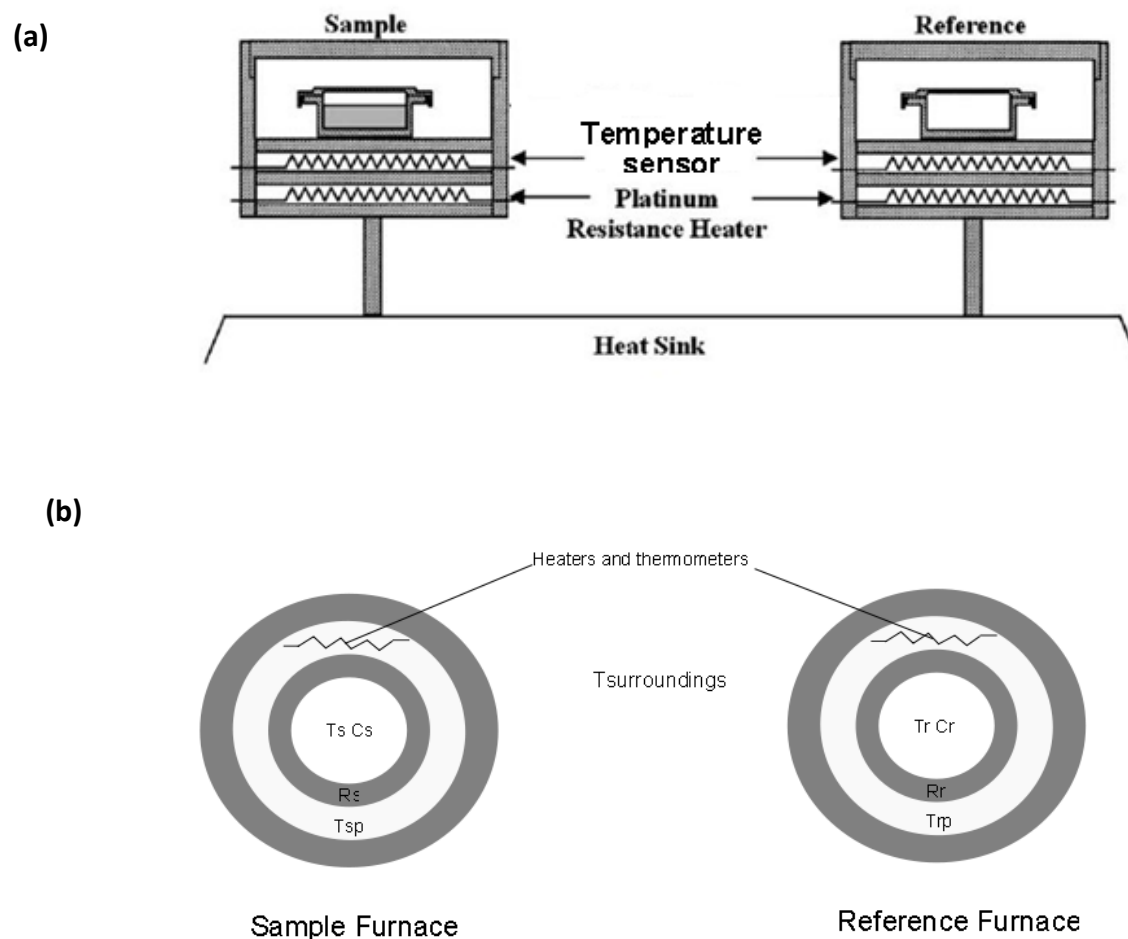


**Figure 3-3** Schematic of a power compensation DSC. The subscripts  $s$  and  $r$  refer to the sample and reference furnaces respectively.  $T$  is the temperature,  $C$  is the heat capacity,  $R$  is the thermal resistance; subscripts  $s$  and  $r$  refer to the actual sample and reference, and  $sp$  and  $rp$  refer to the part of the sample/reference furnaces between the heaters and the actual sample/reference, respectively.

### 3.2.1.2 Other thermal analysis techniques

In a heat flux DSC the instrument signal is derived from the temperature difference established when the sample and reference are heated in the same furnace. A differential thermal analysis instrument (DTA) works on essentially the same principle as a heat flux DSC; the difference lies in the algorithm to convert this difference in temperature into differential power. Increasingly most DTA instruments are being replaced by DSCs for operating temperatures up to 1600 °C, but DTA instruments have still found important use for measurements above 1600 °C due to design advantages.

In temperature modulated DSC, a periodic temperature modulation is superimposed on the constant heating rate of a conventional DSC measurement [15]. This helps in the measurement of a 'dynamic' heat capacity and can be useful in separating effects such as glass transitions and crystallisation if they are superimposed.

### 3.2.2 Melting of pure materials

One of the first quantitative models for the analysis of melting of pure materials using dynamic thermal analysis techniques was provided by Gray [16] and elaborated by Mraw [17]. Melting of a pure substance such as indium is observed to occur over a temperature range owing to the dynamic nature of the DSC measurement. Following Gray's work, melting can be considered to occur over four stages as shown in Figure 3-4.

In Stage I of the melting process the solid increases its temperature due to the heat supplied by the DSC up to the melting point. The equation describing this process is given by Eqn. 3-19 which is essentially the supply of constant electrical power to the sample furnace relative to the reference. Once the melting point is reached, the DSC supplies increasing amounts of heat to overcome the enthalpy of melting ( $H$ ), and the DSC curve at this stage is a straight line of slope=Heating rate/ $R$ . The peak height can be shown to be:

$$\left(\frac{dq}{dt}\right)_{\max} = \frac{t_{\max}}{R} \frac{dT_p}{dt}$$

... Eqn. 3-20

The time period during which the total heat supplied by the DSC equals the enthalpy of melting ( $t_{\max}$ ) is given by:

$$t_{\max} = RC_s \left[ -1 + \left( 1 + \frac{2H}{RC_s^2 \left( \frac{dT_p}{dt} \right)} \right)^{1/2} \right]$$

... Eqn. 3-21

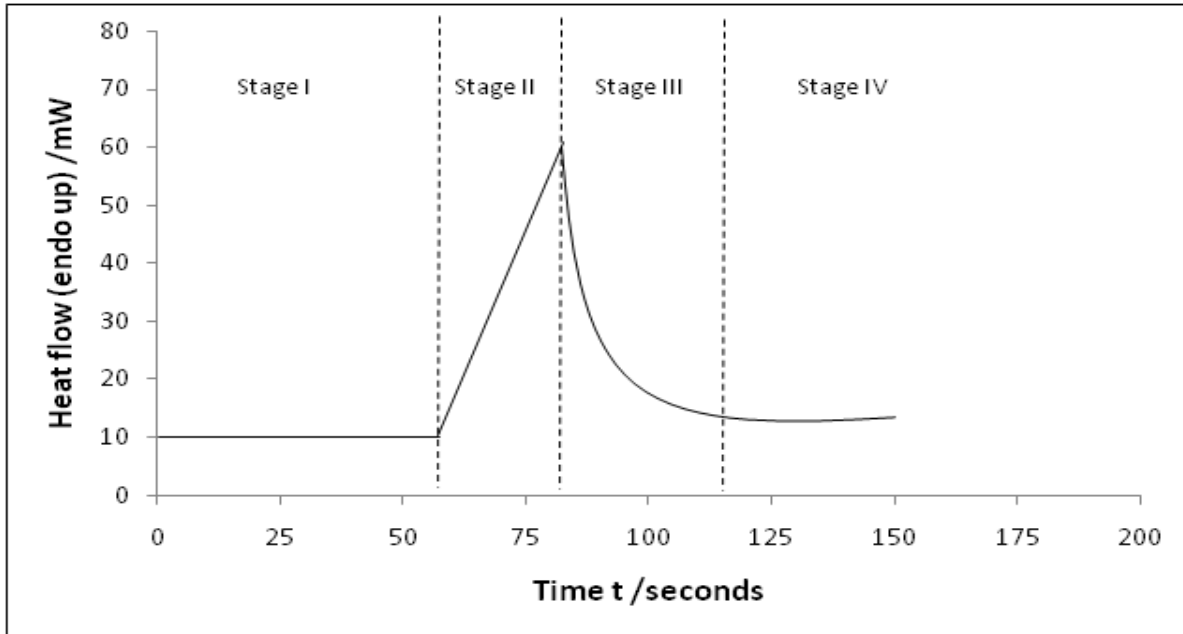


Figure 3-4 DSC melting curve for a pure material

Once the solid has melted completely, the sample furnace tries to ‘catch up’ with the reference (Stage III) and the equation of the DSC curve for this stage is:

$$\frac{dq}{dt} = \left( \frac{dq}{dt} \right)_{\max} e^{-t/RC_s}$$

... Eqn. 3-22

Stage IV of the melting process is the same as stage I, although the heat capacity of the liquid may not necessarily be equal to that of the solid which gives a different constant value of the heat flow.

Since the slope of the line for stage II varies with heating rate, the peak maximum temperature can vary depending on the rate specified by the user. The quantitative advantage of a DSC is that the area enclosed by the peaks gives the enthalpy of the transition directly, and this value is essentially independent of the heat capacity of the sample and the specified heating rate [13].

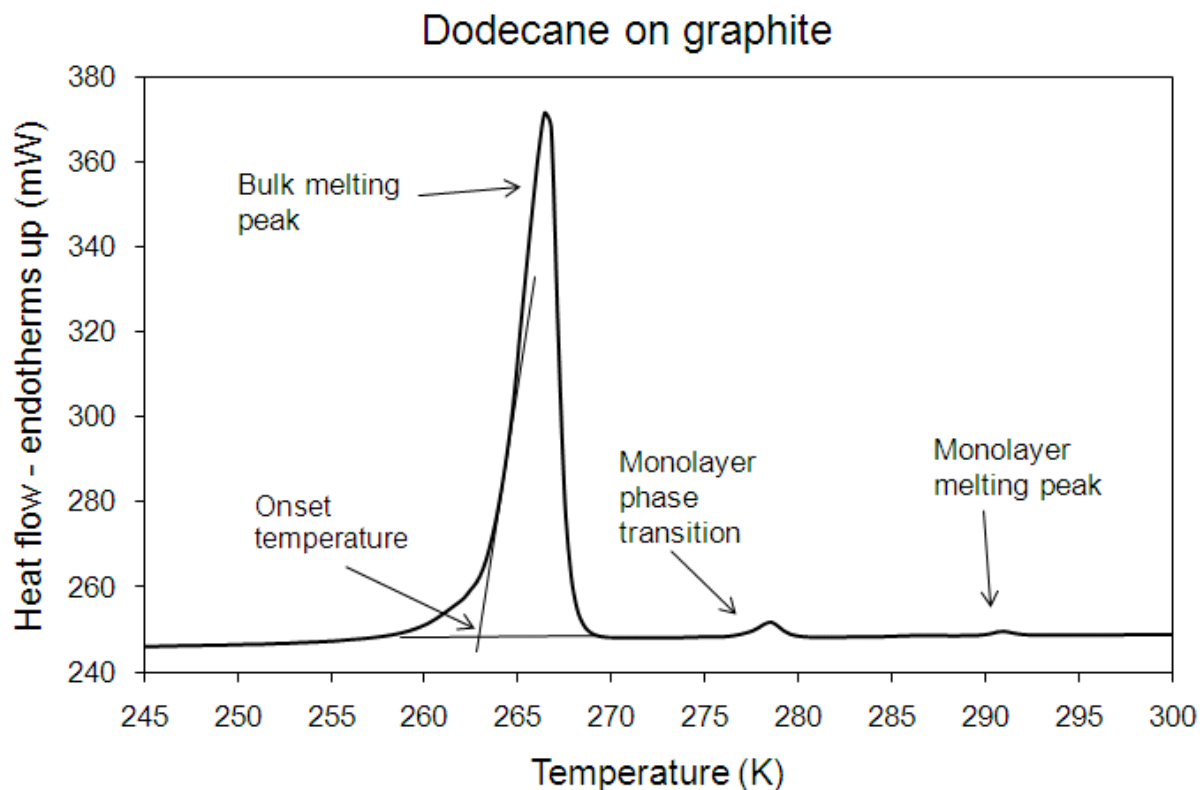


**Figure 3-5** DSC thermogram of dodecane adsorbed on graphite showing a graphical construction to determine the onset temperature of the peak. The intersection of the tangent to the leading edge of the peak with the baseline gives the onset temperature. The weak signal at 291 K is attributed to the monolayer since it is not seen if the graphite substrate is absent. Dodecane possesses an additional solid-solid phase transition in the monolayer at  $\sim 277$  K [18].

Instead of the peak maximum temperature, the peak onset temperature (e.g. for dodecane shown in Figure 3-5) is frequently reported as the melting temperature for bulk peaks since it is much less affected by changes in heating rates. However, for monolayers the peak maximum temperature is reported due to a large uncertainty in estimating the baseline accurately owing to the weak nature of the signal.

### 3.2.3 Thermograms for eutectic and ideal mixtures

Sun and Clarke [19] have modelled the behaviour of solid binary mixtures for cases when there is complete phase separation (eutectic behaviour) and ideal mixing in the solid phase. The line shape of the DSC thermogram has been solved by writing quantitative energy balances. Following their work these two types of mixtures can be studied as briefly explained here.

### 3.2.3.1 Eutectic behaviour

The thermogram for a eutectic mixture can be modelled in four stages as shown in Figure 3-6. The first part of the melting process can be considered the same as that of a pure substance (Eqn. 3-19) with a heat capacity given by:

$$C_{mix} = x_1 C_1 + x_2 C_2$$

... Eqn. 3-23

Here the mole fractions ( $x$ ) correspond to that in the solid de-mixed phase. As explained in §3.1.2 when the temperature reaches the eutectic temperature energy needs to be supplied to melt one of the components completely and the other partly till the composition of the liquid phase becomes the eutectic composition. On the DSC this appears as a peak (the first peak) in Figure 3-6.

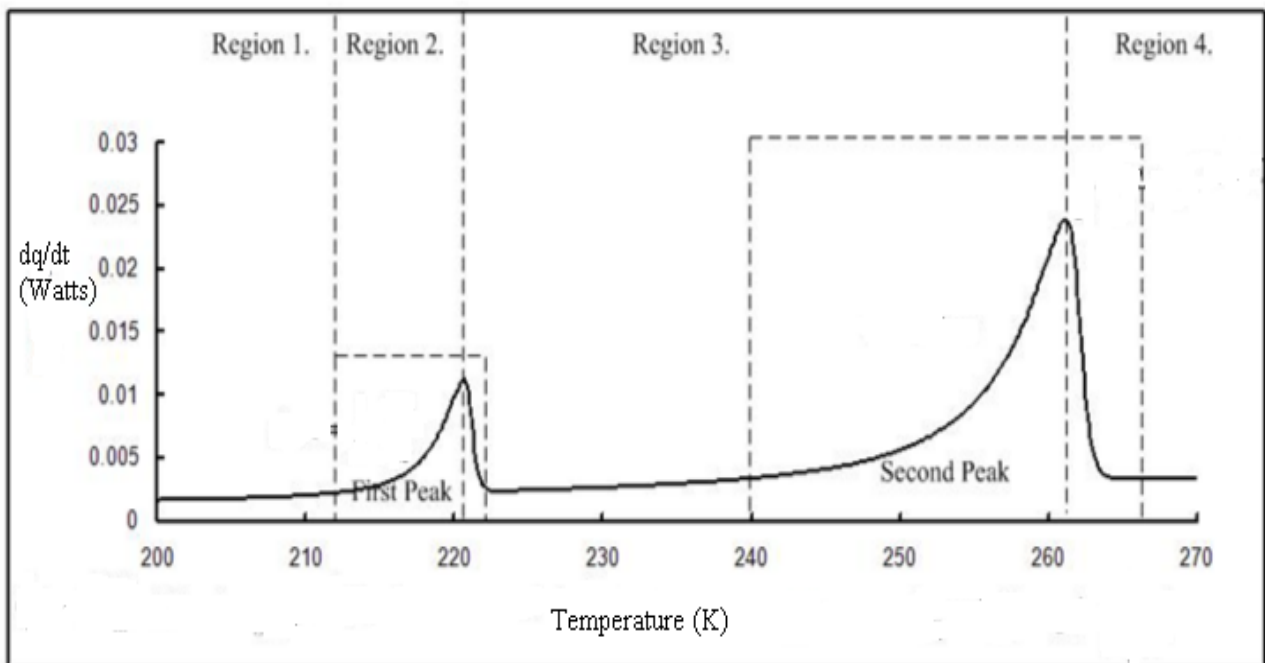


**Figure 3-6** DSC thermogram for a eutectic mixture

Region 2 of the thermogram can also be modelled as the melting of a pure material (explained in §3.2.2) to give a straight line. The mixture enthalpy is the sum of the pure components weighed by the eutectic compositions:

$$\Delta H_{eu} = x_{1,eu} \Delta H_1 + x_{2,eu} \Delta H_2$$

... Eqn. 3-24

Region 3 can be considered as a sum of two heat flows into the sample furnace: one for the sample to ‘catch-up’ with the reference and the other to melt the pure solid. This melting along the liquidus line of the phase diagram (Eqn. 3-8) is thought to be analogous to heating a pure solid (Eqn. 3-19) with a temperature dependant heat capacity:

$$C_{solid} = C_{mix} + C_{effective} = C_{mix} + \frac{d(\Delta H)}{dT} = C_{mix} + x_2 \left( \frac{(\Delta H_1)^2}{RT^2} \right) \left( \frac{x_{1,l}}{(1-x_{1,l})^2} \right)$$

... Eqn. 3-25

Here,  $C_{mix}$  is given by Eqn. 3-23 and the derivative  $\frac{d(\Delta H)}{dT}$  is evaluated along the liquidus (Eqn. 3-8).  $x_2$  is the total mole fraction of component 2 in the system and  $x_{1,l}$  is the mole fraction of 1 in the liquid phase given by Eqn. 3-8. This region of the thermogram necessitates the use of numerical methods and a suitable code has been written in *Fortran* by Sun and Clarke.

Regions 4 and beyond can then be explained using the same principles as that for a pure liquid with a heat capacity given by Eqn. 3-23.

### 3.2.3.2 Ideal mixture

The DSC thermogram of a binary system that mixes ideally in both solid and liquid phases is shown in Figure 3-7. Regions 1 and 3 can be modelled in the same way as the eutectic case (by assuming mixture heat capacities). For region 2 the melting along the liquidus line of the phase diagram (Eqn. 3-6) is again considered analogous to heating a pure solid with a temperature dependant heat capacity (Eqn. 3-25). However, for the ideal mixing case, evaluation of the derivative  $\frac{d(\Delta H)}{dT}$  is more complicated owing to the nature of the liquidus curve equation (Eqn.

3-6). This requires the use of numerical methods as well and the *Fortran* program written by Sun and Clarke generates ideal mixture thermograms for different mole fractions of the components.

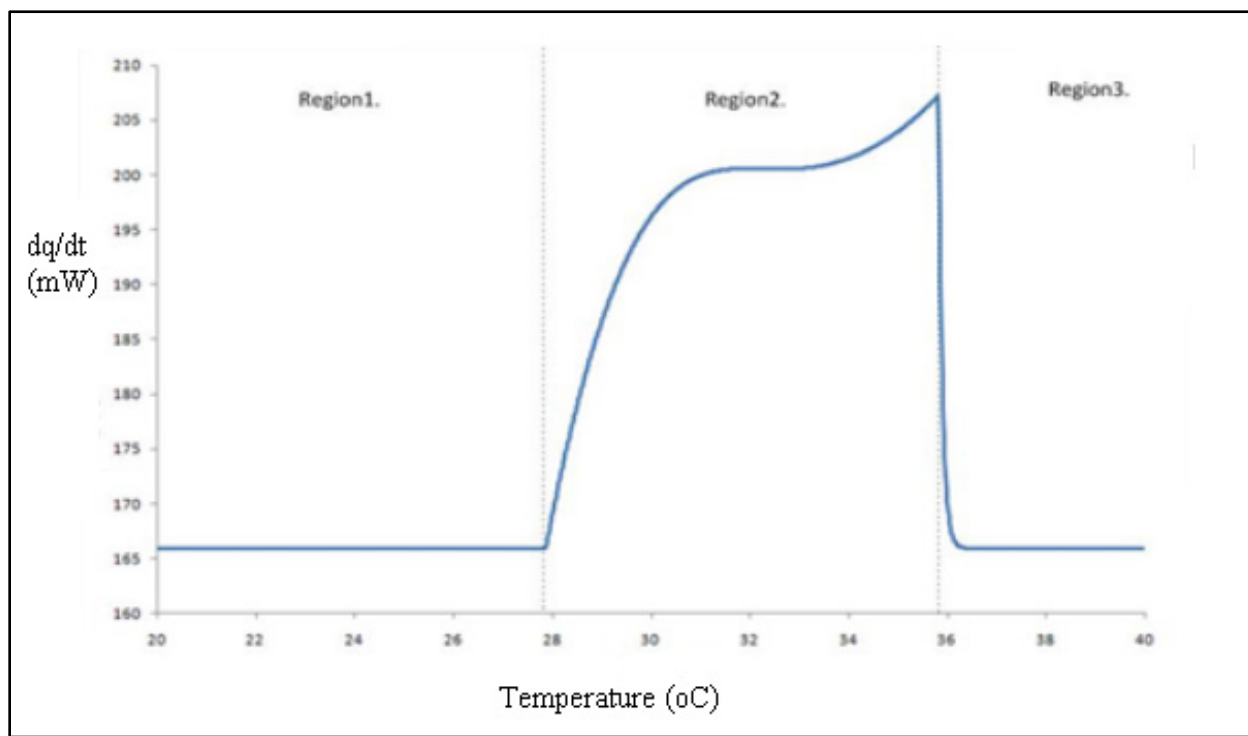


Figure 3-7 Calculated DSC thermogram for an equimolar ideal mixture

### 3.3 Experimental details

The instrument used for this work was a Perkin-Elmer Pyris-1 power compensation DSC with an operating range of  $-170^{\circ}\text{C}$  to  $350^{\circ}\text{C}$ . Samples for the DSC were prepared in the following manner: for the pure amides, a graphite disc weighing 20-25 mg and approximately 1-3 mg of the compound were placed in an aluminium (sample) pan. This corresponds to a surface coverage of about 5-10 monolayers. The lid of the pan was then hermetically sealed using a mechanical crimper. The sample was then annealed at  $180^{\circ}\text{C}$  for two hours and allowed to cool slowly to room temperature overnight. An annealing temperature of  $180^{\circ}\text{C}$  was found to be appropriate given the amide monolayer melting point is typically  $140\text{-}160^{\circ}\text{C}$  [4] which enables adsorption from the liquid phase under equilibrium conditions.

The DSC program used was as follows:

- 1) Hold for 2 min at 30 °C
- 2) Heat from 30 °C to 180 °C at 40 °C/min
- 3) Cool from 180 °C to 30 °C at 40 °C.min
- 4) Heat from 30 °C to 180 °C at 20 °C/min

The sample was held at 30 °C to allow the DSC to equilibrate. Heating at a faster rate provides better sensitivity of the measurement of the enthalpies (which can be found from the area under the DSC curve). Heating at a slower rate provides better resolution of the peaks (since the thermal lag of the sample decreases). The heating and cooling curves were compared to see if the bulk and monolayer melting transitions occurred at approximately the same onset temperature while heating and cooling (this also gave an estimate of the error in the melting temperature). The heating curve was used for subsequent analysis unless shown otherwise.

An indium sample was run at the start of each day to calibrate the instrument. The values for Indium melting point and enthalpy of fusion are 156.6 °C and 28.6 J/g [13]. Any difference between the measured indium values and the standard values was used as a correction factor for all the measurements made on that day.

### 3.4 Summary

Ideal, eutectic and regular solution models for binary mixing in the solid phase have been explained in this chapter and equations describing mixing have been derived. In all cases ideal mixing is assumed in the liquid phase. These equations are modified for mixing in the 2D layer assuming preferential adsorption for one component over the other. The principles behind the use of a differential scanning calorimeter in constructing phase diagrams for binary mixtures have also been presented. DSC thermograms for the melting of pure materials and for eutectic and ideal mixtures can be analysed quantitatively, and the equations have been presented. Experimental details for measuring DSC phase diagrams have also been provided. Results of the adsorption of pure amides and binary mixtures on the surface of graphite will be shown in chapter 6.

### 3.5 References

1. Atkins, P., *Physical Chemistry*. 8th ed. 2006: Oxford University Press.
2. Calvet, T., E. Tauler, M.A. Cuevas-Diarte, J.R. Housty, D. Mondieig, Y. Haget, and J.C. Van Miltenburg, *Application of the "shape-factors method" to purity analysis of compounds by thermal methods*. *Thermochimica Acta*, 1992. **204**(2): p. 271-280.
3. Oonk, H.A.J. and M.T. Calvet, *Equilibrium between phases of matter - Phenomenology and Thermodynamics*. 2008, Dordrecht: Springer.
4. Arnold, T., Clarke, S. M., *Thermodynamic Investigation of the Adsorption of Amides on Graphite from Their Liquids and Binary Mixtures*. *Langmuir*, 2008. **24**(7): p. 3325-3335.
5. Duim, W.C. and S.M. Clarke, *Adsorption and mixing behaviour of ethers and alkanes at the solid/liquid interface*. *J. Phys. Chem. B*, 2006. **110**: p. 23853-23859.
6. Parker, J., S.M. Clarke, and A. Perdigón, *Preferential adsorption of solid monolayers of hydrocarbons over fluorocarbons at the solid/liquid interface*. *Surface Science*, 2007. **601**(18): p. 4149-4153.
7. Brown, C.E., D.H. Everett, and C.J. Morgan, *Thermodynamics of adsorption from solution. The systems (benzene + ethanol)/Graphon and (n-heptane + ethanol)/Graphon*. *J. Chem. Soc., Faraday Trans. 1*, 1975. **71**: p. 883 - 892.
8. Hume-Rothery, W. and G.V. Raynor, *The structure of metals and alloys*. Institute of Metals Monograph and Report Series No. 1. 1962: The Institute of Metals.
9. Clarke, S.M., Messe, L., Adams, J., Inaba, A., Arnold, T., Thomas, R. K., *A quantitative parameter for predicting mixing behaviour in adsorbed layers: the 2D isomorphism coefficient*. *Chemical Physics Letters*, 2003. **373**: p. 480-485.
10. Coutinho, J.A.P., S.I. Andersen, and E.H. Stenby, *Solid-liquid equilibrium of n-alkanes using the chain delta lattice parameter model*. *Fluid Phase Equilibria*, 1996. **117**(1-2): p. 138-145.
11. Matheson Jr, R.R. and P. Smith, *A simple thermodynamic analysis of solid-solution formation in binary systems of homologous extended-chain alkanes*. *Polymer*, 1985. **26**(2): p. 288-292.
12. Smith, J.M., H.C.V. Ness, and M.M. Abbot, *Introduction to Chemical Engineering Thermodynamics*. 7th ed. 2004: McGraw Hill.
13. Laye, P.G., *Differential thermal analysis and differential scanning calorimetry*, in *Principles of Thermal Analysis and Calorimetry*, P. Haines, Editor. 2002, The Royal Society of Chemistry: Cambridge. p. 55-93.
14. Mraw, S.C., *Specific Heat of Solids*. CINDAS Data Series on Material Properties, ed. Y.S. Touloukian and C.Y. Ho. Vol. I-2. 1988: Hemisphere Publishing Corporation.
15. Reading, M., A. Luget, and R. Wilson, *Modulated differential scanning calorimetry*. *Thermochimica Acta*, 1994. **238**: p. 295-307.
16. Gray, A.P., *A simple generalized theory for the analysis of dynamic thermal measurement*. *Analytical calorimetry - proceedings of the American Chemical Society Symposium on Analytical Calorimetry*, San Francisco, California, April 2-5, 1968, ed. R.S. Porter and J.F. Johnson. 1968, New York: Plenum Press.
17. Mraw, S.C., *Mathematical treatment of heat flow in differential scanning calorimetry and differential thermal analysis instruments*. *Rev. Sci. Instrum.*, 1982. **53**(2): p. 228-231.

18. Arnold, T., R.K. Thomas, M.A. Castro, S.M. Clarke, L. Messe, and A. Inaba, *The crystalline structures of the even alkanes hexane, octane, decane, dodecane and tetradecane monolayers adsorbed on graphite at submonolayer coverages and from the liquid*. Phys. Chem. Chem. Phys., 2001. **4**: p. 345-351.
19. Sun, C. and S.M. Clarke, *unpublished work*, University of Cambridge: Cambridge.

# Chapter 4

## Saturated amides - diffraction

---

The adsorption of alkyl amides on graphite has been investigated by neutron and X-ray powder diffraction and the results are presented in this chapter. The method of 2D crystal structure solution from diffraction data for saturated alkyl amides (chain lengths between five and sixteen carbons) adsorbed on graphite is explained. By consideration of a number of members of the homologous series, a new plane group of the amide layers previously unreported has been identified. The calculated structures are discussed in detail in terms of the packing arrangements in the monolayer and the hydrogen bond geometry. Monolayer melting data and diffraction patterns at higher coverage of the amides on graphite are also presented, and the stability of the monolayer is discussed.

### 4.1 Preliminary analysis

Synchrotron X-ray diffraction patterns from even chain-length alkyl amides adsorbed on graphite measured in this study are shown in Figure 4-1. Similar data for odd-chain length amides are shown in Figure 4-2.

All X-ray patterns presented in this chapter were measured on the Materials Science (MS) beamline X04SA at the Swiss Light Source (SLS). Data was collected at 300 K and approximately 0.5 monolayer coverage of the amide on graphite, unless stated otherwise, and as discussed previously in chapter 2. Due to the difficulty of obtaining neutron beam time only a

limited number of neutron diffraction patterns could be obtained, in addition to the high cost of synthesising deuterated amides. These neutron diffraction patterns were measured on the instrument D20 at ILL as discussed in chapter 2, and will be presented in §4.4.

The saw-tooth shaped diffraction patterns of Figure 4-1 and Figure 4-2 confirm that all the amides studied here form solid ordered monolayers on the graphite surface at these coverages and temperatures. The lowest angle peaks in the patterns correspond to  $d$ -spacings (i.e. interplanar spacings) of the order of 20-30 Å. This dimension is of the same order of magnitude as the length of the extended alkyl chain of these adsorbates; it can therefore be concluded that the molecules lie flat on the graphite surface. In such strongly anisotropic unit cells, the lowest angle peaks may be considered to represent a multiple of the long axis of the unit cell ( $a$ -axis), typically the (1,0) or (2,0) reflections, depending upon the symmetry of the structure. These low angle peaks shift towards lower  $q$  values as the chain length is increased, again indicating that the amide molecules lie flat on the surface with the long axis of the molecule having the dominant contribution to the unit cell  $a$ -direction.

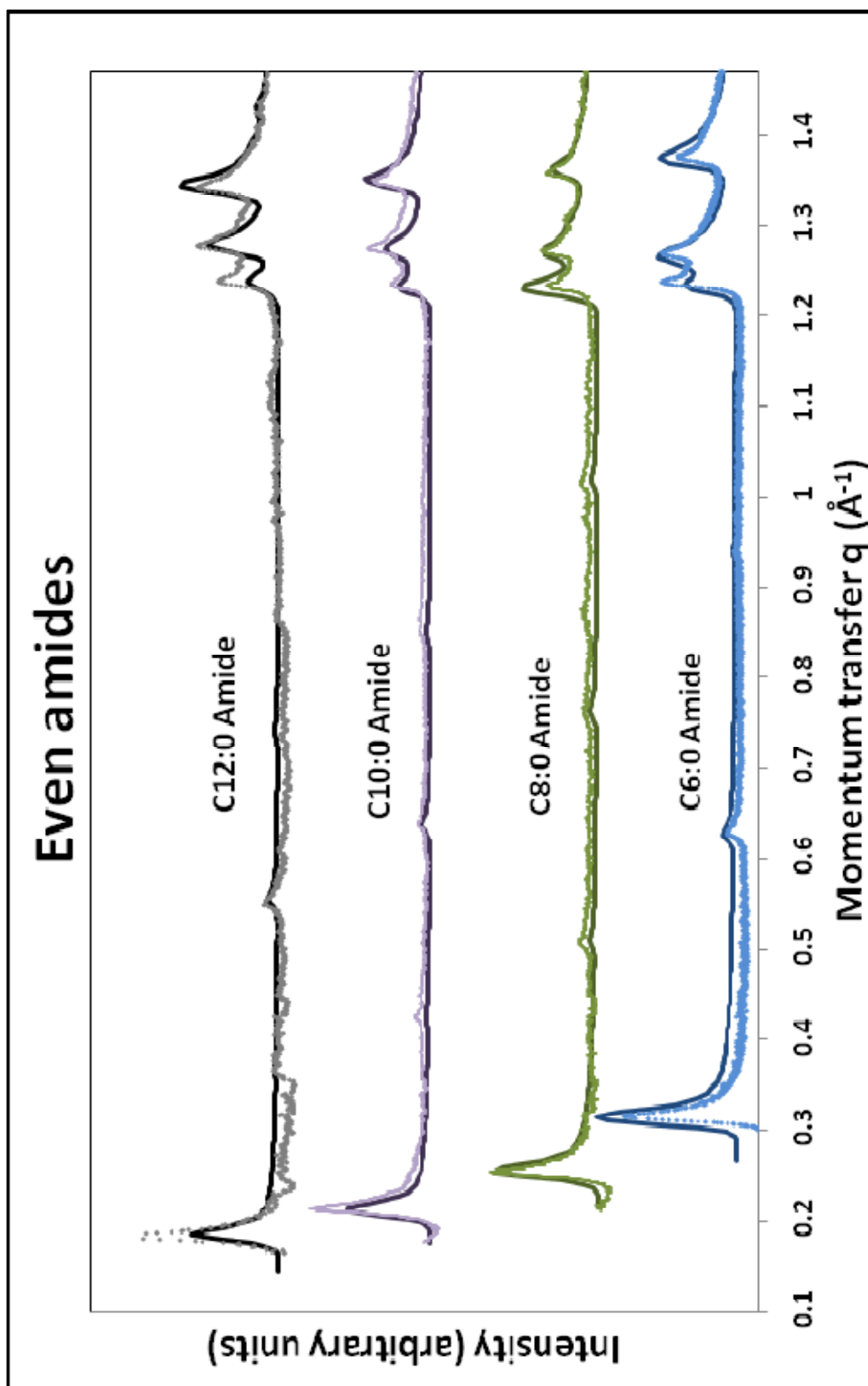


**Figure 4-1** Experimental (lighter shades) and calculated (darker shades) X-ray diffraction patterns from even chain-length amides adsorbed on graphite at 300K at sub-monolayer coverage

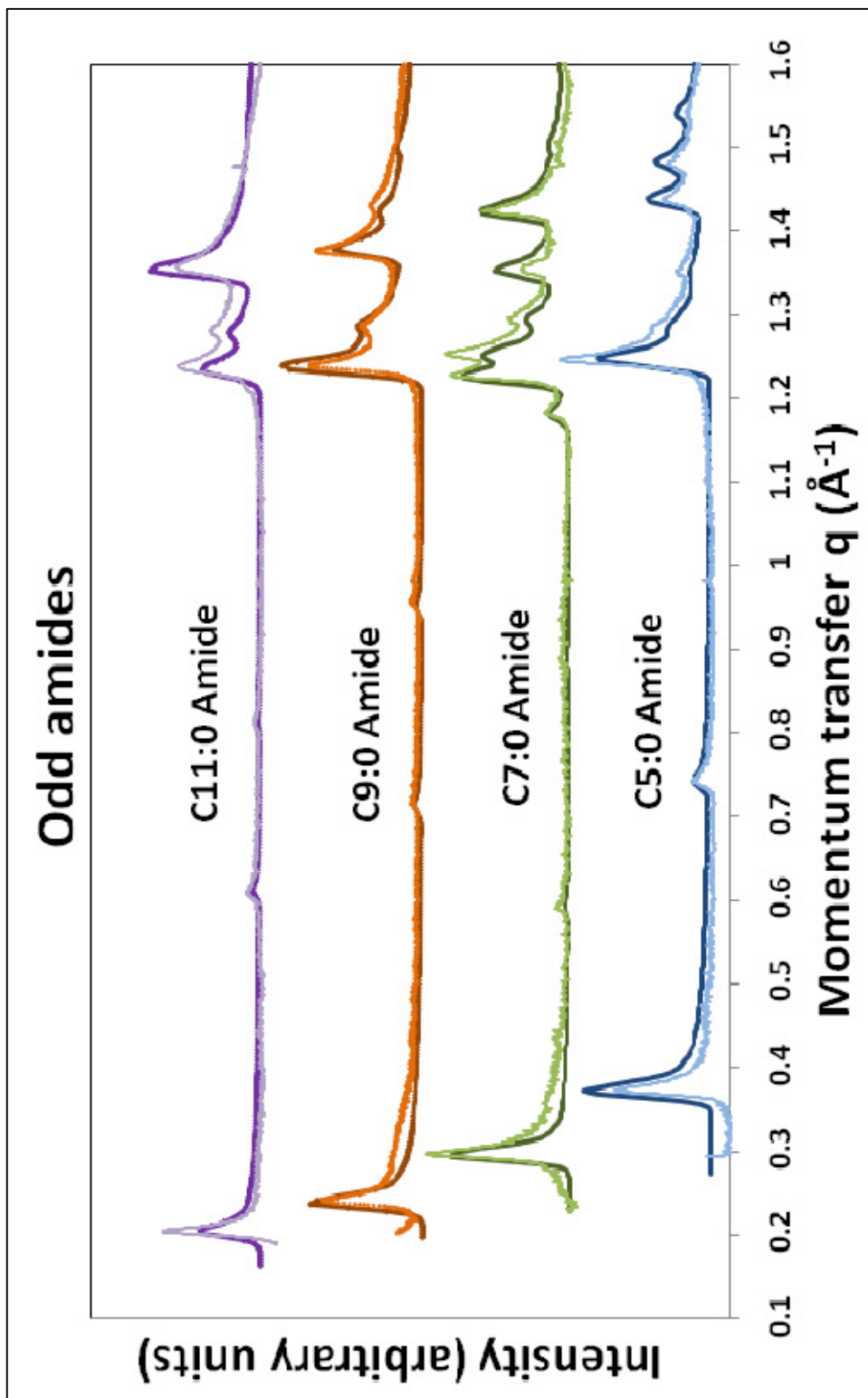


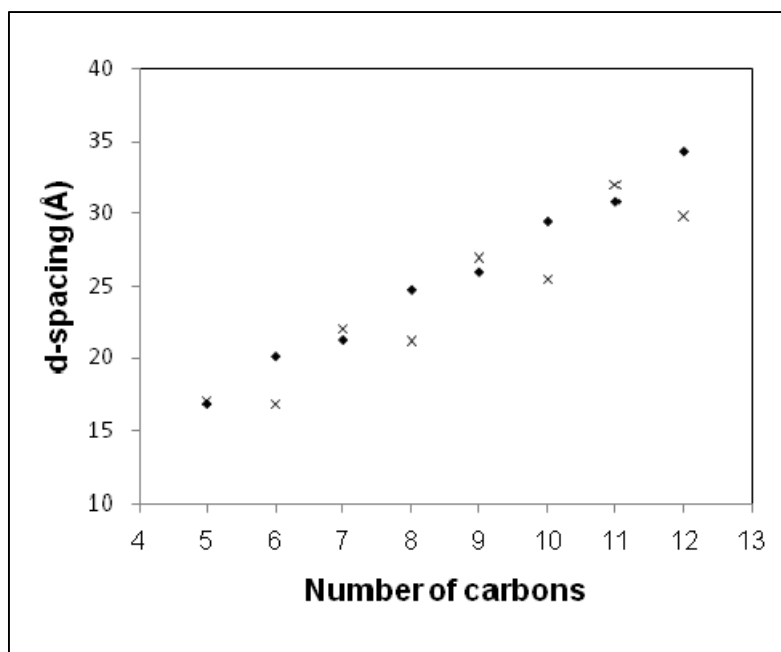
**Figure 4-2** Experimental (lighter shades) and calculated (darker shades) X-ray diffraction patterns from odd chain-length amides adsorbed on graphite at 300K at sub-monolayer coverage

The variation of  $d$ -spacing of the low angle reflection with alkyl chain length of the amide is shown in Table 4-1 and the long  $d$ -spacing of the equivalent alkane monolayer is also shown for comparison. These spacings are plotted in Figure 4-3 and indicate that even alkanes are significantly shorter in the  $a$ -direction as compared to the amides, while odd alkanes are slightly longer. This difference in trends between alkane and amide peak positions suggests a significantly different structure for the amides, which will be shown here.

As discussed in chapter 2, experimental limitations restrict the accessible  $q$  range available and this in turn limits the length of molecules for which the low angle reflections can be observed. Figure 4-1 clearly illustrates that low order monolayer peaks up to the C12:0 amide (12 carbon atoms in the chain) can be seen with the experimental configuration used at the MS beam line. For amides of higher chain lengths, access to lower  $q$  would be required to see the equivalent peaks. For such long molecules, previous experience has shown that it can be very difficult to reliably fit the intensity for the lowest momentum transfer peak due to the very intense small angle scattering from the graphite substrate. Therefore only the peak positions for the (1,0) peaks, which are important for structural solution, have been considered while fitting the X-ray patterns for amides with chain lengths  $\geq 10$  carbons.

It may also be noted from Figure 4-1 and Figure 4-2 that the peaks in the region  $1.2$ - $1.6 \text{ \AA}^{-1}$  in  $q$  are approximately in the same place for all the amides. These peaks can be indexed, as discussed later in this chapter, with a non-zero  $k$  index. This indicates that the side-to-side spacing of the unit cell is mostly unchanged with increasing chain length, as might be expected.

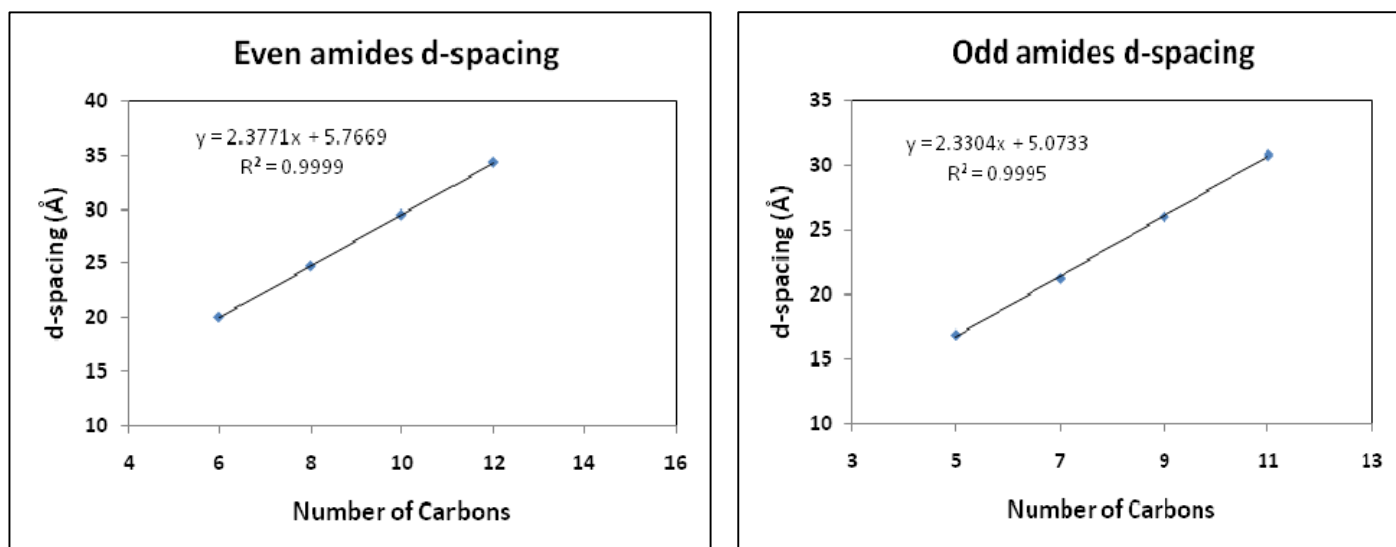
Figure 4-3 indicates that the  $d$ -spacing for the shorter odd amides is slightly less than that predicted by a linear trend for the even homologues. An essentially identical effect has been observed in the  $d$ -values of bulk saturated amides in very early studies of these compounds [1], with even members consistently possessing larger  $d$ -values than odd ones. A similar odd-even variation in the low-angle peak position and crystal structure has been observed previously for alkane [2], carboxylic acid [3] and perfluoroalkane [4] monolayers previously. The variation arises from subtle differences in the monolayer crystal structure and symmetry, and will be discussed further in this chapter.



**Figure 4-3** A plot of  $d$ -spacing of the lowest angle peak as a function of chain length of saturated alkyl amides (points) on graphite. The  $d$ -spacings of alkanes (crosses), from [2, 5], are also plotted for comparison.

**Table 4-1** Peak positions and  $d$ -spacings ( $d$ ) of the alkyl amides and comparison to graphite lattice parameter  $a_g = 2.46 \text{ \AA}$  (subscript  $g$  refers to graphite)

| Number of carbons (N) | Low-angle peak position ( $\text{\AA}^{-1}$ ) | $d$ ( $\text{\AA}$ ) | $d/(\sqrt{3} a_g^*)$ | $d/(a_g)$ | $d$ -spacing of alkane ( $\text{\AA}$ ) (from [2, 5]) |
|-----------------------|---|----------------------|----------------------|-----------|---|
| 5                     | 0.373   | 16.85                | 3.96                 | 6.85      | 17.1  |
| 6                     | 0.313   | 20.07                | 4.71                 | 8.16      | 16.9  |
| 7                     | 0.296   | 21.23                | 4.98                 | 8.63      | 22.0  |
| 8                     | 0.254   | 24.74                | 5.81                 | 10.06     | 21.2  |
| 9                     | 0.242   | 25.95                | 6.09                 | 10.55     | 27.0  |
| 10                    | 0.213   | 29.47                | 6.91                 | 11.96     | 25.5  |
| 11                    | 0.204   | 30.80                | 7.23                 | 12.52     | 32.0  |
| 12                    | 0.183   | 34.22                | 8.06                 | 13.95     | 29.8  |

4.1.1 In-plane tilt of the molecules with respect to the  $a$ -direction

**Figure 4-4**  $d$ -spacing for even and odd chain length amides plotted against chain length

Figure 4-4 shows that the  $d$ -spacing for the lowest angle peak for even and odd chain length amides increases linearly with carbon number. The slope of the straight line passing through all the points for the even amides is  $2.377 \text{ \AA}$  and that for the odd amides is  $2.330 \text{ \AA}$ . If we consider the C-C bond length as  $1.54 \text{ \AA}$  and the C-C-C bond angle as  $114^\circ$  [6], the increment in molecule length as we increase the chain length by two carbons would be  $2.580 \text{ \AA}$ . If the molecular axis and the  $a$ -axis of the unit cell are exactly parallel then the unit cell should also increase by the same amount. The fact that the slope is lower than this indicates that the adsorbed molecule is oriented such that its long chain is inclined at an angle ( $\alpha$ ) to the  $a$ -direction in the graphite plane. The ratio  $2.377/2.580 = \cos \alpha$  shows that the tilt angle  $\alpha$  of the molecular axis to the unit cell  $a$ -direction (illustrated in Figure 4-5) is around  $22\text{-}25^\circ$  for both types of saturated amides. This information can be useful in constraining the full structural solution, as will be discussed later in this chapter.

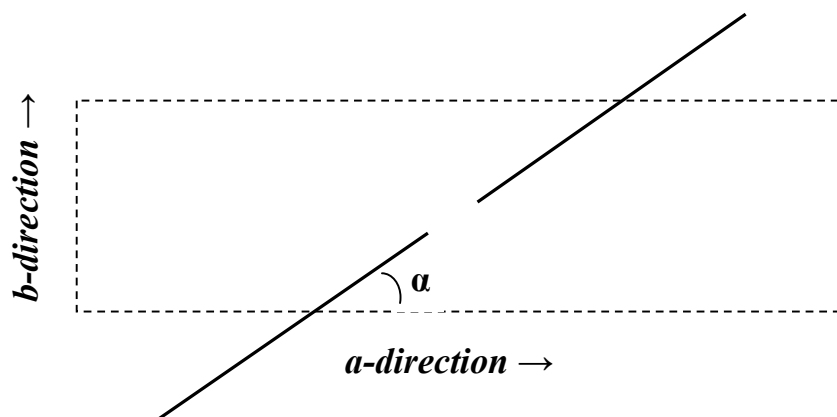


**Figure 4-5** An illustration showing the tilt angle  $\alpha$  of the molecules w.r.t the  $a$ -direction in the graphite plane. The unit cell is shown by the dotted box and the molecules are shown by solid lines

#### 4.1.2 Commensurate monolayers

Addressing the commensurate nature of the solid monolayer using diffraction data requires the identification of any integer related periodicities of the overlayer and the substrate. The most important graphite periodicities are close-to integer multiples of  $a_g$  ( $=2.46 \text{ \AA}$ ) and  $\sqrt{3} a_g$  ( $=4.26 \text{ \AA}$ ), where  $a_g$  is the lattice parameter of the underlying graphite.

The  $d$ -spacings (tabulated in Table 4-1) of the amides C10:0 and C12:0 are indeed identified as close to integral multiples of  $4.26 \text{ \AA}$  ( $n * \sqrt{3} a_g$  with  $n = 7$  and  $8$  respectively) suggesting these amides may be commensurate with the underlying graphite. The odd chain length amides C5:0, C7:0 and C9:0 also appear to be commensurate, with  $n=4, 5$  and  $6$  respectively. On the other hand, C6:0, C8:0, C10:0 and C12:0 amides may also be commensurate with the underlying graphite in a different direction, as the ratios of their  $d$ -spacings to  $a_g$  are approximately integers. However, these conclusions should be treated with caution, as the related periodicities may be coincidental. This kind of powder diffraction cannot unambiguously identify commensurate overlayers but simply a matching periodicity.

## 4.2 Monolayer structure fitting

The amide monolayers have been ‘fitted’ by calculating diffraction patterns of trial structures till satisfactory match is obtained with experimental data, as explained in chapter 2.



**Figure 4-6** Bond lengths and angles for generating an amide molecule for fitting

Due to the presence of only a few reflections in the experimental diffraction patterns, only a limited number of structural parameters can be realistically extracted from the data. Hence the solution is constrained as much as possible by assuming that the molecular bond lengths and angles are the same as those of the bulk crystal. Figure 4-6 shows the bond lengths and angles for an amide molecule used for fitting throughout this work. These have been taken from [6], where the head group bond lengths and angles correspond to that from the gas phase molecule, and for the alkyl tail are typical alkane values. These bond values were refined ( $\pm 3\%$ ) in the final structural solution in accord with bulk observations.

An important constraint is the symmetry of the crystal structure. The molecules were initially indexed to a rectangular unit cell before moving to oblique unit cells if solutions were not found. Assuming one of the possible close-packed symmetries for a two-dimensional unit cell ( $p2$ ,  $pgg$ ,  $pmg$  or  $cm$ ) [7-9], the unit cell parameters can be extracted from the experimental diffraction patterns. Systematic absences were also considered when determining the plane group of the layers.

Another constraint for the amide monolayers, is maintaining optimal hydrogen bonding within the amide dimers and between dimers (§4.3), as is observed in the bulk (3D) crystals [10]. Thus, the most probable symmetries for a hydrogen-bonded dimer are either  $p2$  or  $pgg$ . Other

symmetries which did not have a close-packed structure or optimal hydrogen bonds were also considered, but these did not fit the diffraction patterns and so will not be discussed further. For the initial structural solution these hydrogen bond lengths and angles were kept the same as the bulk; only in the final refinement were they allowed to vary by a small amount.

Some of the fitting parameters used for determining the 2D structures of the alkyl amides were described in chapter 2. The remaining adjustable parameters for each molecule are the size of the unit cell, the molecular positions (in  $x$  and  $y$ ), the in-plane tilt of the molecules w.r.t the  $a$ -axis (discussed in §4.1.1) and rotation of the molecules about their respective molecular axes.

The structure of stearoyl amide (C18:0) adsorbed on graphite [11] as discussed in chapter 1 was used as an initial trial structure to fit the amides. The unit cell, approximately extracted from the STM image was used as an estimate for other homologous amides, after appropriate consideration of the alkyl chain length. The STM structure reports the length of the unit cell ( $a$ -parameter) as approximately 50 Å and the side-to-side packing distance ( $b$ -parameter) of about 4.8 Å. The structures calculated from the diffraction patterns essentially agree qualitatively with the STM molecular arrangement; however, as will be discussed here, diffraction permits structural characterisation to much greater detail than that obtainable by microscopy.

In the next few sections, the structural fits of each saturated alkyl amide will be discussed separately, and the sensitivities of the structural solution analysed by varying some of the key parameters of the fit. These parameters have been varied for all the amides, but are only discussed in detail individually for specific cases. By imposing the constraints discussed above, there are essentially no degrees of freedom available to the molecules as they adsorb on the substrate, as regards to the unit cell, distances between the molecules and rotation angle w.r.t the  $a$ -axis.

In order to quantitatively define the ‘goodness’ of the fits, ‘R-values’ were estimated by comparing observed intensities ( $I$ ) to calculated intensities [12]:

$$R = \frac{\sum |I_{obs}^{1/2} - I_{calc}^{1/2}|}{\sum |I_{obs}^{1/2}|}$$

... Eqn. 4-1

Here, the summation is for all the peaks (h,k) that have been fitted. Thus, the quality of the fit can be seen to improve as the R-value approaches zero. Based on values reported in literature [12-15], if the R-value of the fit is 0.20 or less, then the fit can be considered to be reasonable.

### 4.3 Hydrogen bond geometry

Hydrogen bond energies and geometry have been discussed previously in the introduction (§1.4). Specifically, for the amides, the energies of dimerisation on forming a hydrogen-bond in solution for various amides fall between 10-20 kJ/mol [16, 17]. Van der Waals interaction energies for molecules in the adsorbed layers, reflected in the melting heats of alkanes, are typically 7 kJ/mol [18]. Hence it is expected that the stronger hydrogen bond should dictate the molecular structure on the surface.

In these amide layers there are two types of hydrogen bonds, ‘intra-dimer’ and ‘inter-dimer’ hydrogen bonds, as illustrated in Figure 4-7, i.e. within a single dimer and between adjacent dimers.

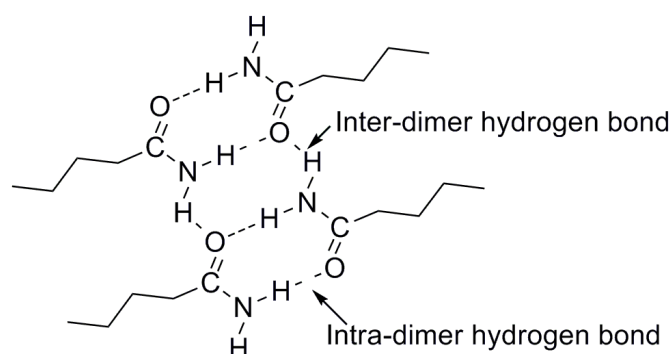


**Figure 4-7** Representative hydrogen bonds for the amides in the adsorbed layer

As explained in chapter 1, the optimal hydrogen bond for the N-H...O contact is achieved when the hydrogen bond is linear [10]. The N-H...O distance is in the range 2.70-3.00 Å for various

amides in the bulk crystals [19], with the bond angles typically  $170^{\circ}$ - $180^{\circ}$  [20]. The N-H...O angle in the inter-dimer bond is about  $120^{\circ}$ . This is a preferred geometry due to the position of the lone pairs on the oxygen atom, as seen in the bulk [10]. The hydrogen-bond parameters extracted from the diffraction patterns for the different saturated amides will be discussed in this chapter and compared to the idealised arrangements discussed above.

## 4.4 Even chain length amides

In this section experimental synchrotron X-ray and neutron diffraction patterns for saturated amides with an even number of carbon atoms (between six and sixteen carbons) in the alkyl chain are presented. Detailed structural analysis is performed for these amides and the monolayer structures are discussed.

### 4.4.1 Hexanamide (C6:0 amide)

Figure 4-8 presents the experimental X-ray and neutron diffraction patterns for C6:0 amide adsorbed on graphite, the calculated patterns and the proposed molecular structure. A good fit was indicated by the calculated R-values for the structure: 0.10 (X-ray fit) and 0.02 (neutron fit) (Table 4-2). The X-ray and neutron patterns were used in combination to solve the structure, since the position of the hydrogen atoms cannot be determined unambiguously by X-ray diffraction, as explained earlier. This is important here in where a focus is the study of the hydrogen bond characteristics. In order to resolve this issue, amides for which both X-ray and neutron patterns were measured were fitted first to the same structure, followed by those for which only the X-ray patterns were available, keeping the amide head group bond lengths and angles constant.

Refinements of the constrained fitting model used here indicate that the calculated structure does indeed consist of two amide molecules which form hydrogen bonds to make a dimer (Figure 4-8 (b)). It can be seen that the second hydrogen atom on nitrogen forms another hydrogen bond with a neighbouring dimer to yield two-dimensional chains, which pack parallel to each other. Hydrogen bond and unit cell parameters for all the amides will be summarised in Table 4-2 on page 4-20.

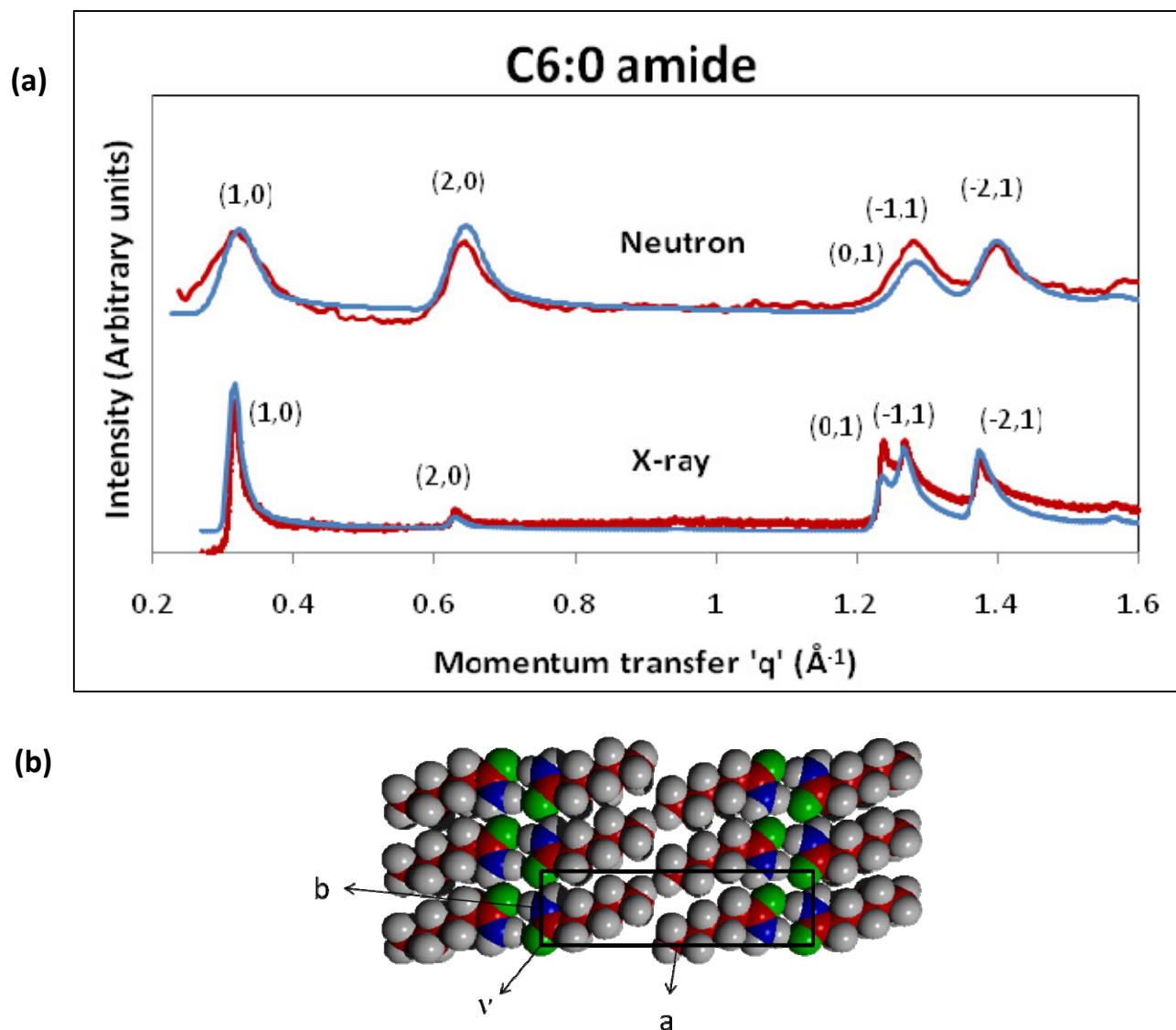


**Figure 4-8 (a)** Calculated (blue) and experimental (red) diffraction patterns from hexanamide adsorbed on graphite. The X-ray pattern measured at SLS was at a coverage of 0.48 monolayers at 300 K, while the neutron pattern was measured on D2O at a coverage of 0.8 monolayers at 10 K. **(b)** Molecular structure that fits the experimental diffraction pattern for C6:0 amide.  $a$  and  $b$  are the unit cell lengths and  $\nu$  is the angle between them. In the figure, the carbon atoms are shown as red, hydrogens as grey, nitrogen as blue and oxygen as green spheres.

Peaks of the same indices in X-ray and neutron patterns are not quite at the same position (Figure 4-8). This is because the patterns were measured at different temperatures and coverage of the amide. Thus the X-ray and neutron patterns were fitted to slightly different structures, although the overall hydrogen bond geometry was approximately maintained (Table 4-2). The unit cell of the neutron structure is compressed slightly in the  $a$ -direction ( $\sim 2\%$ ) since the neutron sample

was at a much lower temperature (10 K) and slightly higher coverage which supports the proposed molecular structure. These differences are similar to those reported previously for other hydrocarbons where an increase in coverage has been shown to result in a slight compression in the unit cell (see [5]). Experiments were performed at two different coverages to ensure that the measured data was from the sub-monolayer structure; not too close to the monolayer completion coverage which may be expected to lead to monolayer compression and structural changes. Both X-ray and neutron patterns possess the same reflections, although the (0,1) and (-1,1) peaks in the neutron pattern strongly overlap making individual peak analysis difficult.

#### 4.4.2 Octanamide (C8:0 amide)

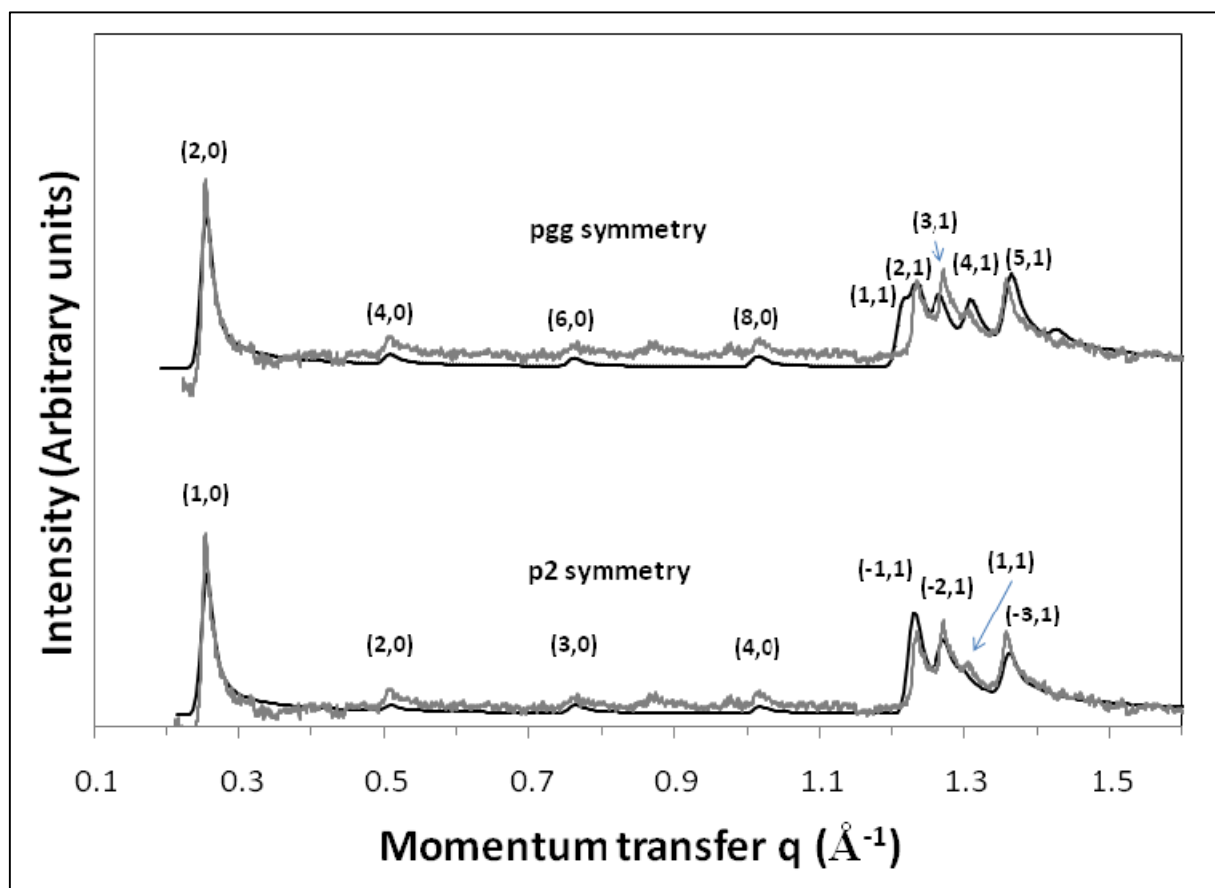
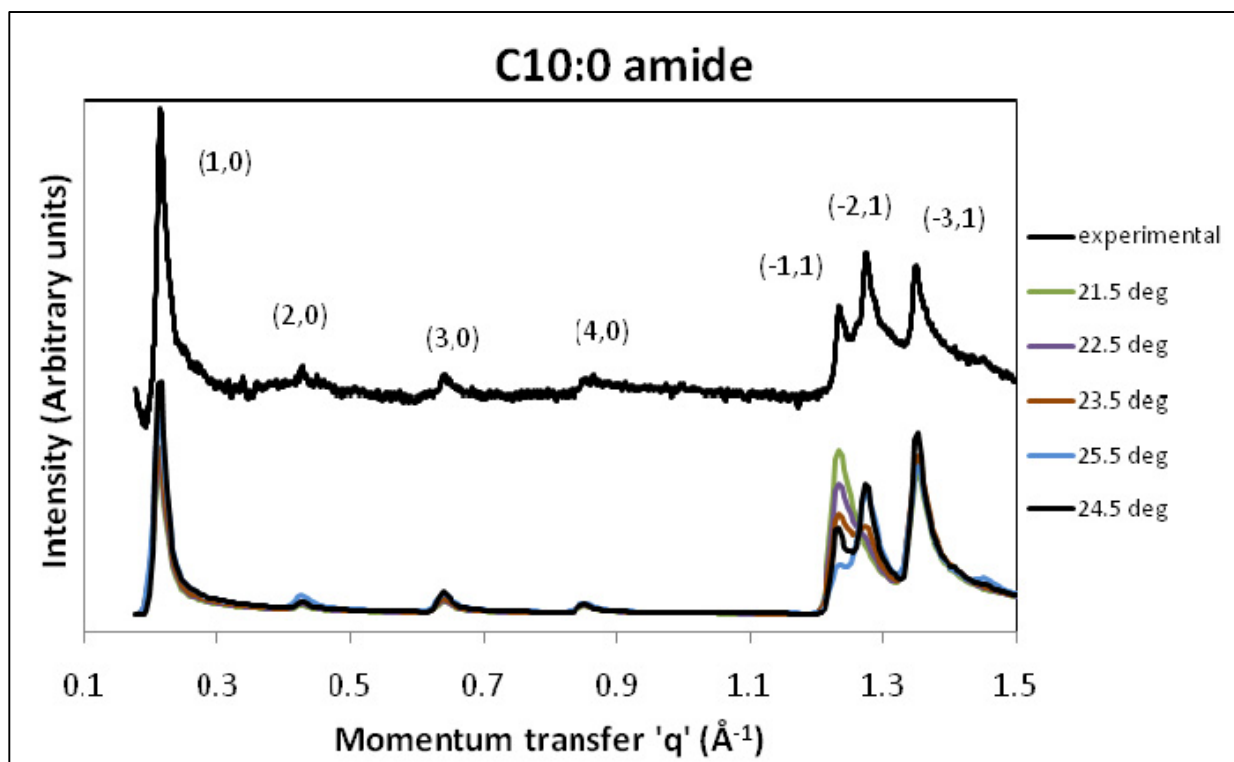


**Figure 4-9** Experimental (light) and calculated (dark) X-ray diffraction patterns from 0.63 monolayers of C8:0 amide adsorbed on graphite at 300 K measured at SLS. The fitted patterns along with the principal reflections for both symmetries are shown

The scattering patterns of octanamide (C8:0) along with calculated patterns of structures with *pgg* and *p2* symmetries are illustrated in Figure 4-9. The structure with *p2* symmetry shows

all the principal peaks in the correct positions with reasonably good intensities; however the unit cell is non-rectangular which is reflected in the deviation of the inter-dimer hydrogen bond from ideal values shown in Table 4-2 (ideal hydrogen bond geometries have been discussed in §4.3). On the other hand, the structure with *pgg* symmetry has a reasonably good fit to the experimental pattern, however, it does not have all the principal peaks in quite the correct positions and also has an extra ‘shoulder’ to the peak at  $1.25 \text{ \AA}^{-1}$ . Considering all the peak positions and intensities the structure with *p2* symmetry is found to be the best fit for this amide, and has an R-value of 0.14 (Table 4-2). For the rest of the amides one structure was found to fit better than all others unambiguously.

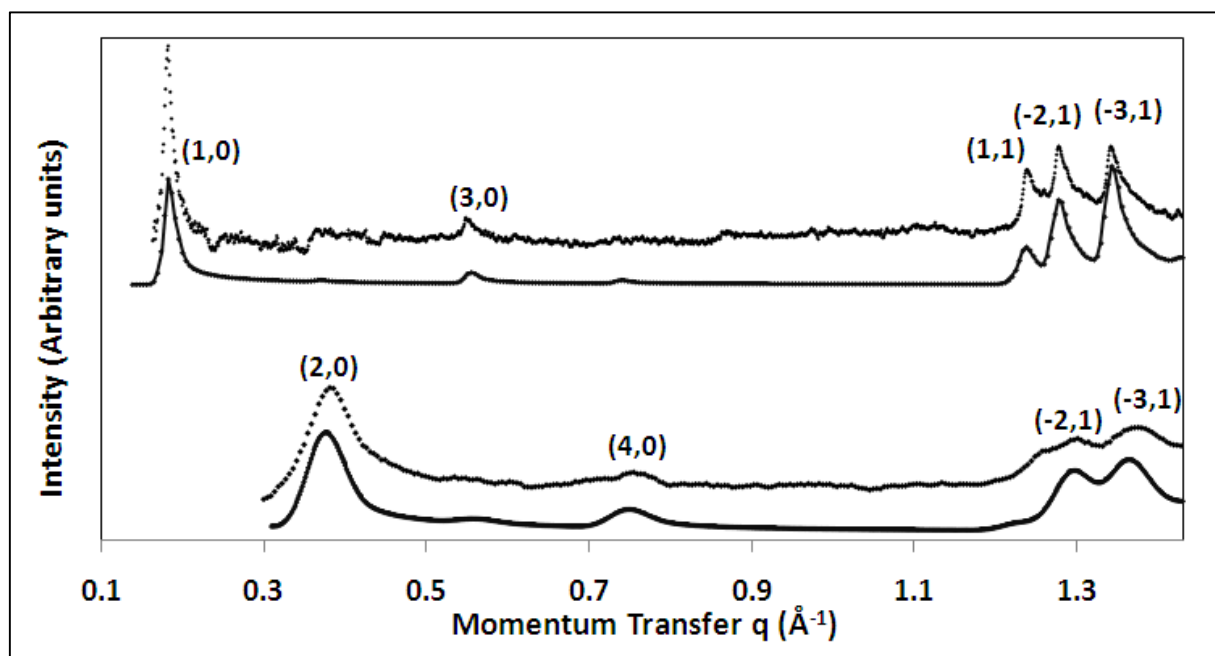
#### 4.4.3 Decanamide (C10:0 amide)



**Figure 4-10** Calculated X-ray diffraction patterns for decanamide with varying molecular tilts w.r.t the *a*-direction of the unit cell. Best match (black line) with the experimental pattern is obtained for a tilt of  $24.5^\circ$  for this molecule (coverage is 0.5 monolayers). The structural parameters and hydrogen bond values are listed in Table 4-2. The experimental pattern was measured at 300 K at a coverage of 0.65 monolayers. The R-value for the best fit was calculated to be 0.12.

The calculated diffraction patterns for all the amides studied here are very sensitive to rotation of the molecule in the graphite plane (Figure 4-5) with error estimates of  $0.5\text{-}1^\circ$  for all the fits. Figure 4-10 shows the variation in the calculated pattern of decanamide with the tilt of the molecules w.r.t. the unit cell  $a$ -axis (Figure 4-5). The  $(-1,1)$  reflection is particularly sensitive to the rotation in this case, as can be seen from Figure 4-10. The structure is isomorphic with hexanamide monolayer (Figure 4-8) with  $p2$  symmetry and hydrogen bonded dimers. The geometries of both the intra-dimer and inter-dimer hydrogen bonds are very sensitive to this rotation angle, and to maintain favourable arrangements the rotation angle is limited to  $21\text{-}25^\circ$ .

#### 4.4.4 Dodecanamide (C12:0 amide)



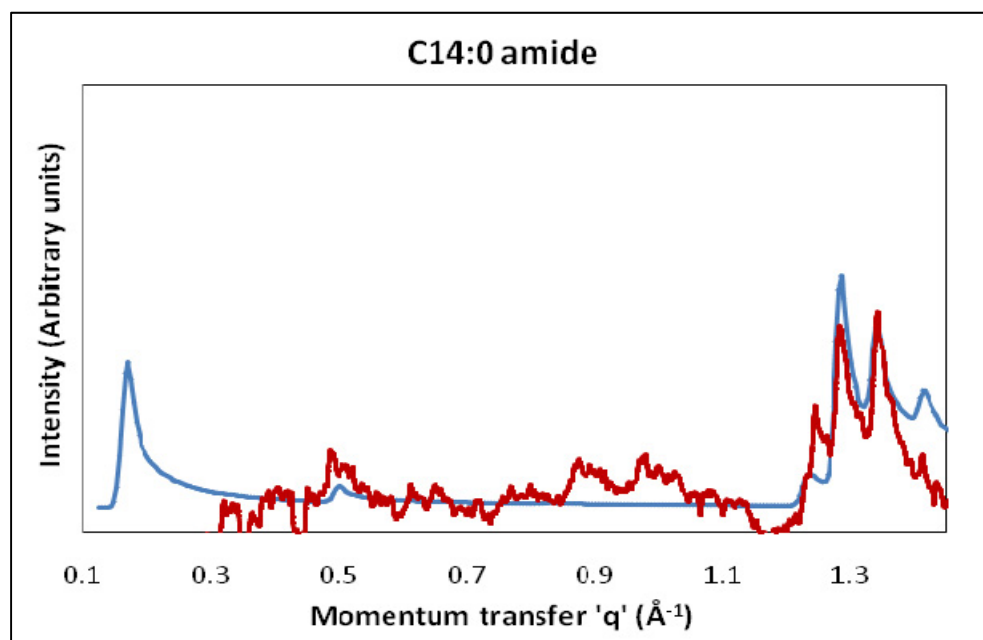
**Figure 4-11** X-ray (top) and neutron (bottom) diffraction patterns (0.57 monolayers and 0.86 monolayers respectively) and their fits for dodecanamide on graphite. The solid lines represent the calculated patterns, and the broken points represent the experimental patterns. The indexing of the principal reflections has been indicated and the parameters relevant to the fit are listed in Table 4-2.

Figure 4-11 presents the experimental and calculated X-ray and neutron diffraction pattern from dodecanamide adsorbed on the surface of graphite. The structure is isomorphic with that of C6:0 amide (Figure 4-8). The R-values for both fits are 0.03 (X-ray) and 0.05 (neutron) (Table 4-2).

Similar to C6:0 amide, the peak positions in the X-ray and neutron data are not exactly at same position. This is attributed to the difference in temperature and coverage between the two

patterns: neutron at 0.8 monolayers (10 K) and X-ray at 0.5 monolayers (300 K). Hence the X-ray and neutron data have been fitted independently to slightly different unit cells while preserving the hydrogen-bonding within and between the dimers.

#### 4.4.5 Tetradecanamide (C14:0 amide) and hexadecanamide (C16:0 amide)



**Figure 4-12** Experimental (red) and calculated (blue) X-ray diffraction patterns for tetradecanamide adsorbed on graphite

Figure 4-12 and Figure 4-13 show fitted diffraction patterns for the amides C14:0 (X-ray data) and C16:0 (neutron data) on graphite respectively. The low angle (1,0) reflection for both these amides cannot be seen due to the long chain length of these molecules as discussed in chapter 2. Data for C14:0 amide is particularly noisy due to the beam time limitations in collecting synchrotron X-ray patterns, where only a short counting time was permitted for this sample. For C16:0 amide, the peaks strongly overlap making individual peaks analysis difficult. This makes the estimation of the *b*-parameter (side to side packing distance) difficult for C16:0 amide and the value found ( $4.9 \pm 0.15 \text{ \AA}$ ) is smaller than that for other even amides ( $5.1\text{-}5.2 \text{ \AA}$ ). This in turn makes the estimation of the inter-dimer hydrogen bond properties more difficult (Table 4-2). A tentative structural assignment for these molecules given the quality of data available suggests

that an isomorphic  $p2$  symmetry structure for C14:0 and C16:0 amides fits with the experimental data.

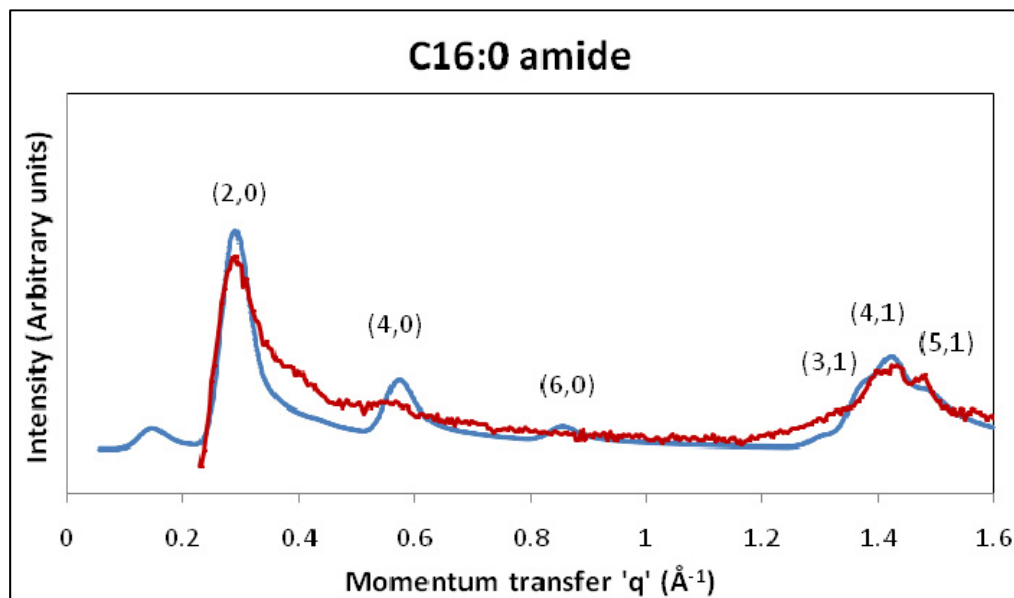


**Figure 4-13** Experimental (red) and calculated (blue) neutron diffraction patterns for 0.8 monolayers of hexadecanamide adsorbed on graphite at 12 K measured on D20

#### 4.4.6 Discussion

Very high quality structural fits of the calculated and experimental diffraction patterns could be found for the even chain length amides with isomorphic  $p2$  symmetry structures. The molecules are all found to lie flat with their molecular axis parallel to the graphite surface. The unit cells are either rectangular or very close to rectangular, with lengths comparable to that of the extended alkyl chain. The fact that the same structure fits both X-ray and neutron diffraction patterns of C6:0 and C12:0 amides, combined with the result that all the even chain length amides discussed here fit with an isomorphic structure, lends weight to the solution. In addition, the highly constrained nature of the fitted structure also supports the solution.

Table 4-2 below summarises the parameters used to fit the diffraction patterns and the hydrogen bond properties calculated from the fitted structures. The unit cell parameters reported here are estimated to be accurate up to 0.3 Å ( $a$ ), 0.05 Å ( $b$ ) and 1° ( $\nu$ , tilt). Exact coverages (monolayers) of the samples calculated from the area per molecule in the unit cell are also shown. Fractional

coordinates for each of the atoms of the molecule which is present in the asymmetric unit are listed in appendix A.

Refinements of the constrained fitting model show that the amide monolayers do indeed form hydrogen bonds as observed in their bulk structures. Pairs of molecules form dimers which can then, due to the additional hydrogen on the nitrogen atom, form further hydrogen bonds with neighbouring dimers to yield extended chains in two dimensions. The hydrogen bonds within the dimer ('intra-dimer' hydrogen bond) calculated for the two-dimensional structures here are all approximately linear and agree very well with the bulk crystals (Table 4-2 below and Table 4-3 on page 4-28). The hydrogen-bond distances reported here are estimated to be accurate up to 0.05 Å and angles up to 4°. There are additional pairs of hydrogen bonds between dimers - 'inter-dimer' hydrogen bonds. The N...O distance for both types of hydrogen bonds compare very well with bulk values. Details of the hydrogen bonds in amide monolayers have been discussed in §4.3 and chapter 1.

It is thus evident that the adsorbed layer is similar to the bulk crystal. This could suggest that the amide bulk crystal could be expected to grow in a layer-by-layer fashion. Many adsorbed alcohols show a similar behaviour, with the formation of multi-layers close to the bulk melting point [21]. This is an important issue, and the formation of additional layers above a monolayer will be investigated in the coverage dependent study of C11:0 amide (chapter 6).

**Table 4-2** Structural parameters and hydrogen bond values for even amides adsorbed on graphite. All even amides have a  $p2$  symmetry structure with two molecules per unit cell.

| Amide                      | Pattern fitted | Unit cell parameters |       |       | Molecular tilt (°) | R-value <sup>+</sup> | Exact coverage | Intra-dimer hydrogen bond |                  | Inter-dimer hydrogen bond |                  |
|----------------------------|----------------|----------------------|-------|-------|--------------------|----------------------|----------------|---------------------------|------------------|---------------------------|------------------|
|                            |                | a (Å)                | b (Å) | v (°) |                    |                      |                | Angle N-H...O (°)         | Length N...O (Å) | Angle N-H...O (°)         | Length N...O (Å) |
| <b>C6:0</b>                | X-ray          | 20.1                 | 5.11  | 91.0  | 23.25              | 0.10                 | 0.48           | 180                       | 3.00             | 120                       | 2.92             |
| <b>C6:0</b>                | neutron        | 19.7                 | 5.08  | 90.0  | 24.50              | 0.02                 | n/a            | 177                       | 3.00             | 124                       | 2.91             |
| <b>C8:0*</b><br><i>p2</i>  | X-ray          | 25.0                 | 5.13  | 98.0  | 23.00              | 0.14                 | 0.63           | 178                       | 2.87             | 106                       | 3.09             |
| <b>C8:0*</b><br><i>pgg</i> | X-ray          | 49.7                 | 5.21  | 90.0  | 21.50              | -                    | -              | 178                       | 2.98             | 119                       | 3.07             |
| <b>C10:0</b>               | X-ray          | 29.7                 | 5.15  | 93.0  | 24.50              | 0.12                 | 0.65           | 176                       | 2.90             | 119                       | 3.00             |
| <b>C12:0</b>               | X-ray          | 34.0                 | 5.15  | 90.0  | 22.40              | 0.03                 | 0.57           | 177                       | 2.94             | 120                       | 3.00             |
| <b>C12:0</b>               | neutron        | 33.9                 | 5.12  | 91.7  | 23.60              | 0.05                 | 0.86           | 178                       | 3.03             | 119                       | 2.97             |
| <b>C14:0</b>               | X-ray          | 38.0                 | 5.12  | 88.5  | 21.00              | -                    | 0.53           | 179                       | 2.80             | 120                       | 2.97             |
| <b>C16:0</b>               | neutron        | 45.2                 | 4.92  | 88.0  | 23.50              | -                    | n/a            | 180                       | 3.05             | 124                       | 2.74             |

\*C8:0 amide is discussed in the text

+The R-value is not defined for the C8:0 amide *pgg* structure as the peaks positions of the calculated and experimental patterns do not coincide. The experimental data qualities for C14:0 and C16:0 amides do not permit an accurate R-value estimation.

The calculated diffraction patterns are found to be sensitive to changes in the in-plane tilt of the molecules w.r.t. the a-axis (discussed in §4.1.1) as shown by the diffraction patterns of C10:0 amide. The tilt angle is found to be between 21-25° for all the calculated structures of the saturated amides, in agreement with the stacking angle (23°) found in closed packed structures of alkyl species [22].

## 4.5 Odd chain length amides

In this section similar structural data on the odd chain length amides is presented. A structural analysis is performed and the details of these monolayers with those of the even amide monolayers presented above are compared.

## 4.5.1 Pentanamide (C5:0 amide)

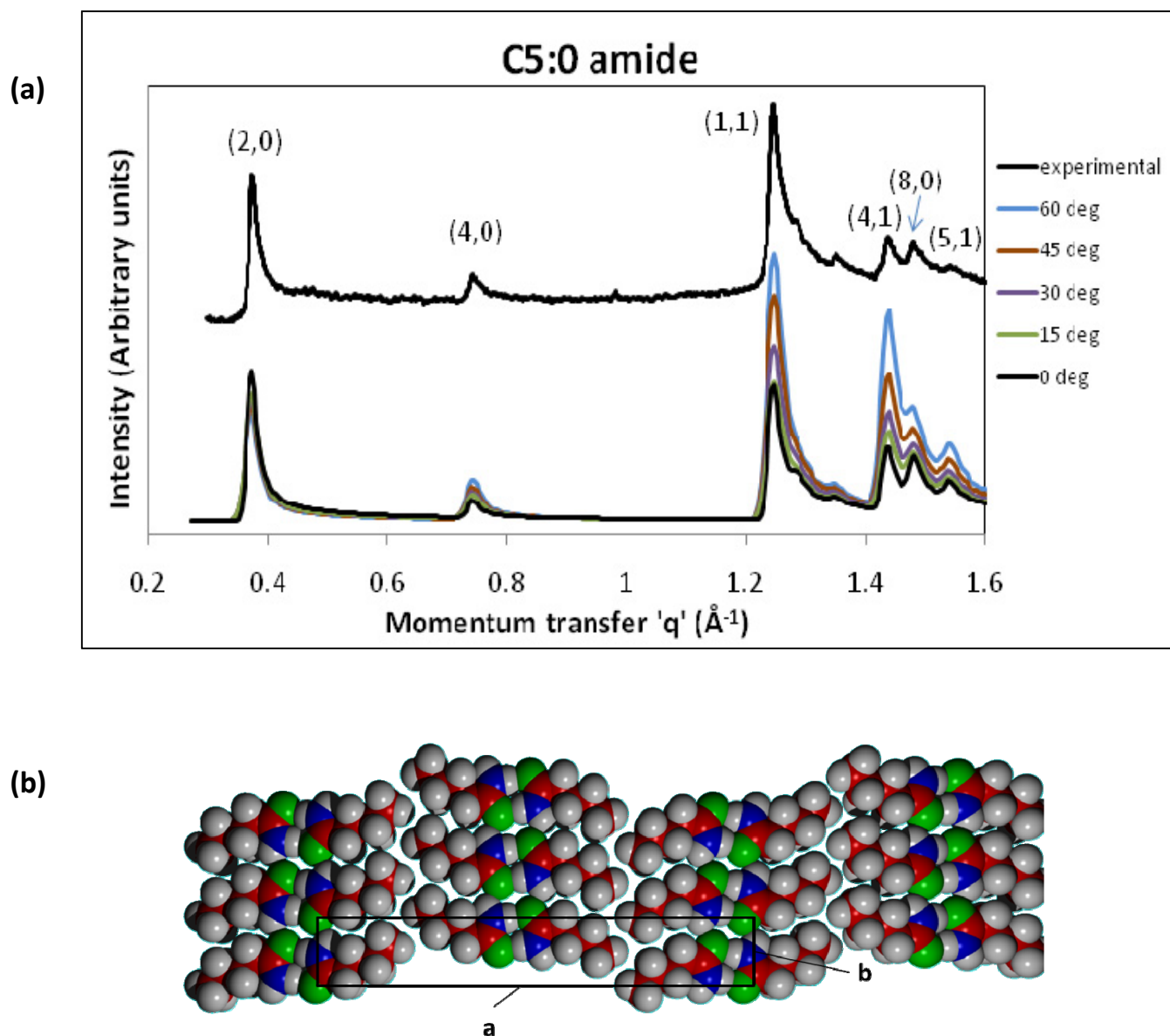


**Figure 4-14** (a) Calculated X-ray diffraction patterns for 0.5 monolayers of pentanamide with different rotations of the molecule about its own axis. The fits are not very sensitive to this axial rotation ( $\pm 20^\circ$ ). Best fit (black line) with the experimental pattern is obtained for a rotation angle of  $0^\circ$  i.e. with the C-C backbone parallel to the plane of the graphite. (b) Monolayer structure that fits the experimental pattern of C5:0 amide. The unit cell and its parameters are shown.

Figure 4-14 shows the calculated and experimental diffraction patterns for pentanamide adsorbed on graphite and the structure that fits the patterns. The molecular arrangement for this amide possesses a different symmetry ( $pgg$ ) as compared to the even amides ( $p2$ ). The structure still consists of optimal hydrogen bonded dimers and chains, but successive chains are now ‘flipped’

as compared to the  $p2$  symmetry case. The hydrogen bond geometry both within the dimer and between dimers and the structural parameters for the best fit of this molecule are shown in Table 4-3 on page 4-28. The difference in packing arrangement for the even and odd members of the series can be due to the presence of a ‘kink’ in the tail of the molecule for the odd members, which makes parallel packing of the chains ( $p2$  symmetry) difficult [23]. However, as will be discussed here, the effect of these forces can be quite subtle.

The calculated patterns for all the amide molecules studied here are not found to be sensitive to the rotation of the molecule about its axis ( $\pm 20^\circ$ ). Best fits are obtained for the plane of the adsorbed molecules lying parallel to the graphite plane, as shown for C5:0 amide in Figure 4-14 (the best fit has an R-value of 0.13, Table 4-3). Similar behaviour has been found for carboxylic acids [23], alkanes [7] and perfluoroalkanes [24] adsorbed on graphite. The (2,0) reflection in the calculated patterns is particularly insensitive to axial rotation while the (1,1) reflection changes in intensity as the molecules are increasingly tilted (Figure 4-14). This is because the arrangement of atoms (electron density) along the  $a$ -direction does not change considerably as the molecules are rotated along their axis as compared to that along the  $b$ -direction. In the case of C5:0 amide which is a relatively short molecule, the intensity of the (2,0) reflection is more reliable and can be used to compare with the intensity of the (1,1) peak to establish the preferred axial rotation.

#### 4.5.2 Heptanamide (C7:0 amide)

The experimental and calculated diffraction patterns of C7:0 amide are shown in Figure 4-15. Isomorphic to C5:0 amide, the low temperature phase of C7:0 amide monolayer has  $pgg$  symmetry at 300 K. The long unit cell for a structure with  $pgg$  symmetry (structural parameters listed in Table 4-3) is reflected by the presence of reflections with higher indices as shown in the figure. This amide, however, possesses an additional high temperature phase as explained below.

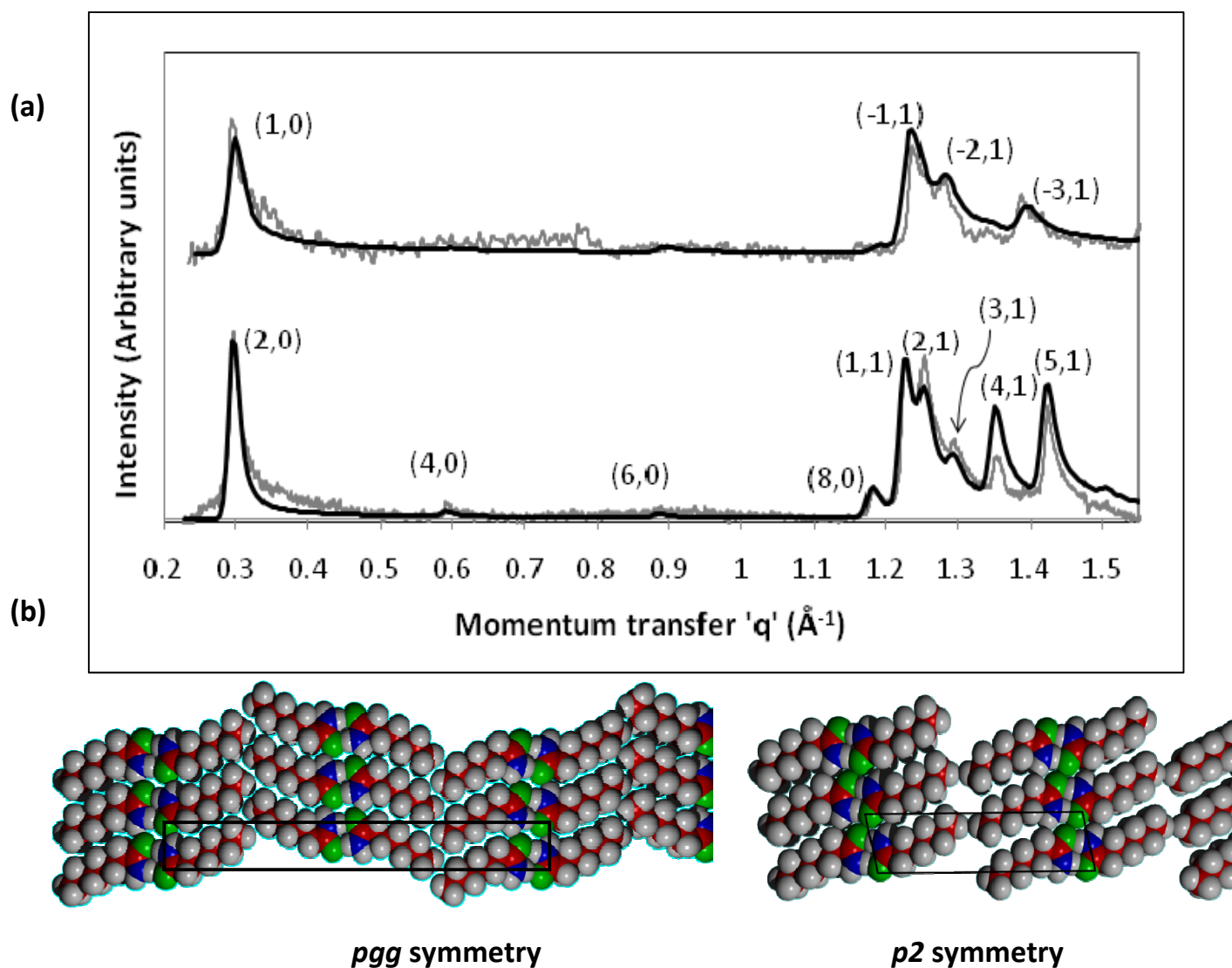


**Figure 4-15** (a) Experimental (light) and calculated (dark) X-ray diffraction patterns from 0.55 monolayers of C7:0 amide adsorbed on graphite. The patterns shown are from a *pgg* plane group at 300 K (bottom) and *p2* plane group at 355 K (top). The indices of the principal reflections are shown. (b) Packing arrangements for the low temperature phase (*pgg* symmetry) and high temperature phase (*p2* symmetry) for C7:0 amide. The unit cells are shown by the solid boxes. R-values are 0.07 (*p2* phase) and 0.10 (*pgg* phase).

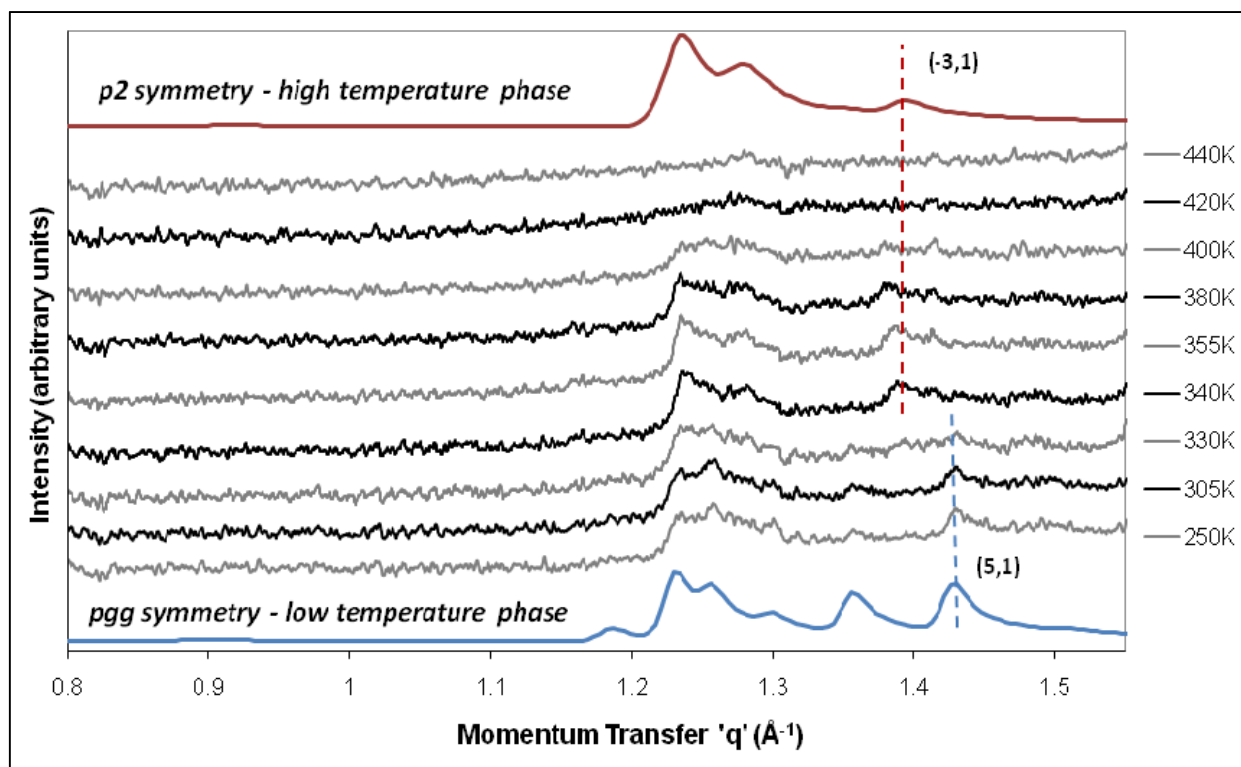


**Figure 4-16** X-ray diffraction patterns from 0.48 monolayers of C7:0 amide on graphite at different temperatures. The graph is shown only for the  $q$ -region that makes this phase change clearly noticeable. The calculated patterns of this amide with a  $pgg$  (blue) plane group which is the low temperature phase and a  $p2$  (red) plane group which is the high temperature phase are shown as solid lines. The vertical dotted lines illustrate the reflections that are most distinctly different in the two phases. The phase change is estimated to occur at 335 K.

Figure 4-16 shows diffraction patterns of C7:0 amide measured at different temperatures. At lower temperatures, the molecule exists in  $pgg$  symmetry packing and as the temperature is increased, the monolayer undergoes a phase change at  $\sim 330$  K to a  $p2$  symmetry phase. The structures and fitted patterns of both phases are shown in Figure 4-15. The vertical lines in Figure 4-16 indicate the reflections that make the phase change readily noticeable: the (5,1) reflection present in the  $pgg$  symmetry phase disappears and the (-3,1) reflection of the  $p2$  symmetry phase appears.

Data from the  $p2$  phase (Figure 4-15 (a)) has a small feature at  $0.75$ - $0.8 \text{ \AA}^{-1}$  which was present at all temperatures, even after the monolayer had completely melted. Hence this is not attributed to the monolayer diffraction and was not considered in the fitting procedure.

As the temperature is increased from 250 K, the molecules in the layer increasingly vibrate and the unit cell expands (1-2%) as can be seen in the slight shift of the patterns towards lower  $q$ -values above 340 K. As the temperature is increased further, the sharp diffraction peaks from the solid layer become increasingly broad till there remains effectively negligible intensity due to scattering from the liquid adsorbate as the monolayer melts [25]. The monolayer melting temperature is estimated at  $420 \pm 5$  K from the diffraction patterns, which, importantly, is considerably higher than the melting temperature of the bulk amide (358 K) [26]. This value compares with the monolayer melting point reported previously by DSC at high coverage of  $\sim 10$ -20 monolayers [26]. This is a very unusual phenomenon where the monolayer melts at a higher temperature than the bulk even at sub-monolayer coverage (17% higher), and has only been reported for alkyl amides studied here [27].

Other alkyl amides with similar chain lengths were also studied by X-ray and neutron diffraction, and these did not exhibit a similar phase change in their 2D layers at sub-monolayer coverage from 200 K up to their melting points (400-430 K).

Interestingly, the low angle peaks (not shown) do not change during the phase transition and it is only the higher angle region that gives an indication of the symmetry present in the structure. It is thus necessary to fit all the peaks up to the first graphite peak at the very least to be able to estimate the correct monolayer structure.

## 4.5.3 Nonanamide (C9:0 amide)

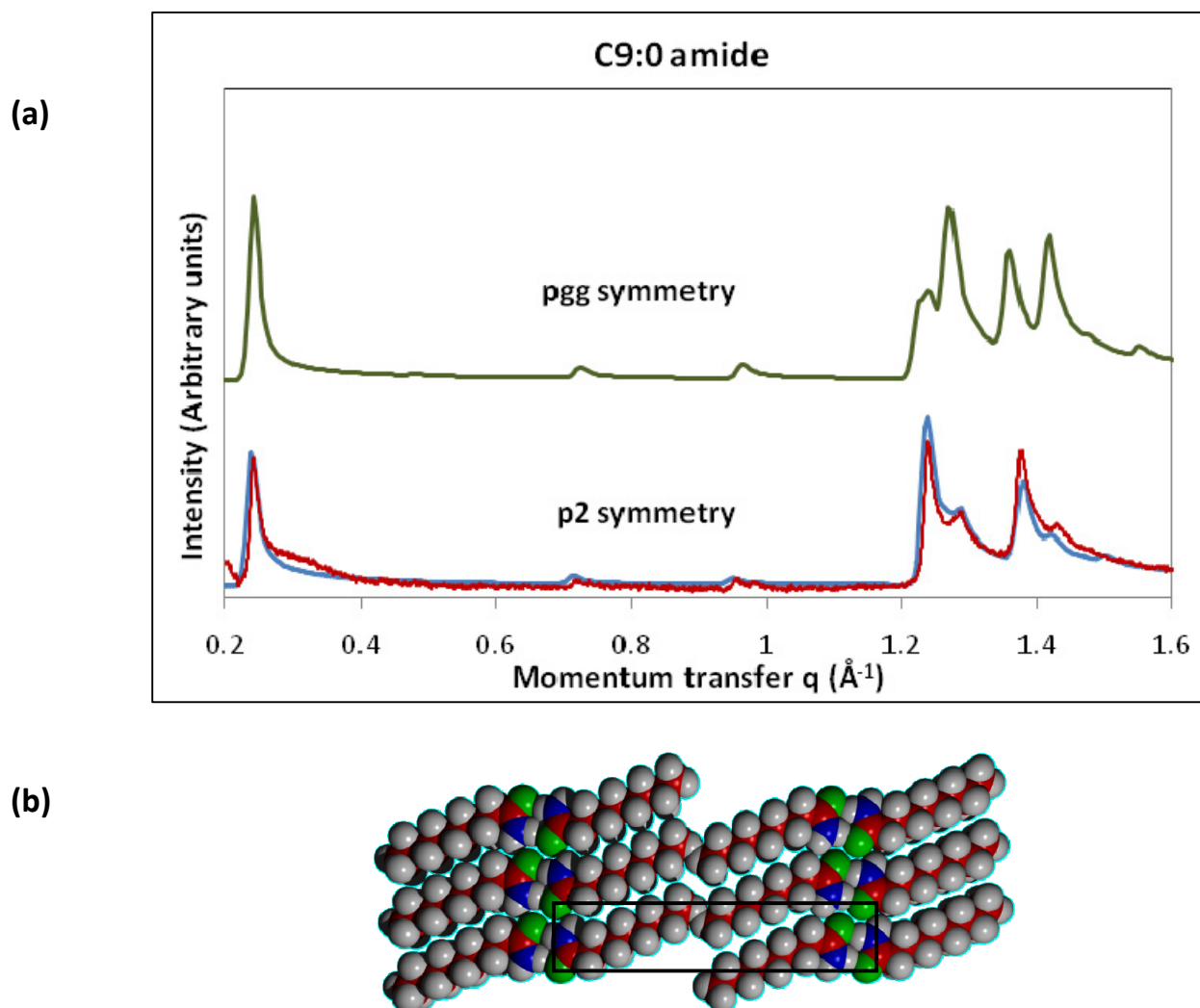


**Figure 4-17** Experimental (red) and calculated (blue) X-ray diffraction patterns from 0.49 monolayers of C9:0 amide adsorbed on graphite at 300 K. The fitted structure has  $p2$  symmetry. The calculated pattern for this amide having  $p2g$  symmetry is also shown (green) illustrating the difference in the structural fits. (b) Molecular arrangement in the  $p2$  symmetry phase for C9:0 amide. The unit cell is shown by the box.

The experimental diffraction pattern of C9:0 amide fits well with a structure having  $p2$  symmetry as shown in Figure 4-17 (R-value=0.08, Table 4-3). However, the data does not fit a  $p2g$  symmetry structure as shown in the figure. Diffraction patterns for this amide were measured as a function of temperature (from 200 K up to the melting point, not shown here) but these did not indicate any phase change in the monolayer at 0.49 monolayer coverage. The fitting parameters for the  $p2$  phase are listed in Table 4-3.

#### 4.5.4 Undecanamide (C11:0 amide)

The diffraction pattern for C11:0 amide fits to a  $p2$  symmetry structure (Figure 4-18), isomorphic to C9:0 amide (Figure 4-17 (b)). The variation of the calculated patterns by changing the intra-dimer hydrogen bond properties is shown in the figure. The best fit is obtained for an N-H...O distance of 2.86 Å and N-H...O angle of  $175^\circ$  (R-value of 0.18, Table 4-3). The diffraction patterns are very sensitive to this hydrogen bond geometry, and changing the N-H...O length has noticeable effects on the peak intensities. Also, making the bond slightly non-linear (N-H...O angle =  $165^\circ$ , red line in the figure) causes the peak intensity of the (-3,1) peak to deviate markedly from the experimental one.

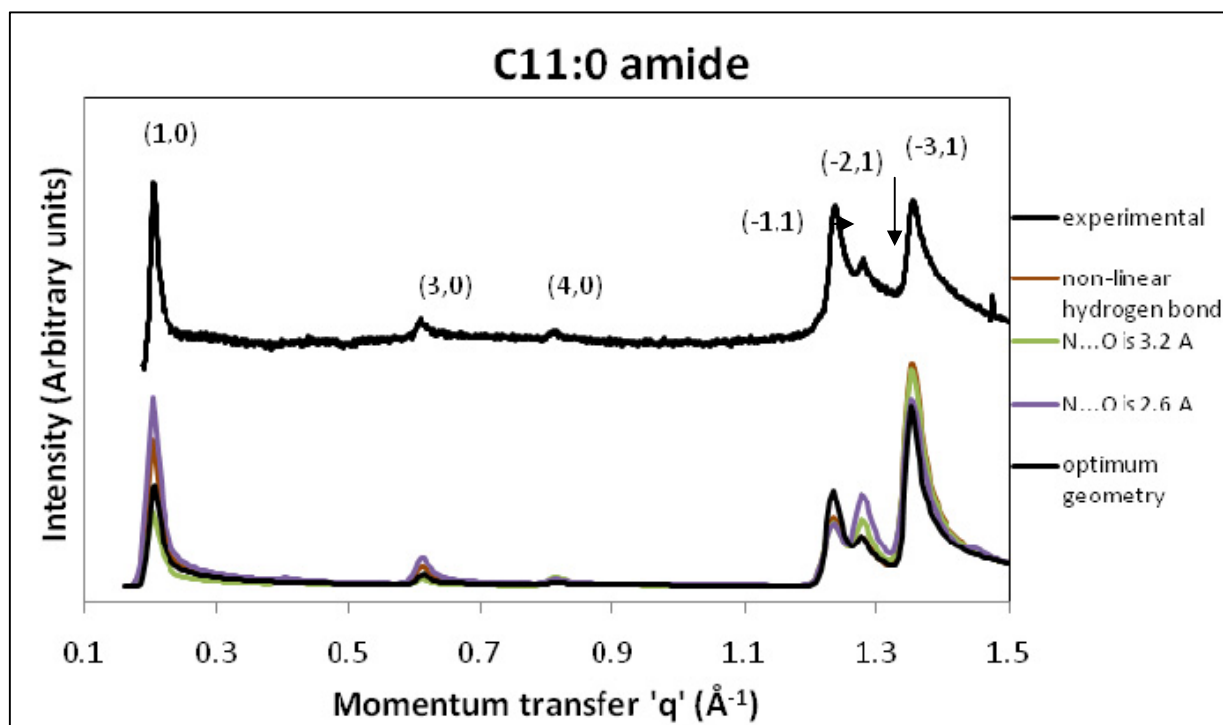


**Figure 4-18** Calculated X-ray diffraction patterns for 0.53 monolayers of C11:0 amide at 300 K. The effect of changing the geometry of the intra-dimer hydrogen bond on the calculated patterns is shown.

#### 4.5.5 Discussion

High quality structural data for odd chain length amides has been presented in this section. The unit cells for the odd amides are found to be rectangular or close to rectangular ( $pgg$  symmetry dictates that the unit cell be exactly rectangular). Table 4-3 provides a summary of structural

parameters used to fit the diffraction patterns of the odd amides and the hydrogen bond properties calculated from the fitted patterns. Exact coverages (monolayers) of the samples calculated from the area per molecule in the unit cell are also listed, and fractional coordinates of the molecules are tabulated in appendix A.

**Table 4-3** Structural parameters and hydrogen bond values for odd amides adsorbed on graphite as measured by X-ray diffraction. There are 2 molecules per unit cell ( $p2$  symmetry) and 4 molecules per unit cell ( $pgg$  symmetry).

| Amide        | R-value | Unit cell parameters |       |              | Molec-ular tilt (°) | Symm-etry       | Exact cover-age | Intra-dimer hydrogen bond |                  | Inter-dimer hydrogen bond |                  |
|--------------|---------|----------------------|-------|--------------|---------------------|-----------------|-----------------|---------------------------|------------------|---------------------------|------------------|
|              |         | a (Å)                | b (Å) | $\gamma$ (°) |                     |                 |                 | Angle N-H...O (°)         | Length N...O (Å) | Angle N-H...O (°)         | Length N...O (Å) |
| <b>C5:0</b>  | 0.13    | 34.0                 | 5.12  | 90.0         | 23.50               | $pgg$           | 0.51            | 175                       | 2.95             | 122                       | 2.95             |
| <b>C7:0</b>  | 0.10    | 42.7                 | 5.17  | 90.0         | 23.50               | $pgg$<br>(300K) | 0.48            | 176                       | 2.95             | 123                       | 3.00             |
| <b>C7:0</b>  | 0.07    | 21.9                 | 5.11  | 101          | 24.75               | $p2$<br>(340K)  | 0.48            | 178                       | 2.67             | 103                       | 3.10             |
| <b>C9:0</b>  | 0.08    | 26.4                 | 5.13  | 94.0         | 22.25               | $p2$            | 0.49            | 172                       | 2.93             | 113                       | 3.04             |
| <b>C11:0</b> | 0.18    | 31.0                 | 5.17  | 91.0         | 22.25               | $p2$            | 0.53            | 175                       | 2.86             | 118                       | 3.03             |

The diffraction results presented in this section show that all the alkyl amides with even chain length possess  $p2$  symmetry as do those with odd chain length C9:0 and longer. However, alkyl amides C5:0 and the low temperature form of C7:0 both possess  $pgg$  symmetry. In the case of C7:0 amide there is evidence of a phase change: a  $pgg$  symmetry low temperature phase transforms into a  $p2$  symmetry high temperature phase before the monolayer melts. Which of the two packing arrangements is adopted by the amides seems to be subtly dependent on the alkyl chain length.

In many alkyl species, packing arrangements for odd and even homologues are different: a difference attributed to the packing of methyl groups at the end of the molecule. Carboxylic acids exhibit an odd-even effect where odd chain-length members of the series possess structures with  $pgg$  symmetry and even members have  $p2$  symmetry [23]. Interestingly in the case of the alkanes on graphite, odd chain-length molecules have a  $cm$  plane group; the shorter *even* alkanes (chain

length  $< 12$ ) adopt the  $pgg$  structure, with the longer even ones reverting to a centred unit cell [2, 5].

The diffraction results of C5:0 amide indicate that the patterns are not sensitive to the rotation of the molecule about its molecular axis, and best fits are found for the C-C-C backbone lying parallel to the graphite plane for all the amides in this work. A structural analysis of C11:0 amide shows that the calculated diffraction patterns are very sensitive to the hydrogen bond geometry, where poor fits to the experimental data are found for the geometry deviating from the idealised arrangement.

It is interesting to see that the side-to-side packing ( $b$ -parameter) of the dimers does not change with increasing chain length, and the unit cell becomes longer only in the  $a$ -direction as the number of carbons is increased for all carbon chain lengths (Table 4-2 and Table 4-3). This implies that the hydrogen bond geometry for both types of hydrogen bonds is essentially the same as the chain length of the carbon atoms is changed.

## 4.6 Melting of the solid monolayers

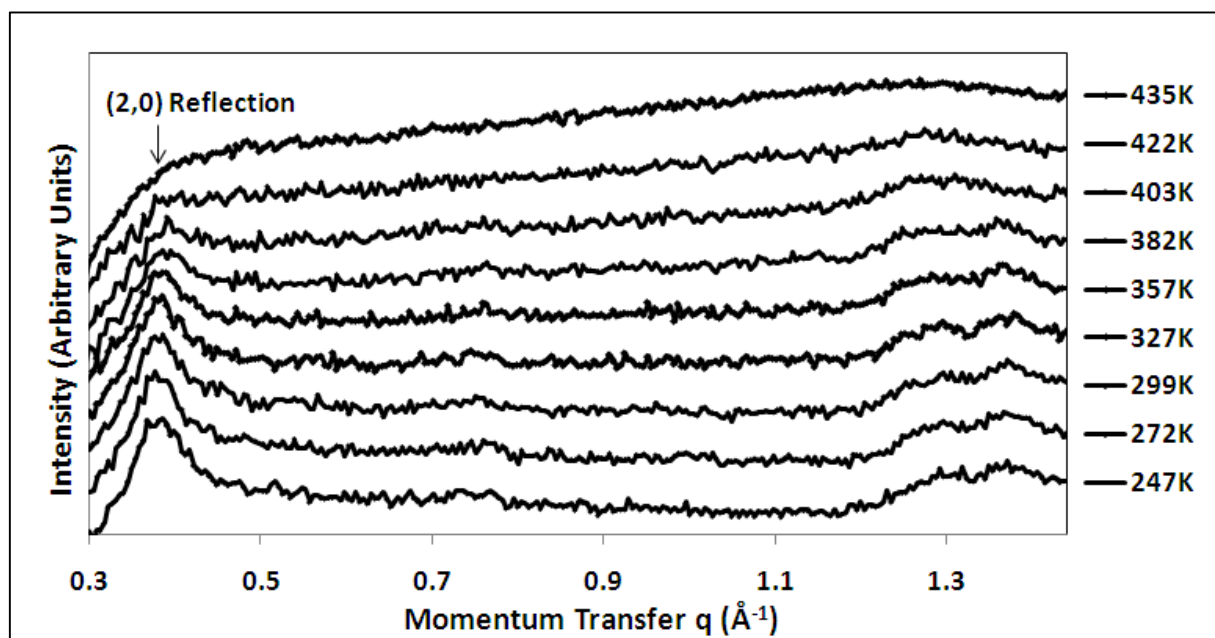


**Figure 4-19** Melting of 0.8 monolayers of C12:0 amide as observed by neutron diffraction on the instrument D20 at ILL

By observing diffraction patterns as a function of temperature, the melting point of the monolayer can be determined with well-defined sharp peaks corresponding to the solid phase becoming much broader peaks typical of a liquid [25] (see, for example, neutron diffraction patterns of dodecanol on graphite [28]). Figure 4-19 shows the variation of the diffraction patterns of dodecanamide at sub-monolayer coverage as the temperature approaches the monolayer melting point. By plotting the peak height of any chosen reflection with temperature and noting the temperature where the peak intensity stops decreasing relative to a baseline, the melting temperature of the monolayer can be estimated. This procedure is explained by plotting the peak height of the (2,0) reflection of C12:0 amide in Figure 4-20.

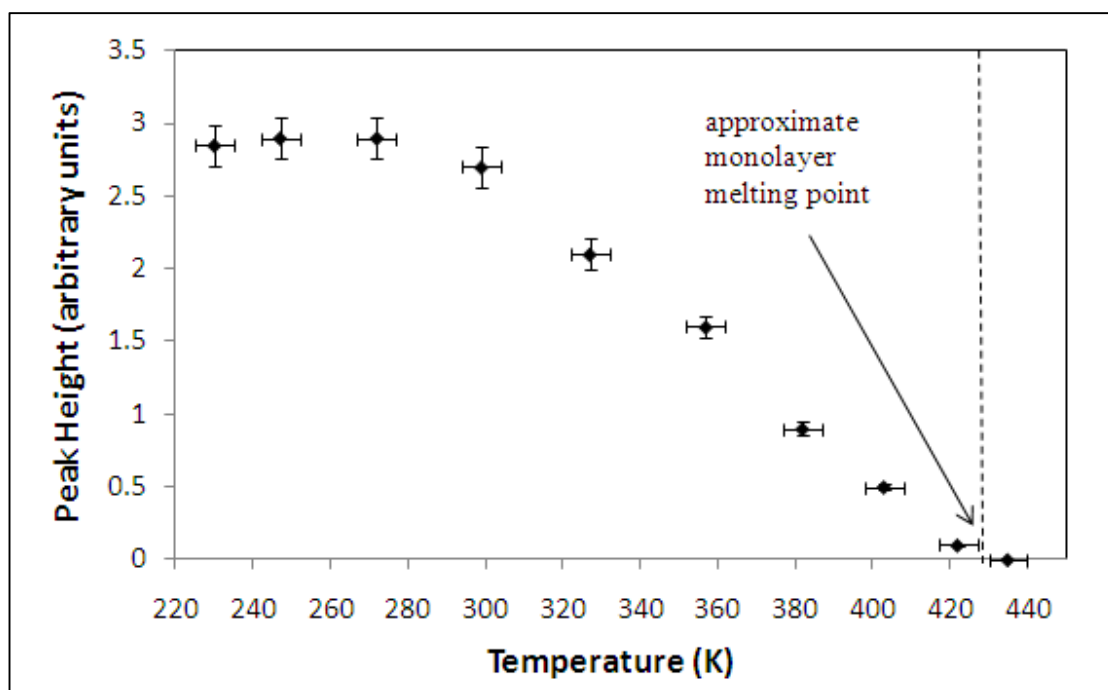


**Figure 4-20** A plot of the (2,0) peak height with temperature for the monolayer of C12:0 amide illustrating the procedure used to estimate the melting point. The monolayer melting temperature shown by the dotted lines is estimated at 428 K. The error bars reflect the approximate error in the temperature ( $\pm 5$  K) and peak height measurement as explained in the text.

The presence of a thermal lag between the cryo-jet and the sample induces some error in the temperature readings. The temperatures noted during the measurement are of the cryostat, and the actual temperature at which the sample is at may be lower as the cryo-stream temperature is ramped up. This thermal lag was reduced as much as possible by taking small (10 K) temperature steps and allowing the sample to equilibrate at that temperature for a few minutes

before measuring the diffraction pattern. The error in temperature reported here is thus  $\pm 5$  K which is essentially the smallest step size of the temperature program.

The 2D melting point for dodecanamide is estimated to be  $428 \pm 5$  K (Figure 4-19). This is in good agreement with the value reported from calorimetric studies (429 K) [26]. Importantly this value is well above that of the pure bulk amide (375 K) [26]. Normally for alkyl species sub-monolayer melting occurs significantly below the usual bulk melting point; in general  $T^{2D}/T^{3D}$  (in Kelvin)  $\sim 0.75$  at sub-monolayer coverages. This is believed to be the first report of such solidification above the usual bulk melting temperature at sub-monolayer coverage which indicates that the amide monolayers are extremely stable. Similar pre-solidification is reported here for several alkyl amides as shown in Table 4-4, which compares the melting temperatures estimated by diffraction (sub-monolayer coverage) and calorimetry ( $\sim 5$ -10 monolayers coverage) (DSC results are presented in chapter 6).

**Table 4-4** A comparison of monolayer (2D) and bulk (3D) melting points (T) as measured by DSC and diffraction. The DSC samples are at an approximate coverage of 5-10 monolayers, and the X-ray diffraction samples at 0.5 monolayers unless stated otherwise. The error in DSC measurements is estimated at 2-5 K, while that from diffraction is 5 K as explained in the text.

| Amide         | $T^{2D}$ (Diffraction)<br>(K) | $T^{2D}$ (DSC)<br>(K) | $T^{3D}$ (DSC)<br>(K) | $T^{2D}/T^{3D}$<br>(DSC) |
|---------------|-------------------------------|-----------------------|-----------------------|--------------------------|
| <b>C7:0</b>   | 410                           | 415                   | 358                   | 1.16                     |
| <b>C9:0</b>   | 410                           | 418                   | 359                   | 1.16                     |
| <b>C10:0</b>  | 440                           | 420                   | 369                   | 1.14                     |
| <b>C11:0</b>  | 405                           | 414                   | 359                   | 1.15                     |
| <b>C12:0*</b> | 428                           | 429                   | 375                   | 1.14                     |
| <b>C14:0</b>  | 439                           | 422                   | 373                   | 1.13                     |

\*Sample at 0.8 monolayer coverage measured by neutron diffraction

### 4.7 High coverage behaviour

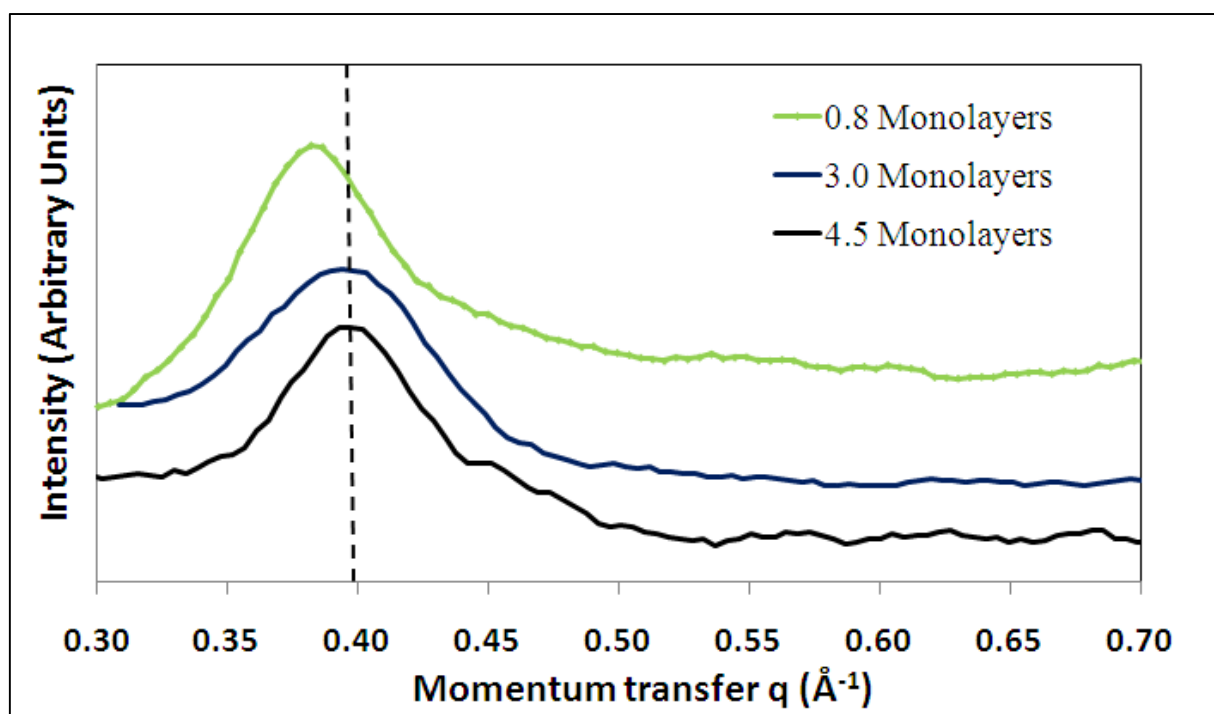


**Figure 4-21** Neutron diffraction data (0.30-0.70  $\text{\AA}^{-1}$ ) for dodecanamide measured on the instrument D20. The 0.8 monolayers pattern is measured at 300 K, while the higher coverage patterns (3 and 4.5 monolayers) are measured at 395 K, with the bulk melt subtracted. The vertical dotted line shows the position of the (1,0) peak for the sample at 0.8 monolayers coverage.

The neutron monolayer patterns at high coverage (3 and 4.5 monolayers) of C12:0 amide on graphite are shown in Figure 4-21. The high coverage monolayer patterns have been measured at 395 K, i.e. a temperature where the bulk material is liquid, but the monolayer is still solid (as explained in chapter 2).

The (1,0) peak position is seen to shift very slightly as the coverage is increased ( $\sim 2\%$ , between 0.8 and 4.5 monolayers). For comparison, alkanes show approximately 3-7% compression [2, 5], while carboxylic acids show 1-3% compression in the  $b$ -direction [23] on increasing the coverage above a monolayer.

The small shift in the  $a$ -direction for the amide layers indicates minimal compression or change in the monolayer at higher coverage. This shows that the layer is indeed stable, a feature that can be attributed to the hydrogen bonding present in the system.

## 4.8 Summary

The two-dimensional sub-monolayer crystalline structures of saturated alkyl amides, pentanamide (C5:0) to hexadecanamide (C16:0), have been calculated using a combination of synchrotron X-ray and neutron diffraction and the results have been presented in this chapter. All the amide molecules studied here are found to form solid ordered layers and lie flat on the graphite surface. The calculated diffraction patterns have been analysed by varying some of the key parameters of the fitting procedure.

Given the constrained fitting procedure used here, it is found that the molecules dimerise, and depending on the number of carbons in the alkyl chain, they adopt a plane group with either  $p2$  symmetry or  $pgg$  symmetry. There is good qualitative agreement with the adsorbed monolayer structures of a related homologue reported by STM, and also with the bulk (3D) crystal structures. The heptanamide (C7:0) monolayer undergoes a solid-solid phase transition at 330 K from a low temperature  $pgg$  to a high temperature  $p2$  phase prior to melting.

The positions of the molecules are consistent with the presence of extensive hydrogen bonds in the monolayer. The structural analysis here provides quantitative detail on the hydrogen bonded arrangements; good fits to the diffraction data are found to isomorphous structures for the amides and similar hydrogen bond geometry as the bulk.

Temperature-dependent diffraction data indicate that the amide monolayers are very stable, with the monolayer of several amides melting at higher temperatures than the respective bulk even at sub-monolayer coverage. Diffraction patterns of dodecanamide at higher coverage show that there is minimal compression in the monolayer, further supporting their stability. The enhanced stabilisation of the monolayer is attributed to the extensive hydrogen bonding present in these systems.

## 4.9 References

1. Wurz, D.H. and N.E. Sharpless, *Amides of Saturated Aliphatic Acids*. Analytical Chemistry, 1949. **21**(12): p. 1446-1448.
2. Arnold, T., C.C. Dong, R.K. Thomas, M.A. Castro, A. Perdigon, S.M. Clarke, and A. Inaba, *The crystalline structures of the odd alkanes pentane, heptane, nonane, undecane, tridecane and pentadecane monolayers adsorbed on graphite at submonolayer coverages and from the liquid*. Phys. Chem. Chem. Phys., 2002. **4**: p. 3430-3435.
3. Bickerstaffe, A.K., Cheah, N. P., Clarke, S. M., Parker, J. E., Perdigon, A., Messe, L., Inaba, A., *The Crystalline Structures of Carboxylic Acid Monolayers Adsorbed on Graphite*. J. Phys. Chem. B, 2006. **110**: p. 5570-5575.
4. Parker, J.E., S.M. Clarke, A.C. Perdigon, and A. Inaba, *The Crystalline Structures of Fluoroalkane Monolayers Adsorbed on Graphite at Submonolayer Coverages*. J. Phys. Chem. C, 2009. **113**(51): p. 21396-21405.
5. Arnold, T., R.K. Thomas, M.A. Castro, S.M. Clarke, L. Messe, and A. Inaba, *The crystalline structures of the even alkanes hexane, octane, decane, dodecane and tetradecane monolayers adsorbed on graphite at submonolayer coverages and from the liquid*. Phys. Chem. Chem. Phys., 2001. **4**: p. 345-351.
6. Lide, D.R., *CRC Handbook of Chemistry and Physics*. 85th ed. 2004.
7. Arnold, T., *The adsorption of alkanes from their liquids and binary mixtures*. 2001, D. Phil Thesis, University of Oxford: Oxford.
8. Kitaigorodskii, A.I., *Molecular crystals and molecules*. Physical chemistry, a series of monographs. 1973, New York: Academic Press.
9. Macgillavry, C.H., *Symmetry aspects of M.C. Escher's periodic drawings*. 1965, Utrecht: Oosthoek.
10. Leiserowitz, L. and G.M.J. Schmidt, *Molecular packing modes. Part III. Primary amides*. J. Chem. Soc. A, 1969: p. 2372 - 2382.
11. Takeuchi, H., S. Kawachi, and A. Ikai, *Differentiation of Chemically Functional Groups in Stearoyl Amide and Anilide with Scanning Tunneling Microscopy*. Jap. J. App. Phys., 1996. **35**: p. 3754-3758.
12. Morishige, K., Y. Tajima, S. Kittaka, S.M. Clarke, and R.K. Thomas, *The structure of chloromethane monolayers adsorbed on graphite*. Mol. Phys., 1991. **72**(2): p. 395-411.
13. Bucknall, R.E., S.M. Clarke, R.A. Shapton, and R.K. Thomas, *The structure of a methyl iodide monolayer adsorbed on graphite*. Mol. Phys., 1989. **67**(2): p. 439 - 446.
14. Clarke, S.M. and R.K. Thomas, *The structure of a bromomethane monolayer adsorbed on graphite*. Molecular Physics, 1991. **72**(2): p. 413 - 423.
15. Inaba, A., H. Chihara, S.M. Clarke, and R.K. Thomas, *The structure and heat capacity of fluoromethane monolayers adsorbed on graphite*. Molecular Physics, 1991. **72**(1): p. 109-120.
16. Pimentel, G.C. and A.L. McClellan, *The Hydrogen Bond*. 1960, San Francisco and London: W. H. Freeman and Co.
17. Vinogradov, S.N. and R.H. Linnell, *Hydrogen Bonding*. 1971: Van Nostrand Reinhold Company.
18. Messe, L., A. Perdigon, S.M. Clarke, A. Inaba, and T. Arnold, *Alkane/Alcohol Mixed Monolayers at the Solid/Liquid Interface*. Langmuir, 2005. **21**(11): p. 5085-5093.

19. Taylor, R., O. Kennard, and W. Versichel, *The geometry of the N-H...O=C Hydrogen Bond. 3. Hydrogen-Bond distances and Angles*. Acta Cryst., 1984. **B40**: p. 280-288.
20. Gavezzotti, A. and G. Filippini, *Geometry of the Intermolecular X-H...Y (X, Y = N, O) Hydrogen Bond and the Calibration of Empirical Hydrogen-Bond Potentials*. J. Phys. Chem., 1994. **98**(18): p. 4831-4837.
21. Findenegg, G.H., *Ordered layers of aliphatic alcohols and carboxylic acids at the pure liquid/graphite interface*. J. Chem. Soc., Faraday Trans. 1, 1973. **69**: p. 1069 - 1078.
22. Comment by Prof. S. Rice (Univ. of Chicago) in *Faraday Discussion Chem. Soc.* (1990). **89**: p. 247.
23. Bickerstaffe, A.K., N.P. Cheah, S.M. Clarke, J.E. Parker, A. Perdigon, L. Messe, and A. Inaba, *The Crystalline Structures of Carboxylic Acid Monolayers Adsorbed on Graphite*. J. Phys. Chem. B, 2006. **110**: p. 5570-5575.
24. Parker, J.E., *Adsorption at the solid/liquid interface: Adsorption and mixing behaviour of fluorinated alkyl species on the surface of graphite*, in *Department of Chemistry*. 2007, PhD thesis, University of Cambridge: Cambridge.
25. Warren, B.E., *X-Ray Diffraction*. 1990: Courier Dover Publications.
26. Arnold, T., Clarke, S. M., *Thermodynamic Investigation of the Adsorption of Amides on Graphite from Their Liquids and Binary Mixtures*. Langmuir, 2008. **24**(7): p. 3325-3335.
27. Bhinde, T., S.M. Clarke, T.K. Phillips, T. Arnold, and J.E. Parker, *Crystalline Structures of Alkylamide Monolayers Adsorbed on the Surface of Graphite*. Langmuir, 2010. **26**(11): p. 8201-8206.
28. Messé, L., A. Perdigon, S.M. Clarke, M.A. Castro, and A. Inaba, *Layer-by-layer surface freezing of linear alcohols at the graphite/liquid interface*. J. Colloid Int. Sci., 2003. **266**(1): p. 19-27.

# Chapter 5

## Unsaturated amides - diffraction

---

Unsaturated amides are useful commercially as friction modifiers in polymer systems and have other applications as described in chapter 1; hence there is considerable interest in their study. However, unsaturated alkyl species on graphite have not received substantial attention in literature, and detailed structural solutions such as those that will be presented here have not been previously reported. A combination of factors, including the availability of third generation synchrotron sources, synthesis of new unsaturated amides and improved data analysis programs have made such a study possible.

The adsorption of unsaturated amides (number of carbons  $\leq 12$ ) on graphite has been studied using synchrotron X-ray diffraction and the results are presented in this chapter. The structures of these unsaturated amides are compared to those of the corresponding saturated amide with the same chain length. The molecular arrangements and hydrogen bond geometry are analysed and explained in terms of the nature and position of the double bond in the alkyl chain.

### 5.1 Experimental details and structural solution

Diffraction patterns for unsaturated amides C6:1 t-2, C6:1 t-3, C9:1 t-2, C11:1 c-10 and C12:1 c-5 are presented in this chapter. Experimental data for C9:1 t-2 amide was measured at

the Materials Science beamline at SLS at 0.5 monolayer coverage and 300 K. All other diffraction patterns were measured on the I11 beamline at Diamond at 0.5 monolayer coverage and 300 K. Due to limitations on the I11 beamline, low angle peaks of unsaturated amides with chain lengths 11 and 12 presented here were not accessible.

Structures for the unsaturated amides were calculated in the same way as for the saturated amides presented in chapter 4. This involved consideration of appropriate plane group symmetry [1] while constraining the number of independently fitted variables as much as possible and maintaining a favourable hydrogen bond geometry [2]. This essentially means that there are no degrees of freedom available to the molecules as they adsorb on the substrate, other than detailed refinements at the final stages. The program for calculating the coordinates of all the atoms for an unsaturated amide molecule for fitting, written as part of this work, has been explained in chapter 2. In these fits, the molecular bond lengths and angles have been taken to be those observed in the bulk crystal and the bond lengths were refined, as similar variations are seen in bulk systems ( $\pm 3\%$ ), but keeping the value of all C-C bond lengths the same [3].

A number of unsaturated amides have been studied and are presented here including odd and even chain lengths, with *cis* and *trans* double bonds which are at different positions in the molecule. However, due to the limited availability of the carboxylic acids from which the unsaturated amides were prepared, as complete a study as presented for the saturated amides is not possible here. In addition, the investigation is also limited to shorter chain lengths by the limitations in accessible scattering angles (as described in chapter 4) which prohibit the observation of important low angle reflections.

## 5.2 Amides with six carbons

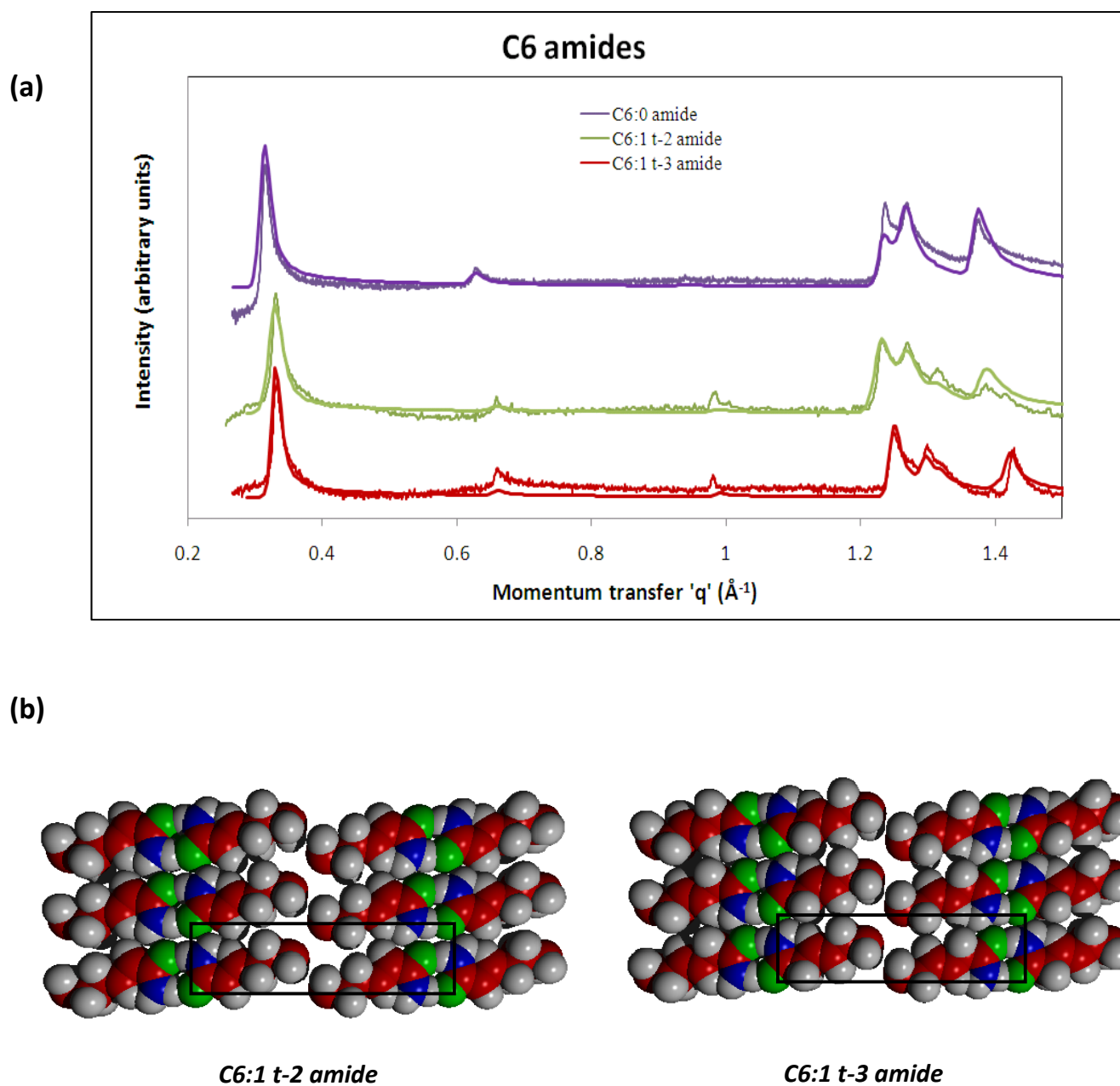


**Figure 5-1** (a) Experimental (points) and calculated (solid lines) X-ray diffraction patterns from amides having six carbon atoms (b) Fitted molecular structures of C6:1 t-2 and C6:1 t-3 amides. The unit cells are indicated by the solid box. The exact coverages of C6:1 t-2 and C6:1 t-3 amides calculated from the fitted patterns are 0.45 and 0.46 monolayers respectively.

The diffraction patterns of saturated and *trans*-unsaturated alkyl amides having six carbon atoms are shown in Figure 5-1 (a). The ‘saw-tooth’ shape of the patterns confirms that these amides all form solid ordered layers on the graphite surface. The diffraction patterns have ‘similar’ peak

positions and intensities, indicating that the structures of these C<sub>6</sub> amides are similar to each other. The unit cell dimensions are comparable to the extended length of the alkyl chain, confirming that these unsaturated amides lie flat on the graphite surface.

The fitted structures for C6:1 t-2 and C6:1 t-3 amides (Figure 5-1 (b) and Table 5-1) show that both these *trans*-unsaturated amides can be fitted to *p2* symmetry unit cells which are very similar in dimensions to that of the saturated amide (discussed in chapter 4). The calculated R-values for the fits are 0.10 (C6:0), 0.10 (C6:1 t-2) and 0.04 (C6:1 t-3) (Table 5-1).

The amides C6:1 t-2 and C9:1 t-2 (discussed below) are particularly interesting to study because the *trans*-double bond is conjugated with the amide group. In the bulk, this is known to result in extended delocalisation of  $\pi$ -electrons near the amide group and enhance the stability of the hydrogen bond [4]. These ‘resonance-assisted hydrogen bonds’ are an interesting class of hydrogen bonds that are stronger than the conventional amide hydrogen bond, with potential for further study and development in the monolayer.

If the monolayers with conjugated amide groups do indeed have enhanced stability, that might also be expected to be reflected in a higher monolayer melting point relative to the saturated amide. Thermodynamic data addressing exactly this point is presented in chapter 6.

There appears to be a contraction of the intra-dimer N...O contact (Table 5-1) to a value less than the usual values for saturated amides (2.7-3.1 Å, chapter 4). This result will be discussed in chapter 6. The intra-dimer hydrogen bonds are slightly non-linear in the unsaturated amides, possibly to accommodate the double bond and maintain a closed-packed structure. Nevertheless, this similarity in the monolayer structure can help explain the mixing behaviour of these amides as will be explained in chapter 6.

**Table 5-1** Fitting parameters and hydrogen bond values for the diffraction patterns of amides with six carbons. There are 2 molecules per unit cell in a  $p2$  symmetry structure.

| Amide           | Unit cell parameters  |                       |                     | Molecular tilt<br>( $^{\circ}$ ) | R-value | Intra-dimer hydrogen bond          |                                     | Inter-dimer hydrogen bond          |                                     |
|-----------------|-----------------------|-----------------------|---------------------|----------------------------------|---------|------------------------------------|-------------------------------------|------------------------------------|-------------------------------------|
|                 | a<br>( $\text{\AA}$ ) | b<br>( $\text{\AA}$ ) | v<br>( $^{\circ}$ ) |                                  |         | Angle<br>N-H...O<br>( $^{\circ}$ ) | Length<br>N...O<br>( $\text{\AA}$ ) | Angle<br>N-H...O<br>( $^{\circ}$ ) | Length<br>N...O<br>( $\text{\AA}$ ) |
| <b>C6:0</b>     | 20.1                  | 5.11                  | 91.0                | 23.25                            | 0.10    | 180                                | 3.00                                | 120                                | 2.92                                |
| <b>C6:1 t-2</b> | 19.1                  | 5.12                  | 91.5                | 19.25                            | 0.10    | 160                                | 2.66                                | 111                                | 3.04                                |
| <b>C6:1 t-3</b> | 19.1                  | 5.04                  | 89.1                | 19.00                            | 0.04    | 161                                | 2.59                                | 114                                | 2.92                                |

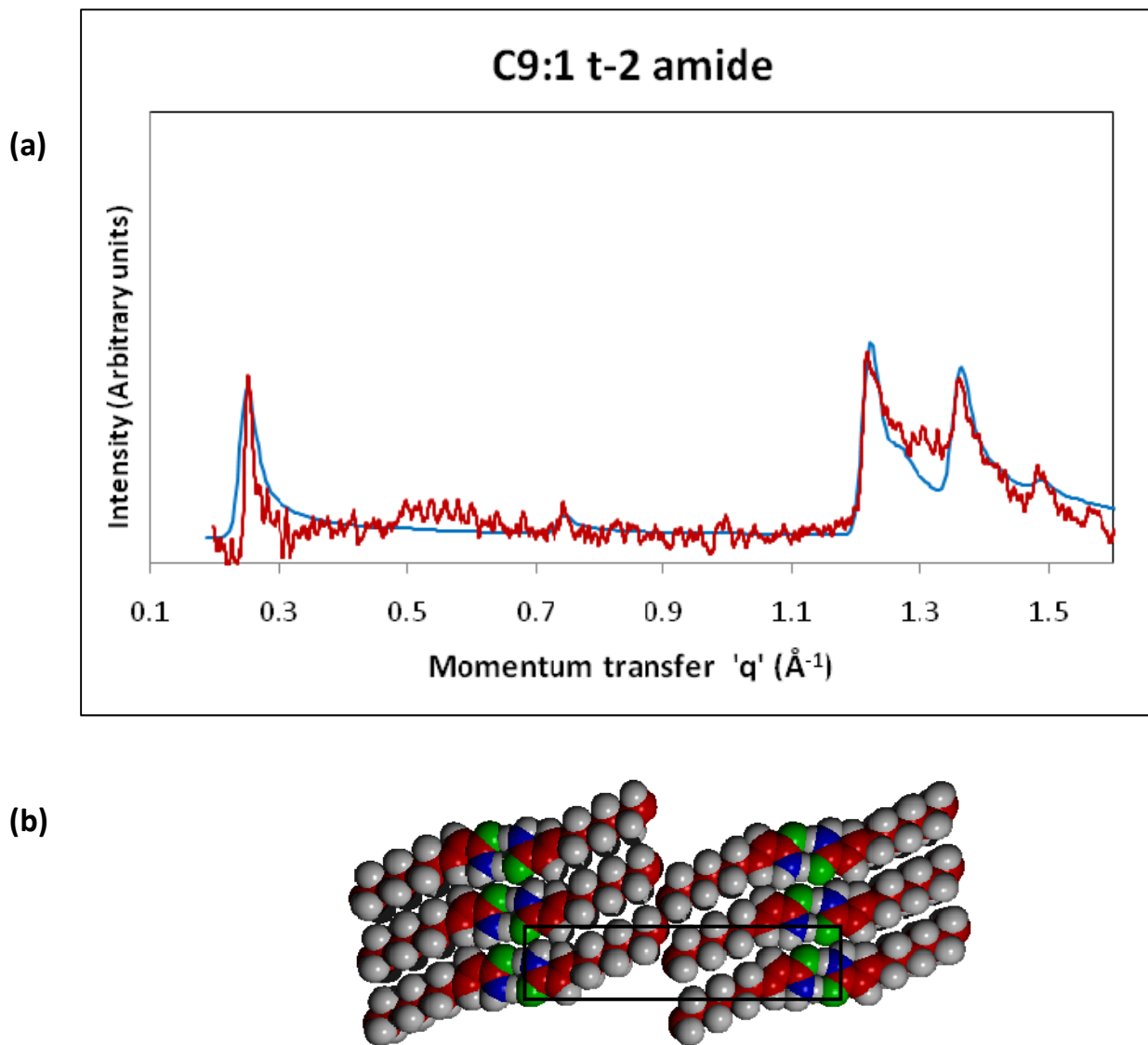
### 5.3 C9:1 t-2 amide

Figure 5-2 presents the calculated and experimental diffraction patterns for a monolayer of C9:1 t-2 amide along with the molecular structure that was used to fit the pattern. The parameters relating to the fit are listed in Table 5-2. The experimental data in Figure 5-2 (a) is somewhat more noisy than ideal and arises from the limited synchrotron beam time available for this sample. However, even within the uncertainty of the data, it is observed that the experimental patterns are found to be in reasonably good agreement with the calculated pattern based on that of the structure found for the other unsaturated amides discussed above, where the data quality was much higher. Hence it is considered very likely that these structures are isomorphic.

Analysis of this structure indicates a  $p2$ -symmetry hydrogen-bonded arrangement, after refinements of the overall constrained fitting procedure (§5.1). The length of the intra-dimer N...O contact within the dimer of C9:1 t-2 amide is again found shorter than the value for the saturated amide (Table 5-2).

Interestingly, unlike C9:0, the C9:1 t-2 amide appears to be commensurate with the underlying graphite since the ratio of its  $a$ -parameter to the graphite lattice parameter (4.26  $\text{\AA}$ ) is an integer (6). This may simply reflect the small changes in the overall molecule length which can now allow a commensurate layer to form for the unsaturated species and not the saturated. However,

it does suggest that the influence of the graphite substrate periodicity is small relative to the other interactions in the system.



**Figure 5-2** (a) Experimental (red) and calculated (blue) X-ray diffraction patterns and (b) fitted molecular structure of C9:1 t-2 amide. The exact coverage of this amide from the fitted pattern is 0.51 monolayers. The unit cell is shown by the solid box.

The unit cell parameters and monolayer structures for the saturated C9:0 and unsaturated C9:1 t-2 amides are very similar. This is very important while considering mixing in the adsorbed

monolayer (chapter 6) where the similarity of molecular size and the replacement of one molecule for another in the mixed crystal lattice is a central issue.

**Table 5-2** Fitting parameters and hydrogen bond values for the diffraction pattern of C9:1 t-2 amide

| Amide    | Unit cell parameters |          |              | Molecular tilt<br>(°) | R-value | Intra-dimer hydrogen bond |                        | Inter-dimer hydrogen bond |                        |
|----------|----------------------|----------|--------------|-----------------------|---------|---------------------------|------------------------|---------------------------|------------------------|
|          | a<br>(Å)             | b<br>(Å) | $\nu$<br>(°) |                       |         | Angle<br>N-H...O<br>(°)   | Length<br>N...O<br>(Å) | Angle<br>N-H...O<br>(°)   | Length<br>N...O<br>(Å) |
| C9:1 t-2 | 25.3                 | 5.12     | 96.8         | 24.25                 | 0.03    | 177                       | 2.53                   | 112                       | 3.11                   |
| C9:0     | 26.4                 | 5.13     | 94.0         | 22.25                 | 0.08    | 172                       | 2.93                   | 113                       | 3.04                   |

## 5.4 C11:1 c-10 amide

C11:1 c-10 amide has a double bond at the end of the molecule. The designation as *cis* or *trans* is therefore inappropriate. This terminal double bond could make the C11:1 c-10 molecule very similar to the saturated amide as demonstrated by its monolayer structure here and its melting point (shown in chapter 6).

The experimental diffraction pattern for C11:1 c-10 amide shows that this amide also forms a solid ordered layer on graphite. The data fits well with the *p2*-symmetry molecular structure shown in Figure 5-3 (R-value = 0.09, Table 5-3). This monolayer structure is very similar to the saturated amide (C11:0, Table 5-3). The influence of the terminal double bond seems to be in the in-plane tilt of the amide w.r.t the *a*-axis; it is smaller (Table 5-3) than that observed for other amide molecules (21-24°), perhaps to accommodate the terminal double bond in the molecule, although a favourable hydrogen bond geometry is still maintained.

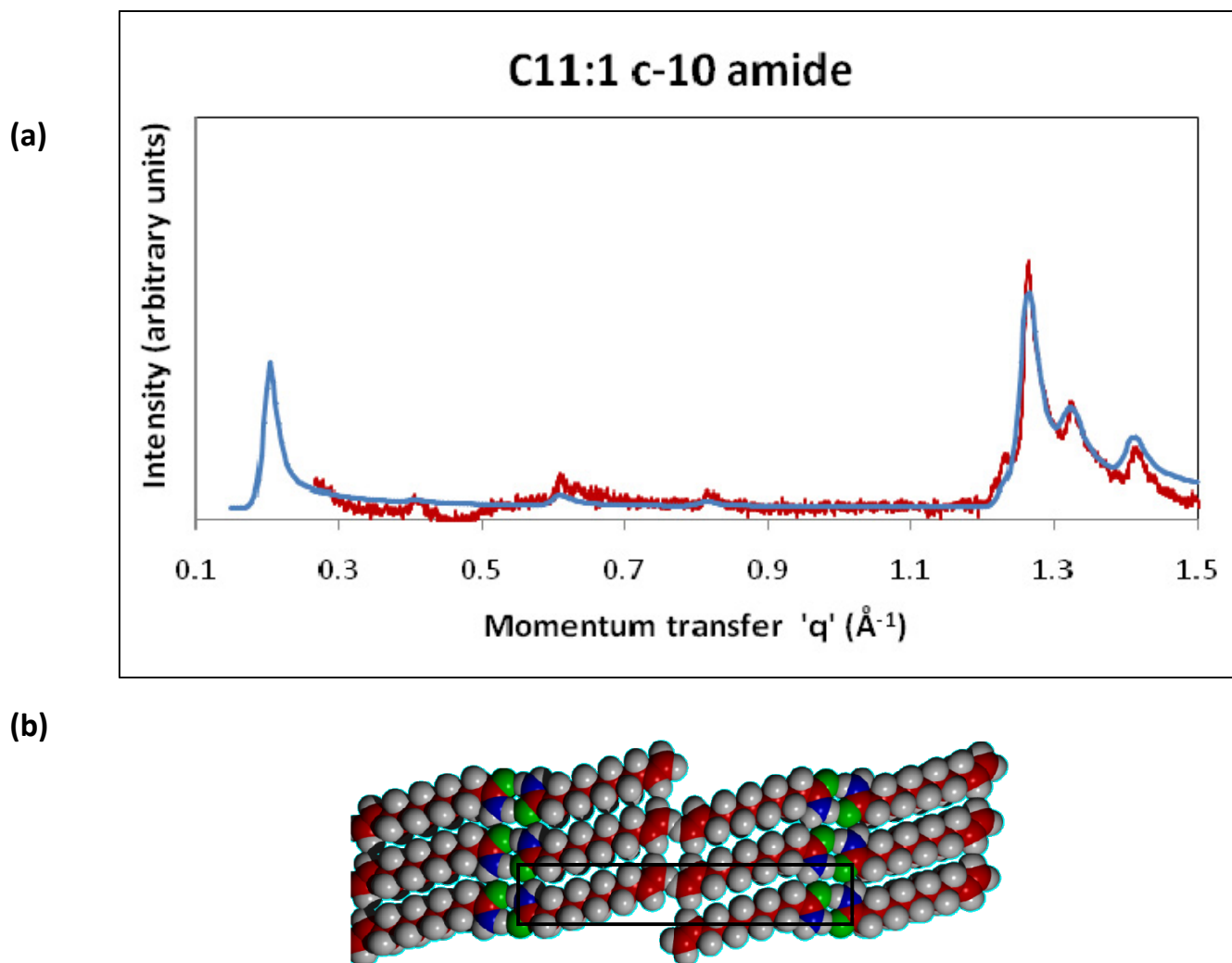


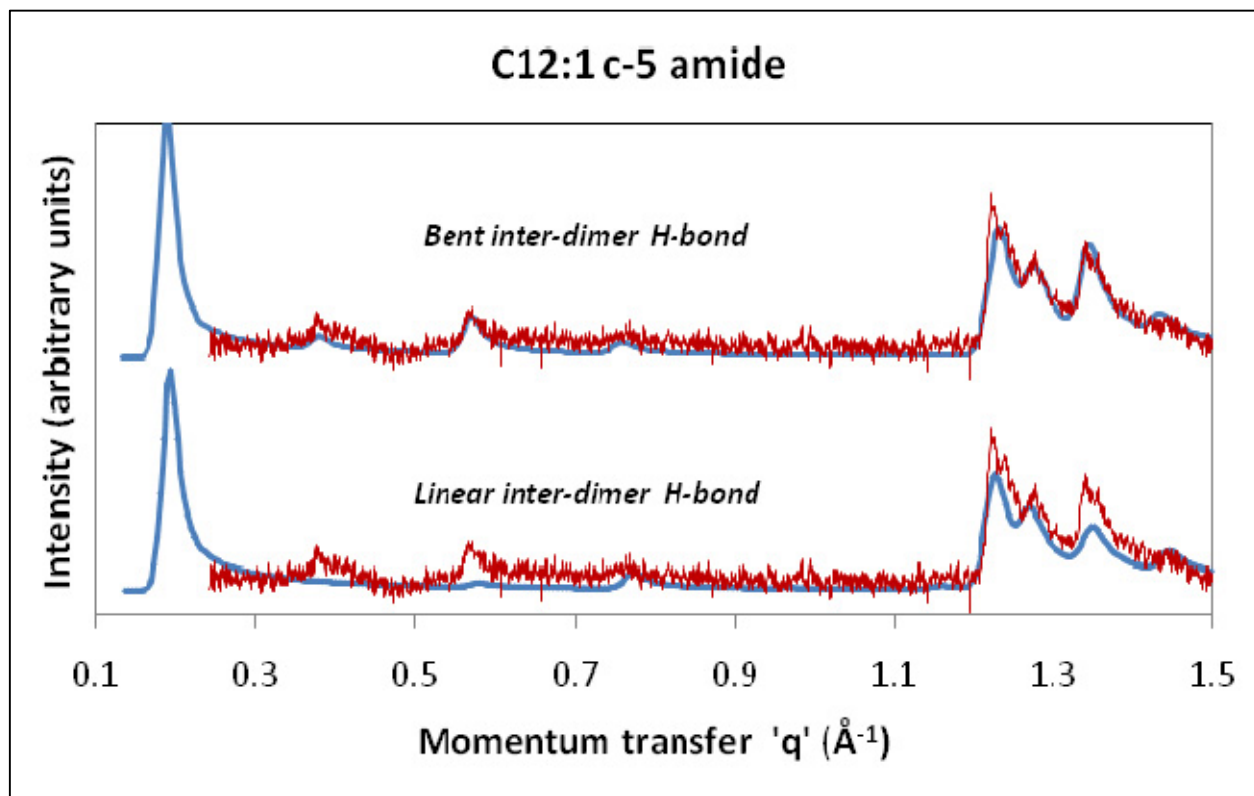
**Figure 5-3** (a) Experimental (red) and calculated (blue) X-ray diffraction patterns and (b) fitted molecular structure of C11:1 c-10 amide. The exact coverage of this amide from the fitted pattern is 0.53 monolayers. The unit cell is shown by the solid box.

**Table 5-3** Fitting parameters and hydrogen bond values for the diffraction pattern of C11:1 c-10 amide

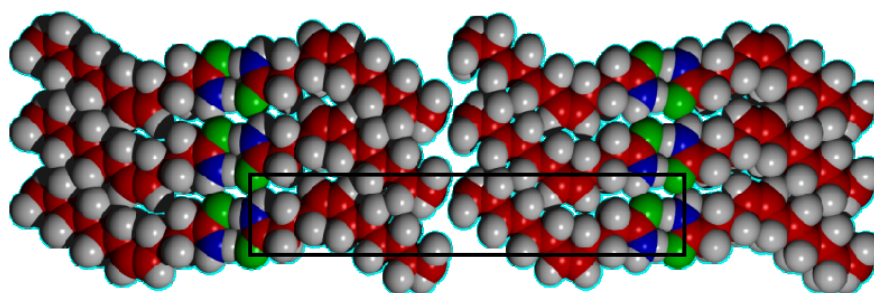
| Amide      | Unit cell parameters |          |          | Molecular tilt<br>(°) | R-value | Intra-dimer hydrogen bond |                        | Inter-dimer hydrogen bond |                        |
|------------|----------------------|----------|----------|-----------------------|---------|---------------------------|------------------------|---------------------------|------------------------|
|            | a<br>(Å)             | b<br>(Å) | v<br>(°) |                       |         | Angle<br>N-H...O<br>(°)   | Length<br>N...O<br>(Å) | Angle<br>N-H...O<br>(°)   | Length<br>N...O<br>(Å) |
| C11:1 c-10 | 31.2                 | 5.13     | 86.0     | 16.00                 | 0.09    | 167                       | 2.88                   | 116                       | 3.01                   |
| C11:0      | 31.0                 | 5.17     | 91.0     | 22.25                 | 0.18    | 175                       | 2.86                   | 118                       | 3.03                   |

## 5.5 C12:1 c-5 amide

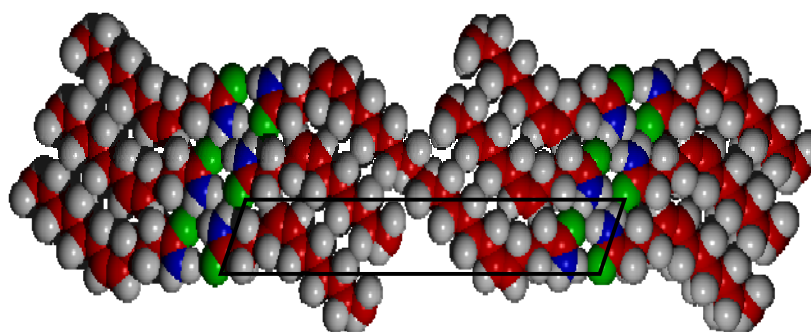
(a)



(b)



*Bent inter-dimer  
hydrogen bond*



**Linear inter-dimer  
hydrogen bond**

**Figure 5-4 (a)** Fitted X-ray diffraction patterns for C12:1 c-5 amide and **(b)** corresponding molecular arrangements. The unit cells are shown by the solid boxes. Two possible fits are shown, one where the inter-dimer bond is bent (favourable) and one where the bond is linear (non-favourable). The fit from the bent inter-dimer bond arrangement has an R-value of 0.06 (Table 5-4). The exact coverage of this amide is 0.54 monolayers.

C12:1 c-5 amide is interesting to study since it has a *cis*-double bond in the middle of the alkyl chain which results in a bend in the molecule; this might give rise to particular packing issues. It is also approximately similar to oleamide (C18:1 c-9), a commercially important amide, in terms of the relative position of the *cis*-double bond ( $\alpha$ ) to the overall chain length ( $n$ ) (this  $\alpha:n$  ratio has been shown to be a rough indicator of the ‘similarity’ of *cis*-unsaturated amide molecules in terms of their melting points [5]). The shorter chain length of this amide compared to oleamide enables the study of this molecule by synchrotron X-ray diffraction as more of the monolayer diffraction pattern is expected to be in the accessible  $q$ -range for C12:1 c-5 amide (as discussed in chapter 2).

Figure 5-4 shows the experimental diffraction pattern of C12:1 c-5 amide together with the calculated diffraction patterns from two different molecular arrangements. The calculated diffraction pattern resulting from a bent N-H...O inter-dimer hydrogen bond, which is the energetically favourable geometry [2], is shown along with one from a linear inter-dimer hydrogen bond (favourable hydrogen bond geometries have been discussed in detail in chapters 1 and 4). The unit cell parameters and hydrogen-bond values for the saturated and *cis*-unsaturated amides having a chain length of 12 carbons are listed in Table 5-4. Note that to arrange the molecules such that the inter-dimer hydrogen bond is linear, the unit cell is required to be highly oblique ( $v=64^\circ$ ).

The differences between the calculated patterns (Figure 5-4 (a)) for the two arrangements are most obvious for the peaks in the range 0.3 to 1 Å. For the linear inter-dimer structure the peaks at 0.4 Å<sup>-1</sup> and 0.6 Å<sup>-1</sup> are much too weak relative to the other observed peaks. The R-value for the linear inter-dimer hydrogen bonded arrangement is also calculated to be high (0.28). Hence it is concluded that the bent-inter dimer bond is the adopted arrangement, and the same result is observed for all the other amide molecules (saturated and unsaturated) considered in this work.

Closer inspection of the unit cell parameters and hydrogen bond geometry of the C12:1 c-5 amide (Table 5-4) shows that these values are remarkably similar to those of the saturated amide (C12:0) and both structures possess the same (*p2*) symmetry; the *cis*-double bond is accommodated in the monolayer while still maintaining favourable hydrogen bond interactions. The similarity between these two amide structures is an important issue while considering mixing and will be discussed in chapter 6.

**Table 5-4** Fitting parameters and hydrogen bond values for amides with 12 carbons

| Amide     | Unit cell parameters |       |       | Molecular tilt (°) | R-value | Intra-dimer hydrogen bond |                  | Inter-dimer hydrogen bond |                  |
|-----------|----------------------|-------|-------|--------------------|---------|---------------------------|------------------|---------------------------|------------------|
|           | a (Å)                | b (Å) | v (°) |                    |         | Angle N-H...O (°)         | Length N...O (Å) | Angle N-H...O (°)         | Length N...O (Å) |
| C12:1 c-5 | 33.3                 | 5.18  | 90.0  | 24.50              | 0.06    | 178                       | 2.80             | 128                       | 2.99             |
| C12:0     | 33.9                 | 5.12  | 91.7  | 23.60              | 0.03    | 178                       | 3.03             | 119                       | 2.97             |

## 5.6 Discussion and summary

Synchrotron X-ray diffraction has been used to investigate the adsorption of unsaturated amides on graphite and the results have been presented in this chapter. All the unsaturated amides studied here form solid crystalline layers and lie flat on the graphite surface.

High quality structural fits have been obtained for all the unsaturated amides. Calculated structures reveal that the unsaturated amides have ‘similar’ structures to the corresponding saturated amide: the molecules are all found to hydrogen bond into dimers with *p2* symmetry, after detailed refinements of the constrained fitting procedure adapted here.

The positions of the atoms in a *trans*-unsaturated molecule are similar to those of the saturated molecule of the same chain length, and this is reflected in the similarity in their monolayer packing arrangements and hydrogen bond geometry. *Trans*-unsaturated amides which have their double bond conjugated to the amide head group have shorter N...O hydrogen bond distances than the corresponding saturated molecule. Only C9:1 t-2 amide appears to be commensurate with the graphite substrate.

Calculated diffraction patterns of C12:1 c-5 amide for two possible arrangements of the inter-dimer hydrogen bond are shown: one with a linear inter-dimer N-H...O hydrogen bond and one with a bent ( $\sim 120^\circ$ ) arrangement. The bent arrangement, which is energetically favourable, is found to be the preferred arrangement, as with all the amides investigated in this work.

Interestingly, in spite of a bend in the alkyl chain caused by the *cis*-double bond in the C12:1 c-5 amide molecule, the monolayer structure is remarkably similar to the saturated amide in terms of the unit cell dimensions and hydrogen bond geometry. The monolayer structures presented here for the unsaturated amides are key in rationalising mixing in the 2D layer which will be discussed in the next chapter.

## 5.7 References

1. Hahn, T., *Space group symmetry*. 4th ed. International tables for crystallography. Vol. A. 1995, London: Kluwer Academic.
2. Leiserowitz, L. and G.M.J. Schmidt, *Molecular packing modes. Part III. Primary amides*. J. Chem. Soc. A, 1969: p. 2372 - 2382.
3. Lide, D.R., *CRC Handbook of Chemistry and Physics*. 85th ed. 2004.
4. Gilli, G. and P. Gilli, *The Nature of the Hydrogen Bond*. International Union of Crystallography Book Series. 2009, New York: Oxford University Press.
5. Arnold, T., Clarke, S. M., *Thermodynamic Investigation of the Adsorption of Amides on Graphite from Their Liquids and Binary Mixtures*. Langmuir, 2008. **24**(7): p. 3325-3335.

# Chapter 6

## Calorimetry

---

The adsorption of a significant number of amides of different chain lengths, both saturated and unsaturated, has been investigated with Differential Scanning Calorimetry (DSC), and the results are presented in this chapter. The adsorption of pure amides from their liquids on graphite will be shown in §6.1. The variation of melting temperatures and enthalpies with alkyl chain length for the saturated amides is discussed. Monolayer behaviour of unsaturated amides is presented and explained based on the position of the double bond relative to the amide group.

Phase diagrams of binary mixtures of saturated amides at higher coverages (5-10 monolayers) will be presented next, and the results interpreted in terms of the structural symmetry of the individual components presented in chapter 4. Saturated/unsaturated amide mixtures will then be considered, and the results again interpreted in terms of the monolayer structures calculated by diffraction (chapters 4 and 5). Finally, results from a coverage dependence study of C11:0 amide using DSC measurements are shown.

## 6.1 DSC of pure amides adsorbed on graphite

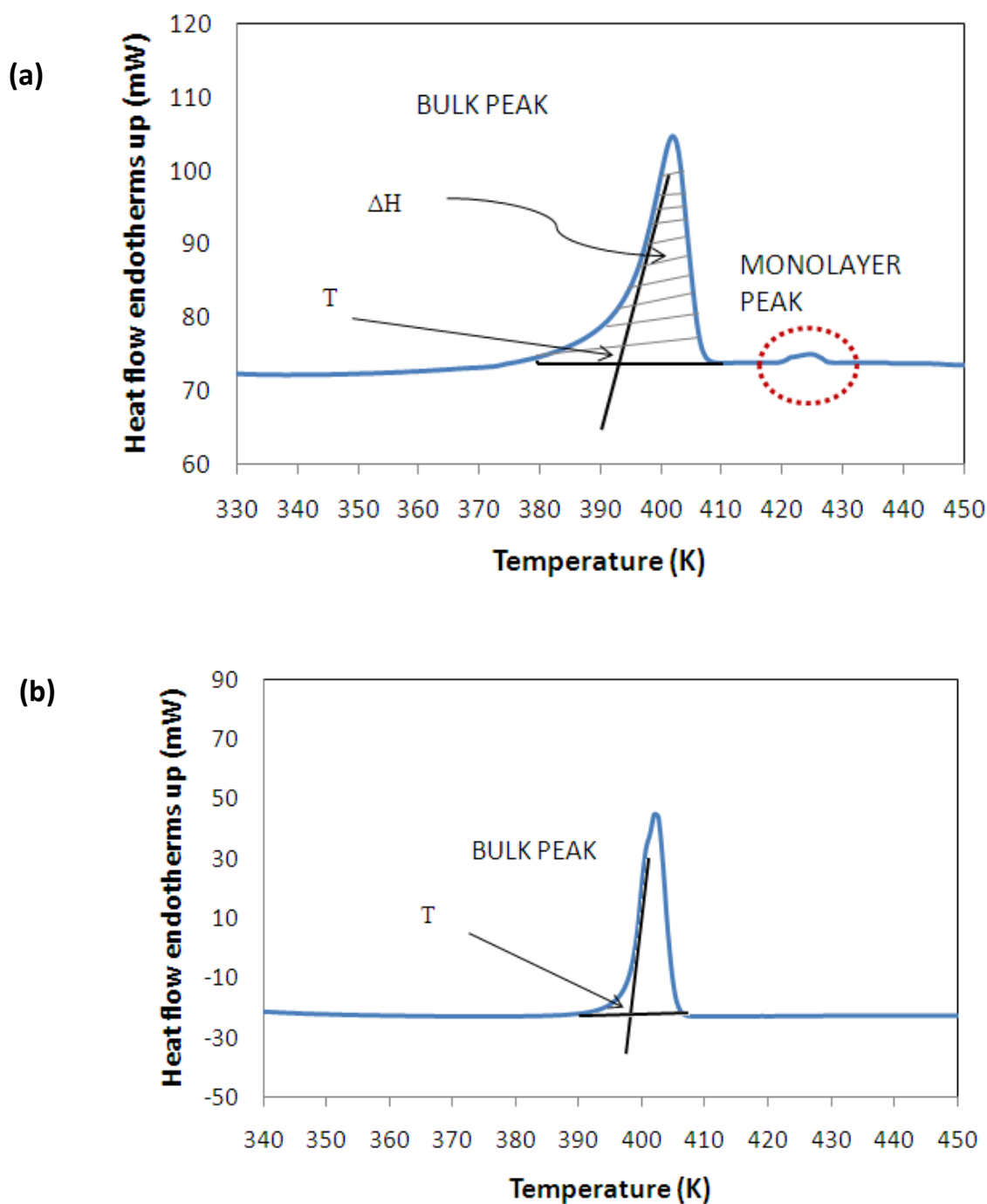


**Figure 6-1** Example DSC thermogram of C9:1 t-2 amide (a) in the presence of graphite and (b) without any graphite. For the bulk peak, the onset temperature (T) is shown, and is reported as the melting point of the pure material.

Representative DSC thermograms for C9:1 t-2 amide, with and without the graphite substrate, are shown in Figure 6-1. The thermogram without graphite shows a relatively large transition which can be attributed to the bulk melting of the amide. The thermogram of the amide with graphite (Figure 6-1 (a)) shows an additional smaller transition at higher temperatures, along with the bulk melting peak which is observed in the pure sample alone. The presence of additional transitions has been reported previously for a variety of alkyl species on graphite in literature (e.g. see carboxylic acids on graphite, [1]).

Since this transition is only seen in the presence of graphite, it can initially be attributed to one arising from the monolayer. This signal can be confirmed to be a monolayer melting transition by a number of techniques (e.g. see aldehydes on graphite, confirmed by neutron scattering, [2]). For this work, the presence of a solid layer of amides has already been confirmed by diffraction techniques (chapters 4 and 5), and the melting of the 2D layer demonstrated. All the adsorbed amides studied in this work show the existence of a monolayer melting transition by DSC above the bulk melting point at ~5-10 monolayer coverage.

### 6.1.1 DSC data

Table 6-1 lists the melting temperatures and enthalpies for both bulk and monolayer transitions for a number of alkyl amides measured by the DSC. These values agree with those of an earlier initial study [3] and bulk values are also found to match closely with those measured in an independent study of Abate et al [4]. However several new amides have been synthesised as part of this work (odd alkyl chain length saturated amides and short chain-length unsaturated amides). DSC data from these amides combined with earlier studies provides additional insights into their surface behaviour, as will be explained here.

The melting enthalpy for the monolayer ( $\Delta H^{2D}$ ) as calculated by the DSC software from the area under the DSC peak is available in units of Joules per gram of graphite adsorbate (J/gg). This was converted into units of kJ/mol of monolayer by considering the specific surface area of graphite and the area per molecule of the amide (which is known from the diffraction patterns, chapters 4 and 5). As explained previously [1, 3], all the amide molecules remain dimerised in

the liquid state after melting, and the melting enthalpy per mole of dimers will be twice that of the monomer. Hence the  $\Delta H^{2D}$  was doubled and these values are listed in Table 6-1.

**Table 6-1** Transition temperatures (T) and melting enthalpies ( $\Delta H$ ) of alkyl amides on graphite as measured by DSC. The errors in these values are estimated as  $\pm 3$  K (temperature) and  $\pm 5$  kJ/mol (enthalpy).

| Amide                     | Monolayer melting $T^{2D}$ (K) | $\Delta H^{2D}$ (kJ/mol) | Bulk melting $T^{3D}$ (K) | $\Delta H^{3D}$ (kJ/mol) | $T^{2D}/T^{3D}$ |
|---------------------------|--------------------------------|--------------------------|---------------------------|--------------------------|-----------------|
| <b>Saturated amides</b>   |                                |                          |                           |                          |                 |
| C5:0                      | 396                            | 14.1                     | 370                       | 15.9                     | 1.07            |
| C6:0                      | 402                            | 11.4                     | 375                       | 16.0                     | 1.07            |
| C7:0                      | 410                            | 38.0                     | 360                       | 17.0                     | 1.14            |
| C9:0                      | 418                            | 48.4                     | 371                       | 21.7                     | 1.13            |
| C11:0                     | 417                            | 57.0                     | 359                       | 28.5                     | 1.16            |
| C12:0                     | 429                            | 38.3                     | 374                       | 32.6                     | 1.15            |
| C15:0                     | 427                            | 63.8                     | 375                       | 41.0                     | 1.14            |
| C17:0                     | 433                            | 48.4                     | 377                       | 46.7                     | 1.15            |
| C19:0                     | 435                            | 62.6                     | 383                       | 56.0                     | 1.14            |
| C20:0                     | 438                            | 50.2                     | 380                       | 42.9                     | 1.15            |
| <b>Unsaturated amides</b> |                                |                          |                           |                          |                 |
| C6:1 t-2                  | 416                            | 10.4                     | 381                       | 15.0                     | 1.09            |
| C6:1 t-3                  | 372                            | 10.0                     | 350                       | 12.6                     | 1.06            |
| C9:1 t-2                  | 426                            | 16.4                     | 394                       | 22.5                     | 1.06            |
| C11:1 c-10                | 412                            | 38.4                     | 358                       | 36.6                     | 1.15            |
| C12:1 c-5                 | 380                            | 24.5                     | 339                       | 15.4                     | 1.12            |

## 6.1.2 Trends in monolayer melting points

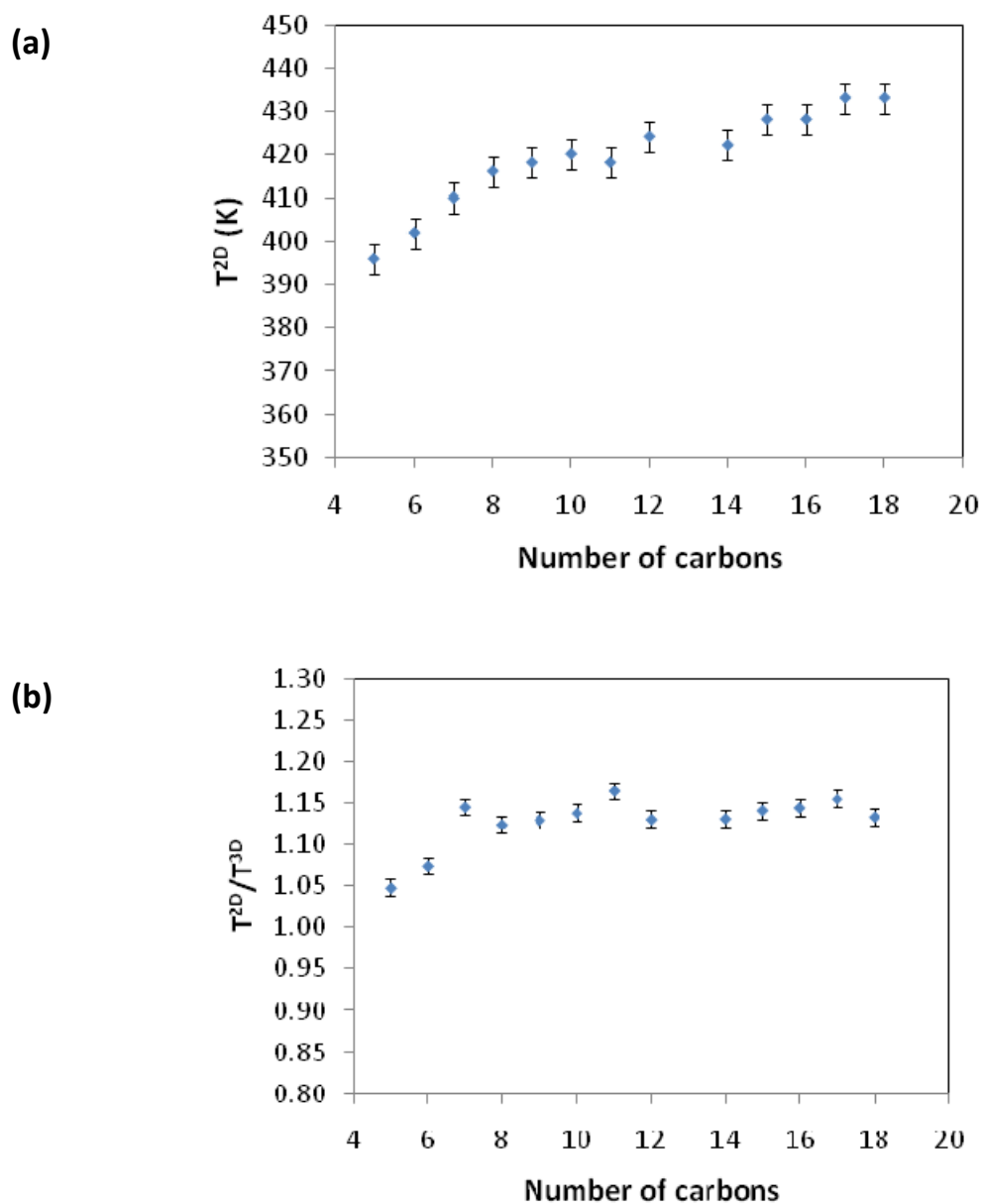


**Figure 6-2** (a) Variation of monolayer melting points of saturated alkyl amides on graphite. Some of the data is taken from [3]. (b) The ratio  $T^{2D}/T^{3D}$  plotted as a function of chain length for saturated amides

The variation of monolayer melting point with alkyl chain length is plotted in Figure 6-2 (a). This graph shows that the monolayer melting points essentially increase with alkyl chain length of the saturated amides. The melting points, however, increase only gradually as the chain length increases (the overall increase is  $\sim 40$  K as the chain length is increased from 5 to 20 carbons).

For comparison, the melting points of alkanes increase by ~220 K when the chain length is increased by the same amount [5]. Many amides studied here, and previously [3], show other transitions in the monolayer by DSC other than the monolayer melting. These could be solid-solid phase transitions within the adsorbed layer or transitions from melting of additional layers. This will be discussed in the coverage dependent study of C11:0 amide in §6.3.

The ratio of the monolayer to bulk melting points,  $T^{2D}/T^{3D}$ , can be used as a relative indicator of the stability of the monolayer compared to the bulk. The monolayer for most of the saturated amides melts considerably higher than the bulk, both at sub-monolayer and also at high coverage (~10-15% higher) i.e. the ratio  $T^{2D}/T^{3D} \sim 1.15$  (Figure 6-2 (b)). The monolayers for a few unsaturated amides (e.g. C16:1 t-2 amide, [3]) melt 20% higher than the bulk at high coverage. This ratio is higher than all other alkyl adsorbates on graphite reported so far. For comparison, fluoroalkane monolayers melt 3% higher, carboxylic acids ~10% higher and alkanes ~13% higher than the bulk at high coverage. As explained in detail in chapters 4 and 5, the enhanced stability of the amide monolayers has been attributed to the presence of an extensive network of hydrogen bonds in these systems.

### 6.1.3 Monolayer melting enthalpies

The monolayer melting enthalpies are found to increase as the chain length of the saturated amides is increased due to an increase in van der Waals interactions in longer molecules (Table 6-1). Most monolayer enthalpies were in the range of 0.5-2.0 Joules/gram of graphite (15-60 kJ/mol).

As discussed in chapter 4, there exists an odd-even variation in the monolayer crystal structures of saturated alkyl amides, and in the bulk melting temperatures and enthalpies [4]. A similar variation is reflected in the melting enthalpies of the monolayer ( $\Delta H^{2D}$ ) shown in Figure 6-3. Odd alkyl amides consistently possess higher melting enthalpies, although the difference between odd-even enthalpies becomes lesser as the chain length is increased. The origin of this effect is thought to be related to the structures of the molecular layers: the alternating directions of the terminal methyl groups in the alkyl chain cause differences in monolayer arrangements for the odd and even homologues [6]. However, an odd-even effect is not apparent in the monolayer melting points of the amides here (Figure 6-2 (a)).

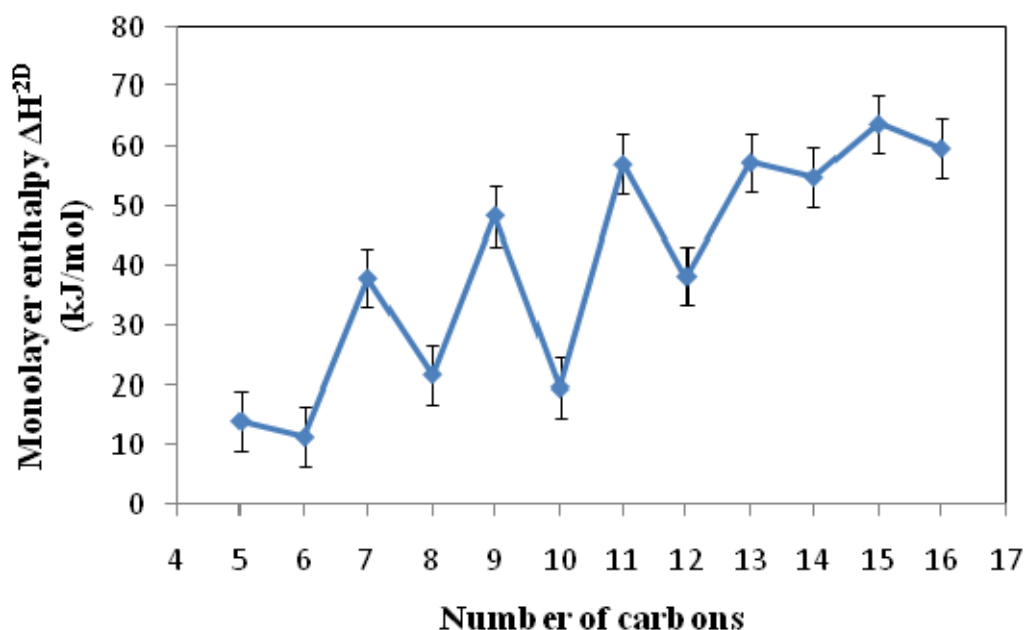


**Figure 6-3** Variation of the monolayer melting enthalpy with chain length of the saturated amides. Some of the data is taken from [3].

Due to uncertainties in estimating the baseline of the weak monolayer transition accurately the monolayer enthalpies are subject to considerable errors ( $\sim 5$ - $10$  kJ/mol). This does not, however, significantly affect the interpretation of the mixing behaviour explained below.

#### 6.1.4 Unsaturated amides

As observed in a previous study [3], the monolayer melting points of unsaturated amides are lower than the corresponding saturated amide due to the influence of the double bond in the packing of the monolayer. The *trans*-unsaturated C6:1 t-2 and C9:1 t-2 amides are an exception to this rule, since the monolayer melting points of these amides are higher compared to their saturated homologues (Table 6-1). A similar effect has been observed for C16:1 t-2 amide previously [3].

In the bulk, a double bond conjugated to an amide head group is known to increase the strength of the hydrogen bonds, and these are an interesting class of ‘resonance assisted hydrogen bonds’ with potential for further study in the monolayers. These hydrogen bonds are characterised by shorter hydrogen bond distances and increased energies of dissociation of the dimer [7]. The diffraction results for C6:1 t-2 and C9:1 t-2 amides (chapter 5) have shown the existence of

shorter intra-dimer hydrogen N-H...O bond lengths. It can be deduced, based on these shorter hydrogen bond lengths, and combined with the monolayer melting points shown here, that the ‘resonance-assistance’ to the hydrogen bond is preserved in the monolayer for these amides.

## 6.2 Binary mixtures of adsorbed amides

Samples containing graphite and varying composition of binary amide mixtures were prepared as described in chapter 3 and analysed by DSC. All data was corrected by measuring the melting temperature of the Indium standard as described in §3.3. When studying adsorption from binary liquid mixtures two issues are considered: the mixing behaviour in the monolayer and extent of any preferential adsorption. As discussed in chapter 3, the phase diagrams obtained from DSC can be quantitatively analysed: the experimental phase diagrams were ‘fitted’ to the regular solution model. The phase diagram lines were calculated given the monolayer melting temperatures and enthalpies of the pure materials (Table 6-1) and trial values of the interaction parameter  $\Omega$  and preferential adsorption coefficient  $K$  (regular solution theory has been explained in chapter 3). This procedure was repeated until satisfactory match with experimental data was obtained. For cases where complete phase separation was observed, the data was directly fitted to the phase separation model using the equations developed in §3.1.2.

As described in detail in chapter 3, a lot of information can be extracted from the DSC thermograms of pure materials and binary mixtures. The models developed by Sun and Clarke [8] can predict the thermograms for a binary mixture for all compositions along the phase diagram for ideal and eutectic mixtures, given the melting points and enthalpies of the pure materials. However, as discussed before, the very weak nature of monolayer peaks makes it extremely difficult to analyse each thermogram quantitatively; faster scan rates on the DSC do not provide good resolution for the two peaks that would be expected during melting in the two phase region. Also, many of the amide mixtures were found to mix non-ideally, and quantitatively modelling thermograms for regular solution mixtures is not trivial. Several amides studied here undergo solid-solid phase transitions both in the monolayer and in the bulk which makes the analysis of the thermograms difficult [3, 4]. Thus, the Full Width at Half Maximum

(FWHM) of the melting peaks was used here to estimate the ‘spread’ of the two-phase region while fitting the phase diagram using the regular solution model.

### 6.2.1 Saturated/saturated amide mixtures

In this section the DSC phase diagrams for saturated/saturated amide mixtures are presented and interpreted with quantitative fits to particular thermodynamic models of mixing. Mixtures of saturated amides with an even number of carbons have been studied previously [3], and in this work mixtures of amides with odd carbons have been considered. The phase diagrams of mixtures of C9:0 amide with other similar chain length homologues (C5:0, C7:0 and C11:0) are shown in this section.

Phase diagrams for bulk mixtures involving C9:0 amide (not presented here) have all been found to completely phase separate or have  $\Omega$  (explained in chapter 2) values close to  $2RT$  which also suggests very poor mixing. This behaviour in the bulk is consistent with the observation that bulk C9:0 amide has a different space group from all the other saturated amides [9], and generally molecules with different space groups are not expected to mix in the solid state (§3.1.5). Mixing in the liquid state is not restricted by such limitations, and ideal mixing has been assumed in the liquid state throughout this work.

## 6.2.1.1 C9:0 and C5:0 mixture

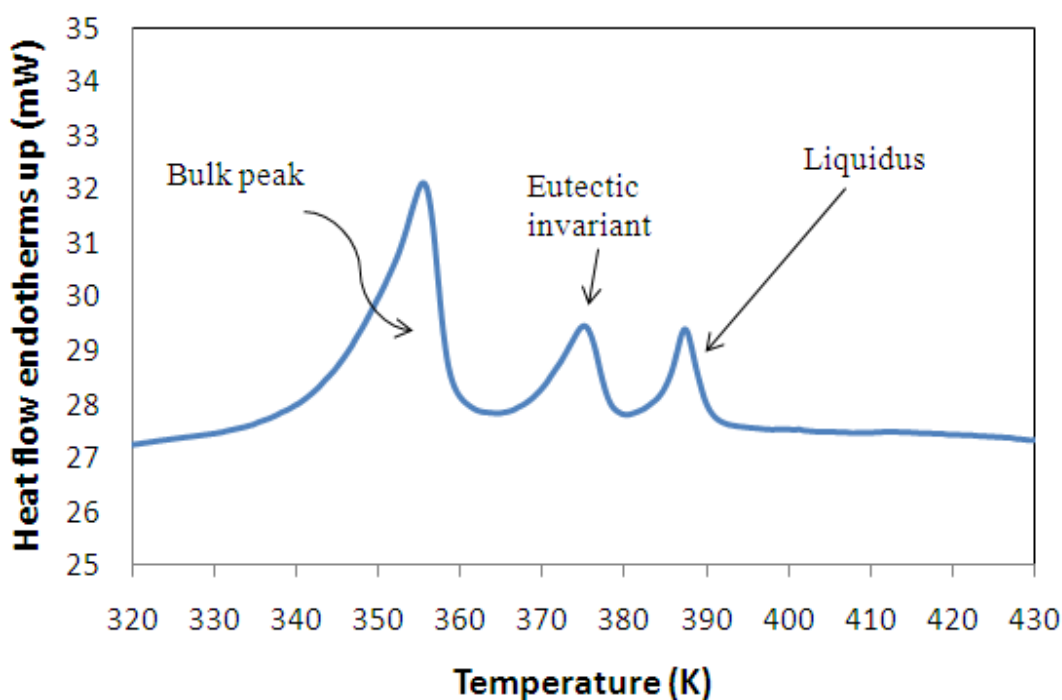


**Figure 6-4** A DSC thermogram for the mixture C9:0 and C5:0 amides on graphite. The mole fraction of C5:0 is 0.63. The bulk peak is indicated, and two distinct transitions arising from the monolayer are assigned as the eutectic invariant (376 K) and the liquidus peak, as explained in the text.

Figure 6-4 shows a DSC thermogram for the binary mixture of C9:0 and C5:0 amides on graphite, where the mole fraction of C5:0 is 0.63. This thermogram shows a relatively larger bulk melting peak and two additional transitions, at 377 K and 388 K. The peak at 377 K was observed at approximately the same temperature for several compositions of this mixture, whereas the higher temperature transition varied with temperature. The significance of these transitions is explained below.

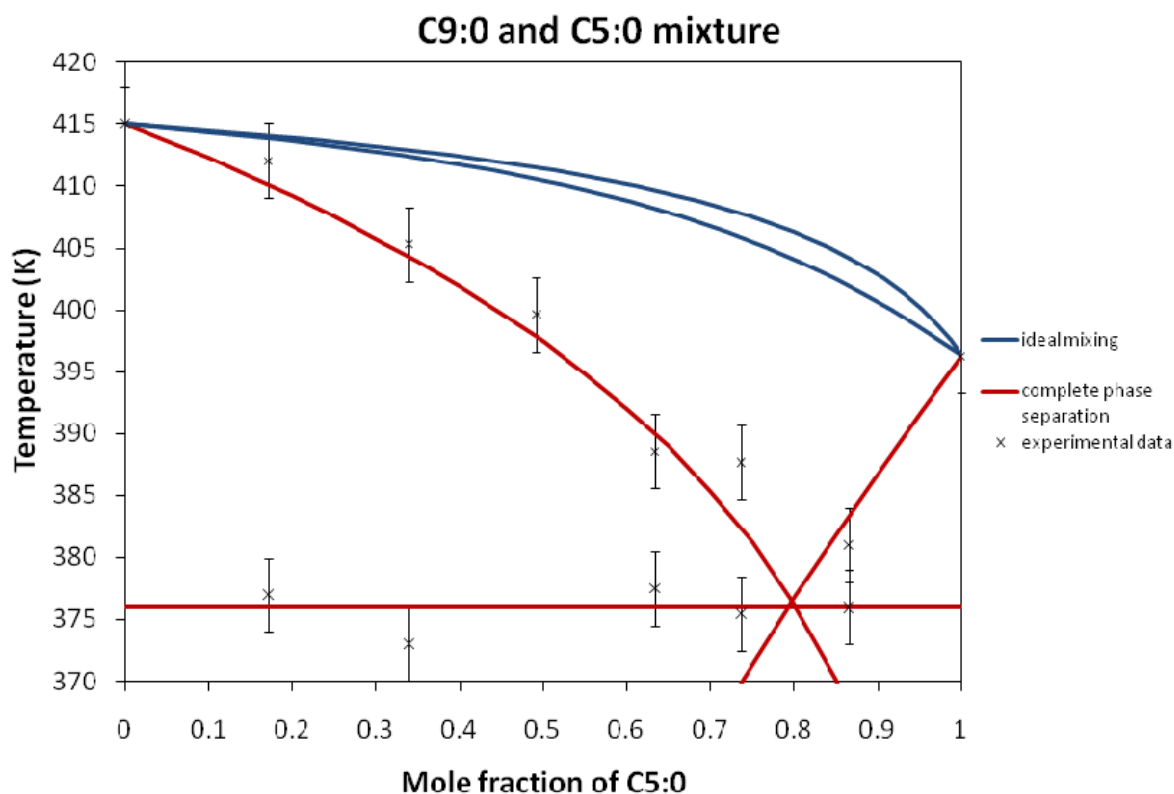


**Figure 6-5** Diagram illustrating a phase separated binary mixture of C9:0 and C5:0 amides on graphite. The calculations assuming ideal mixing are also shown for comparison. Vertical lines represent an error in the temperature measurements due to uncertainties in estimating the baseline of the monolayer peaks accurately

Figure 6-5 shows the monolayer phase diagram for a mixture of C9:0 and C5:0 amides. The red lines in Figure 6-5 are those expected if complete phase separation occurs in the solid monolayer, and the eutectic invariant is also shown (horizontal red line).

Based on the observation that the transition at 377 K in the thermograms (Figure 6-4) remains approximately constant with composition, and the temperatures of the higher melting peaks fit well with a completely phase separated model (Figure 6-5), it can be concluded that the monolayer for this mixture is completely phase separated in the solid state. The low temperature transition in the DSC thermograms can thus be attributed to the eutectic invariant and the higher temperature transition to the liquidus (§3.2.3.1).

The mixing behaviour in the monolayer of the C9:0 and C5:0 amides can be explained in terms of the monolayer structures of the pure materials as calculated by diffraction (chapter 4).

Structures of C9:0 and C5:0 amides have different plane groups ( $p2$  and  $pgg$  respectively). This would prevent mixing in the solid state, where the replacement of one molecule by another in the crystal lattice is a central issue, and result in phase separation [10].

### 6.2.1.2 C9:0 and C7:0 mixture

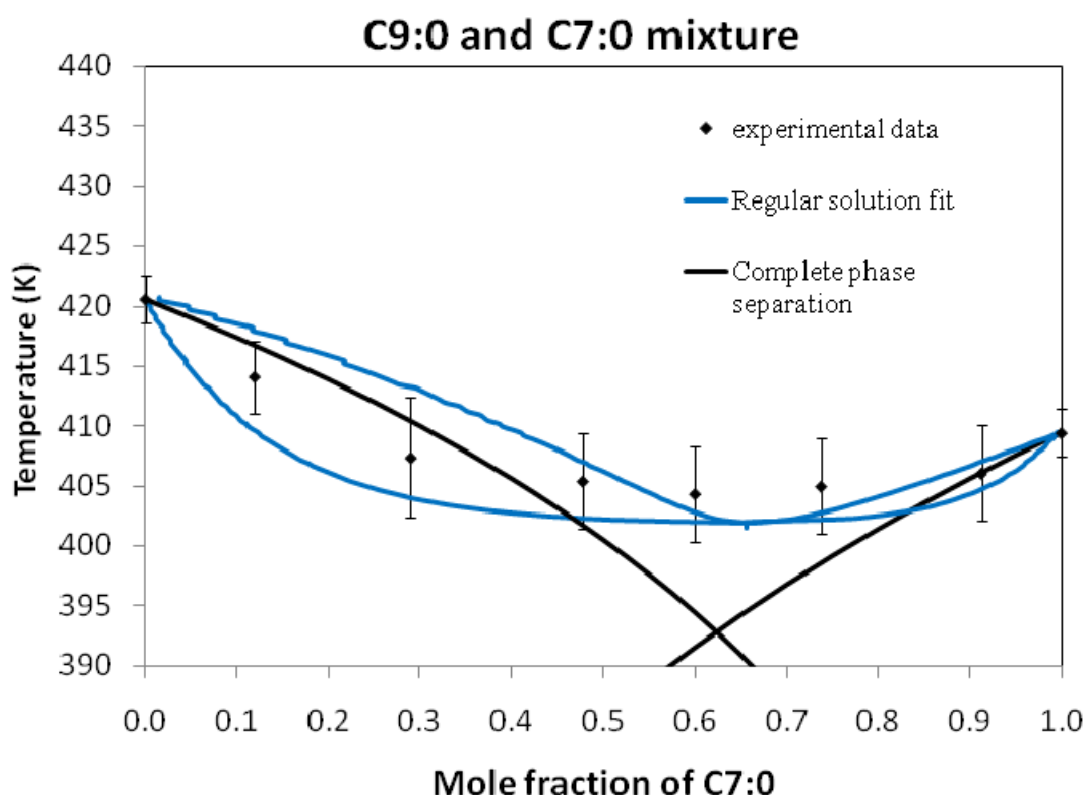


**Figure 6-6** Phase diagram of a mixture of C9:0 and C7:0 amides on graphite illustrating the high degree of non-mixing in the system. The calculated phase boundary lines from the regular solution model and complete phase separation are shown for comparison. The vertical lines on the experimental data indicate the ‘spread’ of the two-phase region as explained in the text.

The binary phase diagram of C9:0 and C7:0 amides on graphite is shown in Figure 6-6. The experimental data agrees more with the regular solution model rather than the calculations for a completely phase separated system, although the mixture does exhibit a very high degree of non-mixing in the monolayer, with  $\Omega$  very close to  $2RT$  (Table 6-2 shown on page 6-14). This means that the solid layer is close to being completely phase separated ( $\Omega$  equals  $2RT$  for onset of phase separation).

The DSC thermograms for this mixture (not presented) showed very broad transitions for the monolayer melting. The broadening is reflected in the ‘height’ of the two-phase region extending over a wider temperature range. This height is a function of the enthalpies of the pure materials, which further supports the regular solution fit to the experimental data (Figure 6-6).

If the solid layer were completely phase separated, then a transition occurring at  $\sim 392$  K (where the phase separation lines intersect in Figure 6-6) and remaining constant with the mixture composition would be expected. However, such a feature was not observed in the thermograms (not shown), which also supports the regular solution fit to the data.

The diffraction results for the individual components presented in chapter 4 can rationalise the mixing behaviour reported here. C7:0 possesses a low temperature *pgg* symmetry phase which is different to the C9:0 amide (*p2* symmetry). However, C7:0 amide undergoes a solid-solid phase transition to the *p2* symmetry structure (chapter 4) which possibly prevents complete phase separation and allows for highly non-ideal mixing.

### 6.2.1.3 C9:0 and C11:0 mixture

Figure 6-7 shows that the experimental data for C9:0 and C11:0 mixture agrees with the regular solution model (i.e. non-ideal mixing) and not with the calculations for a completely phase separated case. This behaviour can again be explained by the monolayer structures presented in chapter 4.

For molecules that have the same plane group, an isomorphism coefficient can be calculated ([10], §3.1.5). Both C9:0 and C5:0 amides have structures which have the same plane group (*p2*) and the isomorphism coefficient for these molecules is 0.82 (Table 6-2). Systems that have an isomorphism coefficient below  $\sim 0.76$  exhibit a high degree of non-mixing, and in excess of  $\sim 0.76$  show increasing extent of partial mixing. Hence, for the C9:0 and C11:0 amide mixture, some amount of deviation from ideal mixing is expected. For comparison, the binary mixture of C<sub>9</sub> and C<sub>11</sub> carboxylic acids exhibits a similar small depression in freezing point ( $\sim 7$  °C) [1].

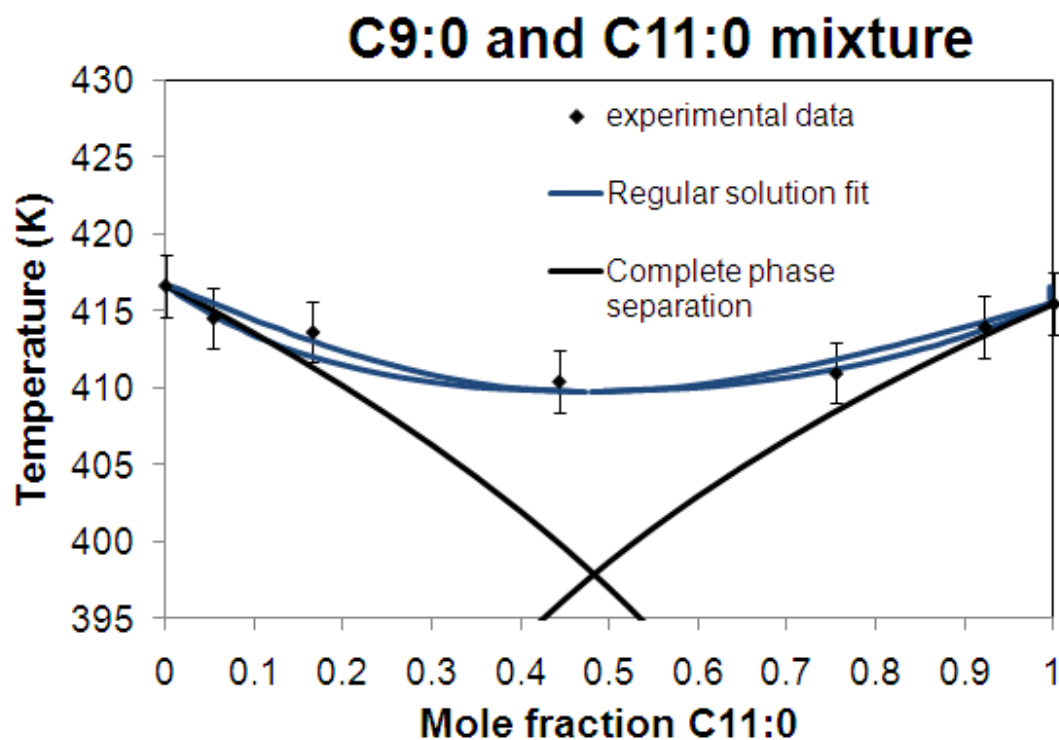


**Figure 6-7** DSC phase diagram for the mixture of C9:0 and C11:0 amides adsorbed on graphite illustrating that the molecules mix on the surface. Vertical lines are the FWHM of the monolayer melting peaks. Regular solution parameters for this fit are listed in Table 6-2.

#### 6.2.1.4 Discussion

**Table 6-2** Fitting parameters for the phase diagrams of saturated/saturated amide mixtures. The errors in  $\Omega$  and  $K$  are  $\sim 0.25$  kJ/mol and 0.1 respectively.

| System     | $\Omega$<br>kJ/mol            | $\Omega/2RT$ | $K$ | Isomorphism<br>coefficient |
|------------|-------------------------------|--------------|-----|----------------------------|
| C9:0/C5:0  | completely phase<br>separated | 1.0          | -   | -                          |
| C9:0/C7:0  | 5.25                          | 0.79         | 0.9 | -                          |
| C9:0/C11:0 | 1.75                          | 0.26         | 1.0 | 0.82                       |

Table 6-2 lists the parameters that were used to fit the monolayer phase diagrams of the saturated/saturated amide mixtures shown in this section. The mixing behaviour reported here is explained by the structural symmetry of the individual mixing components presented in chapter 4.

As well as the interest in the monolayer structures in their own right, this study was also aimed at understanding the results of previous work on the mixing behaviour of amides on graphite [3]. The objective here was to provide a structural basis for the interpretation of the mixing behaviour.

The structures of the even chain length saturated amides presented here help rationalise the mixing behaviour seen in the amide monolayers previously [3]. Mixtures of C8:0 amide with C6:0 and C10:0 amides were found to mix well, and this is explained by the isomorphism of these structures [10] (chapter 3). Mixtures of C8:0 amide with C12:0 and C16:0 amides were found to increasingly demix, a feature that can be attributed to the chain length difference in these molecules rather than differences in their plane groups.

### 6.2.2 Saturated/unsaturated amide mixtures

Phase diagrams for binary mixtures of saturated/unsaturated amides that have the same chain length are presented in this section. Combinations of mixtures where the monolayer structures for both components are available are chosen for study here. The results are then compared with the monolayer structures of the individual components discussed in chapters 4 and 5.

### 6.2.2.1 Saturated/trans-unsaturated amide mixtures

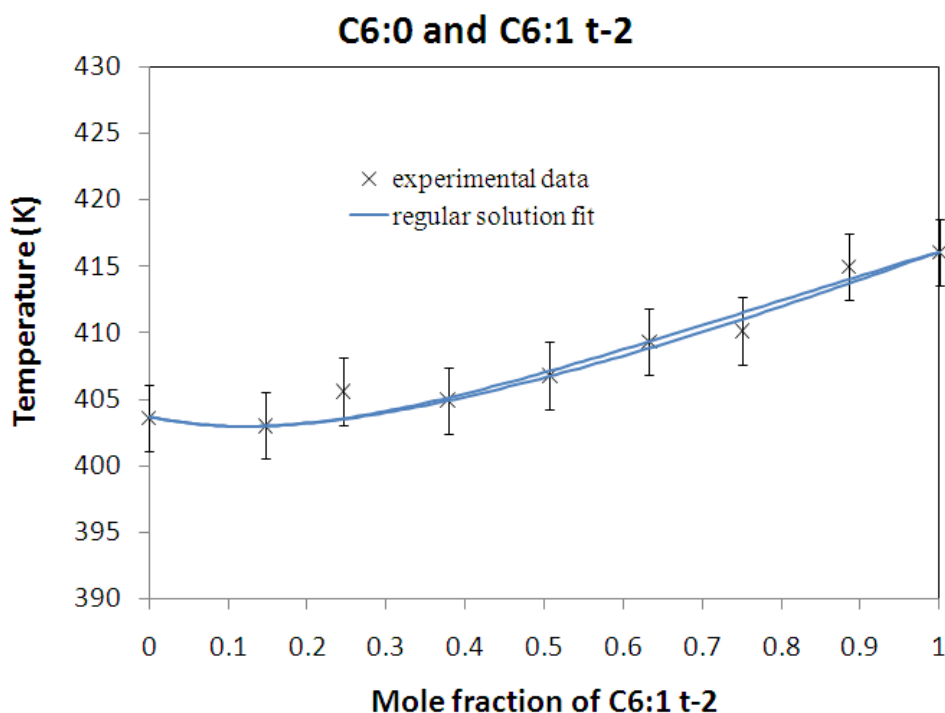


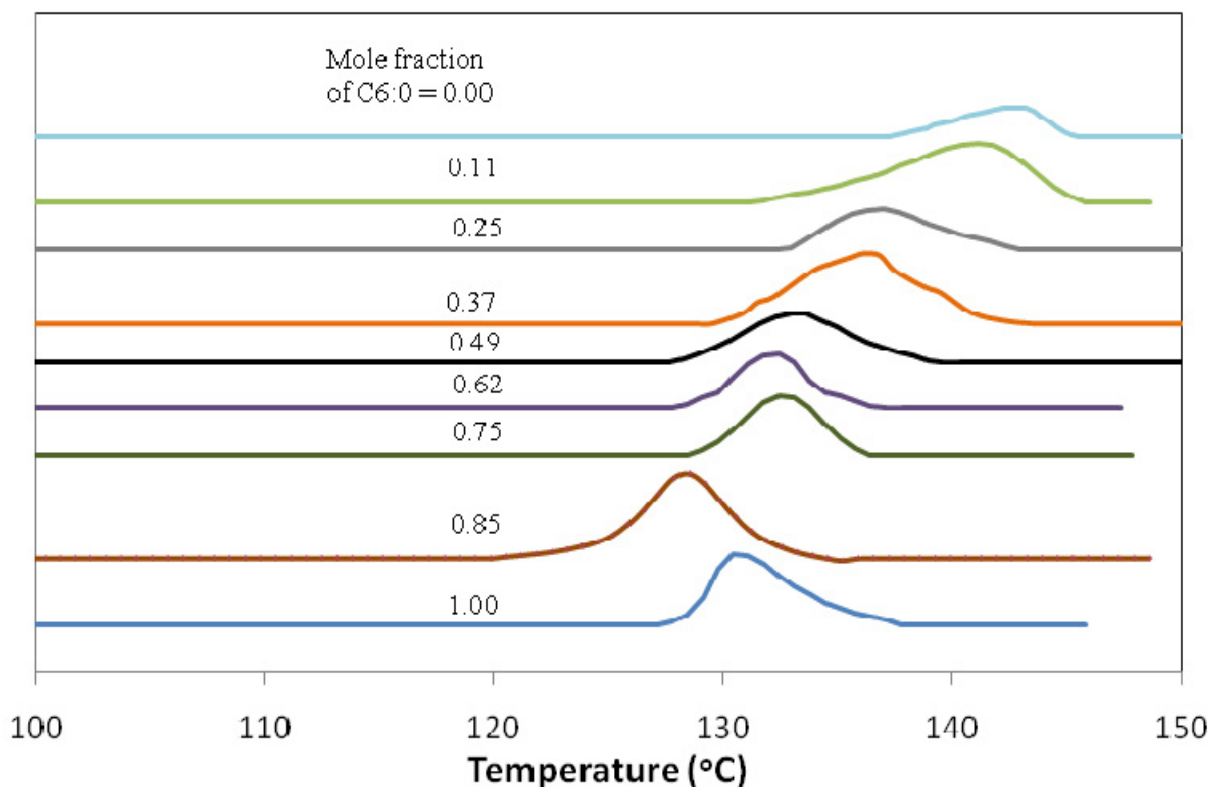
**Figure 6-8** Regular solution fit to the DSC phase diagram of C6:0 and C6:1 t-2 amides adsorbed on graphite. The vertical lines represent the FWHM of the experimental monolayer melting peaks.

The experimentally determined phase diagram for the mixture of C6:0 and C6:1 t-2 amides is shown in Figure 6-8. The data fits well to a regular solution model as shown in the figure. A small value of  $\Omega/2RT$  (Table 6-3 on page 6-20) indicates that the amides mix nearly ideally.

Figure 6-9 shows a series of DSC thermograms for a mixture of C6:0/C6:1 t-2 amides. The monolayer peaks move gradually from the melting point of the higher melting component (C6:1 t-2 amide) to the lower melting component (C6:0 amide).

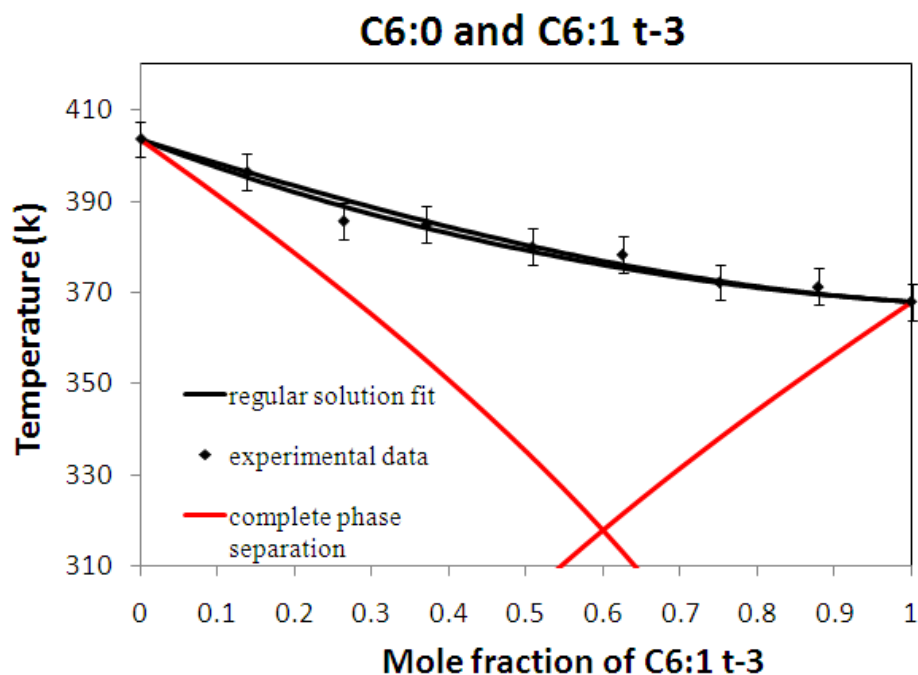
Both components possess similar structures in their monolayers as discussed in chapters 4 and 5, which is reflected in their isomorphism coefficient being close to unity (0.95). Hence essentially ideal mixing is expected for this system.

It can be seen that the ‘width’ of the regular solution calculations (Figure 6-8) is small compared to the width of the monolayer melting peaks (Figure 6-9). This is due to the relatively fast scan rate on the DSC (40 °C.min) which is needed to observe the weak monolayer transitions.



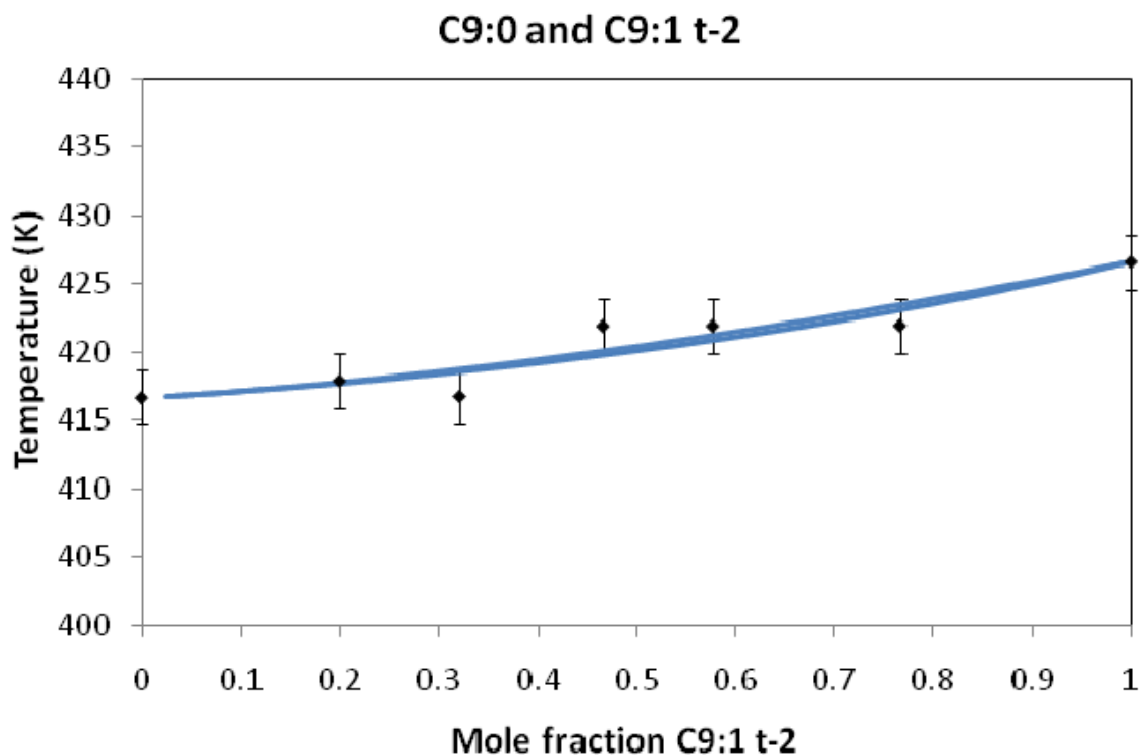
**Figure 6-9** DSC thermograms for a mixture of C6:0 and C6:1 t-2 amides adsorbed on graphite with varying compositions of the mixture. Bulk peaks are not shown for clarity.

Figure 6-10 shows the phase diagram for the monolayer mixture of C6:0/C6:1 t-3 amides and the regular solution parameters are listed in Table 6-3. These amides are found to mix almost ideally and do not exhibit any noticeable depression of freezing point predicted by the phase separation model. This is in agreement with the similar monolayer structures of the individual components described in chapters 4 and 5. Unlike C6:1 t-2 amide where the conjugation of the C=C double bond with the amide head group causes an increase in melting point as shown previously, C6:1 t-3 amide melts at a lower temperature than the saturated amide C6:0.



**Figure 6-10** DSC phase diagram for a binary mixture of C6:0 and C6:1 t-3 amides on graphite. The calculations for a completely phase separated case are also shown for comparison.

The phase diagram for C9:0/C9:1 t-2 amide mixture is shown in Figure 6-11. The amides are again found to mix almost ideally as indicated by the small  $\Omega/2RT$  value and favourable isomorphism coefficient (Table 6-3). C9:1 t-2 amide melts at a higher temperature than the C9:0 amide since the double bond is conjugated with the amide head group.



**Figure 6-11** Binary phase diagram for C9:0 and C9:1 t-2 amides on graphite along with the regular solution fit for this mixture

### 6.2.2.2 Discussion

Table 6-3 summarises the regular solution parameters for the fitted phase diagrams of the saturated/*trans*-unsaturated amide mixtures. Most mixtures are found to mix better in the monolayer than in the bulk as indicated by the  $\Omega$  values, and improved mixing in the monolayer has been reported for several alkyl species previously [11]. A difference in chain length is an important factor in considering preferential adsorption, as explained in chapter 3. In the saturated/unsaturated mixtures studied here, it is found that there is almost no preference for adsorption of either species, since both components have the same chain length. This is seen in the preferential adsorption constant ( $K$ ) values of these mixtures being nearly equal to 1 (Table 6-3).

Table 6-3 Regular solution parameters for mixtures of saturated/*trans*-unsaturated amides on graphite

| System        | $\Omega$<br>kJ/mol | $\Omega/2RT$ | K   | Isomorphism<br>coefficient | Bulk $\Omega$<br>kJ/mol |
|---------------|--------------------|--------------|-----|----------------------------|-------------------------|
| C6:0/C6:1 t-2 | 0.45               | 0.07         | 1.2 | 0.95                       | 2.50                    |
| C6:0/C6:1 t-3 | 0.75               | 0.05         | 1.0 | 0.93                       | 2.60                    |
| C9:0/C9:1 t-2 | 0.25               | 0.04         | 1.0 | 0.97                       | 1.85                    |

In summary, all saturated/*trans*-unsaturated amides are found to mix almost ideally. These observations agree with the monolayer structures of the individual components: all *trans*-unsaturated amides possess very similar structures to the corresponding saturated amide. This is seen in their isomorphism coefficients being close to unity which thus promotes mixing [10].

### 6.2.2.3 Saturated/*cis*-unsaturated amide mixtures

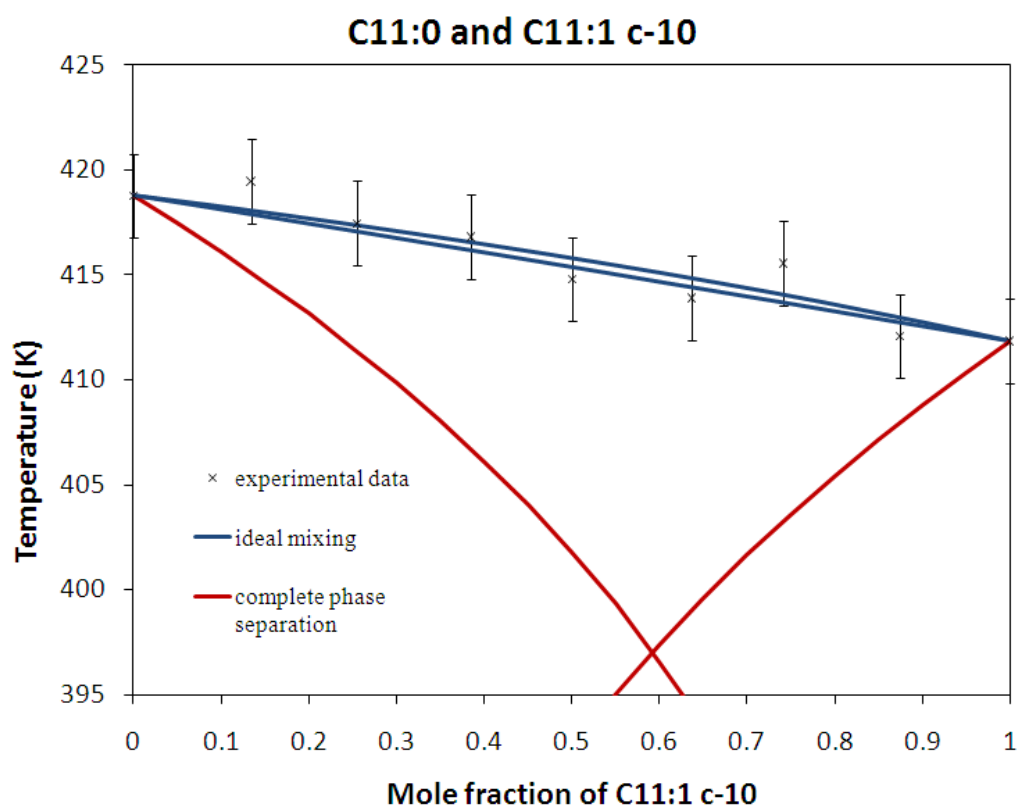
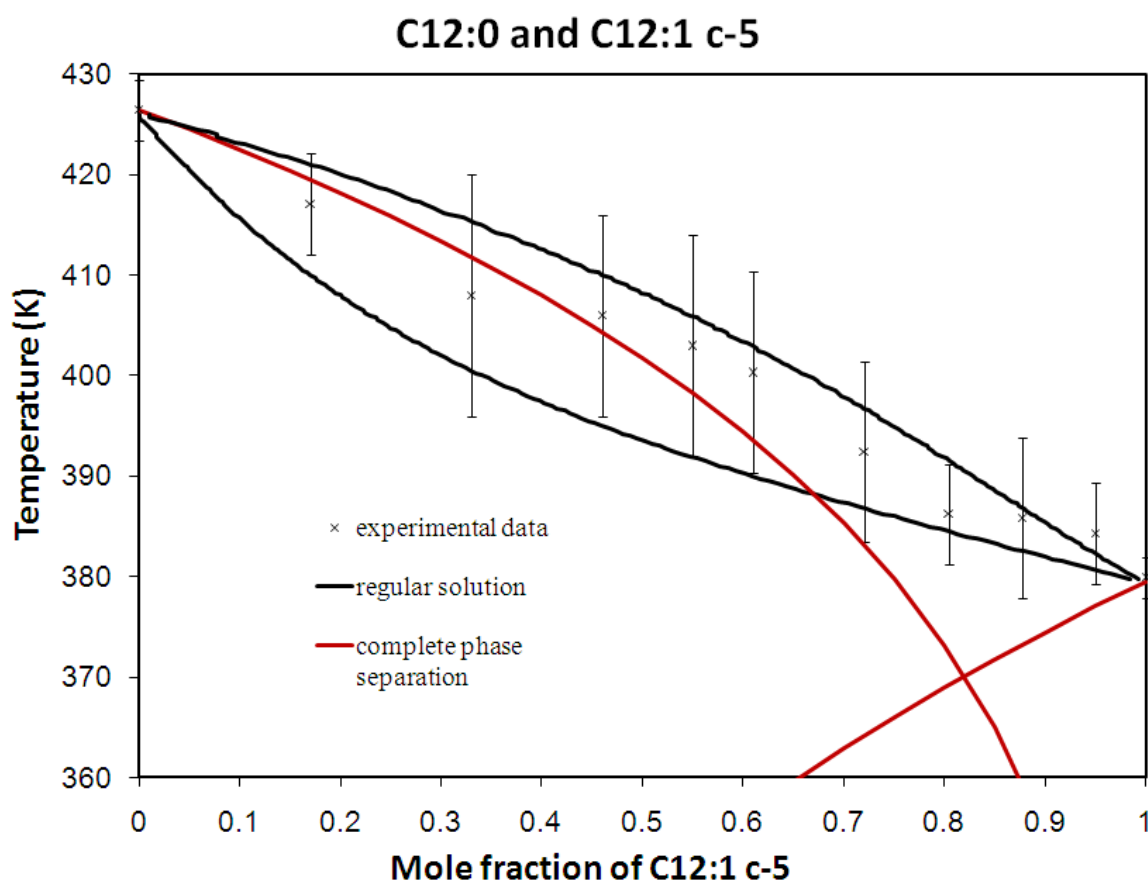


Figure 6-12 Phase diagram for a binary mixture of C11:0 and C11:1 c-10 amides on graphite illustrating that the molecules mix ideally

The binary phase diagram for a mixture of C11:0/C11:1 c-10 amides is shown in Figure 6-12. The data shows that these amides mix ideally in the monolayer. As explained before, the terminal double bond makes the C11:1 c-10 molecule very similar to the saturated amide as suggested by its monolayer structure (chapter 5) and melting point (Table 6-1). This enables favourable interactions between the two molecules, thereby promoting ideal mixing in the monolayer.



**Figure 6-13** DSC phase diagram for a non-ideal mixture of C12:0 and C12:1 c-5 amides on graphite. The phase boundary lines for the completely phase separated case are also shown for comparison. The vertical lines on the experimental data represent the FWHM of the monolayer melting peaks.

Figure 6-13 shows the phase diagram of C12:0 and C12:1 c-5 amides. The monolayer melting peaks in the thermograms were found to be very broad in the middle of the composition range, and were often seen as the superposition of two separate peaks. Hence the vertical lines for the

experimental data in the figure spread over a wide range and this is confirmed by the ‘broad’ regular solution fit to the data.

The fact that these two molecules mix to some extent can be somewhat surprising since the C12:1 *c*-5 amide has a bend in the middle of the alkyl chain, which could make close packing difficult in the mixed solid layer. However, the unit cell dimensions of the structure of C12:1 *c*-5 amide were found to be almost identical to C12:0 as shown in chapter 5, which gives an isomorphism coefficient value of 0.97 (Table 6-4 below). The structures have the same plane group (*p*2) and remarkably similar hydrogen bond geometries. This is a key finding in explaining the mixing behaviour reported here.

Consolidating these facts, the fit to the phase diagram of the C12:0/C12:1 *c*-5 amide can be looked at as a ‘compromise’: the molecules do not mix ideally, but do not phase separate completely either. The value of  $\Omega$  is 30% of that of 2RT (Table 6-4) which suggests there is considerable non-ideality in this mixture. It is difficult to verify the unexpected mixing behaviour of C12:0/C12:1 *c*-5 amides by X-ray diffraction since the experimental patterns for these amides have very similar peak positions (and monolayer structures) to notice any shift in the peaks of the mixture (chapter 5).

As will be discussed in §6.4, every effort was made to ensure that the amides used for this work were of high purity. As listed in appendix B, the purities of C12:0 and C12:1 *c*-5 amides used here were >98%. The DSC samples for all mixtures studied here were prepared at a coverage of ~5-10 monolayers. Thus, even if all the impurity in the samples were adsorbing in preference to the compound of interest, then only a maximum of 0.2 monolayers of the graphite can be covered by the impurity at any time, and this is not expected to greatly affect the observed results.

#### 6.2.2.4 Summary

Table 6-4 summarises the regular solution parameters for the mixtures of the two saturated/*cis*-unsaturated amides on graphite. Again, the molecules are found to mix better in the monolayer than in the bulk as indicated by the  $\Omega$  values. The isomorphism coefficient for both mixtures is again close to unity. C11:0/C11:1 *c*-10 amides are found to mix ideally in the monolayer and

diffraction results provide some insight into the unexpected mixing behaviour of C12:0/C12:1 c-5 amides.

**Table 6-4** Regular solution parameters for mixtures of saturated/*cis*-unsaturated amides on graphite

| System           | $\Omega$<br>kJ/mol | $\Omega/2RT$ | K   | Isomorphism<br>coefficient | Bulk $\Omega$<br>kJ/mol |
|------------------|--------------------|--------------|-----|----------------------------|-------------------------|
| C11:0/C11:1 c-10 | 0.00               | 0.00         | -   | 0.98                       | 0.40                    |
| C12:0/C12:1 c-5  | 2.00               | 0.30         | 0.9 | 0.97                       | 5.00                    |

## 6.3 Coverage dependence study of undecanamide (C11:0 amide) on graphite by DSC

### 6.3.1 C11:0 coverage dependence - introduction

As explained in chapter 1, a variety of adsorbates on graphite show several transitions in their adsorbed layers. These include additional layer melting transitions, solid-solid phase transitions, and monolayer ‘gas-liquid-solid’ transformations [12], which depend on the temperature and coverage.

Many amides show several monolayer transitions on graphite as observed by DSC which are not seen in the pure amide sample alone [3]. The diffraction measurements presented in chapter 3 have already indicated the existence of a solid-solid phase transition for C7:0 amide at sub-monolayer coverage.

Differential Scanning Calorimetry has been used previously to study the adsorbed behaviour of dodecanol on graphite, where the presence of several additional layer melting transitions were identified [13]. As a preliminary study, the behaviour of C11:0 amide adsorbed on graphite as a function of coverage (exposure) is investigated here.

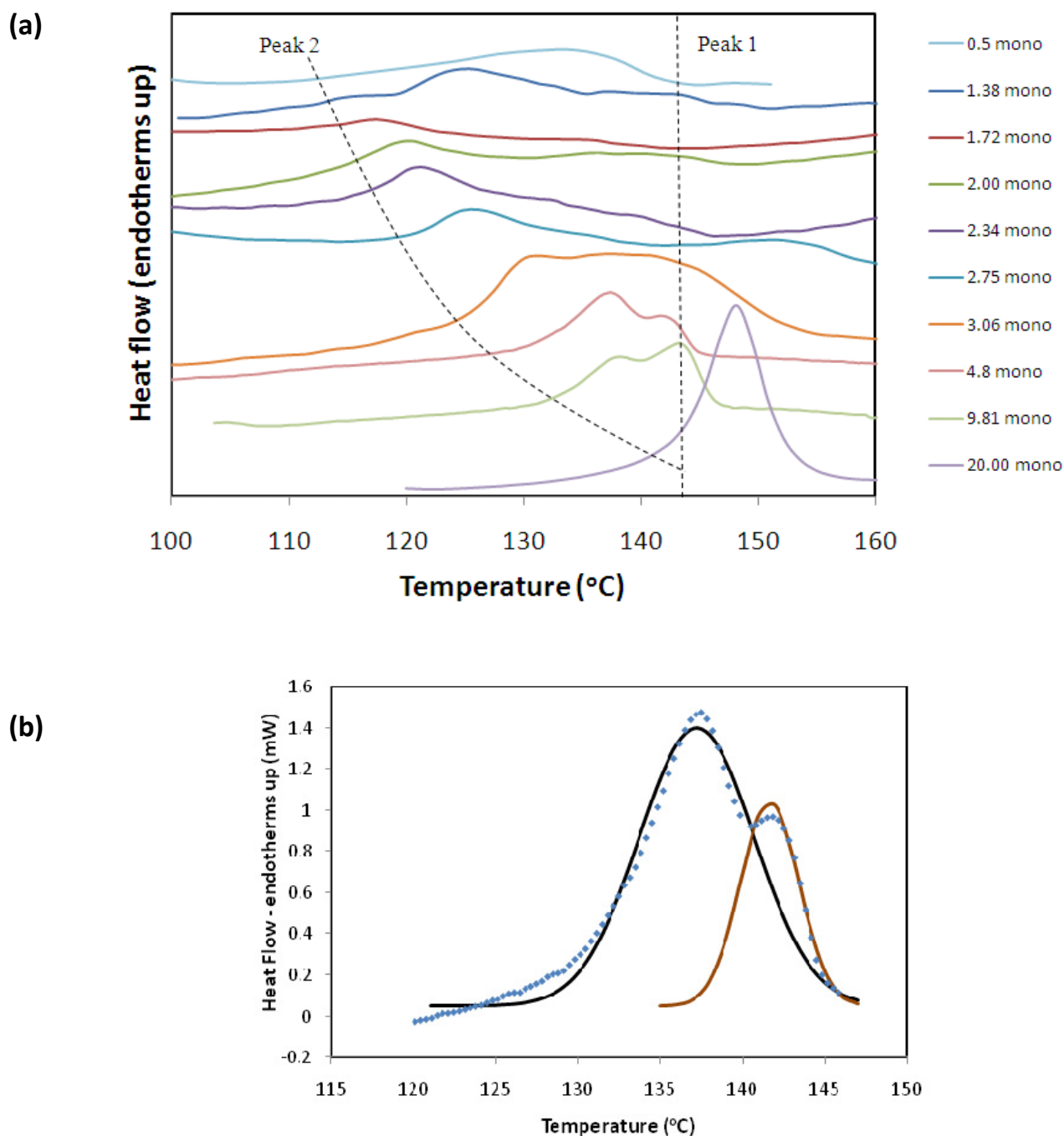
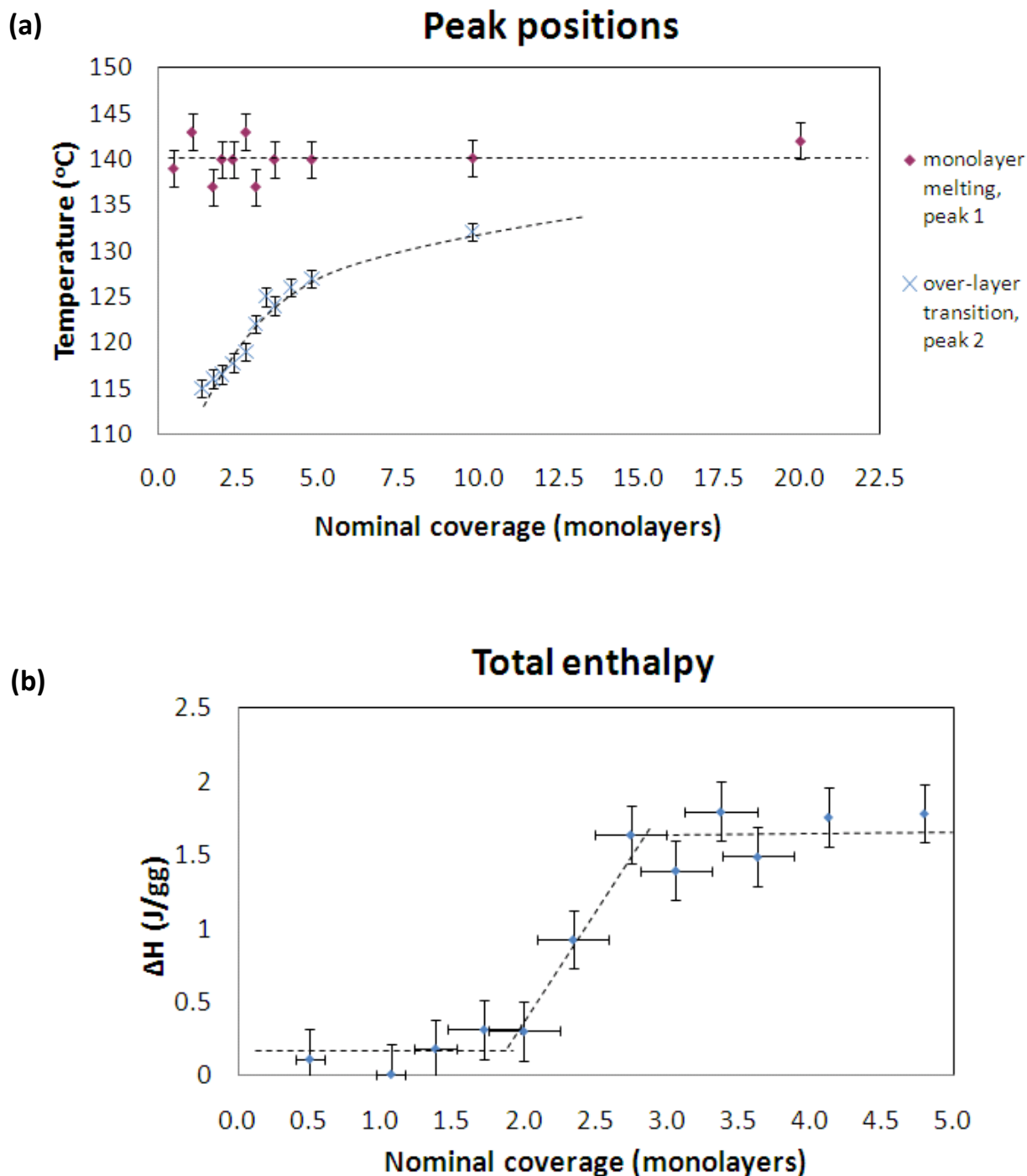


**Figure 6-14 (a)** DSC thermograms of C11:0 amide adsorbed on graphite at different nominal coverages. The dotted lines are a guide to the eye indicating the melting temperatures of the monolayer melting (straight line, peak 1) and the overlayer phase transition (curved line, peak 2). These dotted lines pass through the approximate onset temperatures of the transitions, and not the peak temperatures. Bulk peaks (not shown for clarity) are found to occur at 80-84 °C **(b)** Representative Gaussian fits (solid lines) to overlapping experimental DSC peaks (points) in the thermogram of C11:0 amide at 4.8 monolayers nominal coverage illustrating the procedure used to extract enthalpies. The area enclosed by each peak is given by the area of the Gaussian curve fitted through it.



### 6.3.2 C11:0 coverage dependence - experimental details

This experiment considering low coverage monolayer melting features is experimentally challenging, particularly because the transitions in the thermograms are very weak indeed. The weak nature of the DSC peaks has necessitated the use of very high heating and cooling rates (100-200 °C/min), and the transitions were often identified more easily in cooling rather than heating runs. Even in the best cases there is still significant uncertainty in any single data set. However, collectively the data does exhibit much of the behaviour that is expected and careful peak fitting has been used to extract appropriate trends.

Samples up to a nominal coverage of 4 monolayers were prepared by annealing the weighed sample and graphite under reduced pressure, and samples above 5 monolayers were prepared directly in the DSC pans as discussed in chapter 3. The coverages here are nominal, and are based only on the exposure time rather than on measurement of the actual amount adsorbed.

With such weak peaks, base line subtraction is important. Here the baselines of the raw thermograms data were adjusted by fitting a polynomial through them, similar to the procedure used to correct the curved baselines in diffraction patterns (explained in chapter 2), using regions of the data either side of the peaks where there was background only.

The *Pyris* software of the DSC calculates the areas associated with peaks in the thermograms and therefore the enthalpy of the corresponding transition. As discussed however, owing to the weak nature of the transitions, there can often be a very large error in this enthalpy due to the large uncertainty in estimating the baseline of the peak accurately. This was made more difficult by the peaks overlapping at faster scan rates, required to observe these weak transitions. Hence, the DSC peak shape was fitted by Gaussian functions and the area used to provide an estimate of the monolayer transition enthalpies (illustrated in Figure 6-14 (b)).

### 6.3.3 C11:0 coverage dependence - results and discussion

Figure 6-14 (a) shows the thermograms obtained at different nominal coverages of C11:0 amide on graphite. Thermograms show two transitions above the bulk melting point (~ 83 °C). The higher transition ('peak 1' in the figure) occurs at ~145 °C and remains approximately constant ( $\pm 8$  °C) with coverage (Table 6-5 and Figure 6-15 (a)); this is attributed to be the monolayer melting. In addition, another transition ('peak 2') is observed to occur only at

coverages above a monolayer and its temperature increases as the coverage is increased (Table 6-5 and Figure 6-15 (a)). In some of the samples however, both peaks are not resolved owing to the very fast scanning rates of the DSC and a large, broad transition is observed. The monolayer enthalpies and peak positions are tabulated in Table 6-5.

Figure 6-15 (b) shows the total enthalpy of the two transitions as a function of nominal coverage. The enthalpy is approximately a ‘step’ curve: the enthalpy remains constant up to 1 monolayer, then increases progressively till ~2-3 layers and then remains constant for higher coverages.

Given the extremely weak signals and based on these observations, one could conclude that the peak 2 could be the melting of the second layer, and the increase in the transition temperature could be due to the layer being increasingly compressed with coverage. As explained in chapter 1, several adsorbates on graphite such as the noble gases and alcohols [13] show the formation of a number of layers above a monolayer. This has important implications in understanding the packing of the amide crystals in the bulk: similar to the alcohols the amides can be expected to grow in a layer-by-layer fashion.

**Table 6-5** Summary of the coverage dependence study of C11:0 amide. The temperatures reported here are onset values of the transitions and the enthalpy is in joules per gram of adsorbent (graphite).

| Nominal coverage<br>(monolayers) | Bulk peak <sup>+</sup> |                   | Over-layer transition<br>‘Peak 2’ |                   | Monolayer melting<br>‘Peak 1’ |                   | Total enthalpy<br>$\Delta H$ (J/gg) |
|----------------------------------|------------------------|-------------------|-----------------------------------|-------------------|-------------------------------|-------------------|-------------------------------------|
|                                  | $T^{3D}$ (°C)          | $\Delta H$ (J/gg) | $T^{2D}$ (°C)                     | $\Delta H$ (J/gg) | $T^{2D}$ (°C)                 | $\Delta H$ (J/gg) |                                     |
| 0.50                             | -                      | -                 | -                                 | -                 | 139.0                         | 0.11              | 0.11                                |
| 1.07                             | -                      | -                 | -                                 | -                 | 143.0                         | 0.01              | 0.01                                |
| 1.38                             | -                      | -                 | 115.0                             | 0.18              | NR*                           | -                 | 0.18                                |
| 1.72                             | -                      | -                 | 116.0                             | 0.31              | NR*                           | -                 | 0.31                                |
| 2.00                             | -                      | -                 | 116.5                             | 0.21              | 140.0                         | 0.10              | 0.31                                |
| 2.34                             | -                      | -                 | 117.8                             | 0.93              | NR*                           | -                 | 0.93                                |
| 2.75                             | -                      | -                 | 119.0                             | -                 | 152.0                         | 1.64              | 1.64                                |
| 3.06                             | -                      | -                 | 122.0                             | -                 | 137.0                         | 1.40              | 1.40                                |
| 3.38                             | -                      | -                 | 125.0                             | -                 | 140.5                         | 1.80              | 1.80                                |
| 3.63                             | -                      | -                 | 124.5                             | -                 | 140.0                         | 1.49              | 1.49                                |
| 4.13                             | 80.0                   | -                 | 126.0                             | -                 | 141.2                         | 1.76              | 1.76                                |
| 4.80                             | 82.0                   | 0.40              | 127.0                             | -                 | 140.0                         | 1.79              | 1.79                                |
| 9.81                             | 81.5                   | 2.81              | 132.1                             | 0.79              | 140.2                         | 0.82              | 1.61                                |
| 20.00                            | 82.8                   | 20.64             | -                                 | -                 | 142.0                         | 1.81              | 1.81                                |

\*NR=Peaks not resolved by the DSC <sup>+</sup>bulk peaks not shown in Figure 6-14 for clarity

The bulk melting peak is not observed in most of the samples below 4 layers nominal coverage (Table 6-5) and is readily seen in samples prepared directly in the DSC pans (>5 monolayers). This could be due to the fact that it is hard to adsorb more than a couple of layers of the amide molecules on the graphite surface under reduced pressure, as observed during the sample preparation. It is also equally difficult to measure such small amounts to prepare the samples directly in the DSC pans. Hence owing to these experimental limitations, there is an error associated with the nominal coverage of the samples as shown in Figure 6-15.

## 6.4 A note on purities

Adsorption studies require extremely clean conditions and very pure compounds since a small amount of impurity can easily adsorb in preference to the compound of interest and greatly affect the experimental results at higher coverages. Consistent efforts have been made to assess and optimise the purities of the amide molecules used in this work. A series of analytical tests were performed on each amide compound used: these include elemental analysis,  $^1\text{H}$  and  $^{13}\text{C}$  NMR and Liquid Chromatography/Mass Spectrometry (LC/MS). Each technique offers its own set of advantages and hence their combination has proven to be particularly advantageous. For example, NMR provided some indication about the nature of the impurity, if present. This technique could indicate if there was some amount of saturated impurity present in an unsaturated amide sample and whether some of the unreacted carboxylic acid was still present. Details of these test results for all the amide molecules used here are provided in appendix B.

Since the amide molecules prepared in-house were synthesised from the corresponding carboxylic acid, the amount of nitrogen incorporation (C:N ratio) was used to assess the purity from elemental analysis results. It should be noted that the measurements made at low coverage are far less sensitive to the presence of impurities. The amount of impurity in a monolayer when only one layer is present is typically a couple of percent and has minimal effect on the observed behaviour. Only impurities such as longer homologues which adsorb in preference to the compound of interest will be of greater concern at higher coverages. Given the high purities of the amide samples here (appendix B), the presence of impurities is not expected to affect the experimental results shown here, even at high coverage (up to 10 monolayers).

## 6.5 Summary

The adsorption of alkyl amides on graphite has been investigated by Differential Scanning Calorimetry (DSC), and the results have been presented in this chapter. All amide monolayers studied here exhibit a melting transition as observed by the DSC, at temperatures well above (10-20% above) the bulk melting point.

The monolayer melting temperature of saturated amides increases as the chain length is increased. There exists an 'odd-even effect' in the melting enthalpies of the saturated amides, and an 'odd-even effect' in the monolayer structures has already been presented in chapter 4. Monolayers of most unsaturated amides are found to melt at a temperature lower than that of the saturated amide with the same chain length. However, unsaturated amides that have a trans-double bond conjugated to the amide head group show increased stability in the monolayer compared to their saturated counterparts, as seen in their melting points. This effect is attributed to the extended electron delocalisation around the amide group, which could increase the strength of the hydrogen bond, as observed in similar bulk structures.

Phase diagrams of binary mixtures of saturated/saturated and saturated/unsaturated amides have been measured using DSC and analysed quantitatively using ideal mixing, eutectic and regular solution models. Mixtures of saturated amides are found to mix (non-ideally) in the monolayer if the structural plane groups of the mixing components are the same, and phase separate if not. All saturated/*trans*-unsaturated amide mixtures studied mix essentially ideally, attributed to the similarity in their monolayer structures. Diffraction results have also provided some rationale into the unusual mixing behaviour of C12:0/C12:1 *c*-5 amides. The monolayer structures presented in chapter 4 also explain the mixing behaviour seen in amide layers in a previous study [3].

Results from an investigation of the coverage dependent behaviour of C11:0 amide have been presented. Two transitions have been observed; a monolayer melting transition which essentially remains constant in temperature as the coverage is increased (1-20 monolayers) and an additional transition seen in the thermograms has been attributed to a possible second layer melting transition of the adsorbate.

## 6.6 References

1. Bickerstaffe, A., L. Messe, S.M. Clarke, J. Parker, A. Perdigon, N.P. Cheah, and A. Inaba, *Mixing behaviour of carboxylic acids adsorbed on graphite*. Physical Chemistry Chemical Physics, 2004. **6**(13): p. 3545-3550.
2. Phillips, T.K., T. Bhide, S.M. Clarke, S.Y. Lee, K.S. Mali, and S.D. Feyter, *Adsorption of Aldehydes on a Graphite Substrate: Combined Thermodynamic Study of C6-C13 Homologues with a Structural and Dynamical Study of Dodecanal*. The Journal of Physical Chemistry C, 2010. **114**(13): p. 6027-6034.
3. Arnold, T., Clarke, S. M., *Thermodynamic Investigation of the Adsorption of Amides on Graphite from Their Liquids and Binary Mixtures*. Langmuir, 2008. **24**(7): p. 3325-3335.
4. Abate, L., E. Badea, I. Blanco, and G. Della Gatta, *Heat Capacities and Enthalpies of Solid-Solid Transitions and Fusion of a Series of Eleven Primary Alkylamides by Differential Scanning Calorimetry*. J. Chem. Engg. Data, 2008. **53**(4): p. 959-965.
5. Arnold, T., *The adsorption of alkanes from their liquids and binary mixtures*. 2001, D. Phil Thesis, University of Oxford: Oxford.
6. Bickerstaffe, A.K., N.P. Cheah, S.M. Clarke, J.E. Parker, A. Perdigon, L. Messe, and A. Inaba, *The Crystalline Structures of Carboxylic Acid Monolayers Adsorbed on Graphite*. J. Phys. Chem. B, 2006. **110**: p. 5570-5575.
7. Gilli, G. and P. Gilli, *The Nature of the Hydrogen Bond*. International Union of Crystallography Book Series. 2009, New York: Oxford University Press.
8. Sun, C. and S.M. Clarke, *unpublished work*, University of Cambridge: Cambridge.
9. Turner, J.D. and E.C. Lingafelter, *The X-ray crystallography of the n-aliphatic amides*. Acta Crystallographica, 1955. **8**(9): p. 549-550.
10. Clarke, S.M., Messe, L., Adams, J., Inaba, A., Arnold, T., Thomas, R. K., *A quantitative parameter for predicting mixing behaviour in adsorbed layers: the 2D isomorphism coefficient*. Chemical Physics Letters, 2003. **373**: p. 480-485.
11. Parker, J.E., *Adsorption at the solid/liquid interface: Adsorption and mixing behaviour of fluorinated alkyl species on the surface of graphite*, in *Department of Chemistry*. 2007, PhD thesis, University of Cambridge: Cambridge.
12. Thomy, A., X. Duval, and J. Regnier, *Two-dimensional phase transitions as displayed by adsorption isotherms on graphite and other lamellar solids*. Surf. Sci. Rep., 1981. **1**(1): p. 1-38.
13. Messé, L., A. Perdigon, S.M. Clarke, M.A. Castro, and A. Inaba, *Layer-by-layer surface freezing of linear alcohols at the graphite/liquid interface*. Journal of Colloid and Interface Science, 2003. **266**(1): p. 19-27.

# Chapter 7

## Adsorption at the Polymer/Air Interface

---

Structural and thermodynamic information obtained on the adsorption of alkyl amides on graphite as discussed in the previous chapters has helped improve the current understanding of these systems. Apart from using a graphite substrate which was the primary focus of this work, some efforts into understanding the adsorption of these compounds on polymer surfaces have also been made. This chapter provides a brief overview of the techniques used and presents some of the key results of such studies at the polymer/air interface.

As explained in chapter 1, amide molecules are generally added to the bulk of the polymer, particularly polyethylene and polypropylene, and adsorb at the air interface over time. The kinetics of this migration to the surface is an important factor in the performance of these industrial materials. Previous initial studies have indicated that very low concentrations of the alkyl amides are required in the bulk polymer (<1000 ppm), where only a small amount is adsorbed at the interface, making it very difficult to quantitatively study these systems. Moreover, an additional complication arises from the semi-crystalline nature of these materials; the surfaces are not 'flat' and hence difficult to study using approaches such as X-ray and neutron reflectivity that can provide information on the surface compositions of films. The polystyrene/air interface partly overcomes this problem as opposed to polyethylene, and the use of several techniques here has helped establish some important factors that need to be considered for this system.

In this work, thin films of polystyrene on a silicon wafer substrate with varying amounts of amides were prepared by spin coating. The wafers were then tested for coefficient of friction. Overall film thicknesses were estimated using ellipsometry and refined using X-ray reflection. To analyse the details of the amide layer on the surface, neutron reflection has been used.

## 7.1 Background

The experimental techniques of neutron, X-ray and light reflection used in this work to study the adsorption of amides at the polymer/air interface are explained briefly in this section.

### 7.1.1 Neutron reflection

#### 7.1.1.1 Basic theory

Neutron reflection can provide information about the structure and composition of films of thicknesses of the order of molecular dimensions. The neutron refractive index ( $n$ ) of a medium is [1]:

$$n = 1 - \frac{\lambda^2 N_d b}{2\pi} + i \frac{\lambda N_d \sigma_a}{4\pi}$$

... Eqn. 7-1

where  $N_d$  is the atomic number density,  $b$  is the bound coherent scattering length,  $\sigma_a$  is the absorption cross-section and  $\lambda$  is the neutron wavelength. The product  $N_d b = \rho$  is the neutron scattering length density (SLD). The neutron SLD varies across the periodic table and hydrogen and deuterium possess very different SLDs. This makes neutron reflection a very useful tool as media can be ‘contrast matched’ to highlight certain layers [2]. For most organic materials the imaginary part of Eqn. 7-1 can be neglected, as the absorption cross-section is small. The refractive index for most materials is less than unity which results in total external reflection below a particular critical angle ( $\theta_c$ ), which depends on the scattering length densities of the two bulk phases.

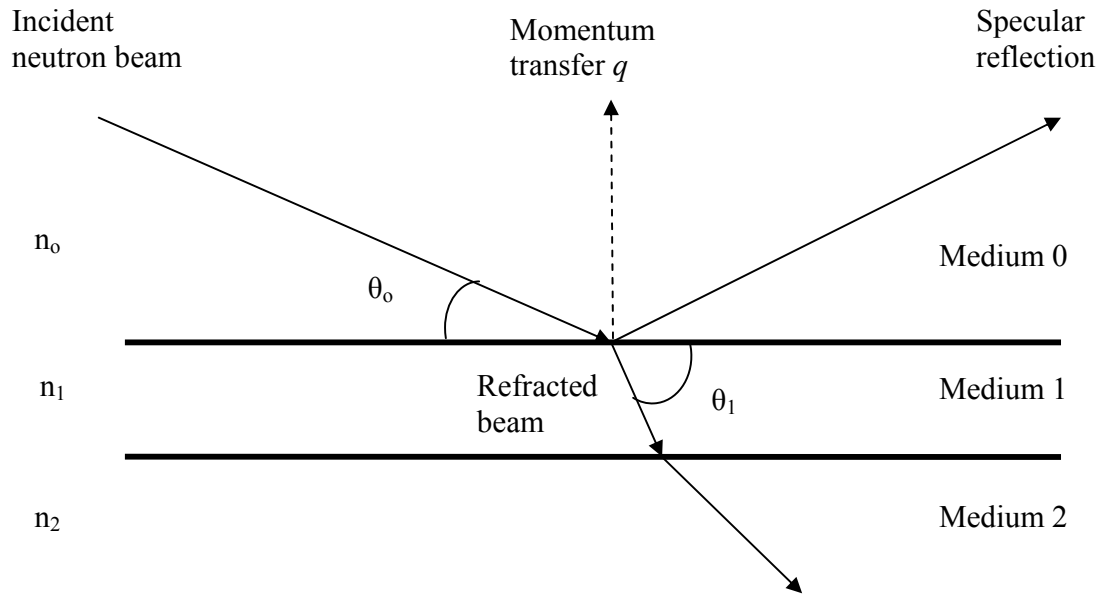


**Figure 7-1** Neutron reflection at an interface between two bulk media of refractive indices  $n_0$  and  $n_2$

Figure 7-1 shows that the momentum transfer vector for specular neutron reflection (i.e. angle of incidence = angle of reflection) is perpendicular to the interface, and thus this technique can provide information about the variation in composition normal to the interface. The specular reflection at an interface between two bulk media can be described by Fresnel's law. For a single film on a substrate, the interference of the waves from within the film results in a reflectivity ( $R$ ) profile of the form:

$$R = \left| \frac{r_{01} + r_{12} e^{2i\beta}}{1 + r_{01} r_{12} e^{2i\beta}} \right|^2$$

... Eqn. 7-2

Here  $r_{ij}$  is the Fresnel coefficient at the  $ij$  interface, given by:

$$r_{ij} = \frac{s_i - s_j}{s_i + s_j}$$

... Eqn. 7-3

In this equation  $s_i = n_i \sin \theta_i$  and  $\beta$  is the optical path length in the film given by  $\beta = (2\pi / \lambda)n_1 d \sin \theta_1$  [1], where  $n_l$  is the (complex) refractive index of medium  $l$  and  $d$  is the film thickness. A similar approach can be adopted for 2-3 layers [1].

For the systems considered here, the reflectivity is 1 till the critical angle  $\theta_c$  is reached and then decays as  $q^{-4}$  giving a profile with ‘fringes’ starting from a critical edge. An example profile for a polystyrene film containing amide is shown in Figure 7-2. The ‘width’ of the fringes is related to the thicknesses of the layers and the ‘height’ is related to the scattering length density contrast between the different layers.

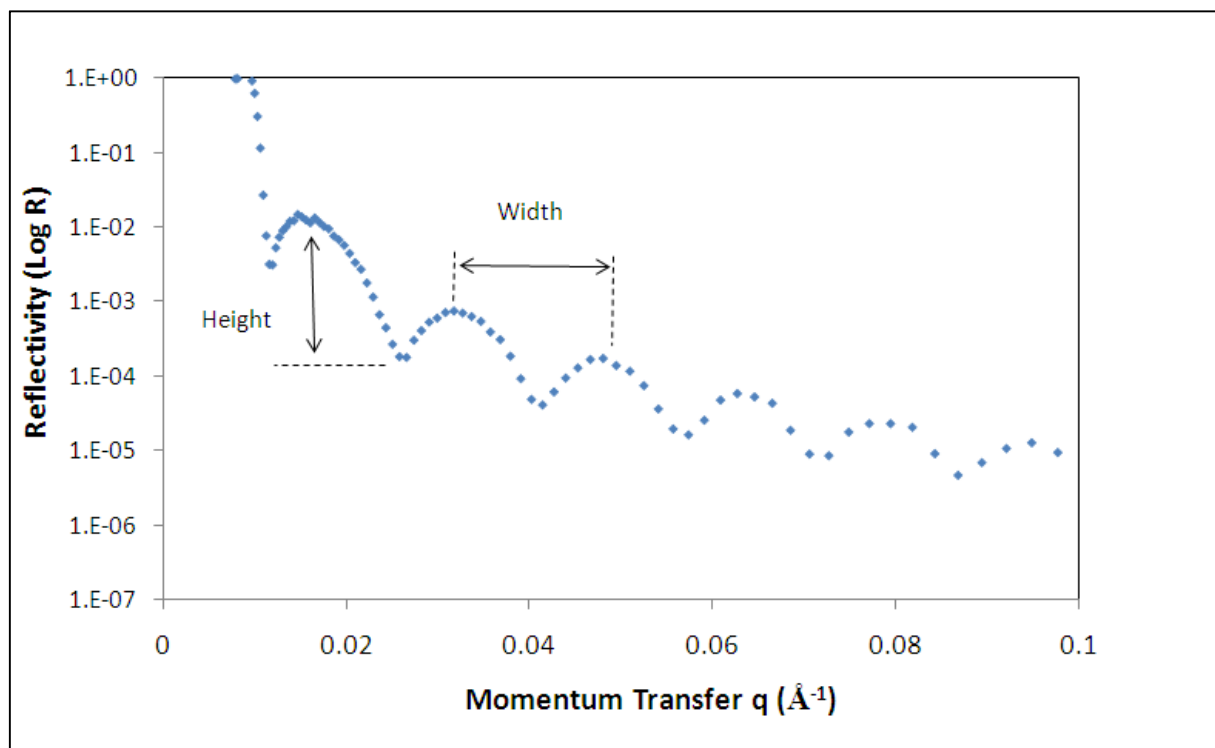


**Figure 7-2** Experimental neutron reflectivity data for an amide containing sample in polystyrene on a silicon substrate

### 7.1.1.2 Instrument description and modelling

Neutron reflectivity measurements in this work were made on the SURF instrument at ISIS, U.K. [3]. In order to measure the intensity of the specular reflected neutron beam over the desired range of  $q$  (momentum transfer), reflectometers can operate in either monochromatic mode or time-of-flight mode, depending upon the neutron source [4]. In monochromatic mode,

the angle of incidence is varied, whereas in time-of-flight mode with a polychromatic beam, data is collected at a few angles. Measurements on SURF at ISIS (a pulsed neutron source) were made at two-three angles to cover the desired  $q$ -range ( $0.01$  to  $0.2 \text{ \AA}^{-1}$ ).

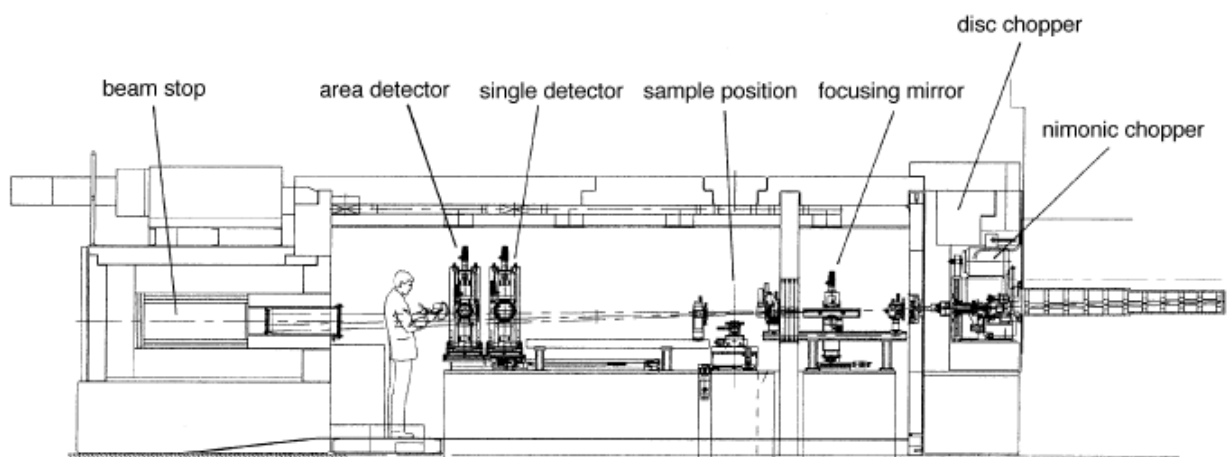


**Figure 7-3** Schematic layout of the SURF reflectometer. From [5]

Figure 7-3 shows a set-up of the SURF instrument at ISIS. The available range of  $q$  on SURF is  $0.01$  to  $1.1 \text{ \AA}^{-1}$ . The width of the incident neutron beam is controllable, with a maximum of  $60 \times 10 \text{ mm}$  and is defined by the varying the positions of four slits. The detector used here was a  $^3\text{He}$  gas detector (Figure 7-3).

The reflectivity data was analysed using the *Parratt32* reflectivity software developed at HMI Berlin. *Parratt32* calculates reflectivity profiles from multi layers with adjustable thicknesses and SLDs and compares them to the experimental profile. The adsorption of amides on the polystyrene/air interface was analysed assuming the multilayer structure shown in Figure 7-4.

Since many of the layer thicknesses and a few SLDs are unknown, complementary techniques like ellipsometry and X-ray reflection have been used to constrain the model for neutron reflection fitting as explained in this chapter.

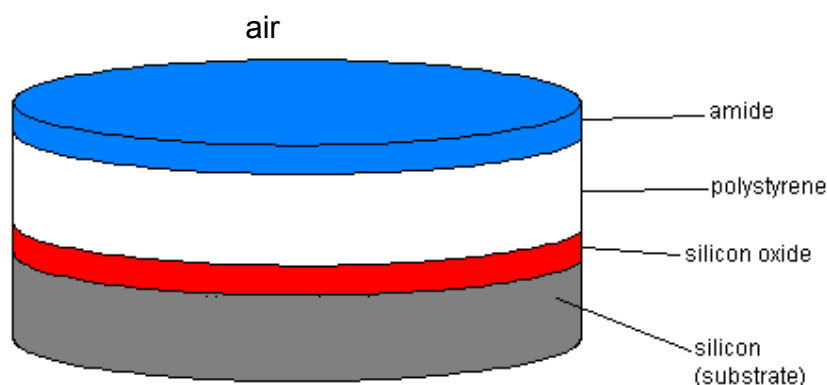


**Figure 7-4** Multilayer model. Layer thicknesses are not to scale.

### 7.1.2 X-ray reflectivity

Specular X-ray reflection is based on the same principles as neutron reflection explained above. For X-rays, the refractive index of a medium can be expressed as [6]:

$$n = 1 - \frac{\lambda^2 \rho_e r_e}{2\pi} + i \frac{\lambda \mu}{4\pi}$$

... Eqn. 7-4

The neutron SLD (Eqn. 7-1) is replaced here by the X-ray SLD= $\rho_e r_e$ , where  $\rho_e$  is the electron density of the medium and  $r_e$  is the classical electron radius;  $\mu$  is the absorption length. The technique relies on the difference between the electron density of the different layers or between the layer and the substrate. Similar to neutron reflection, X-ray reflectivity profiles also have a critical angle of incidence ( $\theta_c$ ) below which the X-rays are totally externally reflected (i.e. reflectivity=1). The value for the critical angle can be calculated for small angles:

$$\theta_c = \sqrt{\frac{\rho_e r_e}{\pi}} \lambda$$

... Eqn. 7-5

The reflectivity is the same as Eqn. 7-2 but with the neutron refractive index replaced by that of X-rays, and reflectivity profiles with ‘fringes’ are again obtained for the samples considered

here. Unlike neutrons, the X-ray SLD increases linearly across the periodic table which means that ‘contrast matching’ is difficult.

### 7.1.3 Ellipsometry

When linearly polarised light is incident on a sample, a phase shift in the parallel as well as perpendicular component of light takes place upon reflection. This phase shift is in general not the same for both components, resulting in the reflected beam becoming elliptically polarised. If the polarisation for the incident beam is known, necessary information can be obtained by measuring the state of polarization of the reflected beam [7]. The ellipsometer equations relate the two quantities below to the layer thicknesses of the sample:

$$\Delta = \delta_1 - \delta_2$$

$$\tan \Psi = \frac{|r_p|}{|r_s|}$$

... Eqn. 7-6

Here,  $\delta_1$  is the phase difference between the  $p$ -wave and the  $s$ -wave before reflection, and  $\delta_2$  is this difference after reflection.  $r_p$  and  $r_s$  are the reflection coefficients for the  $p$  and  $s$  components of the light.  $\Delta$  can vary between  $0^\circ$  and  $360^\circ$  and  $\Psi$  between  $0^\circ$  and  $90^\circ$ . The measured intensity ( $R$ ) is proportional to  $r^2$ . The measured intensity and phase information ( $\Delta$  and  $\Psi$ ) are related to the layer thicknesses of interest by an expression similar to Eqn. 7-2 with the appropriate refractive index of the medium for the wavelengths here and appropriate settings of the ellipsometer optical components.

Refinements of the technique include taking these measurements at different wavelengths (spectroscopic) or different angles of incidence. The data collected can be fitted to a model having a number of different dielectric layers on a substrate (Figure 7-4).

### 7.1.4 Coefficient of friction measurements

The static coefficient of friction on the surface of the coated silicon wafers can be measured using a simple inclined-plane arrangement. For this work, a small Teflon disc was placed on the surface of a wafer kept on a glass shelf and one end of the shelf could be raised carefully from the horizontal. The angle  $\theta$  (Figure 7-5) at which the disc begins to slide gives the static coefficient of friction ( $\mu$ ):

$$\mu = \tan \theta = \frac{h}{l}$$

... Eqn. 7-7

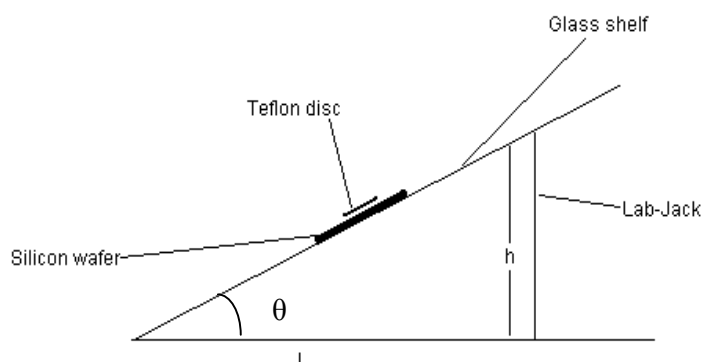


**Figure 7-5** An inclined plane for friction measurements

The measurements here were repeated 3-4 times by placing the disc at different parts of the silicon wafer to check for consistency, and an average coefficient of friction was calculated.

The inclined plane method permits friction measurements to be made quickly and the trends obtained were fairly consistent. Using this method a good estimate of the range of amide concentrations required for friction reduction and some estimate of the surface-migration time-scale of the amide was obtained. However, the surface of the wafer was found to be contaminated by sliding the Teflon disc over it. After repeated measurements, the surface was also found to be visibly scratched. Hence these wafers could not be used for further testing by other methods.

This consistency in the friction coefficient trends shown here was verified by another technique. A *micro-tribometer* (developed in-house at the engineering department at Cambridge) was used for coefficient of friction testing where a small Teflon ball moved across the surface of the wafer and the normal and tangential forces on the ball were measured by piezo devices. This technique gave exactly the same trends (results not shown here) as that seen by the inclined plane method although the absolute values of the friction coefficients were different owing to the change in geometry of the surfaces in contact. A drawback of the *micro-tribometer* was that extremely high pressures ( $\sim 2$  MPa) were exerted on the sample surface by the ball since it had a very small contact area. This visibly damaged the surface layer and hence this technique was not pursued further.

## 7.2 Experimental details

### 7.2.1 Materials

The substrate was mono-crystalline (1,1,1) single-side polished silicon wafers 0.5 mm/5 mm thick with a diameter of 2" purchased from Siltronix. The roughness (estimated by the supplier) was less than 8 Å, and the thickness of the silicon oxide layer on the surface was measured using ellipsometry prior to spin coating (below). For neutron experiments, 5 mm thick silicon wafers were used directly as supplied with no treatment other than rinsing with toluene. Wafers for friction testing (0.5 mm) were reused after cleaning with concentrated nitric acid and toluene.

The polystyrene was purchased from Polymer Laboratories and had a (weight-averaged) molecular weight of 111,400 and a Polydispersity Index (PDI) of 1.02. Two amides were chosen for study here: erucamide (C22:1 c-13) for friction measurements was supplied by Croda Europe Ltd., U.K. Perdeuterated dodecanamide for neutron experiments (C12:0 D-amide) was synthesised from perdeuterated dodecanoic acid. Both amides were analysed for purity by elemental analysis, NMR and Liquid-Chromatography-Mass Spectrometry (Appendix B) and were found to be > 96% pure. C12:0 D-amide was used in protonated polystyrene for neutron reflection to maximise the scattering length density contrast [2].

Toluene was supplied by Sigma-Aldrich (> 99.9% pure). All glassware was thoroughly cleaned using concentrated nitric acid and a surfactant solution (DECON 90) overnight before use.

### 7.2.2 Sample preparation and characterisation

Spin coating was used to produce a uniform polystyrene film on the silicon surface. The coating solution spreads on the wafer by centrifugal force while the solvent evaporates, yielding a film which is uniform on the nanometre scale. The thickness of the film is a function of the solute concentration, viscosity, spin speed and drying time (evaporation rate) [8]. Higher spin speeds and higher spin times result in thinner films. Also, a higher solution viscosity gives thicker films.

A freshly-prepared solution of the polymer with amide in a volatile solvent (toluene) was dispensed on a silicon wafer and spun at a high speed (4000 rpm). The solutions were prepared for different concentrations of the amide in the polymer (in parts per million by weight, PPM).

The spin coater used was a Laurell Technologies WS-400 model. Various combinations of spin speeds and times were tried here and the thickness of the polystyrene layer estimated by ellipsometry (below). In order to obtain consistent film thicknesses ( $\pm 5$  nm) the following optimised spin-coating parameters were used throughout the work:

- *Dispense stage*: Dispense 1-2 mL of the coating solution while the wafer is stationary. Spin at 500 rpm for 15 seconds.
- *Spin stage*: Spin at 4000 rpm for 30 seconds

Two ellipsometers were used to estimate film thicknesses and their results were compared for consistency: a spectroscopic ellipsometer (alpha-SE) manufactured by J. A. Woollam and Co. and an imaging ellipsometer (Nanofilm EP<sup>3</sup>) manufactured by Accurion GmbH. Optical data for the silicon oxide layer and the polystyrene layer were used from the ellipsometer software as supplied by the manufacturer.

X-ray reflectivity measurements were performed on the lab-based Bruker AXS D8 Advance Diffractometer at Diamond Light Source, U.K. The incident X-ray beam had a wavelength of 1.5406 Å (Copper K<sub>α</sub> radiation). A germanium (0,2,2) monochromator was used, with slit combinations of 0.1 mm for the primary beam and 2.0 mm for the reflected beam. These produced a finely focused beam with a footprint covering ~ 10 mm of the sample. Data was

analysed using the *Parratt32* reflectivity software with the multilayer model shown in Figure 7-4.

All samples for neutron reflection experiments were freshly prepared. The thicknesses of the silicon oxide and polystyrene films were measured on the ellipsometer. The thickness of the polystyrene (+amide) layer was refined by fitting the X-ray reflectivity profiles. This value ( $\pm 5$  Å) was used in fitting neutron reflection data for the total thickness of the amide + polymer layer in order to constrain the final model.

Samples were measured on the SURF instrument immediately after preparation and after annealing at 100 °C for 1 hour. They were then measured on the ellipsometer and the X-ray reflectivity device. The annealing time and temperature was chosen based on friction measurements as explained in the following section.

## 7.3 Results and Discussion

### 7.3.1 Coefficient of friction

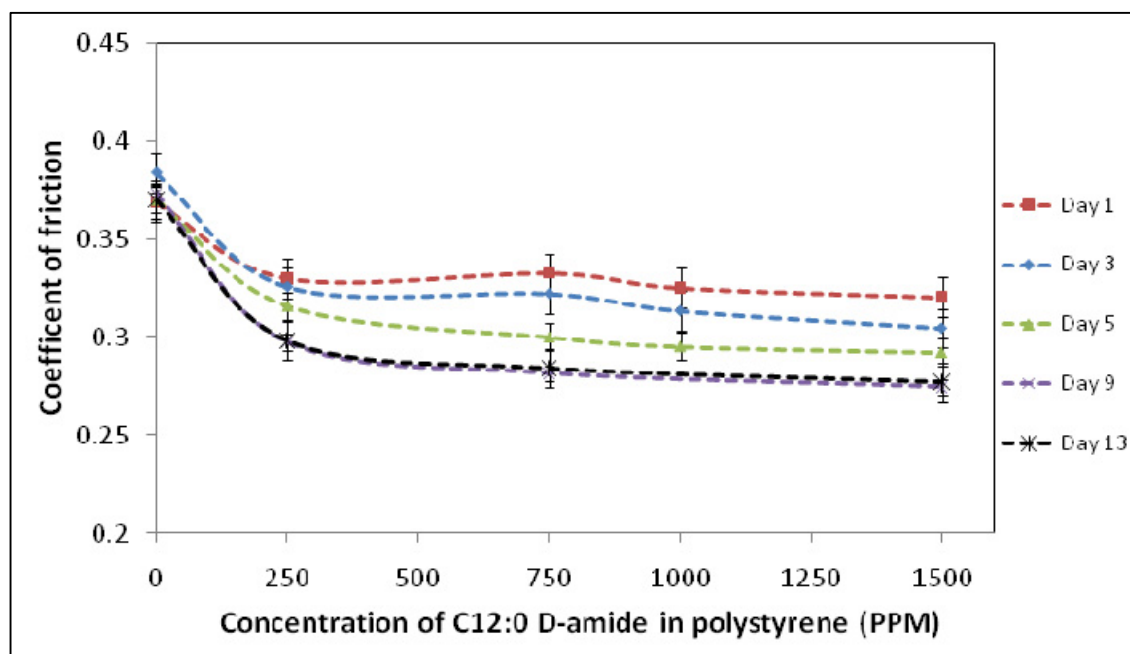


**Figure 7-6** Variation of the friction coefficient of the polymer surface with C12:0 D-amide additive and with time (low concentration region shown). The dotted lines are a guide to the eye.

The variation in the friction coefficient with concentration of C12:0 D-amide additive in the polystyrene film was studied. Measurements were repeated over a period of two weeks on the inclined plane and the results are shown in Figure 7-6.

From the figure, it can be seen that the coefficient of friction drops by 20-30% with a small amount of amide in the film (250 ppm in the bulk). The value then remains approximately constant for a large range of concentrations (up to 12000 ppm, not shown for clarity).

The friction coefficient gradually decreases for all samples over time and stops decreasing after ~13 days. The values were remeasured up to a period of 30 days (not shown for clarity) and no further decrease in friction was observed.

Figure 7-7 shows the results of the variation of friction coefficient with concentration and time of erucamide. The trends observed are similar to those of C12:0 D-amide discussed above. Very similar results have been obtained for erucamide in polyethylene films, where a sharp decrease in friction coefficient has been observed with low bulk loading of the amide (~1000 ppm) [9].

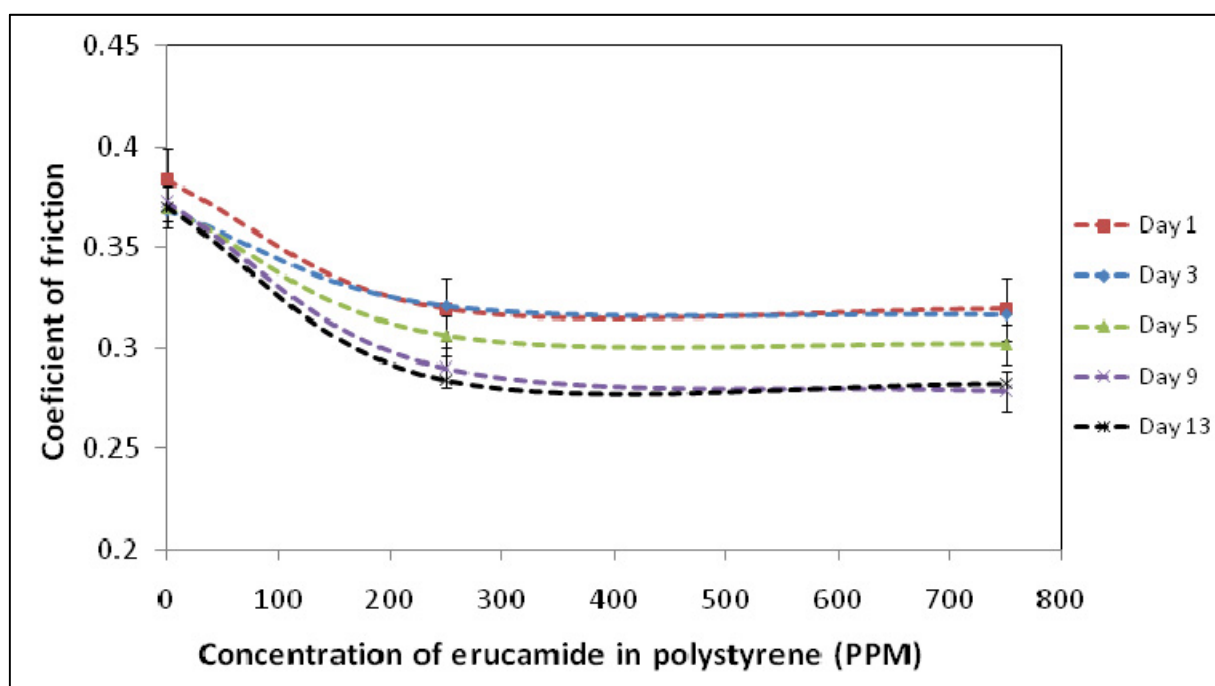


**Figure 7-7** Variation of the friction coefficient of the polymer surface with erucamide additive and with time (low concentration region shown). Day 1 = same days as prepared. The dotted lines are a guide to the eye.

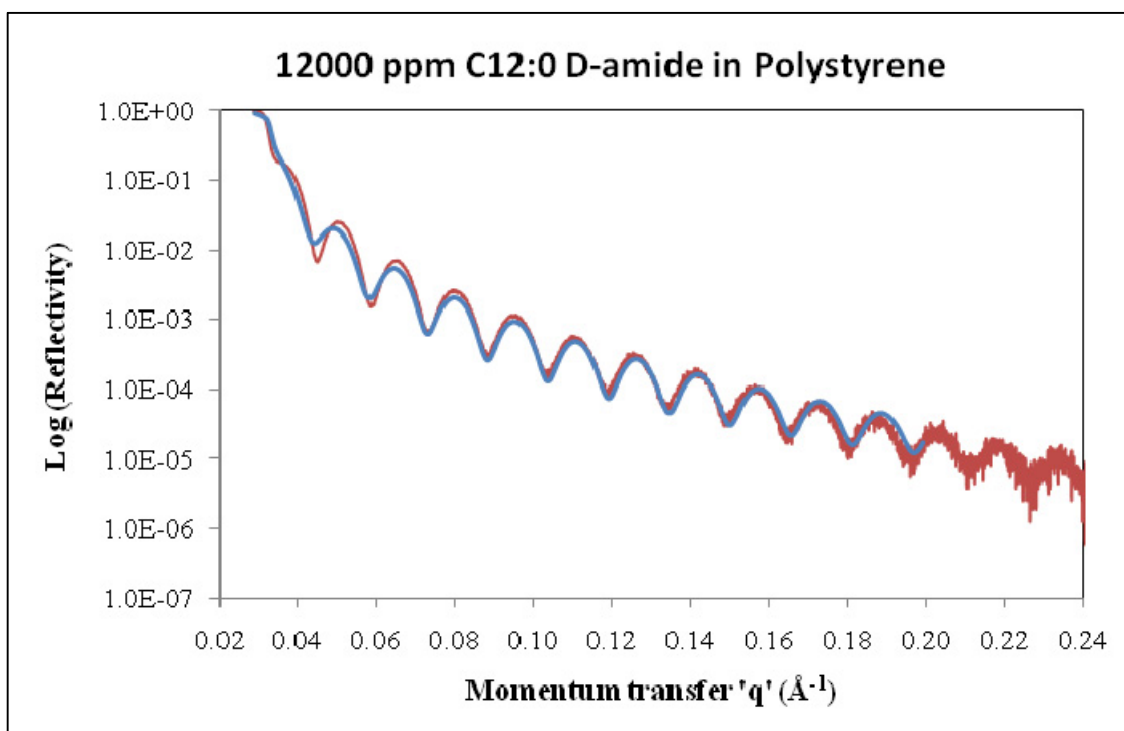
From these results, it can be hypothesised that the amide additive migrates from the bulk to the surface of the polymer, and small amounts of the additive are effective in friction modification [10]. Some additive is present on the surface as soon as the film is prepared. Over time (~14 days) more molecules can migrate to the surface, and similar time scales have been observed for erucamide in polypropylene films [11]. Increasing the bulk concentration of the amide does not cause greater friction reduction beyond a ‘critical’ additive concentration [9]. Indeed, in polyethylene films, microscopy has revealed that the surface film need not be completely covered by the amide for a reduction in friction to be observed and that these additives exist in domains on the surface [10, 12].

To increase the migration rates of the amide to the polymer surface, the effect of heat treatment on the freshly prepared wafers was studied by measuring the friction coefficient before and after annealing. After annealing films containing C12:0 D-amide for 1 hour at 100 °C, inclined-plane tests revealed that the coefficient of friction dropped to the ‘equilibrium’ value (0.27, Figure 7-6) i.e. the value after 13 days without heat treatment. However, when the same sample was kept at room temperature and measured after 2-3 days, the friction coefficient returned to the value for bare polystyrene (0.37). This was thought to be due to the loss of erucamide from the surface due to evaporation, where the annealing might have caused most of the bulk amide to migrate to the surface rather quickly. The friction measurements above (i.e. without annealing) were made up to a period of 30 days, and it cannot be ascertained whether the friction coefficient returns to the bare polystyrene value for these samples at longer times.

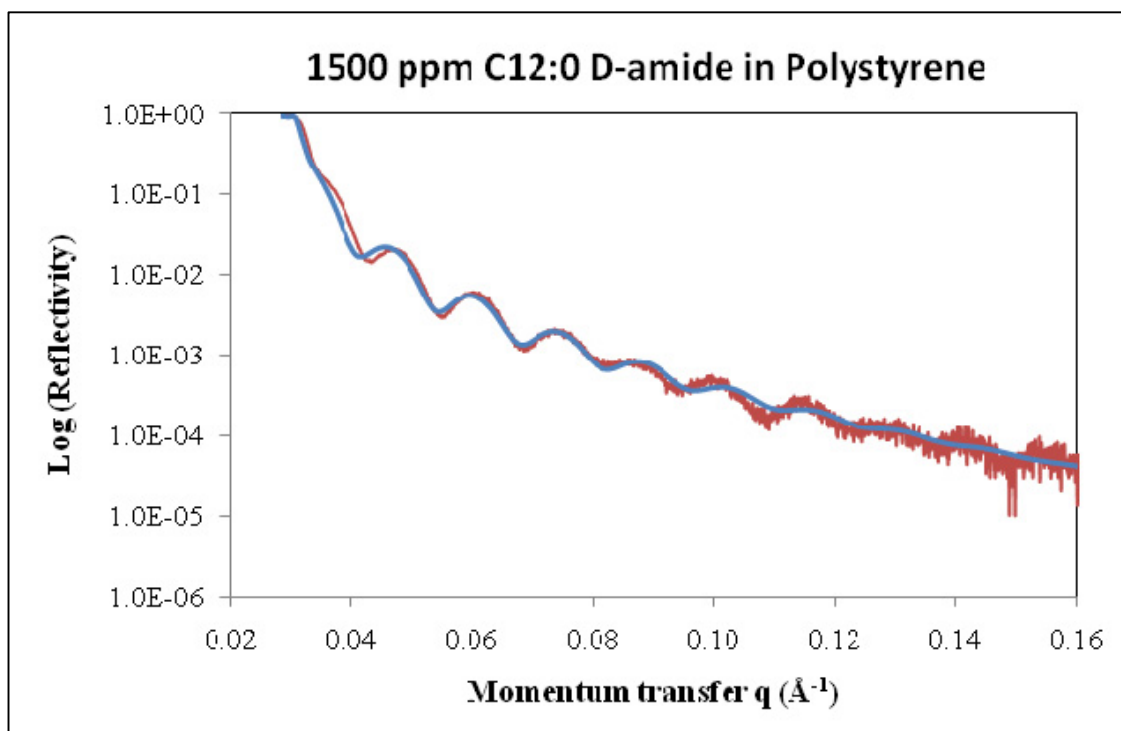
Thus, a concentration range has been identified for preparing the amide-containing films for initial X-ray and neutron reflection experiments, the results of which will be discussed below.

## 7.3.2 X-ray reflectivity

(a)



(b)



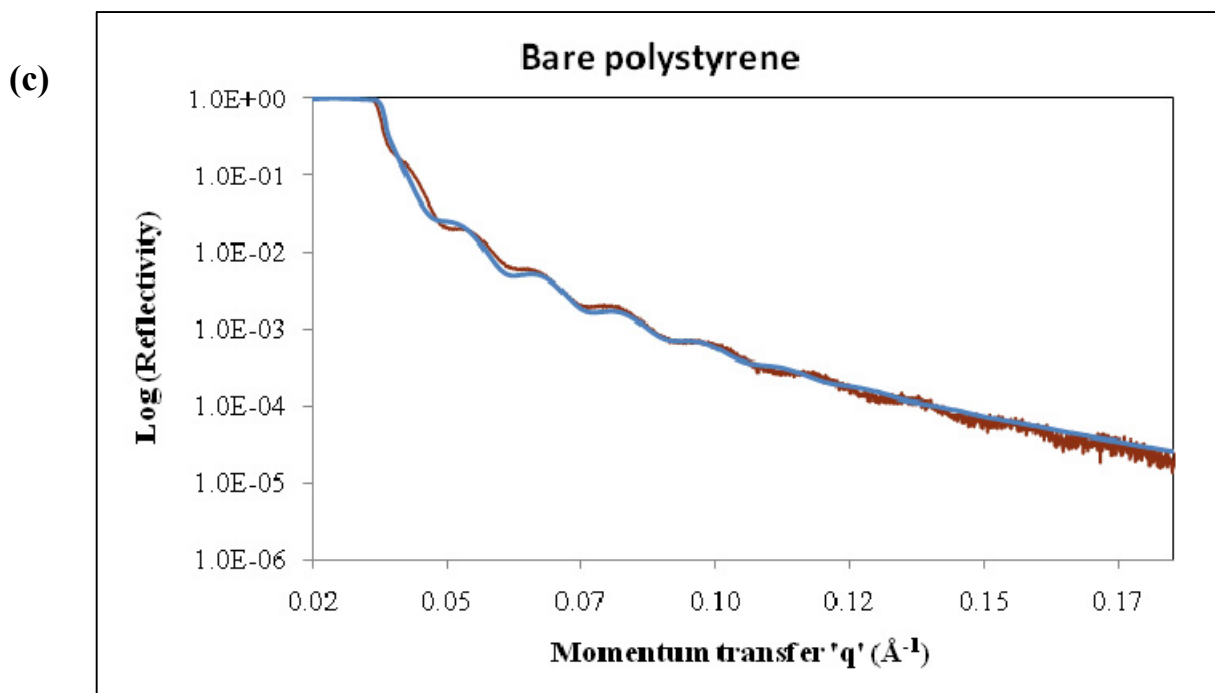


**Figure 7-8** X-ray reflectivity profiles measured (red lines) and calculated (blue lines) for polystyrene films on silicon with different amounts of C12:0 D-amide. The concentrations of the amide in each case are: (a) 12000 ppm (b) 1500 ppm and (c) 0 i.e. bare polystyrene.

Figure 7-8 shows the X-ray reflectivity profiles for polystyrene films on silicon with different concentrations of C12:0 D-amide. The profiles clearly show a well defined critical edge and formation of fringes. The damping of the fringes (Figure 7-8 (b) and (c)) indicate that these samples have a higher surface roughness compared to the 12000 ppm sample (Figure 7-8 (a)) [6]. X-ray reflectivity profiles were only available for the samples that were already annealed and measured on the SURF instrument (neutron reflection results are shown in §7.3.3).

The simulated reflectivity profiles (blue lines) were calculated assuming the multilayer model (Figure 7-4). These profiles in Figure 7-8 agree well with the experimental data and the results are summarised in Table 7-1.

The amide and the polystyrene layers were treated as one layer since it was found that the X-rays could not distinguish the amide layer at the surface from the polystyrene layer due to the similarity in its X-ray scattering length density (i.e. electron density) (as seen by the SLD of the polystyrene layer remaining constant, Table 7-1). Fairly constant SLDs for the SiO<sub>2</sub> layer were obtained, as expected.

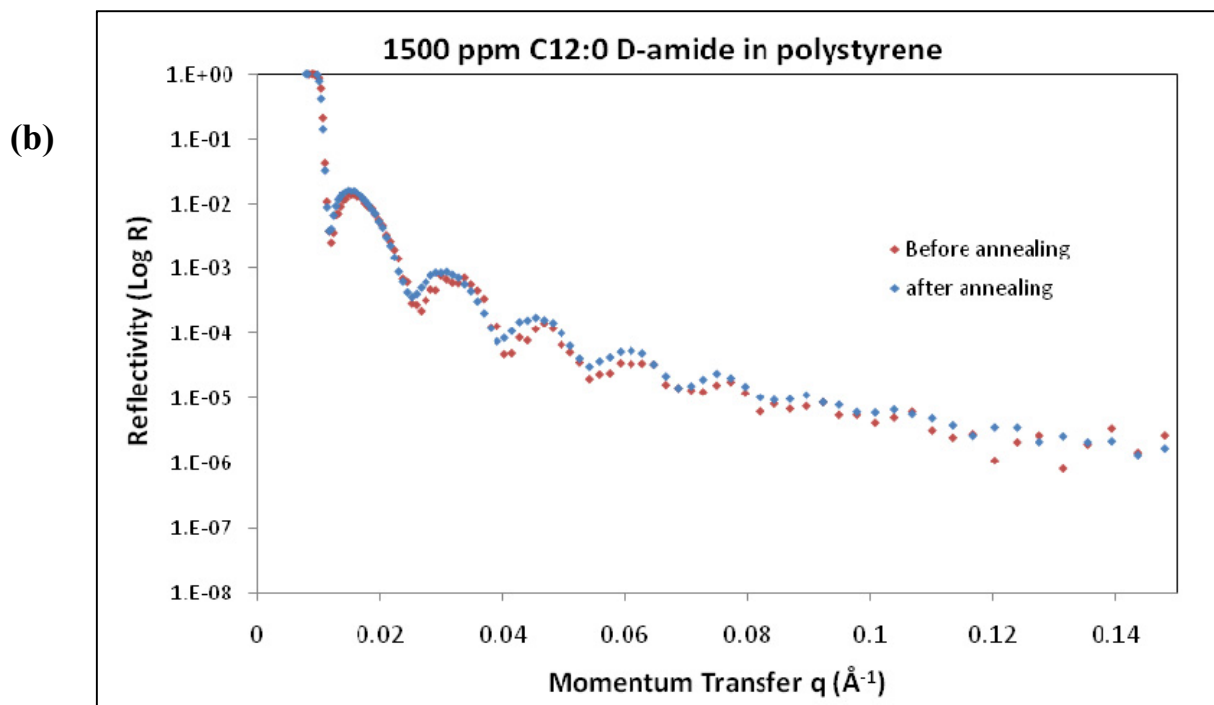
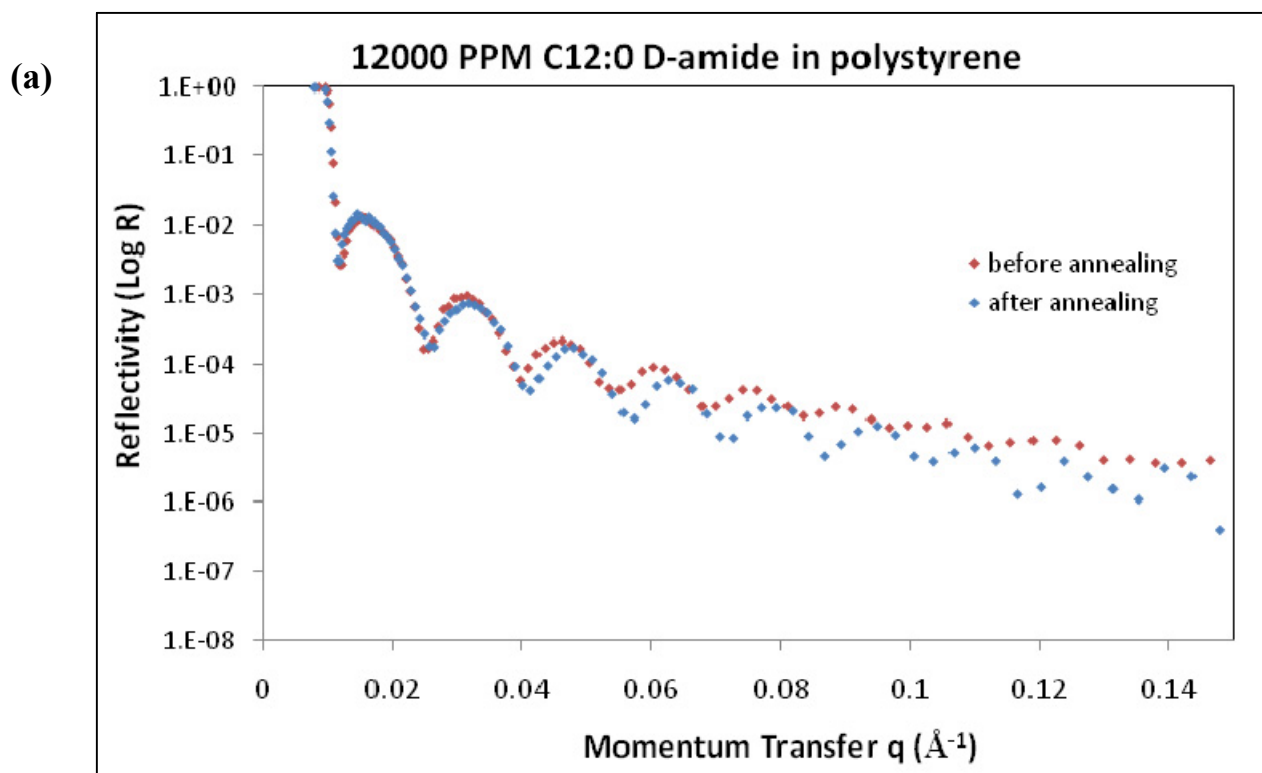
As explained earlier, the thickness of the polystyrene layer thickness measured using ellipsometry was used as an initial estimate and then refined until satisfactory match with the experimental X-ray reflectivity profiles was obtained. The SiO<sub>2</sub> layer thickness measured by ellipsometry for these samples were between 15 and 17 ( $\pm 5$ ) Å, and these match with those obtained by fitting the X-ray (Table 7-2) and neutron (Table 7-3) reflectivity profiles.

**Table 7-1** Thicknesses and scattering length densities (SLDs) of layers on silicon estimated by simulating X-ray reflectivity profiles. The thicknesses/roughness are estimated with an accuracy of  $\pm 5$  Å and SLDs with  $\pm 0.5 \cdot 10^{-6}$  Å<sup>-2</sup>

| Concentration<br>of amide in<br>Polystyrene<br>(PPM) | SiO <sub>2</sub> layer |  | Polystyrene layer |  | Surface<br>roughness<br>of silicon<br>(Å) |
|--|------------------------|--|-------------------|--|---|
|  | Thickness (Å)          | SLD*10 <sup>6</sup> (Å <sup>-2</sup> ) | Thickness (Å)     | SLD*10 <sup>6</sup> (Å <sup>-2</sup> ) |   |
| 0  | 12                     | 21.00                                  | 407               | 6.80                                   | 21  |
| 1500   | 20                     | 22.00                                  | 434               | 6.80                                   | 18  |
| 12000  | 12                     | 21.00                                  | 401               | 6.80                                   | 5   |

The estimation of the overall film thickness by X-ray reflectivity is a very important constraint in the neutron reflection fitting procedure and will be explained below.

## 7.3.3 Neutron reflection



(c)

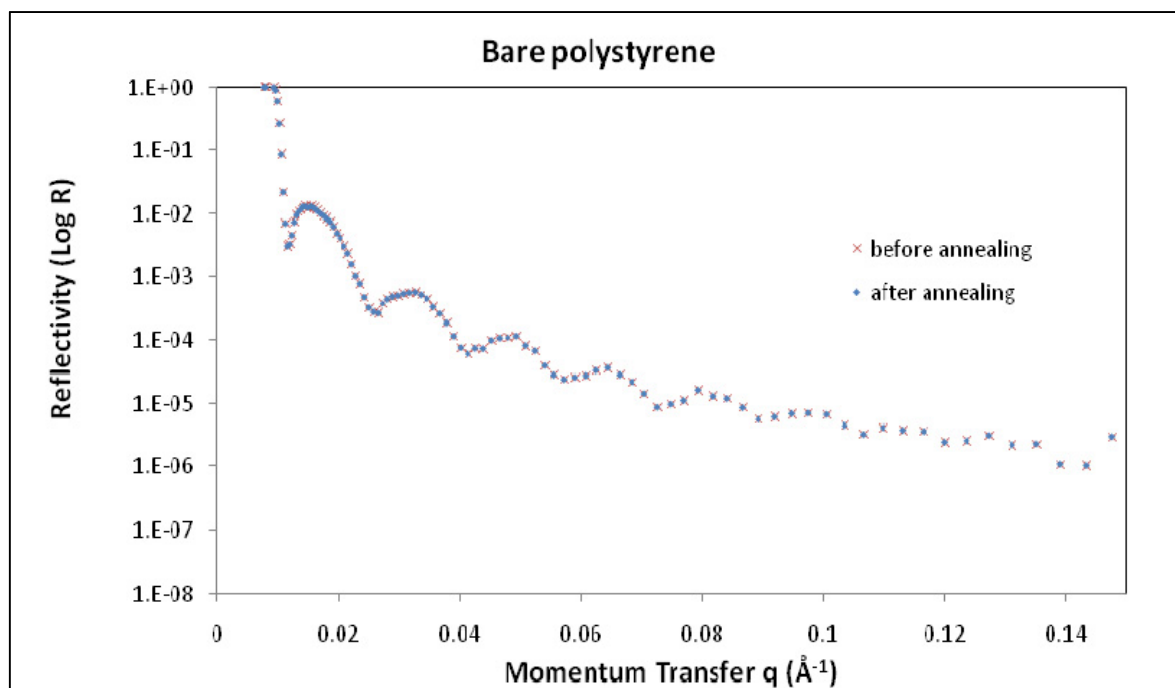


**Figure 7-9** Experimental neutron reflection profiles of C12:0 D-amide in protonated polystyrene (a) Polystyrene with 12000 PPM C12:0 D-amide (b) Polystyrene with 1500 PPM C12-D amide (c) Bare polystyrene. A change in the reflectivity profiles is observed for films containing amide before and after annealing

The experimental neutron reflection profiles from samples containing varying amounts of amides in the bulk polymer are shown in Figure 7-9. These profiles show a well-defined critical edge and the formation of 'fringes'. As explained previously, neutron reflection measurements were made before and after annealing the prepared samples. Profiles for the bare polystyrene film (no amide additive, Figure 7-9 (c)) are almost identical before and after annealing indicating that there is no change in the surface composition of this film, and no apparent solvent loss from the samples. Figure 7-9 (a) and (b) clearly show a shift in the reflectivity curve measured after annealing, suggesting some change in the surface of the films. The dependence of these changes on the surface composition of the system will be discussed below.

## 7.3.3.1 Presence of an amide layer

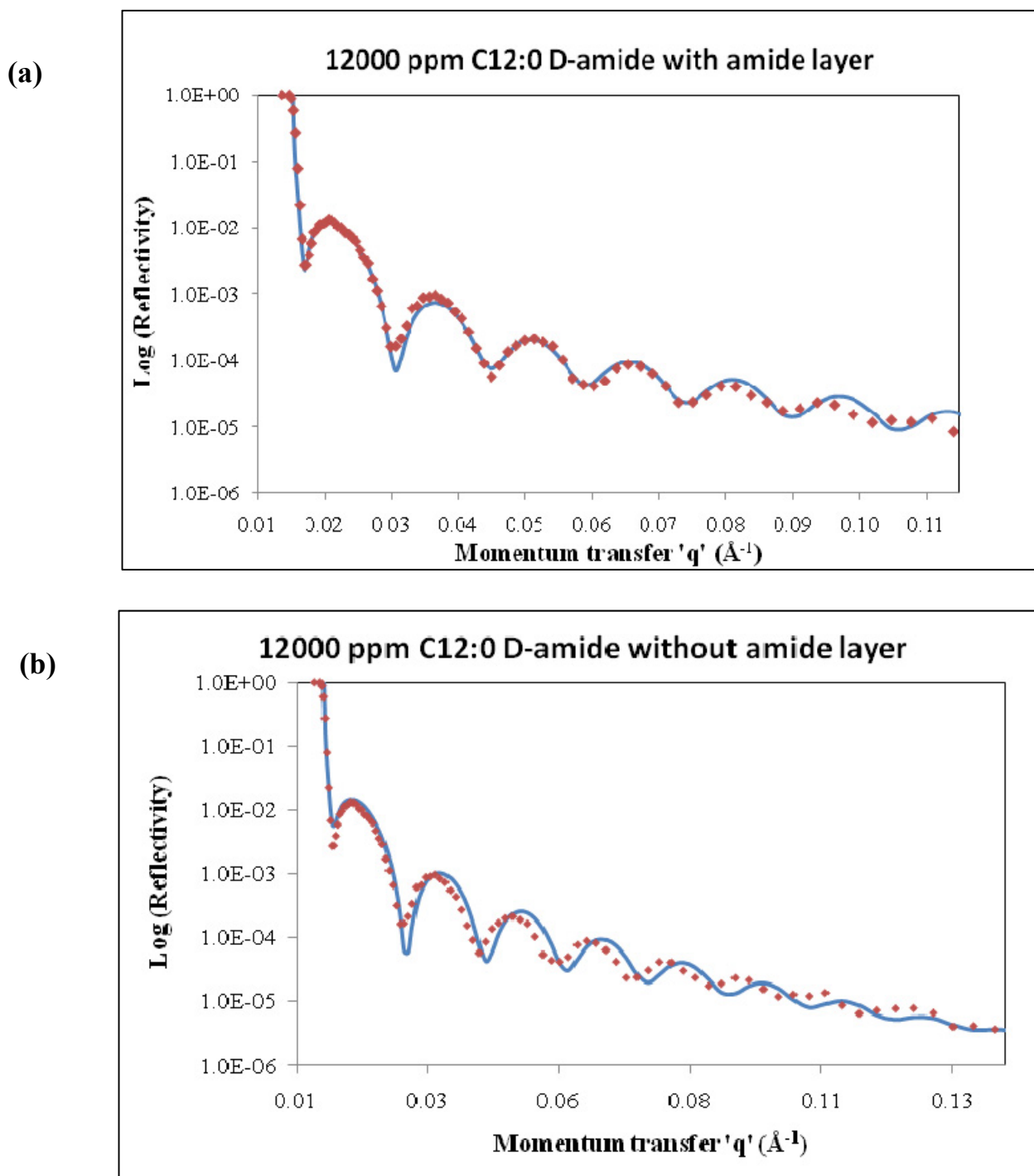
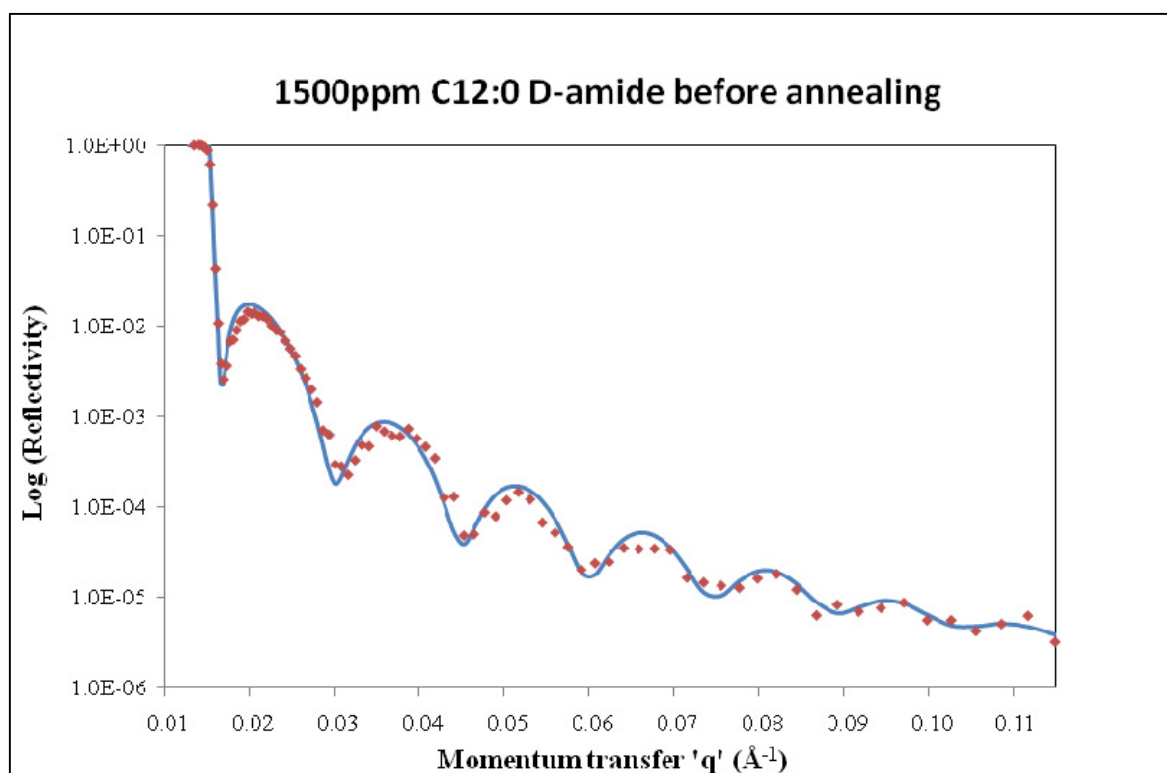


**Figure 7-10** Calculated reflectivities (blue lines) and experimental neutron reflection data (red points) for the sample with 12000 ppm C12:0 D-amide in polystyrene, before annealing. Figure (a) shows the calculated profile assuming that there is an amide layer at the surface, and (b) shows a fit with no amide layer. In both cases the total thickness of the film is that estimated by X-ray reflectivity ( $401 \pm 5 \text{ \AA}$ ).

Figure 7-10 shows calculated reflectivity profiles for the sample containing 12000 ppm (bulk loading) for two different cases: with and without an amide layer on the surface (Figure 7-4). The fits have been constrained such that the total thickness of the film is the same as that estimated by the X-ray reflectivity fits (i.e.  $401 \pm 5 \text{ \AA}$ , Table 7-1). For the case when there is no amide layer assumed, a poor match is obtained between the fringe spacings of the calculated profiles and the experimental data in Figure 7-10 (b); the fringe spacings are related to the thickness of the different layers present (§7.1.1). However with an amide layer a good fit is obtained (fitted parameters are listed in Table 7-2). Thus, it can be seen that, for the first time, neutron reflection provides evidence for the existence of an amide layer on the surface.

### 7.3.3.2 Changes in surface amounts of amides

(a)



(b)

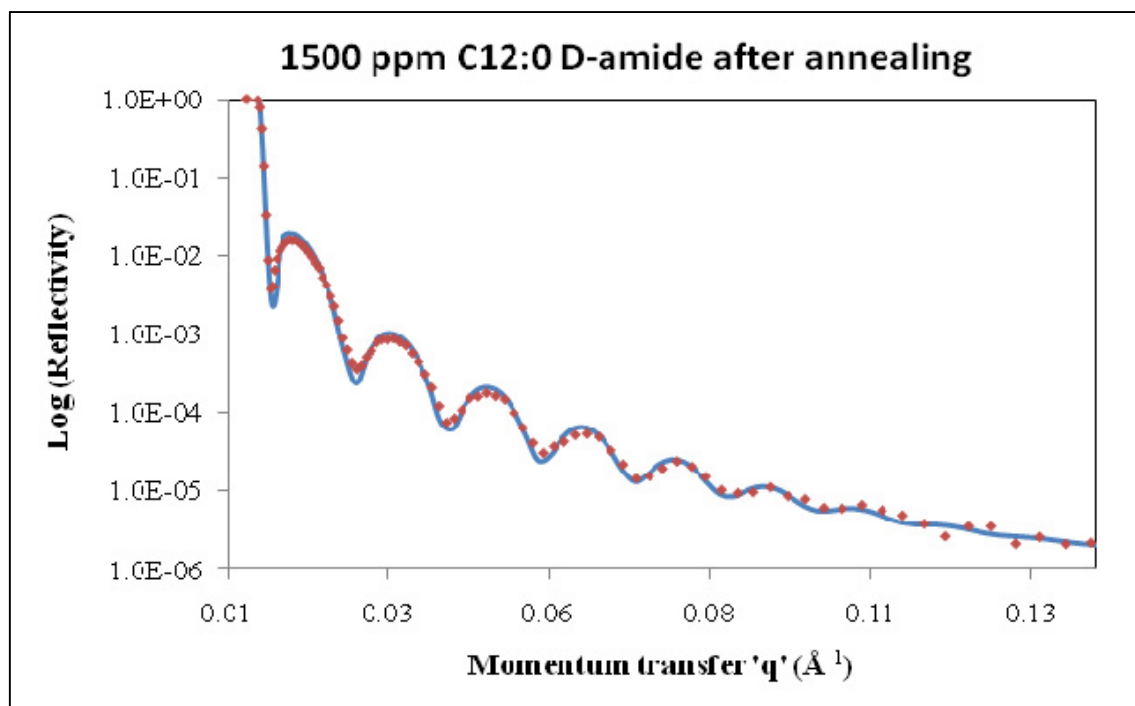


**Figure 7-11** Fitted neutron reflectivity profiles (blue lines) and experimental data (red points) for the sample with a bulk loading of 1500 ppm for the amide (a) before annealing and (b) after annealing

Figure 7-11 shows the fitted neutron reflection data for a sample with 1500 ppm amide in the bulk. The calculated parameters for the different layers (Table 7-2) indicate that there is some amide present on the surface before annealing. The reflectivity profile after annealing the sample can be fitted to the same values of the SiO<sub>2</sub> and polystyrene layer before annealing, by *only* increasing the thickness and SLD of the amide layer (Table 7-2) (this increase is beyond the error estimates of the fitted parameters). A similar result is obtained for the 12000 ppm sample, although the high bulk loading of this sample could be responsible for a smaller change in the surface adsorption of the amide before and after annealing. This provides evidence of an increase in the concentration of the amide on the polystyrene/air interface with annealing. In these fits the overall film thickness has again been constrained by X-ray reflection results (Table 7-1).

Results from fitting the neutron reflectivity data are shown in Table 7-2 and discussed in §7.3.3.4.

**Table 7-2** Parameters calculated by fitting neutron reflection data. The thicknesses ( $d$ ) are estimated with an accuracy of  $\sim \pm 5 \text{ \AA}$  and scattering length densities (SLDs) with  $\sim \pm 0.05 \cdot 10^{-6} \text{ \AA}^{-2}$ . The fits are shown and discussed in the text.

| Amide<br>in PS<br>(PPM) | SiO <sub>2</sub> layer |  | Polystyrene layer |  |                  |   | Amide layer     |  |              |  |
|-------------------------|------------------------|--|-------------------|--|------------------|---|-----------------|--|--------------|--|
|                         | Before annealing       |  | After annealing   |  | Before annealing |   | After annealing |  |              |  |
|                         | $d$<br>(\AA)           | SLD*<br>$10^6$<br>(\AA <sup>-2</sup> ) | $d$<br>(\AA)      | SLD*<br>$10^6$<br>(\AA <sup>-2</sup> ) | $d$<br>(\AA)     | SLD<br>$\cdot 10^6$<br>(\AA <sup>-2</sup> ) | $d$<br>(\AA)    | SLD*<br>$10^6$<br>(\AA <sup>-2</sup> ) | $d$<br>(\AA) | SLD*<br>$10^6$<br>(\AA <sup>-2</sup> ) |
| 0                       | 14                     | 3.96                                   | 402               | 1.42                                   | 402              | 1.42  | n/a             | n/a                                    | n/a          | n/a                                    |
| 1500                    | 16                     | 3.92                                   | 421               | 1.43                                   | 421              | 1.43  | 10              | 1.70                                   | 18           | 1.90                                   |
| 12000                   | 16                     | 3.96                                   | 380               | 1.37                                   | 378              | 1.38  | 18              | 2.00                                   | 18           | 2.20                                   |

### 7.3.3.3 Estimating the surface composition of the amide film

The surface concentration ( $\Gamma$ , mol/m<sup>2</sup>) of the amide from the neutron reflection data can be estimated by:

$$\Gamma = \frac{\rho_{amide} d \phi_{amide}}{RMM_{amide}}$$

... Eqn. 7-8

Here  $\rho_{amide}$  is the bulk density of the amide ( $=0.9 \text{ g/cm}^3$  for dodecanamide),  $d$  is the amide layer thickness (listed in Table 7-2), and  $RMM_{amide}$  is the relative molecular mass of C12:0 D-amide ( $=218 \text{ g/mol}$ ). This equation can be derived by a mass calculation of the amide on the surface. The volume fraction of the amide at the interface is given by the ratio of the SLD of the amide estimated here to the SLD of a completely deuterated amide layer ( $=6.6 \cdot 10^{-6} \text{ \AA}^{-2}$ ) [4]:

$$\phi_{amide} = \frac{SLD}{SLD_{d-amide}}$$

... Eqn. 7-9

A surface average area per amide molecule ( $a$ ) adsorbed at the interface is then:

$$a = \frac{1}{\Gamma N_A}$$

... Eqn. 7-10

A mass calculation for the total concentration of the amide ( $\text{mol/m}^3$ ) in the bulk polystyrene (PS) layer gives:

$$c_{amide}^{bulk} = \frac{x\rho_{PS}}{RMM_{amide}}$$

... Eqn. 7-11

Here  $x$  refers to the mass ratio of amide to polystyrene (in PPM) in the bulk, prior to spin coating. It is assumed here that this ratio remains the same in the polymer layer after spin coating, after accounting for the amide that has migrated to the surface (Eqn. 7-8). The surface concentrations of the amides, provided for the first time by neutron reflection, and the area per molecule are listed in Table 7-3 and discussed in the following section. The ratios of the total amount of amide present on the surface to that remaining in the bulk are also given in Table 7-3.

**Table 7-3** Surface concentration of the amide and area per molecule adsorbed for the different neutron reflection fits

| Bulk concentration of amide (PPM) | Before annealing                 |                      |                    | After annealing                  |                      |                    |
|-----------------------------------|----------------------------------|----------------------|--------------------|----------------------------------|----------------------|--------------------|
|                                   | $\Gamma$ ( $\mu\text{mol/m}^2$ ) | $a$ ( $\text{\AA}$ ) | Surface:bulk ratio | $\Gamma$ ( $\mu\text{mol/m}^2$ ) | $a$ ( $\text{\AA}$ ) | Surface:bulk ratio |
| 1500                              | 0.181                            | 918                  | 1.33               | 0.225                            | 735                  | 2.49               |
| 12000                             | 0.250                            | 663                  | 0.12               | 0.303                            | 548                  | 0.15               |

### 7.3.3.4 Discussion

Good quality fits were obtained to the neutron reflection data after constraining the overall thickness of the polymer film by a combination of ellipsometry and X-ray reflection. The

presence of an amide layer on the polymer surface is indicated by the fitted neutron reflection profiles.

It is found that the reflectivity profile of the sample containing the bare polystyrene does not change before and after annealing (Figure 7-9 (c) and Table 7-2) which shows that there is no change in the surface composition of the film after the annealing process, as might be hoped for. For polymer films containing amides, an increase in the amount of amide adsorbed on the film is observed after the annealing process (Table 7-2 and Table 7-3). The surface amounts are also found to increase as the bulk concentration of the sample increases, again in line with expectations and other measurements.

The friction measurements presented in §7.3.1 agree with the neutron reflection results here. A small amount of amide is found to be present before annealing the sample by the friction measurements, and neutron reflection fits (Figure 7-10 and Table 7-2) also show that there is some amide present on the surface prior to annealing. For the amide-containing polystyrene films, the coefficient of friction was found to decrease gradually over time (~13 days) and after annealing the freshly prepared sample (§7.3.1), and this can be related to an increase in the amount of amide at the surface after the annealing process as shown by neutron reflection (Table 7-3).

It is found that the amount of amide on the surface for the 1500 ppm sample is more than that present in the bulk by a factor of 1.3-2.5 (Table 7-3). In contrast, the surface amount of amide for the 12000 ppm sample is lower than the bulk by a factor of 10. This shows that increasing the bulk concentration of the amide does not result in a proportionate increase in the surface concentration. This result again relates with the coefficient of friction measurements which show that, beyond a particular bulk concentration (500-1000 ppm), the friction does not decrease substantially with increasing bulk concentration of the amide.

The area per dodecanamide molecule, which was found to lie flat on the graphite surface, can be calculated by diffraction from the unit cell dimensions as 87.55 Å<sup>2</sup> (Table 4-2). Areas per amide molecule estimated by the neutron reflection fits (Table 7-3) show that, on an average, there is plenty of area available on the surface of the polymer for the molecules. This indicates that the coverage of the amides on the polymer surface is very low indeed. The molecules could 'lie flat'

on the polymer surface given the area available, but this cannot be concluded based on the results here. There could be a possibility of the existence of discrete domains of the amide molecules at the interface, as these have been found on the surface of polyethylene previously [10].

## 7.4 Summary

This preliminary study shows that the amides studied here adsorb at the polystyrene/air interface. The techniques of friction measurements, ellipsometry and X-ray and neutron reflection have been used in combination to study these systems. Coefficient of friction measurements indicate that small amounts of amide reduce friction at the polymer surface. The trends observed here for the change in the friction coefficient with time and with total bulk concentration of the amide agree with literature.

X-ray and neutron reflectivity profiles have been simulated assuming a ‘multilayer’ model for the different layers on the silicon substrate. By using a combination of ellipsometry and X-ray reflectivity, overall film thicknesses have been constrained.

Neutron reflection is shown to provide evidence for the existence of an amide layer on the surface. Quantitative information of the amide on the surface has been provided for the first time. Surface concentrations of the amides on polystyrene have been estimated and these have found to increase with an increase in bulk loading of the amide and with annealing. The coefficient of friction measurements agree with the neutron reflection results: some amount of amide is present on the surface immediately after sample preparation, and the decrease in the friction coefficient corresponds to an increase in the surface concentration of the amide.

## 7.5 References

1. Penfold, J. and R.K. Thomas, *The application of the specular reflection of neutrons to the study of surfaces and interfaces*. Journal of Physics: Condensed Matter, 1990. **2**(6): p. 1369.
2. Crowley, T.L., E.M. Lee, E.A. Simister, and R.K. Thomas, *The use of contrast variation in the specular reflection of neutrons from interfaces*. Physica B: Condensed Matter, 1991. **173**(1-2): p. 143-156.
3. Bucknall, D.G., P. J., J.R.P. Webster, A. Zarbakhsh, R.M. Richardson, R. A., J.S. Higgins, and R.A.L. Jones. *SURF - A second generation neutron reflectometer*. in *Proc ICANS XIII, PSI Proceedings*. 1995.
4. Hellsing, M.S. and A.R. Rennie, *Effect of concentration and addition of ions on the adsorption of Aerosol-OT to Sapphire*. Langmuir, 2010. **26**(18): p. 14567-14573.
5. Penfold, J., et al., *Recent advances in the study of chemical surfaces and interfaces by specular neutron reflection*. Journal of the Chemical Society, Faraday Transactions, 1997. **93**(22): p. 3899-3917.
6. Holy, V., U. Pietsch, and T. Baumbach, *High-Resolution X-Ray Scattering From Thin Films and Multilayers*. Springer Tracts in Modern Physics. Vol. 149. 1998, New York: Springer.
7. Tompkins, H.G. and W.A. McGahan, *Spectroscopic Ellipsometry and Reflectometry*: John Wiley and Sons Inc.
8. Meyerhofer, D., *Characteristics of resist films produced by spinning*. Journal of Applied Physics, 1978. **49**(7): p. 3993-3997.
9. Ramirez, M.X., K.B. Walters, and D.E. Hirt, *Relationship between Erucamide Surface Concentration and Co-efficient of Friction of LLDPE film*. J. Vinyl Additive Tech., 2005. **11**: p. 9-12.
10. Allan, D., B.J. Briscoe, and D. Tabor, *Lubrication of polythene by oleamide and stearamide-II*. Wear, 1973. **25**: p. 393-397.
11. Dragnevski, K.I., A.M. Donald, S.M. Clarke, and A. Maltby, *Novel applications of ESEM and EDX for the study of molecularly thin amide monolayers on polymer films*. Colloids and Surfaces A: Physicochem. Engg. Aspects, 2009. **337**(1-3): p. 47-51.
12. Ramirez, M.X., D.E. Hirt, and L.L. Wright, *AFM Characterization of Surface Segregated Erucamide and Behenamide in Linear Low Density Polyethylene Film*. Nano Letters, 2002. **2**(1): p. 9-12.

# Chapter 8

## Future directions

---

This work has shown that a combination of techniques can be used to characterise monolayers of alkyl amides adsorbed on the solid/air, solid/liquid and polymer/air interfaces. Structural information has proven to be key in understanding monolayer self-assembly and rationalising mixing in the adsorbed layer. Suggestions for immediate and longer term future work are proposed here, along with results of some initial investigations already undertaken.

### **8.1 Hydrogen bonded monolayers: alkyl ureas**

#### **8.1.1 Introduction**

Alkyl ureas are a class of organic compounds that possess an additional nitrogen atom in the chain adjacent to the amide group as shown in Figure 8-1. These are used commercially in pharmaceutical drugs, cosmetics and polymeric materials (e.g. urea-formaldehyde resins). An initial investigation into the adsorption of alkyl ureas on graphite by DSC has been performed, and the results are shown below.

#### **8.1.2 Experimental details**

Three alkyl ureas have been used in this initial study (shown in Figure 8-1). These were purchased from Sigma-Aldrich and were obtained as trial samples (<50 mg). Sample preparation

and experimental details for measuring DSC thermograms have been described in detail in chapter 3.

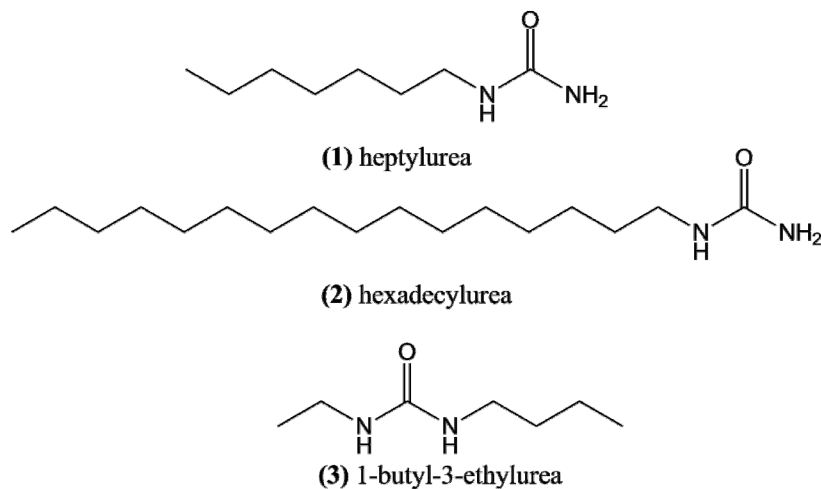


**Figure 8-1** Alkyl ureas used in this study

### 8.1.3 Results and further work

The melting points and enthalpies measured by DSC for the bulk and monolayer of three alkyl ureas adsorbed on graphite are shown in Table 8-1. The bulk (3D) melting points match well with those available in literature ( $\pm 5$  K) [1]. DSC thermograms for these materials show additional transitions in the adsorbed layer that are absent in the pure sample (without graphite) and could possibly be solid-solid phase transitions or melting of additional layers.

**Table 8-1** Transition temperatures (T) and melting enthalpies ( $\Delta H$ ) of alkyl ureas on graphite measured by DSC. The errors in these values are estimated as  $\pm 3$  K (temperature) and  $\pm 5$  kJ/mol (enthalpy). The alkyl ureas are shown in Figure 8-1.

| Alkyl urea | Monolayer melting point $T^{2D}$ (K) | $\Delta H^{2D}$ (kJ/mol) | Bulk melting point $T^{3D}$ (K) | $\Delta H^{3D}$ (kJ/mol) | $T^{2D}/T^{3D}$ |
|------------|--------------------------------------|--------------------------|---------------------------------|--------------------------|-----------------|
| (1)        | 405                                  | 24.69                    | 368                             | 14.70                    | 1.10            |
| (2)        | 436                                  | 47.13                    | 361                             | 42.67                    | 1.20            |
| (3)        | 407                                  | 25.14                    | 321                             | 15.40                    | 1.26            |

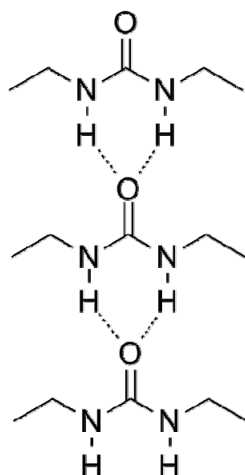


**Figure 8-2** ‘Chelated’ hydrogen bonds in urea groups

Interestingly, the ratio of the monolayer to bulk melting point ( $T^{2D}/T^{3D}$ ) for these materials is exceptionally high, higher than that reported for the amides in this work and other alkyl species in literature. Alkyl ureas are known to pack in extensive hydrogen bonded chains in the bulk as shown in Figure 8-2; the urea group is planar due to delocalisation of electrons [2]. A double (‘chelated’) hydrogen bond is observed, where the oxygen atom acts as a hydrogen bond receptor from two N-H donor groups [3]. Indeed, initial investigations of alkyl ureas adsorbed on the 1-octanol/graphite interface by STM [4] and in Langmuir layers on water [5] show similar ordering of the molecules.

A more detailed study into the structures and phase behaviour of these materials by X-ray diffraction is proposed here. A systematic study on the structural phases (and possible phase transitions) for alkyl ureas with different chain lengths and different positions of the urea group within the chain can be performed. Investigating the pure monolayer and binary mixing behaviour by DSC can provide more insight into the relative monolayer stability and the surface behaviour of these important compounds.

## 8.2 Amides at the polymer/air interface

Results from an initial study on the adsorption of alkyl amides at the polymer air/interface have been presented in chapter 7. Neutron reflection, used in combination with X-

ray reflection and ellipsometry, was demonstrated to be a successful technique in providing evidence for the existence of an amide layer at the interface for the first time. Neutron reflection was shown to be advantageous in that it can provide quantitative information on the amounts of amides adsorbed at the interface. This, in turn, has been used to rationalise observations of friction measurements at the polymer surface (chapter 7).

In order to gain a detailed understanding on the adsorption of amides at the polymer surface, a systematic investigation into the variation in surface amounts with various bulk amounts of amides is proposed. It is suggested to use neutron reflection, combined with X-ray reflection and ellipsometry, as explained in chapter 7. In this way, an ‘adsorption isotherm’ i.e. a plot of surface composition with various bulk concentrations can be measured. This information on the surface composition of the layer can help rationalise the friction measurements presented here. Such experiments will be indispensable in understanding and improving the commercial processes where these amides are important.

## 8.3 Mixing in amide monolayers on graphite

### 8.3.1 X-ray diffraction

As explained in chapter 1, mixing in alkane monolayers on graphite has been studied using different techniques. Figure 8-3 shows X-ray diffraction patterns from a sub-monolayer mixture of octane and nonane on graphite. The patterns for pure octane and pure nonane have individual peaks that have very different  $q$ -values (e.g. 0.58 and 0.46  $\text{\AA}^{-1}$ , respectively) [6]. The gradual shift in the peak positions in the composition range  $0.4 \leq X_{C9} \leq 1.0$  indicates mixing occurs in the monolayer in this composition range, and the appearance of the pure-component peaks between  $0 \leq X_{C9} \leq 0.4$  indicates phase separation occurs between the pure octane and the mixed system.

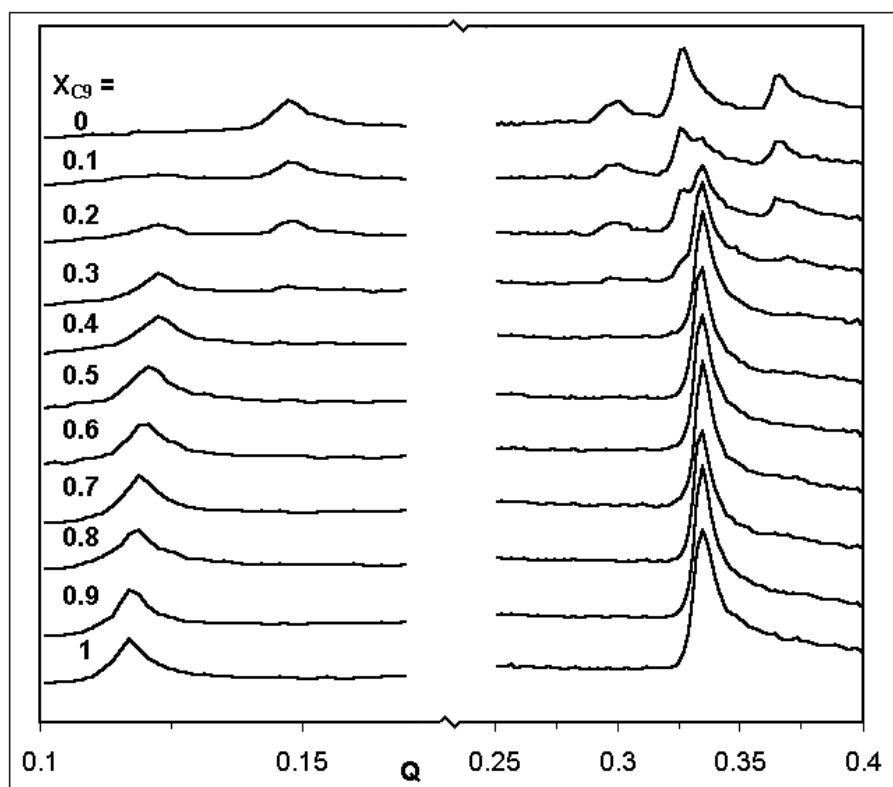


**Figure 8-3** X-ray diffraction patterns for varying compositions of the octane/nonane mixture at 0.8 monolayer coverage (from [6])

As discussed in chapter 6, the monolayer phase behaviour of the amides C12:0 and C12:1 c-5 on graphite studied by DSC showed that there was some degree of non-ideal mixing in the solid layer, in spite of the differences in the molecular architecture of the two mixing components (the *cis*-unsaturated amide has a bend in the molecule whereas the saturated amide does not). X-ray diffraction for the mixture could be used to confirm this possibly unexpected mixing behaviour. However, the two amides were found to possess structures that are very similar with regard to the unit cell dimensions and hydrogen bond geometry, as reflected in the diffraction patterns for these being very alike in peak positions and intensities (chapter 5). This was thought to inhibit an X-ray diffraction study similar to the octane/nonane mixture, where the peak separation is large, and gradual peak shifts can be easily identified.

However, a recent X-ray diffraction investigation into the sub-monolayer mixing behaviour of C<sub>11</sub> and C<sub>12</sub> carboxylic acids, which have similar peak positions, has been performed [7]. The diffraction peak intensity for the mixture could be expressed as a linear sum of the pure

component peak intensities, thereby indicating phase separation in the solid layer. A similar experiment is proposed for the C12:0/C12:1c-5 amide system, to validate the results observed by DSC in this work.

### 8.3.2 High coverage mixtures by DSC

An initial DSC study into the mixing behaviour of alkyl amides has been reported by Arnold and Clarke, and various binary mixtures of saturated/saturated and saturated/unsaturated amides were studied [8], as explained in this work. Particularly, for the saturated/saturated mixtures, mixtures of even chain length amides were investigated, and this work has addressed the mixing between the odd members. The mixing behaviour for the mixtures, studied here and previously [8], has been strongly supported by the 2D crystal structures calculated by diffraction in this work: mixing was observed to occur if the two components had the same symmetry and phase separation if not (for similar chain length molecules).

As part of a larger study in understanding the mixing behaviour in the amide monolayers, mixtures of odd and even amides of similar chain lengths (e.g. C5:0/C6:0, C7:0/C8:0 etc.) can be investigated systematically. A study by DSC is suggested first, and also by X-ray diffraction if necessary.

## 8.4 Molecular dynamics simulations

Molecular Dynamics (MD) simulations have been used to understand the adsorption and melting behaviour of alkanes on graphite by Taub et al and other workers [9-13]. These simulations have investigated the melting process and solid-solid phase transitions in the 2D layers.

The phase behaviour of heptanamide (C7:0) discussed in chapter 4 showed that this odd chain length amide changed phase from *pgg* to *p2* with temperature. Diffraction results suggested that the interactions of the terminal methyl carbons in the molecule might be responsible for this phase change, and that the two phases could have very similar energies.

Empirical hydrogen bond force fields in amide crystals have been parameterised using *6-exp* or *6-12* functions of the form  $E=Aexp(-Br)-Cr^{-6}$  (or variations thereof) supplemented by coulomb-

type interactions [14, 15] (where  $A$ ,  $B$  and  $C$  are constants and  $r$  is the distance from the hydrogen bond). Amide hydrogen bonds have been studied previously using MD simulations in the bulk crystals and in solution (e.g. see [16]).

In order to obtain a more quantitative picture of the relative weights of the interaction energies involved and the effect they may have on structure, it is suggested here to perform MD simulations on alkyl amides with chain lengths between 6-8 carbons on graphite. It is known that results from MD simulations are dependent on the appropriate definition and size of the system and values of the parameters involved, and hence these results would need support from the diffraction results already presented here.

## 8.5 Longer term directions

Control over the behaviour of two-dimensional self-assembled systems is an important issue due to their diverse applications, such as molecular electronics [17], thin films and design of functional materials [18-20]. Understanding the structural organisation of molecular layers is indispensable in gaining control over their surface behaviour.

For example, in designing optimal molecules in an effort to drive miniaturisation in electronics, three components of the molecule need to be considered: the surface active head group which binds effectively to the electrode in question, the alkyl chain/backbone of the molecule and the functional group at the end of the molecule which ensures good contact to the other electrode [17]. In another example, nano-porous networks of adsorbed molecules which have specific functional groups can have useful applications, such as sensors for specific molecules, and catalysis [18]. Since most molecules pack in a 'close-packed' manner, designing such porous networks can be challenging and requires choice of appropriate functional molecules.

Hydrogen bonding and other non-covalent interactions are an important component of molecular design owing to their directionality and range of energies involved. The strength of the hydrogen bond can be changed by appropriate choice of the hydrogen bonded head groups, and van der Waals attraction between molecules can be controlled by changing the length of the alkyl chain and the component atoms/groups in the chain. As already indicated in this work, differences in

interactions between the terminal methyl groups in the alkyl chain (van der Waals attractions) possibly cause the amides to arrange in different structural phases. These different structures affect the monolayer behaviour (melting enthalpies) and binary mixing behaviour of these amides.

## 8.6 References

1. *CrossFire Beilstein database (Elsevier)*. 2010 [cited; Available from: <http://www.reaxys.com>].
2. Kitaigorodskii, A.I., *Molecular crystals and molecules*. Physical chemistry, a series of monographs. 1973, New York: Academic Press.
3. Gilli, G. and P. Gilli, *The Nature of the Hydrogen Bond*. International Union of Crystallography Book Series. 2009, New York: Oxford University Press.
4. De Feyter, S. and F.C. De Schryver, *Self-Assembly at the Liquid/Solid Interface: STM Reveals*. *The Journal of Physical Chemistry B*, 2005. **109**(10): p. 4290-4302.
5. Dreger, K., B. Zou, Z. Mu, H.J. Galla, L. Chi, H. Fuchs, and H.J. SchÃ¶fer, *Synthesis and Surface Properties of New Ureas and Amides at Different Interfaces*. *Langmuir*, 2006. **22**(4): p. 1619-1625.
6. Arnold, T., *The adsorption of alkanes from their liquids and binary mixtures*. 2001, D. Phil Thesis, University of Oxford: Oxford.
7. Alba, M.D., A.K. Bickerstaffe, M.A. Castro, S.M. Clarke, S. Medina, C. Millán, M.M. Orta, E. Pavón, and A.C. Perdigón, *Phase separation of carboxylic acids on graphite surface at submonolayer regime*. *The European Physical Journal - Special Topics*, 2009. **167**(1): p. 151-156.
8. Arnold, T., Clarke, S. M., *Thermodynamic Investigation of the Adsorption of Amides on Graphite from Their Liquids and Binary Mixtures*. *Langmuir*, 2008. **24**(7): p. 3325-3335.
9. Yang, H., Z.-S. Li, Z.-Y. Lu, and C.-C. Sun, *Molecular dynamics simulations study on the melting process of n-heptane layer(s) adsorbed on the graphite (0 0 1) surface*. *Surface Science*, 2006. **600**(6): p. 1213-1220.
10. Diama, A., B. Matthies, K.W. Herwig, F.Y. Hansen, L. Criswell, H. Mo, M. Bai, and H. Taub, *Structure and phase transitions of monolayers of intermediate-length n-alkanes on graphite studied by neutron diffraction and molecular dynamics simulation*. *The Journal of Chemical Physics*, 2009. **131**(8): p. 084707-10.
11. Hansen, F.Y., K.W. Herwig, B. Matthies, and H. Taub, *Intramolecular and Lattice Melting in n-Alkane Monolayers: An Analog of Melting in Lipid Bilayers*. *Physical Review Letters*, 1999. **83**(12): p. 2362.
12. Hansen, F.Y., J.C. Newton, and H. Taub, *Molecular dynamics studies of the melting of butane and hexane monolayers adsorbed on the basal-plane surface of graphite*. *J. Chem. Phys.*, 1993. **98**(5): p. 4128-4141.

13. Krishnan, M., S. Balasubramanian, and S.M. Clarke, *An atomistic simulation study of a solid monolayer and trilayer of n-hexane on graphite*. Journal of Chemical Physics, 2003. **118**(11): p. 5082.
14. Gavezzotti, A. and G. Filippini, *Geometry of the Intermolecular X-H...Y (X, Y = N, O) Hydrogen Bond and the Calibration of Empirical Hydrogen-Bond Potentials*. J. Phys. Chem., 1994. **98**(18): p. 4831-4837.
15. Hagler, A.T., E. Huler, and S. Lifson, *Energy functions for peptide and proteins. I. Derivation of a consistent force field including the hydrogen bond in amide crystals*. Journal of the American Chemical Society, 1974. **96**(17): p. 5319.
16. Campa, A., A. Giansanti, and A. Tenenbaum, *Vibrational properties of the amide group in acetanilide: A molecular-dynamics study*. Physical Review B, 1987. **36**(8): p. 4394.
17. Hylke, B.A. and B. Bert de, *Electrical conduction through single molecules and self-assembled monolayers*. Journal of Physics: Condensed Matter, 2008. **20**(1): p. 013001.
18. Kudernac, T., S. Lei, J.A.A.W. Elemans, and S. De Feyter, *Two-dimensional supramolecular self-assembly: nanoporous networks on surfaces*. Chemical Society Reviews, 2009. **38**(2): p. 402-421.
19. Thalacker, C., A. Miura, S.D. Feyter, F.C.D. Schryver, and F. Wurthner, *Hydrogen bond directed self-assembly of core-substituted naphthalene bisimides with melamines in solution and at the graphite interface*. Organic & Biomolecular Chemistry, 2005. **3**(3): p. 414-422.
20. Boncheva, M., D.A. Bruzewicz, and G.M. Whitesides, *Millimeter-scale self-assembly and its applications*. Pure & Appl.Chem., 2003. **75**(5): p. 621-630.

## Chapter 9

### Concluding remarks

---

The adsorption of alkyl amides on the surface of graphite has been investigated by a combination of techniques which include neutron and X-ray powder diffraction and differential scanning calorimetry. Structural information obtained by diffraction techniques in these layers has proven to be key in understanding the functionality of these commercially important materials. Thermodynamic measurements by DSC have provided important information regarding mixing in the adsorbed layers and these have been supported by the diffraction results.

The two-dimensional crystalline structures of saturated alkyl amides, pentanamide (C5:0) to hexadecanamide (C16:0), calculated using synchrotron X-ray and neutron diffraction at sub-monolayer coverage, indicate that all the amide molecules lie flat on the graphite surface. By considering a number of members of the homologous series, the plane groups of the amide layers have been identified. The molecules form dimers which in turn form chains, and depending on the number of carbons in the alkyl chain, adopt a plane group with either  $p2$  or  $pgg$  symmetry. There is good qualitative agreement with the adsorbed monolayer structures of a related homologue reported by STM for the  $p2$  symmetry structures, and also with the bulk (3D) crystal structures.

The positions of the molecules indicate the presence of extensive hydrogen bonds in the monolayer which dominate the system. A comprehensive analysis has revealed the symmetry of the monolayer structures and geometry of the hydrogen bonded structures to greater detail.

An odd-even effect in the monolayer structures and melting enthalpies has been observed. Shorter odd chain length saturated amides have structures with *pgg* symmetry (C5:0), while longer odd amides have *p2* symmetry (C9:0 and C11:0), and all even amides studied here were found to have *p2* symmetry at 300 K. The heptanamide (C7:0) monolayer undergoes a phase transition at 330 K from a low temperature *pgg* to a high temperature *p2* phase prior to melting. Other similar chain length amides did not exhibit a solid-solid phase transition in their layers at sub-monolayer coverage. A coverage dependent study of C11:0 amide revealed a transition corresponding to the possible melting of the second layer of the adsorbate, similar to adsorbed alcohols and noble gases on graphite reported previously.

Diffraction patterns for dodecanamide (C12:0) show that there is minimal change in the molecular structure at higher coverages, in contrast with other alkyl species such as alkanes which show a 2-5% compression in the monolayer at higher coverage. The monolayers of several amides melt at a much higher temperatures compared to the bulk amide even at sub-monolayer coverage. These results show that the amide layers are very stable, with higher stability than that seen before for similar species adsorbed on graphite. These results are attributed to the extensive hydrogen bonding present in these systems.

The shorter length unsaturated amides ( $C_n \leq 12$ ) studied here have structures that are similar to the corresponding saturated amide: the molecules hydrogen bond into dimers with *p2* symmetry. *Trans*-unsaturated amides which have their double bond conjugated to the amide head group have shorter N...O hydrogen bond distances than the corresponding saturated molecule. This has been attributed to the extended delocalisation around the amide group which strengthens the hydrogen bond, in accord with similar bulk systems.

Monolayer phase diagrams for binary mixtures of amides have been measured by DSC and fitted to different thermodynamic models such as ideal mixing, phase separation and regular solution models. Most systems are found to mix better in the monolayer than in the bulk which agrees

with the observations of other alkyl species in literature. In all cases there is almost no preference for adsorption of either species for both component amides that have the same chain length.

The DSC results are strongly supported by the monolayer structures of the individual mixing components: odd chain length saturated amides were found mix if the monolayer structures have the same symmetry, and phase separate if the symmetry was different. Depending on the nature and position of the double bond, saturated/unsaturated amides of the same chain length were found to behave nearly ideally in the solid layer. Diffraction results have provided some insight into the mixing behaviour of saturated/*cis*-unsaturated (C12:0/C12:1 *c*-5) amides.

An initial investigation into the adsorption of amides at the polystyrene/air interface has been made. Coefficient of friction measurements indicate that small amounts of amides are observed to reduce friction at the polymer surface and the trends seen agree with literature. X-ray and neutron reflectivity profiles have been simulated assuming a 'multilayer' model for the different layers on the silicon substrate which agree with experimental data. Neutron reflection has provided evidence for the existence of an amide layer on the surface for the first time. Quantitative information on the amount of amide present on the surface has been presented, and these results relate with friction measurements. An increase in the surface amount of amide is shown to correspond to a decrease in surface friction.

Several areas of further study have been suggested. Preliminary studies on alkyl ureas adsorbed on graphite reveal the formation of extremely stable monolayers, and a systematic structural investigation of these molecules can help understand their self-assembly. A detailed investigation into the adsorption of amides at the polymer/air interface is proposed. A combination of X-ray and neutron reflection and ellipsometry can be used to quantitatively understand the surface composition of the polymer films and further rationalise the friction measurements. X-ray diffraction on the mixing behaviour of C12:0/C12:1 *c*-5 amides is suggested to validate the results observed by DSC. Finally, longer term directions for adsorbed monolayers have been discussed.

# Appendices

## A. Fitted atomic coordinates

---

The atomic coordinates for the fitted X-ray and neutron diffraction patterns presented in chapters 4 and 5 are listed here. The coordinates are for the single repeating motif in the asymmetric unit for the structures. Symmetry operations to generate the remaining molecules from the coordinates given here have been explained in §2.6.

In the following tables,  $X_{frac}$  and  $Y_{frac}$  are given as fractions (w.r.t the unit cell lengths) and  $Z_{abs}$  is the absolute distance (Å) of the atom above the C-C-C plane of the molecule (which is parallel to the graphite plane). The unit cell dimensions for each of the structures have been given in chapters 4 and 5.

Table A-1 Pentanamide, C5:0 (*pgg* phase)

| Atom | X <sub>frac</sub> | Y <sub>frac</sub> | Z <sub>abs</sub> (Å) | Atom | X <sub>frac</sub> | Y <sub>frac</sub> | Z <sub>abs</sub> (Å) |
|------|-------------------|-------------------|----------------------|------|-------------------|-------------------|----------------------|
| O    | -0.0288           | -0.1184           | 0.0000               | C    | 0.1087            | 0.2254            | 0.0000               |
| N    | -0.0181           | 0.3094            | 0.0000               | H    | 0.1161            | 0.1119            | 0.8950               |
| C    | -0.0049           | 0.0747            | 0.0000               | H    | 0.1161            | 0.1119            | -0.8950              |
| C    | 0.0395            | 0.0253            | 0.0000               | C    | 0.1335            | 0.4748            | 0.0000               |
| H    | 0.0469            | -0.0882           | 0.8950               | H    | 0.1261            | 0.5883            | 0.8950               |
| H    | 0.0469            | -0.0882           | -0.8950              | H    | 0.1261            | 0.5883            | -0.8950              |
| C    | 0.0643            | 0.2748            | 0.0000               | H    | -0.0477           | 0.3424            | 0.0000               |
| H    | 0.0569            | 0.3883            | 0.8950               | H    | 0.1649            | 0.4305            | 0.0000               |
| H    | 0.0569            | 0.3883            | -0.8950              | H    | -0.0015           | 0.4760            | 0.0000               |

Table A-2 Hexanamide, C6:0 (*p2* phase)

| X-ray pattern |                   |                   |                      | Neutron pattern |                   |                   |                      |
|---------------|-------------------|-------------------|----------------------|-----------------|-------------------|-------------------|----------------------|
| Atom          | X <sub>frac</sub> | Y <sub>frac</sub> | Z <sub>abs</sub> (Å) | Atom            | X <sub>frac</sub> | Y <sub>frac</sub> | Z <sub>abs</sub> (Å) |
| O             | -0.0494           | -0.1178           | 0.0000               | O               | -0.0492           | -0.1225           | 0.0000               |
| N             | -0.0289           | 0.3106            | 0.0000               | N               | -0.0326           | 0.3094            | 0.0000               |
| C             | -0.0079           | 0.0750            | 0.0000               | C               | -0.0088           | 0.0746            | 0.0000               |
| C             | 0.0669            | 0.0242            | 0.0000               | C               | 0.0680            | 0.0301            | 0.0000               |
| H             | 0.0789            | -0.0897           | 0.8950               | D               | 0.0814            | -0.0833           | 0.8950               |
| H             | 0.0789            | -0.0897           | -0.8950              | D               | 0.0814            | -0.0833           | -0.8950              |
| C             | 0.1103            | 0.2735            | 0.0000               | C               | 0.1098            | 0.2841            | 0.0000               |
| H             | 0.0984            | 0.3874            | 0.8950               | D               | 0.0964            | 0.3975            | 0.8950               |
| H             | 0.0984            | 0.3874            | -0.8950              | D               | 0.0964            | 0.3975            | -0.8950              |
| C             | 0.1851            | 0.2227            | 0.0000               | C               | 0.1866            | 0.2396            | 0.0000               |
| H             | 0.1971            | 0.1088            | 0.8950               | D               | 0.1999            | 0.1262            | 0.8950               |
| H             | 0.1971            | 0.1088            | -0.8950              | D               | 0.1999            | 0.1262            | -0.8950              |
| C             | 0.2285            | 0.4719            | 0.0000               | C               | 0.2283            | 0.4936            | 0.0000               |
| H             | 0.2166            | 0.5859            | 0.8950               | D               | 0.2150            | 0.6070            | 0.8950               |
| H             | 0.2166            | 0.5859            | -0.8950              | D               | 0.2150            | 0.6070            | -0.8950              |
| C             | 0.3033            | 0.4212            | 0.0000               | C               | 0.3051            | 0.4491            | 0.0000               |
| H             | 0.3152            | 0.3072            | 0.8950               | D               | 0.3184            | 0.3357            | 0.8950               |
| H             | 0.3152            | 0.3072            | -0.8950              | D               | 0.3184            | 0.3357            | -0.8950              |
| H             | -0.0788           | 0.3445            | 0.0000               | H               | -0.0839           | 0.3391            | 0.0000               |
| H             | 0.3323            | 0.6037            | 0.0000               | D               | 0.3328            | 0.6349            | 0.0000               |
| H             | 0.0001            | 0.4771            | 0.0000               | H               | -0.0048           | 0.4791            | 0.0000               |

Table A-3 Heptanamide, C7:0

| Atom | <i>pgg</i> phase  |                   |                      | <i>p2</i> phase   |                   |                      |
|------|-------------------|-------------------|----------------------|-------------------|-------------------|----------------------|
|      | X <sub>frac</sub> | Y <sub>frac</sub> | Z <sub>abs</sub> (Å) | X <sub>frac</sub> | Y <sub>frac</sub> | Z <sub>abs</sub> (Å) |
| O    | -0.0228           | -0.1205           | 0.0000               | -0.0503           | -0.1284           | 0.0000               |
| N    | -0.0142           | 0.3027            | 0.0000               | -0.0158           | 0.3093            | 0.0000               |
| C    | -0.0037           | 0.0705            | 0.0000               | -0.0045           | 0.0720            | 0.0000               |
| C    | 0.0300            | 0.0239            | 0.0000               | 0.0607            | 0.0302            | 0.0000               |
| H    | 0.0360            | -0.0883           | 0.8950               | 0.0678            | -0.0844           | 0.8950               |
| H    | 0.0360            | -0.0883           | -0.8950              | 0.0678            | -0.0844           | -0.8950              |
| C    | 0.0489            | 0.2594            | 0.0000               | 0.1080            | 0.2764            | 0.0000               |
| H    | 0.0430            | 0.3717            | 0.8950               | 0.1009            | 0.3910            | 0.8950               |
| H    | 0.0430            | 0.3717            | -0.8950              | 0.1009            | 0.3910            | -0.8950              |
| C    | 0.0827            | 0.2128            | 0.0000               | 0.1731            | 0.2346            | 0.0000               |
| H    | 0.0886            | 0.1005            | 0.8950               | 0.1802            | 0.1200            | 0.8950               |
| H    | 0.0886            | 0.1005            | -0.8950              | 0.1802            | 0.1200            | -0.8950              |
| C    | 0.1016            | 0.4483            | 0.0000               | 0.2204            | 0.4808            | 0.0000               |
| H    | 0.0957            | 0.5606            | 0.8950               | 0.2133            | 0.5954            | 0.8950               |
| H    | 0.0957            | 0.5606            | -0.8950              | 0.2133            | 0.5954            | -0.8950              |
| C    | 0.1354            | 0.4017            | 0.0000               | 0.2856            | 0.4390            | 0.0000               |
| H    | 0.1413            | 0.2894            | 0.8950               | 0.2927            | 0.3244            | 0.8950               |
| H    | 0.1413            | 0.2894            | -0.8950              | 0.2927            | 0.3244            | -0.8950              |
| C    | 0.1543            | 0.6372            | 0.0000               | 0.3329            | 0.6851            | 0.0000               |
| H    | 0.1483            | 0.7494            | 0.8950               | 0.3257            | 0.7997            | 0.8950               |
| H    | 0.1483            | 0.7494            | -0.8950              | 0.3257            | 0.7997            | -0.8950              |
| H    | -0.0379           | 0.3354            | 0.0000               | -0.0614           | 0.3386            | 0.0000               |
| H    | 0.1793            | 0.5933            | 0.0000               | 0.3807            | 0.6446            | 0.0000               |
| H    | -0.0010           | 0.4676            | 0.0000               | 0.0173            | 0.4816            | 0.0000               |

Table A-4 Octanamide, C8:0 (*p*2 phase)

| Atom | X <sub>frac</sub> | Y <sub>frac</sub> | Z <sub>abs</sub> (Å) | Atom | X <sub>frac</sub> | Y <sub>frac</sub> | Z <sub>abs</sub> (Å) |
|------|-------------------|-------------------|----------------------|------|-------------------|-------------------|----------------------|
| O    | -0.0427           | -0.1190           | 0.0000               | H    | 0.1854            | 0.5757            | -0.8950              |
| N    | -0.0150           | 0.3111            | 0.0000               | C    | 0.2497            | 0.4098            | 0.0000               |
| C    | -0.0043           | 0.0740            | 0.0000               | H    | 0.2563            | 0.2951            | 0.8950               |
| C    | 0.0534            | 0.0227            | 0.0000               | H    | 0.2563            | 0.2951            | -0.8950              |
| H    | 0.0600            | -0.0920           | 0.8950               | C    | 0.2902            | 0.6546            | 0.0000               |
| H    | 0.0600            | -0.0920           | -0.8950              | H    | 0.2836            | 0.7693            | 0.8950               |
| C    | 0.0939            | 0.2675            | 0.0000               | H    | 0.2836            | 0.7693            | -0.8950              |
| H    | 0.0873            | 0.3822            | 0.8950               | C    | 0.3478            | 0.6033            | 0.0000               |
| H    | 0.0873            | 0.3822            | -0.8950              | H    | 0.3545            | 0.4886            | 0.8950               |
| C    | 0.1515            | 0.2162            | 0.0000               | H    | 0.3545            | 0.4886            | -0.8950              |
| H    | 0.1581            | 0.1016            | 0.8950               | H    | -0.0543           | 0.3460            | 0.0000               |
| H    | 0.1581            | 0.1016            | -0.8950              | H    | 0.3758            | 0.7862            | 0.0000               |
| C    | 0.1921            | 0.4610            | 0.0000               | H    | 0.0126            | 0.4779            | 0.0000               |
| H    | 0.1854            | 0.5757            | 0.8950               |      |                   |                   |                      |

Table A-5 Nonanamide, C9:0 (*p*2 phase)

| Atom | X <sub>frac</sub> | Y <sub>frac</sub> | Z <sub>abs</sub> (Å) | Atom | X <sub>frac</sub> | Y <sub>frac</sub> | Z <sub>abs</sub> (Å) |
|------|-------------------|-------------------|----------------------|------|-------------------|-------------------|----------------------|
| O    | -0.0392           | -0.1141           | 0.0000               | C    | 0.2368            | 0.3993            | 0.0000               |
| N    | -0.0178           | 0.3118            | 0.0000               | H    | 0.2443            | 0.2849            | 0.8950               |
| C    | -0.0050           | 0.0754            | 0.0000               | H    | 0.2443            | 0.2849            | -0.8950              |
| C    | 0.0513            | 0.0196            | 0.0000               | C    | 0.2732            | 0.6450            | 0.0000               |
| H    | 0.0589            | -0.0949           | 0.8950               | H    | 0.2656            | 0.7595            | 0.8950               |
| H    | 0.0589            | -0.0949           | -0.8950              | H    | 0.2656            | 0.7595            | -0.8950              |
| C    | 0.0878            | 0.2652            | 0.0000               | C    | 0.3295            | 0.5892            | 0.0000               |
| H    | 0.0802            | 0.3797            | 0.8950               | H    | 0.3370            | 0.4747            | 0.8950               |
| H    | 0.0802            | 0.3797            | -0.8950              | H    | 0.3370            | 0.4747            | -0.8950              |
| C    | 0.1440            | 0.2095            | 0.0000               | C    | 0.3659            | 0.8349            | 0.0000               |
| H    | 0.1516            | 0.0950            | 0.8950               | H    | 0.3584            | 0.9494            | 0.8950               |
| H    | 0.1516            | 0.0950            | -0.8950              | H    | 0.3584            | 0.9494            | -0.8950              |
| C    | 0.1805            | 0.4551            | 0.0000               | H    | -0.0554           | 0.3491            | 0.0000               |
| H    | 0.1729            | 0.5696            | 0.8950               | H    | 0.4055            | 0.7861            | 0.0000               |
| H    | 0.1729            | 0.5696            | -0.8950              | H    | 0.0065            | 0.4759            | 0.0000               |

Table A-6 Decanamide, C10:0 (*p*2 phase)

| Atom | X <sub>frac</sub> | Y <sub>frac</sub> | Z <sub>abs</sub> (Å) | Atom | X <sub>frac</sub> | Y <sub>frac</sub> | Z <sub>abs</sub> (Å) |
|------|-------------------|-------------------|----------------------|------|-------------------|-------------------|----------------------|
| O    | -0.0337           | -0.1210           | 0.0000               | H    | 0.2142            | 0.3316            | 0.8950               |
| N    | -0.0189           | 0.3056            | 0.0000               | H    | 0.2142            | 0.3316            | -0.8950              |
| C    | -0.0051           | 0.0737            | 0.0000               | C    | 0.2364            | 0.6945            | 0.0000               |
| C    | 0.0454            | 0.0297            | 0.0000               | H    | 0.2285            | 0.8065            | 0.8950               |
| H    | 0.0532            | -0.0823           | 0.8950               | H    | 0.2285            | 0.8065            | -0.8950              |
| H    | 0.0532            | -0.0823           | -0.8950              | C    | 0.2869            | 0.6505            | 0.0000               |
| C    | 0.0754            | 0.2806            | 0.0000               | H    | 0.2947            | 0.5385            | 0.8950               |
| H    | 0.0675            | 0.3926            | 0.8950               | H    | 0.2947            | 0.5385            | -0.8950              |
| H    | 0.0675            | 0.3926            | -0.8950              | C    | 0.3169            | 0.9014            | 0.0000               |
| C    | 0.1259            | 0.2367            | 0.0000               | H    | 0.3090            | 1.0134            | 0.8950               |
| H    | 0.1337            | 0.1247            | 0.8950               | H    | 0.3090            | 1.0134            | -0.8950              |
| H    | 0.1337            | 0.1247            | -0.8950              | C    | 0.3674            | 0.8575            | 0.0000               |
| C    | 0.1559            | 0.4876            | 0.0000               | H    | 0.3752            | 0.7455            | 0.8950               |
| H    | 0.1480            | 0.5996            | 0.8950               | H    | 0.3752            | 0.7455            | -0.8950              |
| H    | 0.1480            | 0.5996            | -0.8950              | H    | -0.0526           | 0.3350            | 0.0000               |
| C    | 0.2064            | 0.4436            | 0.0000               | H    | 0.3874            | 1.0410            | 0.0000               |
|      |                   |                   |                      | H    | 0.0011            | 0.4732            | 0.0000               |

Table A-7 Undecanamide, C11:0 (*p*2 phase)

| Atom | X <sub>frac</sub> | Y <sub>frac</sub> | Z <sub>abs</sub> (Å) | Atom | X <sub>frac</sub> | Y <sub>frac</sub> | Z <sub>abs</sub> (Å) |
|------|-------------------|-------------------|----------------------|------|-------------------|-------------------|----------------------|
| O    | -0.0324           | -0.1132           | 0.0000               | C    | 0.2266            | 0.6398            | 0.0000               |
| N    | -0.0178           | 0.3093            | 0.0000               | H    | 0.2192            | 0.7533            | 0.8950               |
| C    | -0.0049           | 0.0747            | 0.0000               | H    | 0.2192            | 0.7533            | -0.8950              |
| C    | 0.0435            | 0.0194            | 0.0000               | C    | 0.2750            | 0.5845            | 0.0000               |
| H    | 0.0509            | -0.0941           | 0.8950               | H    | 0.2824            | 0.4709            | 0.8950               |
| H    | 0.0509            | -0.0941           | -0.8950              | H    | 0.2824            | 0.4709            | -0.8950              |
| C    | 0.0723            | 0.2631            | 0.0000               | C    | 0.3038            | 0.8281            | 0.0000               |
| H    | 0.0649            | 0.3767            | 0.8950               | H    | 0.2964            | 0.9417            | 0.8950               |
| H    | 0.0649            | 0.3767            | -0.8950              | H    | 0.2964            | 0.9417            | -0.8950              |
| C    | 0.1206            | 0.2078            | 0.0000               | C    | 0.3521            | 0.7728            | 0.0000               |
| H    | 0.1280            | 0.0942            | 0.8950               | H    | 0.3595            | 0.6593            | 0.8950               |
| H    | 0.1280            | 0.0942            | -0.8950              | H    | 0.3595            | 0.6593            | -0.8950              |
| C    | 0.1495            | 0.4514            | 0.0000               | C    | 0.3810            | 1.0165            | 0.0000               |
| H    | 0.1421            | 0.5650            | 0.8950               | H    | 0.3735            | 1.1300            | 0.8950               |

|   |        |        |         |   |         |        |         |
|---|--------|--------|---------|---|---------|--------|---------|
| H | 0.1421 | 0.5650 | -0.8950 | H | 0.3735  | 1.1300 | -0.8950 |
| C | 0.1978 | 0.3961 | 0.0000  | H | -0.0501 | 0.3462 | 0.0000  |
| H | 0.2052 | 0.2826 | 0.8950  | H | 0.4150  | 0.9680 | 0.0000  |
| H | 0.2052 | 0.2826 | -0.8950 | H | 0.0014  | 0.4721 | 0.0000  |

Table A-8 Dodecanamide, C12:0 (*p2* phase)

| X-ray pattern |                   |                   |                      | Neutron pattern |                   |                   |                      |
|---------------|-------------------|-------------------|----------------------|-----------------|-------------------|-------------------|----------------------|
| Atom          | X <sub>frac</sub> | Y <sub>frac</sub> | Z <sub>abs</sub> (Å) | Atom            | X <sub>frac</sub> | Y <sub>frac</sub> | Z <sub>abs</sub> (Å) |
| O             | -0.0292           | -0.1139           | 0.0000               | O               | -0.0284           | -0.1182           | 0.0000               |
| N             | -0.0172           | 0.3096            | 0.0000               | N               | -0.0195           | 0.3078            | 0.0000               |
| C             | -0.0047           | 0.0748            | 0.0000               | C               | -0.0052           | 0.0743            | 0.0000               |
| C             | 0.0396            | 0.0201            | 0.0000               | C               | 0.0395            | 0.0257            | 0.0000               |
| H             | 0.0467            | -0.0935           | 0.8950               | D               | 0.0474            | -0.0872           | 0.8950               |
| H             | 0.0467            | -0.0935           | -0.8950              | D               | 0.0474            | -0.0872           | -0.8950              |
| C             | 0.0651            | 0.2647            | 0.0000               | C               | 0.0633            | 0.2743            | 0.0000               |
| H             | 0.0580            | 0.3783            | 0.8950               | D               | 0.0554            | 0.3872            | 0.8950               |
| H             | 0.0580            | 0.3783            | -0.8950              | D               | 0.0554            | 0.3872            | -0.8950              |
| C             | 0.1093            | 0.2100            | 0.0000               | C               | 0.1080            | 0.2256            | 0.0000               |
| H             | 0.1164            | 0.0964            | 0.8950               | D               | 0.1160            | 0.1127            | 0.8950               |
| H             | 0.1164            | 0.0964            | -0.8950              | D               | 0.1160            | 0.1127            | -0.8950              |
| C             | 0.1349            | 0.4546            | 0.0000               | C               | 0.1319            | 0.4742            | 0.0000               |
| H             | 0.1278            | 0.5682            | 0.8950               | D               | 0.1239            | 0.5871            | 0.8950               |
| H             | 0.1278            | 0.5682            | -0.8950              | D               | 0.1239            | 0.5871            | -0.8950              |
| C             | 0.1791            | 0.3999            | 0.0000               | C               | 0.1766            | 0.4256            | 0.0000               |
| H             | 0.1862            | 0.2863            | 0.8950               | D               | 0.1845            | 0.3127            | 0.8950               |
| H             | 0.1862            | 0.2863            | -0.8950              | D               | 0.1845            | 0.3127            | -0.8950              |
| C             | 0.2047            | 0.6445            | 0.0000               | C               | 0.2004            | 0.6742            | 0.0000               |
| H             | 0.1976            | 0.7581            | 0.8950               | D               | 0.1925            | 0.7871            | 0.8950               |
| H             | 0.1976            | 0.7581            | -0.8950              | D               | 0.1925            | 0.7871            | -0.8950              |
| C             | 0.2489            | 0.5898            | 0.0000               | C               | 0.2451            | 0.6255            | 0.0000               |
| H             | 0.2560            | 0.4762            | 0.8950               | D               | 0.2531            | 0.5126            | 0.8950               |
| H             | 0.2560            | 0.4762            | -0.8950              | D               | 0.2531            | 0.5126            | -0.8950              |
| C             | 0.2745            | 0.8344            | 0.0000               | C               | 0.2690            | 0.8741            | 0.0000               |
| H             | 0.2674            | 0.9480            | 0.8950               | D               | 0.2610            | 0.9870            | 0.8950               |
| H             | 0.2674            | 0.9480            | -0.8950              | D               | 0.2610            | 0.9870            | -0.8950              |
| C             | 0.3187            | 0.7797            | 0.0000               | C               | 0.3137            | 0.8255            | 0.0000               |

|   |         |        |         |   |         |        |         |
|---|---------|--------|---------|---|---------|--------|---------|
| H | 0.3258  | 0.6661 | 0.8950  | D | 0.3216  | 0.7126 | 0.8950  |
| H | 0.3258  | 0.6661 | -0.8950 | D | 0.3216  | 0.7126 | -0.8950 |
| C | 0.3442  | 1.0243 | 0.0000  | C | 0.3375  | 1.0741 | 0.0000  |
| H | 0.3371  | 1.1379 | 0.8950  | D | 0.3296  | 1.1870 | 0.8950  |
| H | 0.3371  | 1.1379 | -0.8950 | D | 0.3296  | 1.1870 | -0.8950 |
| C | 0.3885  | 0.9696 | 0.0000  | C | 0.3822  | 1.0255 | 0.0000  |
| H | 0.3956  | 0.8560 | 0.8950  | D | 0.3902  | 0.9126 | 0.8950  |
| H | 0.3956  | 0.8560 | -0.8950 | D | 0.3902  | 0.9126 | -0.8950 |
| C | -0.0467 | 0.3461 | 0.0000  | H | -0.0494 | 0.3403 | 0.0000  |
| H | 0.4055  | 1.1489 | 0.0000  | D | 0.3980  | 1.2075 | 0.0000  |
| H | -0.0001 | 0.4729 | 0.0000  | H | -0.0036 | 0.4739 | 0.0000  |

Table A-9 Tetradecanamide, C14:0 (*p*2 phase)

| Atom | X <sub>frac</sub> | Y <sub>frac</sub> | Z <sub>abs</sub> (Å) | Atom | X <sub>frac</sub> | Y <sub>frac</sub> | Z <sub>abs</sub> (Å) |
|------|-------------------|-------------------|----------------------|------|-------------------|-------------------|----------------------|
| O    | -0.0261           | -0.1098           | 0.0000               | H    | 0.2290            | 0.4374            | 0.8950               |
| N    | -0.0155           | 0.3142            | 0.0000               | H    | 0.2290            | 0.4374            | -0.8950              |
| C    | -0.0042           | 0.0760            | 0.0000               | C    | 0.2455            | 0.7947            | 0.0000               |
| C    | 0.0354            | 0.0138            | 0.0000               | H    | 0.2391            | 0.9102            | 0.8950               |
| H    | 0.0418            | -0.1016           | 0.8950               | H    | 0.2391            | 0.9102            | -0.8950              |
| H    | 0.0418            | -0.1016           | -0.8950              | C    | 0.2851            | 0.7326            | 0.0000               |
| C    | 0.0582            | 0.2557            | 0.0000               | H    | 0.2914            | 0.6171            | 0.8950               |
| H    | 0.0518            | 0.3711            | 0.8950               | H    | 0.2914            | 0.6171            | -0.8950              |
| H    | 0.0518            | 0.3711            | -0.8950              | C    | 0.3079            | 0.9744            | 0.0000               |
| C    | 0.0978            | 0.1935            | 0.0000               | H    | 0.3015            | 1.0899            | 0.8950               |
| H    | 0.1042            | 0.0781            | 0.8950               | H    | 0.3015            | 1.0899            | -0.8950              |
| H    | 0.1042            | 0.0781            | -0.8950              | C    | 0.3475            | 0.9123            | 0.0000               |
| C    | 0.1206            | 0.4354            | 0.0000               | H    | 0.3539            | 0.7968            | 0.8950               |
| H    | 0.1143            | 0.5508            | 0.8950               | H    | 0.3539            | 0.7968            | -0.8950              |
| H    | 0.1143            | 0.5508            | -0.8950              | C    | 0.3703            | 1.1541            | 0.0000               |
| C    | 0.1602            | 0.3732            | 0.0000               | H    | 0.3639            | 1.2696            | 0.8950               |
| H    | 0.1666            | 0.2578            | 0.8950               | H    | 0.3639            | 1.2696            | -0.8950              |
| H    | 0.1666            | 0.2578            | -0.8950              | C    | 0.4099            | 1.0920            | 0.0000               |
| C    | 0.1830            | 0.6151            | 0.0000               | H    | 0.4163            | 0.9765            | 0.8950               |
| H    | 0.1767            | 0.7305            | 0.8950               | H    | 0.4163            | 0.9765            | -0.8950              |
| H    | 0.1767            | 0.7305            | -0.8950              | H    | -0.0419           | 0.3557            | 0.0000               |
| C    | 0.2226            | 0.5529            | 0.0000               | H    | 0.4251            | 1.2695            | 0.0000               |
|      |                   |                   |                      | H    | -0.0002           | 0.4757            | 0.0000               |

Table A-10 Hexadecanamide, C16:0 (*p*2 phase)

| Atom | X <sub>frac</sub> | Y <sub>frac</sub> | Z <sub>abs</sub> (Å) | Atom | X <sub>frac</sub> | Y <sub>frac</sub> | Z <sub>abs</sub> (Å) |
|------|-------------------|-------------------|----------------------|------|-------------------|-------------------|----------------------|
| O    | -0.0212           | -0.1231           | 0.0000               | D    | 0.1951            | 1.0282            | 0.8950               |
| N    | -0.0148           | 0.3219            | 0.0000               | D    | 0.1951            | 1.0282            | -0.8950              |
| C    | -0.0040           | 0.0777            | 0.0000               | C    | 0.2347            | 0.8588            | 0.0000               |
| C    | 0.0296            | 0.0263            | 0.0000               | D    | 0.2407            | 0.7407            | 0.8950               |
| D    | 0.0356            | -0.0917           | 0.8950               | D    | 0.2407            | 0.7407            | -0.8950              |
| D    | 0.0356            | -0.0917           | -0.8950              | C    | 0.2524            | 1.1183            | 0.0000               |
| C    | 0.0473            | 0.2858            | 0.0000               | D    | 0.2464            | 1.2363            | 0.8950               |
| D    | 0.0413            | 0.4039            | 0.8950               | D    | 0.2464            | 1.2363            | -0.8950              |
| D    | 0.0413            | 0.4039            | -0.8950              | C    | 0.2860            | 1.0669            | 0.0000               |
| C    | 0.0809            | 0.2345            | 0.0000               | D    | 0.2920            | 0.9489            | 0.8950               |
| D    | 0.0869            | 0.1164            | 0.8950               | D    | 0.2920            | 0.9489            | -0.8950              |
| D    | 0.0869            | 0.1164            | -0.8950              | C    | 0.3037            | 1.3264            | 0.0000               |
| C    | 0.0986            | 0.4939            | 0.0000               | D    | 0.2976            | 1.4445            | 0.8950               |
| D    | 0.0925            | 0.6120            | 0.8950               | D    | 0.2976            | 1.4445            | -0.8950              |
| D    | 0.0925            | 0.6120            | -0.8950              | C    | 0.3373            | 1.2750            | 0.0000               |
| C    | 0.1322            | 0.4426            | 0.0000               | D    | 0.3433            | 1.1570            | 0.8950               |
| D    | 0.1382            | 0.3245            | 0.8950               | D    | 0.3433            | 1.1570            | -0.8950              |
| D    | 0.1382            | 0.3245            | -0.8950              | C    | 0.3550            | 1.5345            | 0.0000               |
| C    | 0.1499            | 0.7021            | 0.0000               | D    | 0.3489            | 1.6526            | 0.8950               |
| D    | 0.1438            | 0.8201            | 0.8950               | D    | 0.3489            | 1.6526            | -0.8950              |
| D    | 0.1438            | 0.8201            | -0.8950              | C    | 0.3885            | 1.4831            | 0.0000               |
| C    | 0.1834            | 0.6507            | 0.0000               | D    | 0.3946            | 1.3651            | 0.8950               |
| D    | 0.1895            | 0.5326            | 0.8950               | D    | 0.3946            | 1.3651            | -0.8950              |
| D    | 0.1895            | 0.5326            | -0.8950              | H    | -0.0373           | 0.3562            | 0.0000               |
| C    | 0.2011            | 0.9102            | 0.0000               | D    | 0.4002            | 1.6732            | 0.0000               |
|      |                   |                   |                      | H    | -0.0030           | 0.4952            | 0.0000               |

Table A-11 C6:1 t-2 amide ( $p2$  phase)

| Atom | X <sub>frac</sub> | Y <sub>frac</sub> | Z <sub>abs</sub> (Å) | Atom | X <sub>frac</sub> | Y <sub>frac</sub> | Z <sub>abs</sub> (Å) |
|------|-------------------|-------------------|----------------------|------|-------------------|-------------------|----------------------|
| O    | -0.0539           | -0.1063           | 0.0000               | C    | 0.1906            | 0.1760            | 0.0000               |
| N    | -0.0235           | 0.3148            | 0.0000               | C    | 0.2405            | 0.3939            | 0.0000               |
| C    | -0.0064           | 0.0743            | 0.0000               | H    | 0.2304            | 0.5106            | 0.8950               |
| H    | 0.0973            | -0.1747           | 0.0000               | H    | 0.2304            | 0.5106            | -0.8950              |
| C    | 0.0682            | 0.0056            | 0.0000               | C    | 0.3151            | 0.3251            | 0.0000               |
| C    | 0.1150            | 0.2119            | 0.0000               | H    | 0.3252            | 0.2084            | 0.8950               |
| H    | 0.1017            | 0.4176            | 0.8950               | H    | 0.3252            | 0.2084            | -0.8950              |
| H    | 0.1017            | 0.4176            | -0.8950              | H    | -0.0750           | 0.3622            | 0.0000               |
| H    | 0.2016            | 0.0485            | 0.8950               | H    | 0.0103            | 0.4727            | 0.0000               |
| H    | 0.2016            | 0.0485            | -0.8950              |      |                   |                   |                      |

Table A-12 C6:1 t-3 ( $p2$  phase)

| Atom | X <sub>frac</sub> | Y <sub>frac</sub> | Z <sub>abs</sub> (Å) | Atom | X <sub>frac</sub> | Y <sub>frac</sub> | Z <sub>abs</sub> (Å) |
|------|-------------------|-------------------|----------------------|------|-------------------|-------------------|----------------------|
| O    | -0.0530           | -0.1071           | 0.0000               | H    | 0.2008            | -0.0309           | -0.8950              |
| N    | -0.0267           | 0.3201            | 0.0000               | H    | 0.2259            | 0.5148            | 0.8950               |
| C    | -0.0072           | 0.0756            | 0.0000               | H    | 0.2259            | 0.5148            | -0.8950              |
| H    | 0.0796            | -0.1142           | 0.8950               | C    | 0.2382            | 0.3851            | 0.0000               |
| H    | 0.0796            | -0.1142           | -0.8950              | C    | 0.3127            | 0.3250            | 0.0000               |
| C    | 0.0683            | 0.0046            | 0.0000               | H    | 0.3240            | 0.2063            | 0.8950               |
| H    | 0.0842            | 0.4196            | 0.0000               | H    | 0.3240            | 0.2063            | -0.8950              |
| C    | 0.1151            | 0.2360            | 0.0000               | H    | -0.0789           | 0.3692            | 0.0000               |
| C    | 0.1853            | 0.1782            | 0.0000               | H    | 0.0056            | 0.4799            | 0.0000               |
| H    | 0.2008            | -0.0309           | 0.8950               |      |                   |                   |                      |

Table A-13 C9: t-2 amide ( $p2$  phase)

| Atom | X <sub>frac</sub> | Y <sub>frac</sub> | Z <sub>abs</sub> (Å) | Atom | X <sub>frac</sub> | Y <sub>frac</sub> | Z <sub>abs</sub> (Å) |
|------|-------------------|-------------------|----------------------|------|-------------------|-------------------|----------------------|
| O    | 0.0340            | -0.2555           | 0.0000               | C    | 0.3189            | 0.2980            | 0.0000               |
| N    | 0.0574            | 0.1695            | 0.0000               | H    | 0.3264            | 0.1861            | 0.8950               |
| C    | 0.0699            | -0.0621           | 0.0000               | H    | 0.3264            | 0.1861            | -0.8950              |
| H    | 0.1496            | -0.2756           | 0.0000               | C    | 0.3572            | 0.5474            | 0.0000               |
| C    | 0.1279            | -0.1072           | 0.0000               | H    | 0.3497            | 0.6593            | 0.8950               |
| C    | 0.1632            | 0.1138            | 0.0000               | H    | 0.3497            | 0.6593            | -0.8950              |
| H    | 0.1531            | 0.3117            | 0.8950               | C    | 0.4152            | 0.5023            | 0.0000               |
| H    | 0.1531            | 0.3117            | -0.8950              | H    | 0.4227            | 0.3904            | 0.8950               |
| H    | 0.2301            | -0.0182           | 0.8950               | H    | 0.4227            | 0.3904            | -0.8950              |
| H    | 0.2301            | -0.0182           | -0.8950              | C    | 0.4535            | 0.7517            | 0.0000               |
| C    | 0.2219            | 0.1043            | 0.0000               | H    | 0.4461            | 0.8636            | 0.8950               |
| C    | 0.2609            | 0.3431            | 0.0000               | H    | 0.4461            | 0.8636            | -0.8950              |
| H    | 0.2534            | 0.4550            | 0.8950               | H    | 0.0186            | 0.1997            | 0.0000               |
| H    | 0.2534            | 0.4550            | -0.8950              | H    | 0.0830            | 0.3362            | 0.0000               |

Table A-14 C11:1 c-10 amide ( $p2$  phase)

| Atom | X <sub>frac</sub> | Y <sub>frac</sub> | Z <sub>abs</sub> (Å) | Atom | X <sub>frac</sub> | Y <sub>frac</sub> | Z <sub>abs</sub> (Å) |
|------|-------------------|-------------------|----------------------|------|-------------------|-------------------|----------------------|
| O    | -0.0326           | -0.0923           | 0.0000               | C    | 0.1983            | 0.2673            | 0.0000               |
| N    | -0.0166           | 0.3223            | 0.0000               | H    | 0.2209            | 0.6118            | 0.8950               |
| C    | -0.0046           | 0.0783            | 0.0000               | H    | 0.2209            | 0.6118            | -0.8950              |
| H    | 0.0503            | -0.1281           | 0.8950               | C    | 0.2279            | 0.4929            | 0.0000               |
| H    | 0.0503            | -0.1281           | -0.8950              | H    | 0.2827            | 0.2866            | 0.8950               |
| C    | 0.0433            | -0.0092           | 0.0000               | H    | 0.2827            | 0.2866            | -0.8950              |
| H    | 0.0659            | 0.3354            | 0.8950               | C    | 0.2758            | 0.4055            | 0.0000               |
| H    | 0.0659            | 0.3354            | -0.8950              | H    | 0.2984            | 0.7501            | 0.8950               |
| C    | 0.0729            | 0.2165            | 0.0000               | H    | 0.2984            | 0.7501            | -0.8950              |
| H    | 0.1278            | 0.0102            | 0.8950               | C    | 0.3053            | 0.6312            | 0.0000               |
| H    | 0.1278            | 0.0102            | -0.8950              | H    | 0.3723            | 0.3573            | 0.0000               |
| C    | 0.1208            | 0.1291            | 0.0000               | C    | 0.3532            | 0.5437            | 0.0000               |
| H    | 0.1434            | 0.4736            | 0.8950               | C    | 0.3806            | 0.7427            | 0.0000               |
| H    | 0.1434            | 0.4736            | -0.8950              | H    | 0.4155            | 0.7178            | 0.0000               |
| C    | 0.1504            | 0.3547            | 0.0000               | H    | -0.0486           | 0.3807            | 0.0000               |
| H    | 0.2052            | 0.1484            | 0.8950               | H    | 0.0031            | 0.4730            | 0.0000               |
| H    | 0.2052            | 0.1484            | -0.8950              | H    | 0.3701            | 0.9499            | 0.0000               |

Table A-15 C12:1 c-5 amide (*p*2 phase)

| Atom | X <sub>frac</sub> | Y <sub>frac</sub> | Z <sub>abs</sub> (Å) | Atom | X <sub>frac</sub> | Y <sub>frac</sub> | Z <sub>abs</sub> (Å) |
|------|-------------------|-------------------|----------------------|------|-------------------|-------------------|----------------------|
| O    | -0.0293           | -0.1179           | 0.0000               | C    | 0.3874            | -0.3812           | 0.0000               |
| N    | -0.0195           | 0.3061            | 0.0000               | H    | 0.2684            | 0.3556            | 0.8950               |
| C    | -0.0054           | 0.0757            | 0.0000               | H    | 0.2684            | 0.3556            | -0.8950              |
| H    | 0.0495            | -0.0808           | 0.8950               | H    | 0.2524            | -0.2634           | 0.8950               |
| H    | 0.0495            | -0.0808           | -0.8950              | H    | 0.2524            | -0.2634           | -0.8950              |
| C    | 0.0416            | 0.0305            | 0.0000               | H    | 0.3372            | 0.0738            | 0.8950               |
| H    | 0.0593            | 0.3993            | 0.8950               | H    | 0.3372            | 0.0738            | -0.8950              |
| H    | 0.0593            | 0.3993            | -0.8950              | H    | 0.3213            | -0.5452           | 0.8950               |
| C    | 0.0672            | 0.2880            | 0.0000               | H    | 0.3213            | -0.5452           | -0.8950              |
| H    | 0.1221            | 0.1316            | 0.8950               | H    | 0.4061            | -0.2080           | 0.8950               |
| H    | 0.1221            | 0.1316            | -0.8950              | H    | 0.4061            | -0.2080           | -0.8950              |
| C    | 0.1142            | 0.2429            | 0.0000               | H    | -0.0499           | 0.3353            | 0.0000               |
| H    | 0.1198            | 0.6677            | 0.0000               | H    | -0.0030           | 0.4727            | 0.0000               |
| C    | 0.1397            | 0.5004            | 0.0000               | H    | 0.3710            | -0.5636           | 0.0000               |
| C    | 0.1809            | 0.4643            | 0.0000               | C    | 0.2497            | 0.1825            | 0.0000               |
| H    | 0.2033            | 0.6176            | 0.0000               | C    | 0.2711            | -0.0903           | 0.0000               |
| H    | 0.1836            | 0.0184            | 0.8950               | C    | 0.3186            | -0.0994           | 0.0000               |
| H    | 0.1836            | 0.0184            | -0.8950              | C    | 0.3399            | -0.3721           | 0.0000               |
| C    | 0.2022            | 0.1916            | 0.0000               |      |                   |                   |                      |

## B. Sample purities

---

As explained in §6.4, consistent efforts have been made in this work to estimate and improve the purities of the amide samples to ensure that experimental results are not affected by the presence of impurities. The purities of the amides, both prepared and purchased, have been assessed by  $^1\text{H}$  (and  $^{13}\text{C}$ ) NMR, elemental analysis and liquid chromatography/mass spectrometry (LC/MS). The combined results of these analytical tests were used to assess the final purity of the sample, as will be shown below.

The results of the different tests for each of the amide samples used in this work are detailed below. For the elemental analysis results, masses of each of the elements are expressed as a percentage of the total, and the ratios of carbon to nitrogen atoms for each amide are shown. The deviation of this ratio with the expected value was used to estimate purity (as a percentage).

The  $^1\text{H}$  NMR results show the peak positions (in ppm) of each of the protons in the amide molecule, and numbers in brackets are the approximate areas under the NMR peaks, written in terms of the number of protons. For  $^{13}\text{C}$  NMR, the peak positions are given for the different carbon atoms.

LC/MS values are in mass/charge. The amounts (%) of the different eluted fractions refer to the total ion current of that fraction relative to the total ion current of all fractions, estimated from

the areas of the features in the chromatography data. The amounts within each fraction (%) refer to the current of the ion relative to the largest contributor in that fraction at 100%.

## Results

### SATURATED SAMPLES

#### Valeric acid amide (C5:0) – prepared

Elemental analysis (average of two runs) C% 59.41, H% 11.03, N% 13.865: C/N = 5.00. Purity 99.93%  
<sup>1</sup>H NMR CDCl<sub>3</sub> solvent 7.2ppm, CONH<sub>2</sub> 5.7ppm (2), CH<sub>2</sub>-CO<sub>2</sub> 2.2ppm (2), CH<sub>2</sub>-CH<sub>3</sub> 1.6ppm (2), CH<sub>2</sub>-CH<sub>2</sub> 1.38 ppm (2) and -CH<sub>3</sub> 0.9 ppm (3).  
 LC/Mass spec Positive ion: Main peak (M+1) 101.97(100%). (M+1+<sup>13</sup>C) 103.28 (3%).  
 C<sub>5</sub>H<sub>11</sub>NO = 101 No evidence of other homologues.

#### Hexanoic acid amide (C6:0) – purchased

From certificate of analysis Aldrich product number 293393, batch 11128AD, purity GC 99.9%, IR conforms  
 Elemental analysis C% 62.72, H% 11.62, N% 12.175: C/N = 6.01. Purity 99.9%  
<sup>1</sup>H NMR CDCl<sub>3</sub> solvent 7.2ppm, multiplet CONH<sub>2</sub> 5.5ppm (2), triplet CH<sub>2</sub>-CO<sub>2</sub> 2.2ppm (2), multiplet CH<sub>2</sub>-CH<sub>3</sub> 1.65ppm (2), broad feature and multiplet CH<sub>2</sub>-CH<sub>2</sub> 1.3 ppm (4) and triplet -CH<sub>3</sub> 0.89 ppm (3). Possible weak impurity peak at 1.8ppm (0.19 protons)

#### Heptanoic acid amide (C7:0) – prepared

Elemental analysis C% 64.93, H% 11.70, N% 10.77: C/N = 7.03. Purity 99.57%  
<sup>1</sup>H NMR CDCl<sub>3</sub> solvent 7.3ppm, CONH<sub>2</sub> (doublet) 5.92ppm (2), CH<sub>2</sub>-CO<sub>2</sub> (triplet) 2.2ppm (2), CH<sub>2</sub>-CH<sub>3</sub> 1.6ppm (2) (multiplet), CH<sub>2</sub>-CH<sub>2</sub> (multiplet) 1.34 ppm (6) and -CH<sub>3</sub> (triplet) 0.9 ppm (3).  
 LC/MS Main peak 130.12 (M+1) (100%)  
 C<sub>7</sub>H<sub>15</sub>NO = 129 No evidence of other homologues.

<sup>13</sup>C NMR (CDCl<sub>3</sub> solvent) C=O 175.7 ppm, alkyl peaks at 35.9 ppm, 31.5 ppm, 28.9 ppm, 25.5 ppm, 22.5, ppm, 14.0 ppm  
No evidence of other homologues.

**Octanoic (caprylic) acid amide (C8:0) – prepared**

Elemental analysis (average of two runs) C% 67.13, H% 12.05, N% 9.83: C/N = 7.97. Purity 99.55%

<sup>1</sup>H NMR CDCl<sub>3</sub> solvent 7.2ppm, CONH<sub>2</sub> 5.7ppm (2), CH<sub>2</sub>-CO<sub>2</sub> 2.2ppm (2), CH<sub>2</sub>-CH<sub>3</sub> 1.6ppm (2), CH<sub>2</sub>-CH<sub>2</sub> 1.38 ppm (8) and -CH<sub>3</sub> 0.9 ppm (3).

LC/Mass spec Positive ion: Main peak (M+1) 144.31 (100%). (M+1+<sup>13</sup>C) 145.45 (5%).  
C<sub>8</sub>H<sub>17</sub>NO = 143 (M+42) 185.5 (11%). No evidence of other homologues.

**Nonanoic acid amide (C9:0) – prepared**

Elemental analysis (average of two runs) C% 68.48, H% 11.99, N% 8.75: C/N = 9.13. Purity 98.68%

<sup>1</sup>H NMR CDCl<sub>3</sub> solvent 7.25ppm, CONH<sub>2</sub> multiplet 5.4ppm (2), triplet CH<sub>2</sub>CO 2.2ppm (2), Multiplet CH<sub>2</sub>-CH<sub>3</sub> 1.62ppm (2), broad feature and multiplet CH<sub>2</sub>-CH<sub>2</sub> 1.3ppm (10) and triplet -CH<sub>3</sub> 0.86ppm (3).

LC/MS Main peak 158.31 (M+1) (100%)

C<sub>9</sub>H<sub>19</sub>NO = 157 No evidence of other homologues.

<sup>13</sup>C NMR (CDCl<sub>3</sub> solvent) C=O 175.7 ppm, alkyl peaks at 35.9 ppm, 31.8 ppm, 29.3 ppm, 29.1 ppm, 25.5 ppm, 22.6 ppm, 14.1 ppm

**Decanamide (C10:0) – prepared**

Elemental analysis (average of two runs) C% 70.06, H% 12.55, N% 8.26: C/N = 9.89. Purity 98.91%

<sup>1</sup>H NMR CDCl<sub>3</sub> solvent 7.2ppm, CONH<sub>2</sub> (doublet) 5.7ppm (2), CH<sub>2</sub>-CO<sub>2</sub> (triplet) 2.2ppm (2), CH<sub>2</sub>-CH<sub>3</sub> 1.6ppm (2) (multiplet), CH<sub>2</sub>-CH<sub>2</sub> (multiplet) 1.38 ppm (12) and -CH<sub>3</sub> (triplet) 0.9 ppm (3).

|  |  |
|--|--|
| LC/Mass spec Positive ion:   | Four fractions eluted:   |
| $C_{10}H_{21}NO = 171$   | First fraction (2%): 144.26 (100%), 171.44 (83%).  |
| Conclusion: mainly desired material with small amounts of unsaturated and longer impurities. | Second, main fraction (75%): Main peak (M+1) 172.4(100%). (M+42) 213.53, (M+42+ $^{13}C$ ) 214.58. |
|  | Third fraction (10%): (M-2+1) 170.39 (100%)  |
|  | Fourth fraction (12%): 326.72 (100%)   |

**Undecanamide (C11:0) – prepared**

|  |  |
|--|--|
| Elemental analysis (average of two runs) | C% 70.44, H% 12.19, N% 7.04: C/N = 11.67. Purity 93.94%  |
| $^1H$ NMR                                | $CDCl_3$ solvent 7.25ppm, $CONH_2$ multiplet 5.4ppm (2), triplet $CH_2CO$ 2.2ppm (2), Multiplet $CH_2-CH_3$ 1.62ppm (2), broad feature and multiplet $CH_2-CH_2$ 1.28ppm (14) and triplet $-CH_3$ 0.86ppm (3). |
| LC/MS                                    | Main peak 186.5 (M+1) (100%)   |
| $C_{11}H_{23}NO = 185.3$                 | No evidence of other homologues.   |
| $^{13}C$ NMR ( $CDCl_3$ solvent)         | C=O 175.7 ppm, alkyl peaks at 35.9 ppm, 31.9 ppm, 29.6 ppm, 29.5 ppm, 29.3, ppm, 29.2 ppm, 29.1 ppm, 25.5 ppm, 22.7 ppm, 14.1 ppm  |
|  | No evidence of other homologues.   |

**Dodecanamide (C12:0) – purchased**

|  |  |
|--|--|
| Elemental analysis (average of two runs) | C% 72.24, H% 12.80, N% 7.045: C/N = 11.96. Purity 99.64%   |
| $^1H$ NMR                                | $CDCl_3$ solvent 7.2ppm, $CONH_2$ (doublet) 5.7ppm (2), $CH_2-CO_2$ (triplet) 2.2ppm (2), $CH_2-CH_3$ 1.6ppm (2) (multiplet), $CH_2-CH_2$ (multiplet) 1.38 ppm (16) and $-CH_3$ (triplet) 0.9 ppm (3). |
| LC/Mass spec Negative ion:               | Main peak (M-1) 198.18 (100%). (M-1+ $^{13}C$ ) 199.45 (13%), 234.16 (11%), 244.19 (8%), 274.2 (8%).   |
| $C_{12}H_{25}NO = 199$                   | No evidence of other homologues.   |
| $^{13}C$ NMR ( $CDCl_3$ solvent)         | C=O 175.7 ppm, alkyl peaks at 36.0 ppm, 31.9 ppm, 29.6 ppm, 29.5 ppm, 29.3, ppm, 29.2 ppm, 29.1 ppm, 25.5 ppm, 22.7 ppm, 14.1 ppm (1 alkyl carbon peak unresolved)                                     |
|  | No evidence of other homologues.   |

**Tetradecanamide (C14:0) – purchased**

|   |  |
|---|--|
| Elemental analysis (average of two runs)  | C% 74.16, H% 12.985, N% 6.2: C/N = 13.95. Purity 99.62%  |
| <sup>1</sup> H NMR  | CDCl <sub>3</sub> solvent 7.2ppm, CONH <sub>2</sub> 5.7ppm (2), CH <sub>2</sub> -CO <sub>2</sub> 2.2ppm (2), CH <sub>2</sub> -CH <sub>3</sub> 1.65ppm (2), CH <sub>2</sub> -CH <sub>2</sub> 1.38 ppm (20) and -CH <sub>3</sub> 0.9 ppm (3).  |
| LC/Mass spec Positive ion:  | Five fractions eluted  |
| C <sub>14</sub> H <sub>29</sub> NO = 227  | First fraction (1%): 172.48 (M-4CH <sub>2</sub> +1) (100%), 213.6 (M+42) (75%), 177.37 (39%)   |
| Conclusion: mainly desired component with both longer and shorter homologues (+/- 2CH <sub>2</sub> , +/- 4CH <sub>2</sub> ) and some doubly unsaturated material. | Second fraction (10%): 200.56 (M-2CH <sub>2</sub> +1) (100%), 242.64 (M-2CH <sub>2</sub> +42 (75%), 227.63 (M-2+1) (50%).<br>Third fraction (70%): (M+1) 228.64 (100%). (M+1+ <sup>13</sup> C) 229.65 (14%). (2M+1) 455.91 (29%), (M+42) 269.68 (79%).<br>Fourth fraction (15%): 256.69 (M+2CH <sub>2</sub> +1) (93%), 297.74 (M+2CH <sub>2</sub> +CH <sub>3</sub> CN+1) (100%)<br>Fifth fraction (5%): 284.73 (M+4CH <sub>2</sub> +1) (83%), 325.77 (M+4CH <sub>2</sub> +42) (100%) |

**Hexadecanamide (C16:0) – purchased**

|  |  |
|--|--|
| Elemental analysis (average of two runs)   | C% 75.10, H% 13.22, N% 5.41: C/N = 16.19. Purity 92.18%  |
| <sup>1</sup> H NMR   | CDCl <sub>3</sub> solvent 7.29ppm, CONH <sub>2</sub> 5.4ppm (2), CH <sub>2</sub> -CO <sub>2</sub> 2.2ppm (2), CH <sub>2</sub> -CH <sub>3</sub> 1.65 (2), CH <sub>2</sub> -CH <sub>2</sub> 1.38 ppm (24) and -CH <sub>3</sub> 0.9 ppm (3).  |
| LC/MS  | Three fractions:   |
| C <sub>16</sub> H <sub>33</sub> NO = 255   | First fraction (9%): 228.64 (M-2CH <sub>2</sub> +1) (100%), 242.66 (M-CH <sub>2</sub> +1) (43%), 283.72 (M-CH <sub>2</sub> +CH <sub>3</sub> CN+1) (45%).   |
| Conclusion: mainly desired material with shorter and longer homologue (+/- CH <sub>2</sub> ) impurities. | Second Fraction (74%): Main peak (M+1) 256.7(100%). (M+1+ <sup>13</sup> C) 257.71 (14%), Dimer (2M+1) 511.97 (40%), (2M+1+ <sup>13</sup> C) 512.97 (14%). (M+CH <sub>3</sub> CN+1) 297.74 (79%), 298.75 (M+42+ <sup>13</sup> C) (16%).<br>Third Fraction (17%): 284.73 (M+CH <sub>2</sub> +1) (90%), 325.79 (M+CH <sub>2</sub> +42) (100%) |

## UNSATURATED SAMPLES

**C6:1 t-2 amide – prepared**

|   |  |
|---|--|
| Elemental Analysis (Average of two runs)        | C 61.15%, H 9.45%, N 11.95%: C/N = 5.97. Purity 99.5%  |
| <sup>1</sup> H NMR                              | CDCl <sub>3</sub> solvent 7.25ppm, Multiplet <b>CH-CH</b> 6.8 ppm (1), Doublet <b>CH-CO</b> 5.8 ppm (1), <b>CONH<sub>2</sub></b> broad feature 5.6 ppm (2), multiplet <b>CH-CH<sub>2</sub></b> 2.1 ppm (2), Quartet <b>CH<sub>2</sub>-CH<sub>3</sub></b> 1.4 ppm (2), and triplet <b>-CH<sub>3</sub></b> 0.9 ppm (3). Possible weak impurity peaks at: 4.4ppm (~0.09), 2.7ppm (~0.17). |
| LC/MS   | Three fractions eluted   |
| C <sub>6</sub> H <sub>11</sub> NO = 113.2       | First fraction (92.2%): 114 (M+1) (100%), 96.7 (M-17) (25%)<br>Second fraction (5.6%): 150.2 (100%), 152.2 (40%)<br>Third fraction (2.2%): 210.4 (100%). (M-CH <sub>3</sub> CN+1) 168.3<br>Mainly desired material   |
| <sup>13</sup> C NMR (CDCl <sub>3</sub> solvent) | C=O 168.0 ppm, C=C at 146.9 ppm and 122.4 ppm, alkyl peaks at 40.2 ppm, 34.1 ppm, 13.7 ppm. Impurity peaks at 171.6 ppm, 58.5 ppm, 45.1 ppm, 42.0 ppm, 19.6 ppm, 13.4 ppm<br>Mainly desired material with some saturated impurity  |

**C6:1 t-3 amide – prepared**

|   |  |
|---|--|
| Elemental Analysis (Average of two runs)        | C 62.83%, H 9.62%, N 12.18%: C/N = 6.02. Purity 99.75%   |
| <sup>1</sup> H NMR                              | CDCl <sub>3</sub> solvent 7.25ppm, Multiplet <b>CH-CH<sub>2</sub></b> 5.7 ppm (1), <b>CONH<sub>2</sub></b> broad feature 5.6 ppm (2), Multiplet <b>CH-CH<sub>2</sub></b> 5.5 ppm (1), doublet <b>CH<sub>2</sub>-CO</b> 2.9 ppm (2), Quintet <b>CH<sub>2</sub>-CH<sub>3</sub></b> 2 ppm (2) and triplet <b>-CH<sub>3</sub></b> 0.9 ppm (3). |
| LC/MS   | Main peak 114 (M+1) (100%), 96.7 (M-17) (25%)  |
| C <sub>6</sub> H <sub>11</sub> NO = 113.2       | No evidence of other homologues.   |
| <sup>13</sup> C NMR (CDCl <sub>3</sub> solvent) | C=O 174.0 ppm, C=C at 138.1 ppm and 121.4 ppm, alkyl peaks at 39.9 ppm, 25.5 ppm, 13.5 ppm<br>No evidence of other homologues.   |

**C9:1 t-2 amide – prepared**

|   |   |
|---|---|
| Elemental Analysis (Average of two runs)        | C 69.20%, H 10.94%, N 9.03%: C/N = 8.94. Purity 99.28%  |
| <sup>1</sup> H NMR                              | CDCl <sub>3</sub> solvent 7.25ppm, Multiplet CH-CH 6.8 ppm (1), doublet CH-CO 5.8 ppm (1), CONH <sub>2</sub> broad peak 5.4 ppm (2), Quartet CH <sub>2</sub> -CH 2.2 ppm (2), Multiplet CH <sub>2</sub> -CH <sub>3</sub> 1.4 ppm (2), Broad feature and multiplet -CH <sub>2</sub> - 1.2 ppm (6), triplet CH <sub>3</sub> 0.8 ppm (3) |
| LC/MS   | Two fractions eluted  |
| C <sub>9</sub> H <sub>17</sub> NO = 155.2       | First fraction (4.8%): 130.1 (M+1) (100%), 171.4 (55%)<br>Second fraction (95.2%): (M+1) 156.2 (100%), (M+CH <sub>3</sub> CN+1) 197.5 (40%)   |
| <sup>13</sup> C NMR (CDCl <sub>3</sub> solvent) | C=O 168.1 ppm, C=C at 147.2 ppm and 122.2 ppm, alkyl peaks at 32.1 ppm, 31.6 ppm, 28.8 ppm, 28.1 ppm, 22.6 ppm, 14.1 ppm.   |

**C11:1 c-10 amide – prepared**

|  |   |
|--|---|
| Elemental Analysis (Average of two runs)                       | C 71.88%, H 11.64%, N 7.7%: C/N = 10.90. Purity 98.96%  |
| <sup>1</sup> H NMR   | Solvent 7.2 ppm, CONH <sub>2</sub> 5.4ppm (2), CH <sub>2</sub> =CH- 5.8ppm (1) and 4.9 ppm (2), triplet CH <sub>2</sub> -CO <sub>2</sub> 2.2ppm (2), 2.0ppm (2), 1.6 ppm (2), broad multiplet CH <sub>2</sub> -CH <sub>2</sub> 1.3 ppm (10) |
| LC/MS  | Four fractions:   |
| C <sub>11</sub> H <sub>21</sub> NO = 183                       | First fraction (4%): 183.47 (M-1+1) (100%)<br>Second main fraction (60%): 184.45 (M+1) (100%). 149.29.  |
| Conclusion: mainly desired material with some longer material. | Third fraction (7%): 149.21, 205.46, 397.71, 433.61, 471.64<br>Fourth fraction (28%): 184.47 (M+1), 368.73 (2M+1), 433.68, 617.79.  |

**C12:1 c-5 amide – prepared**

|                    |   |
|--------------------|---|
| Elemental Analysis | C 72.49%, H 11.38%, N 7.17%: C/N = 11.79. Purity 98.25% |
|--------------------|---|

|   |  |
|---|--|
| <sup>1</sup> H NMR  | Solvent 7.2 ppm and 1.55ppm, multiplet CONH <sub>2</sub> and –CH=CH- 5.3ppm (4), triplet CH <sub>2</sub> -CO <sub>2</sub> 2.2ppm (2), 2.0ppm (4), multiplet 1.6 ppm (2), broad multiplet CH <sub>2</sub> -CH <sub>2</sub> 1.3 ppm (24) and triplet -CH <sub>3</sub> 0.87 ppm (3).                |
| <sup>13</sup> C NMR (CDCl <sub>3</sub> solvent)   | C=O 175.2 ppm, C=C at 131.3 ppm and 128.4 ppm, alkyl peaks at 35.2 ppm, 31.8 ppm, 29.7 ppm, 29.0, ppm, 27.3 ppm, 26.5 ppm, 25.4 ppm, 22.6 ppm, 14.1 ppm<br>No evidence of other homologues.  |
| LC/MS<br>C <sub>12</sub> H <sub>23</sub> NO = 197   | Main peak 198.5 (M+1) (100%), 181.4 (M-17) 20%<br>No evidence of other homologues.   |
| <b>C22:1 c-13 (erucamide) – purchased</b>   | Aldrich 280577 batch 09207PO<br>From certificate of analysis:<br>Elemental: C 78.33%, H 12.59%, N 4.09%, Purity 99.68%<br>GL chromatography 88.0%, IR conforms to structure  |
| <sup>1</sup> H NMR  | Solvent 7.2 ppm, multiplet CONH <sub>2</sub> and –CH=CH- 5.3ppm (4), triplet CH <sub>2</sub> -CO <sub>2</sub> 2.2ppm (2), multiplet 2.0ppm (4), multiplet 1.6 ppm (2), broad multiplet CH <sub>2</sub> -CH <sub>2</sub> 1.3 ppm (28) and triplet -CH <sub>3</sub> 0.87 ppm (3).                  |
| LC/Mass spec Positive ion:<br>C <sub>22</sub> H <sub>41</sub> NO = 335<br>Conclusion: desired material with some significant amount of saturated and doubly unsaturated impurities. | First broad fraction (22%): 334.74 (M-2+1), 317.75, 282.71, 280.68, 263.65, 278.65, 261.57.<br>Second fraction (12%): 336.77 (M+1) (100%), (M+1+ <sup>13</sup> C) 337.76 (21%), 672.04 (2M+1) (30%). 310.76 (66%)<br>Third, main fraction (66%): 338.77 (M+2+1), 339.77 (M+2+1+ <sup>13</sup> C) |

## Discussion

### NMR

All NMR data indicate no evidence of unreacted acid groups which are evident in the starting materials. NMR peaks for most samples can be assigned with quantitatively correct proton ratios (within experimental error) based on the expected structure, and weak amounts of impurities are detected by NMR data for some of the samples.

### Elemental analysis

The elemental analysis data can be used to determine the ratio of carbon to nitrogen atoms in the samples. This provides an indication of the presence of other alkyl homologues in the samples, and can be used to estimate the purity of the sample based on deviations from the expected ratio. From the results, most of the samples have a C/N ratio in agreement with that expected to within 5%.

### Liquid Chromatography/Mass Spectrometry

The most common ions present in the positive ion detection mode refer to: (M+1) the expected mass of the desired sample +1 mass unit, (M+1+<sup>13</sup>C) the expected mass of the desired component with <sup>13</sup>C isotope +1, (2M+1) the dimer of the desired sample, and (2M+1+<sup>13</sup>C) the dimer of the desired sample with a <sup>13</sup>C isotope +1. (M+42) is assigned as an adduct of the desired material with acetonitrile (CH<sub>3</sub>CN+H) from the solvent system used in the HPLC. The LC/MS measurements were made sometime after the thermodynamic measurements and although samples were kept refrigerated there is the possibility that some degradation may have occurred.

The general conclusion that can be drawn from the LC/MS data is that the majority of saturated samples are essentially pure. The unsaturated samples are also reasonably pure materials but some indicate the presence of other homologues and doubly unsaturated materials.

## Summary

The final purity estimates for the amides were made comparing the C:N ratio from the elemental analysis results to the expected value. These have been noted for each of the samples above, and a majority of the samples have a very high level of purity. NMR combined with LC/MS give some indication of the nature of the impurity for some of the samples.

In the context of the present work, the impurities that may have most influence on any adsorbed surface layer are of most concern. In general, it has been found that only longer homologues are preferentially adsorbed in a mixture. Any significant surface enhancement effect is also minimised by the relatively small total amount of adsorbate present in the sample that will also restrict the total amount of any impurity on the surface. Indeed, samples for all diffraction measurements were below a monolayer in coverage, and all DSC samples were at most 10 monolayers in coverage. This implies that the effect of any impurities is not expected to have a significant effect on the observed surface behaviour, given the high level of purity of almost all of the samples.